Magnetotelluric and Controlled-Source Electromagnetic Pre-Injection Study of Aquistore CO_2 Sequestration Site, Near Estevan, Saskatchewan, Canada

By
Joseph McLeod

A Thesis submitted to the Faculty of Graduate Studies of
The University of Manitoba
In partial fulfilment of the requirements of the degree of

MASTER OF SCIENCE

Clayton H. Riddell Faculty of Environment, Earth, and Resources
Department of Geological Sciences
University of Manitoba
Winnipeg, Manitoba
October 2016

Abstract

Surface electromagnetic (EM) methods were tested prior to CO_2 injection at the PTRC Aquistore site at Estevan, Saskatchewan to determine their applicability to carbon sequestration monitoring.

Magnetotelluric surveys in 2013, 2014 and 2015 resulted in successful definition of the pre-injection response and electrical resistivity model for the Williston Basin at Aquistore. These datasets define spatially uniform MT responses with a high level of repeatability.

Controlled-source EM (CSEM) studies using a horizontal electric dipole transmitter have also been implemented at Aquistore. Preliminary analyses demonstrate that the CSEM experiment is well-designed, with measurable signal levels at all sites and a configuration that maximizes sensitivity to the sequestration reservoir. However, theoretical sensitivity modeling indicates that extremely large volumes of injected CO_2 are required to produce measurable anomalies in the CSEM response. Greater sensitivity of both magnetotellurics and CSEM to the resistivity of shallower strata suggests these methodologies have superior application in leakage monitoring.

Summary

Aquistore is an independent research and monitoring project managed by the Petroleum Technology Research Centre (PTRC), which intends to demonstrate that storing carbon dioxide (CO_2) deep underground into a sandstone formation is a safe, workable solution to reduce greenhouse gases. The project is located near Estevan, in southeastern Saskatchewan, where CO_2 is being captured from the Boundary Dam power station, and injected to the base of the Phanerozoic Williston Basin to be stored in a saline aquifer at 3.4 km depth. In this study, magnetotelluric (MT) and surface controlled-source electromagnetic (CSEM) methods are tested in a pre-injection setting at Aquistore for their applicability to sequestration monitoring goals. The MT and CSEM methods are complementary in their ability to resolve structures at different scales using different current systems.

Pre-injection MT soundings were conducted in 2013, 2014 and 2015 over a 2.5 km × 8.5 km area surrounding the Aquistore injection well. The resistivity structure of the Phanerozoic is one-dimensional and spatially uniform from 0.001 to 10 s: the apparent resistivity decreases from ~8 Ωm to ~2 Ωm in this period range. Spectral and polarization analyses indicate that broadband noise in period bands of 0.05 to 1 s and 0.0077 to 0.0125 s recorded in 2014 is associated with a CO_2 pipeline. At frequencies outside these bands, the MT responses define small differences between surveys (< 3%). Using an optimal MT response from these datasets and constraints from a resistivity well-log, a 1D inversion has recovered a representative 18-layer resistivity model for the Williston Basin sedimentary sequence for the study area. From 1D modeling, the MT method shows limited sensitivity to changes in the reservoir layer. Shallower units such as the Upper Watrous demonstrate greater sensitivity.

CSEM surveys in 2013 and 2015 used a 1 km, 30 A electric horizontal dipole source. Recordings of the radial electric field component were made along an inline receiver profile at offsets up to 9.5 km. Preliminary characterization of these recordings indicates that the transmitted signals are observable at each of the profile locations.

Fréchet derivatives of the CSEM response indicate sensitivity of the response to changes in the Williston Basin electrical properties at the level of the reservoir. Intermediate induction number soundings achieve sensitivity of the apparent resistivity and phase responses to changes in the log conductivity at the depth of the reservoir on the order of 0.012 Ωm/m and 0.22^{o}/m at a transmission frequency of 0.5 Hz and offsets of 7.5-9.5 km.

One-dimensional CSEM modeling of a CO_2 saturated 50 Ωm reservoir layer indicates that CO_2 injection would cause a phase change of ~4.5˚, which should be measurable using reasonable experimental conditions. Three-dimensional modeling shows that the 50 Ωm CO_2 plume would need to have a diameter of ~5 km for the scattered fields to produce a phase anomaly of 1.94˚ and ~3 km for an anomaly of 0.75 ˚, the probable smallest level of detection. The surface CSEM methodology is more optimally suited for monitoring for CO_2 leakage into shallower, relatively conductive geological formations such as the Colorado and Upper Watrous Formations at depths of 1,000 to 1,500 m.

Acknowledgements

First and foremost, my thanks go to my co-advisors, Ian Ferguson and Jim Craven, each of whom have invested a large amount of time and energy into this project and into my education. Without their mentorship, I could not have realized this achievement.

I am indebted to several individuals who have aided in the fieldwork for this project: Brian Roberts, Jason Silliker, Brian Bancroft, Eric Roots, and Tijana Liveda all participated in the acquisition of data. Thanks to Abderazzak Bouchedda and Bernard Giroux of Institut Nationale de la Recherche Scientifique for providing and operating the CSEM transmitter equipment. Collaborations with staff from Groundmetrics Inc. including the late Andy Hibbs, Todor Petrov, Adam Agundes, and Joe Pendleton are also appreciated. Contributions from these individuals have been vital to the research and have made the fieldwork a memorable and enjoyable experience.

A number of people within the Department of Geological Sciences at the University of Manitoba have been a constant source of support throughout the completion of this thesis. In particular, Andrew Frederiksen and Puyan Mojabi provided excellent feedback on the research and the manuscript. I would like to acknowledge Mulu Serzu and Ademola Adetunji for their technical aid, and Graduate Chair Bob Elias, as well as Brenda Miller, Steven Brown and Pam Achtemichuck for their administrative support.

Thanks to fellow graduate students Tim Hayward for assistance with computer programming, and Taras Zaporozan and Reid Campbell for being affable labmates.

I must also acknowledge the Petroleum Technology Research Centre for providing borehole resistivity log data. Finally, my gratitude goes to Don White of NRCan and the Eco Energy Innovation Initiative for funding this research.

Table of Contents

List of Figures

List of Tables

Chapter 1: Introduction

1.1 The Aquistore project

The Aquistore project is a large-scale carbon dioxide (CO_2) capture and sequestration initiative, taking place to the southwest of Estevan, Saskatchewan (Figure 1.1). Emissions of CO_2 generated from SaskPower's nearby Boundary Dam Power Station (Figure 1.2) are being captured and injected in liquid form deep into stable sedimentary packages of the Williston Basin for long-term storage (Aquistore, 2016). The overall aim of the project is to reduce greenhouse gas emissions coming from a fixed source of CO_2 discharge, while demonstrating the effectiveness of using geological formations as a sequestration reservoir (Whittaker and Worth, 2011). Carbon capture and storage (CCS), in combination with renewable energy technologies, is potentially an important means of mitigating anthropogenic climate change.

Figure 1.1: Location of the Aquistore project and the Williston Basin (Klappstein and Rostron, 2014). Copyright by Elsevier. Used with permission.

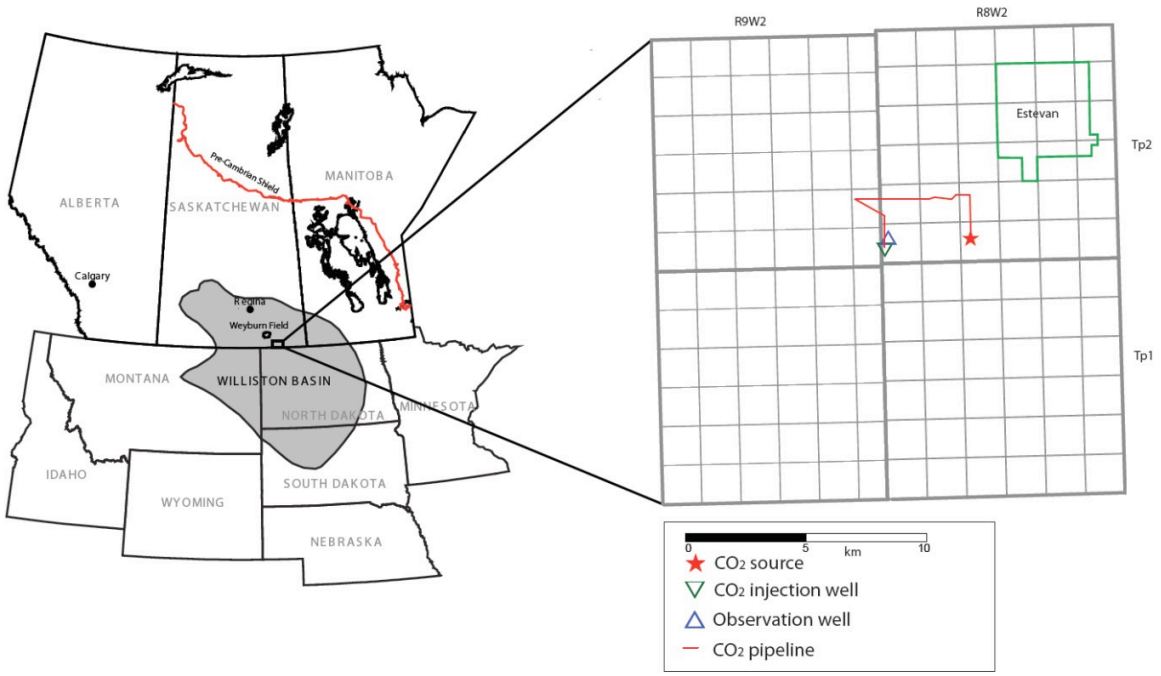

The injection well pad is located at 49°05'39.4" N, 103°04'42.1" W (UTM 5439716 m northing, 640285 m easting, zone 13), a distance of ~ 2 km from the power station. The well pad includes both an injection well and observation well (PTRC INJ-5-6-2-8W2 and PRTC OBS-5-6-2-8W2).

Figure 1.2: SaskPower's Boundary Dam power station. Carbon capture unit circled in red. Modified from SaskPower (2013). Copyright by SaskPower. Used with permission.

The sedimentary units being used for geological storage are the Winnipeg and Deadwood Formations, which are located at the base of the Williston Basin and have many characteristics that are ideal for sequestration. This section of the sedimentary sequence consists of porous rock, capable of storing vast amounts of injected fluid. At depths greater than 3 km, these formations lie beneath all regional oil reservoirs and potash-bearing rocks, and thus have limited economic value (Aquistore, 2016). Impermeable layers of rock, both above and below the reservoir, provide seals against potential leakage. The tectonically stable setting of the Williston Basin is also an important aspect for the long-term storage goals (Aquistore, 2016).

An essential part of the project is monitoring of the subsurface response to the injected fluid. During injection, the CO_2 will push away the host fluid and form a saturated region or plume beneath the injection well. In a pre-injection modeling study, Whittaker and Worth (2011) estimated that the CO_2 plume would reach a diameter of 3 km if injection occurred at 600 tonnes/day for 2 years followed by injection at 1,600 tonnes/day for 23 years. The continued injection of CO_2 is dependent on the integrity of the sealing units and on the subsurface distribution of the fluid. A suite of monitoring techniques is being utilised at the Aquistore site to ensure that these requirements are being satisfied at multiple stages of the injection (Aquistore, 2016). These include surface and borehole based geophysical measurements as well as geochemical sampling.

The Aquistore project has been in development since 2009 (Figure 1.3). Originally, the project's goal was to capture carbon emissions from an oil refinery in Regina, and to sequester the CO_2 at a depth of 2,200 m at a distance of 8 km from the city. These first plans were halted when the refinery and sequestration site partners disassociated themselves from the project. In 2010, Aquistore relocated its plans to Estevan with an aim to capture 2,000 tons of CO_2 per day (Global CCS Institute, 2015). Since that time, the installation of CCS infrastructure at the Boundary Dam station and the injection site has included retrofitting the carbon capture unit, drilling of the injection and monitoring wells, and construction of transport pipelines. Baseline characterizations of the injection site have been underway since 2012 (Global CCS Institute, 2015).

Figure 1.3: Timeline of Aquistore project, 2009-2013 (Global CCS Institute, 2015). Copyright by Global CCS Institute. Used with permission.

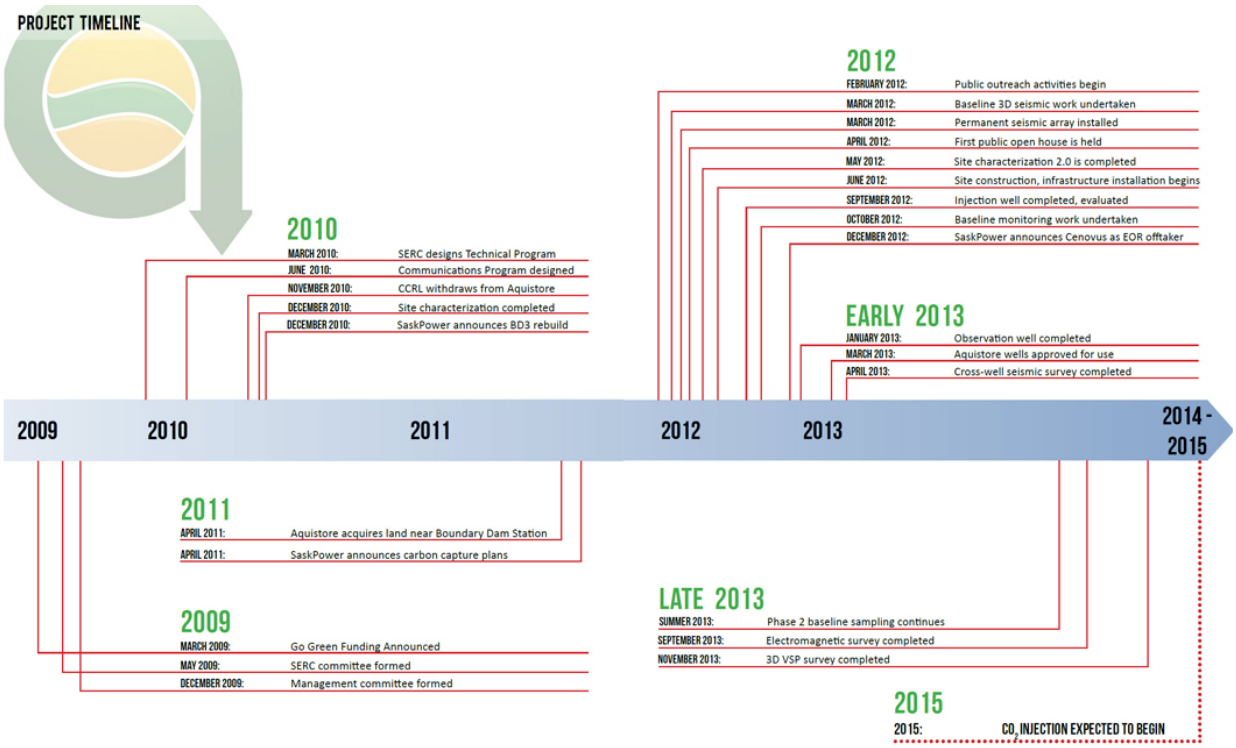

Carbon capture began in October, 2014 and injection began in April, 2015 (Aquistore, 2016). It was reported that as of February, 2016, 35,000 tonnes of CO_2 had been injected at a rate of 500 tonnes a day (Aquistore, 2016).

1.2 Study objectives

As a subset of Aquistore's monitoring program, this research examines the feasibility of using surface-based electromagnetic (EM) methods for time-lapse monitoring at the injection site. Initially, the goal of the M.Sc. research project was to use EM recordings made before and after fluid injection in order to image the changes to the reservoir due to the CO_2 volume. Due to delays in the commencement of injection and time constraints of the M.Sc. project, this objective was not feasible. Instead the focus of this study shifted to the determination of baseline EM responses for two complementary methods: magnetotellurics (MT) and controlled-source EM

(CSEM). These techniques are used for characterization of the pre-injection EM responses, electrical resistivity structure, and EM noise conditions in a 2.5 km × 8.5 km area surrounding the Aquistore injection well. Three separate NRCan field campaigns in 2013, 2014, and 2015 resulted in the acquisition of three MT datasets and two CSEM datasets. A CSEM survey was not completed in 2014. In addition to these data-driven approaches, theoretical modeling of the CSEM response to the injected CO_2 plume and sensitivity of the CSEM response to changes in the Williston Basin electrical properties are examined in the study. The plume formed by the injection of a significant volume of fluid is expected to form an electrically resistive body in contrast to the more conductive saline aquifers of the storage complex. The theoretical spatial, temporal, and frequency domain variations in the measurements are studied to determine the range of baseline responses.

Key research questions to be addressed in this study include:

- What are the MT and CSEM responses of geological structures in an area within 10 km of the injection well?
- Are the measured MT responses sufficiently repeatable for time-lapse monitoring?
- What are the noise conditions at Aquistore, and do these affect the implementation of EM monitoring techniques?
- What is the electrical resistivity structure of the Williston Basin at the Aquistore site and specifically what is the resistivity of the storage complex?
- What theoretical changes to the MT and CSEM responses will be caused by the formation of a CO_2 saturated reservoir?
- Can the proposed MT and CSEM methodology successfully detect or monitor CO_2 injection at Aquistore?

The findings of this study may be used to guide future efforts to image the CO_2 plume.

This study represents a pilot project for the use of EM methods in CCS applications. The findings of this work will enhance the efforts of researchers examining the application of EM methods in other CCS projects, e.g. Ketzin, Germany (Streich *et al*., 2010; Bergmann *et al*., 2012; Grayver *et al*., 2014) and Hontomín, Spain (Escalas *et al*., 2013; Ogaya, *et al*., 2013; Vilamajo *et al.*, 2015). There has been an over-reliance on seismic methods in previous CCS monitoring studies (Zhdanov *et al*., 2013). At Aquistore, seismic surveys will likewise dominate the characterization of the evolving reservoir (Aquistore, 2016). The extent to which EM methods will form a source of complementary information to the existing time-lapse seismic methods will be assessed.

1.3 Thesis outline

This thesis will present results of the study that fulfill the stated objectives by first reviewing relevant concepts relating to CCS, the geological setting of the injection site, EM theory and MT and CSEM methodologies (Chapters 2-4). Chapter 5 documents the acquisition and processing of the three separate EM surveys that have been conducted in the area of the injection well, including both MT and CSEM components. The analysis of the first two of these MT datasets is presented in Chapter 6 in order to characterize the MT responses and ambient EM noise in the study area. A preliminary characterization of CSEM data is also provided. Quantitative calculations defining the level of spatial and temporal variations of the MT responses are described in Chapter 7. These methods are used to examine the extent to which the MT responses are repeatable for the purpose of time-lapse imaging and to assess the spatial uniformity of responses. Chapter 8 describes 1D inversion of the MT responses, using

constraints from borehole resistivity data, to form a representative resistivity model of the sedimentary rocks of the Williston Basin. The sensitivity of EM responses to the parameters of simplified resistivity models is examined in Chapter 9 using Fréchet derivatives and forward modelling. This theoretical modeling provides insight into the detectability of CO_2 saturated regions for different injection and leakage scenarios. The thesis concludes with an integrated summary of the project's results and recommendations for future work (Chapter 10).

1.4 Author's contribution

The author was involved in all aspects of data acquisition, processing, and analysis of the NRCan MT and CSEM studies at Aquistore except for the 2013 MT and CSEM field-work. During the 2013 field-work he participated in a parallel CSEM survey being conducted at the Aquistore site by Groundmetrics Inc. (GMI). With the exception of a pre-survey report (Hibbs, 2013) the results of the GMI CSEM survey were not made available to the author during the thesis research and will therefore not be discussed here. In the 2014 and 2015 NRCan fieldwork sessions, the author made contributions to planning in the form of compilations and reports on data from the previous years' work. He participated in MT instrument calibration, MT site installations, site visits, and site retrieval, was responsible for maintaining the in-field log of activities, and he conducted most of the MT data archiving and in-field MT data processing. All of the subsequent work on data processing and analysis, inversion and modeling described in the thesis was done by the author. The author collaborated with his advisors in preparing two Government of Canada Open File publications describing intermediate stages of progress on the research (McLeod *et al.*, 2014b; McLeod *et al*., 2015c) and in preparing a number of conference presentations: EMIW (McLeod *et al*., 2014a; McLeod *et al*., 2016), AGU GAC-MAC Joint

Assembly (McLeod *et al.*, 2015a), IUGG General Assembly, (McLeod *et al*., 2015b), and CSPG-CSEG Geoconvention (McLeod *et al*., 2015d).

Chapter 2: Introduction to Carbon Capture and Sequestration

2.1 Introduction

As a result of the increased energy demands of the 21st century, global CO_2 emissions have risen to the highest levels on record (Smit *et al*., 2014). There is no singular solution for reduction of these emissions; a number of simultaneous actions are required to mitigate the increasing rate of greenhouse gas emissions. These include improving the efficiency of energy producers, changing the practices of agricultural and forestry sectors, further developing renewable energy sources, and diligently reducing industrial and civilian carbon footprints (Smit *et al*., 2014). Carbon capture and sequestration (CCS) technology can potentially play a significant role in alleviating the burden on the fossil fuel industry in this endeavour. The applicability of CCS to the existing energy production infrastructure of the coal burning industry provides an immediate means of eliminating CO_2 waste products at large-scale stationary emitters.

At Aquistore, captured carbon products from the Boundary Dam power station will be transported to the injection well via pipeline. Of an anticipated 3,000 tons of CO_2 captured by SaskPower each day, 2,000 tons will be destined for geological storage. The remaining CO_2 will be sold to Cenovus Energy for the purposes of enhanced oil recovery (SaskPower, 2013; Aquistore, 2016).

2.2 Carbon capture

Energy production at coal-fired power plants is achieved by burning the fuel source in the presence of oxygen. This reaction produces high-pressure steam which is used to power electric turbines. A simplified version of this reaction is given by (Smit *et al*., 2014):

$$Fuel + O_2 \rightarrow Heat + CO_2 + H_2O \quad (2.1)$$

Not included in this idealized reaction are unwanted components of the flue gas such as nitrous and sulphuric oxides, and traces of Hg. These products arise because the combustion reaction uses neither pure coal nor pure O_2. Prior to venting the flue gas, it is necessary to remove these contaminants (Smit *et al*., 2014).

In a broad classification, the different methods of CO_2 capture can be separated into oxyfuel combustion, pre-combustion, and post-combustion capture systems (Gibbins and Chalmers, 2008). The choice between these three usually depends on which type of flue gas-CO_2 separation scheme can be most easily fitted to a power plant. For example post-combustion systems are generally much easier to accommodate within existing plants, whereas a new plant may consider using a pre-combustion or oxyfuel combustion arrangement (Smit *et al.*, 2014). In either case, the addition of a carbon capture step to the energy production process will diminish the plant's efficiency and come at an economic cost. The optimal reduction of these two issues will involve plant-specific factors, and thus none of these systems can be considered favorable to the alternatives in a general sense.

For oxyfuel combustion, the fuel source is burned with purified O_2. The separation of oxygen from (mostly) nitrogen gases is done using a cryogenic separation unit (Smit *et al.*, 2014). The produced flue gas will then consist of CO_2 and condensable water vapour. These two components can be easily separated prior to compression of the CO_2 for geological storage (Gibbins and Chalmers, 2008; Smit *et al.*, 2014). The primary energy inefficiency associated with this method is oxygen separation process; the CO_2 capture is relatively inexpensive.

In a pre-combustion system, the fuel is gasified to provide a synthesis gas of CO and H_2 prior to burning (Gibbins and Chalmers, 2008). Subsequently, steam is added, causing the water-gas shift:

$$CO + H_2O \rightarrow CO_2 + H_2 \qquad (2.2)$$

The CO_2 is then separated, using a physical solvent as pressures are lowered, and leaving behind a hydrogen-rich fuel gas. This process does not require heat, and is therefore a very energy efficient method of CO_2 separation. However, there is a loss of energy associated with both the mass of CO_2 that is captured before passing through the turbines and the fuel gasification (Gibbins and Chalmers, 2008).

The post-combustion separation of CO_2 involves just one extra step in the process: in addition to the removal of SO_X and NO_X gases, the CO_2 is also separated from the flue gas via absorption by a solvent.

Figure 2.1: Flow chart representing the different types of carbon capture systems (Gibbins and Chalmers, 2008). Copyright by Elsevier. Used with permission.

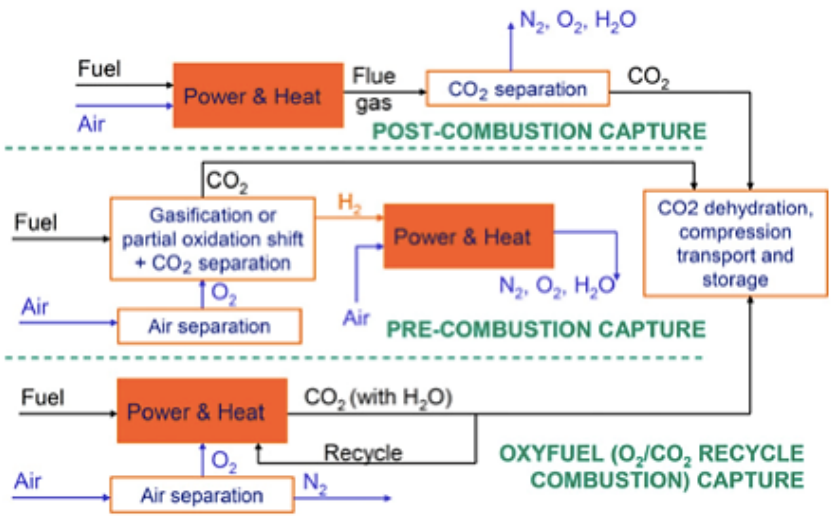

The mechanism of carbon capture used at the Boundary Dam Power Station is an amine-based, post-combustion system (Aquistore, 2016). Prior to being released into the atmosphere,

the waste gases are treated with an amine solvent to remove CO_2. The CO_2 is then dehydrated and compressed for transport and storage, while the solvent undergoes a heating and cooling cycle that allows it to be reused (Gibbins and Chalmers, 2008).

2.3 Carbon sequestration

Long-term storage of CO_2 is possible in a number of different geological settings (Figure 2.2). In conjunction with oil field operations, injection can be into either depleted reservoirs or actively producing ones as a part of enhanced recovery. Using CO_2 for resource extraction provides added value to the carbon capture process. Likewise, coal bed methane extraction can be improved with CO_2 injection. Uneconomic geologic targets for injection include saline aquifers and sometimes coal beds (IPCC, 2005; Smit *et al*., 2014). Igneous and metamorphic rock formations are unsuitable as storage reservoirs as they lack injectivity and are often too fractured to effectively seal in a sequestered fluid (Bachu, 2003).

Figure 2.2: Types of CO_2 sequestration reservoirs (CO2CRC, 2008). Copyright by CO2CRC. Used with permission.

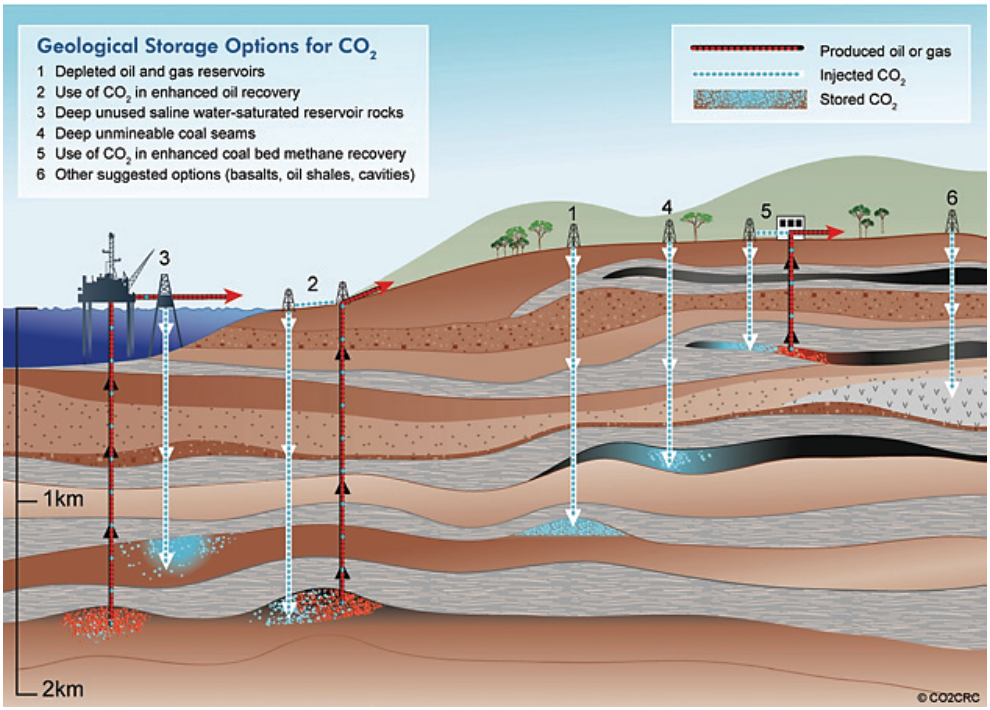

In evaluating sedimentary basins for their CCS potential, consideration must be given to tectonic, geothermal and hydrogeological factors. A tectonically stable location is necessary to ensure secure storage over long time scales. The temperature and pressure regime at the depth of the targeted formation must also be agreeable; CO_2 is stored as a supercritical fluid to allow for higher density storage and to minimize fluid migration by buoyancy forces. The temperature and pressure must therefore be in excess of 31.1°C and 7.38 MPa for a reservoir to be suitable for CCS (Figure 2.3) (Bachu, 2003; Martin Nordbotten *et al*., 2005; Benson and Cole, 2008). Given this condition, the depth of injection and storage becomes important. Pressure and temperature gradients are highly variable, but as an approximate criterion, the minimum depth for a storage complex would need to be 800 m, assuming a geothermal gradient of 25°C/km and a hydrostatic pressure gradient (Holloway and Savage, 1993; Bachu, 2003). Deeper reservoirs are therefore preferable due to their greater likelihood of meeting the supercritical condition, and for greater security of storage. Finally, porosity and permeability are important factors controlling storage volume and injectivity (Bachu, 2003).

Figure 2.3: Phase diagram of CO_2 (Martin Nordbotten *et al*., 2005). Copyright by Springer. Used with permission.

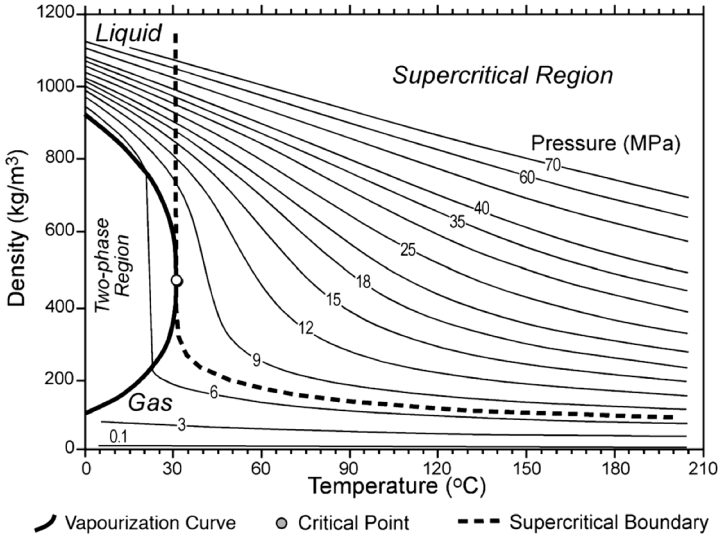

As the chosen reservoir for Aquistore sequestration, the base of the Williston Basin is well-suited for carbon storage. The intracratonic setting is optimal, and the deep saline aquifer of the Cambrian-Ordovician strata provides an excellent reservoir. The depth of this storage complex is 3.4 km, and any CO_2 injected to this depth will remain in a dense supercritical phase (Figure 2.4).

Figure 2.4: Phase distribution of CO_2 at the top of the Silurian in the Williston Basin, Saskatchewan and Manitoba (Bachu, 2002). Copyright by AGS/AER. Used with permission; https://open.alberta.ca/licence.

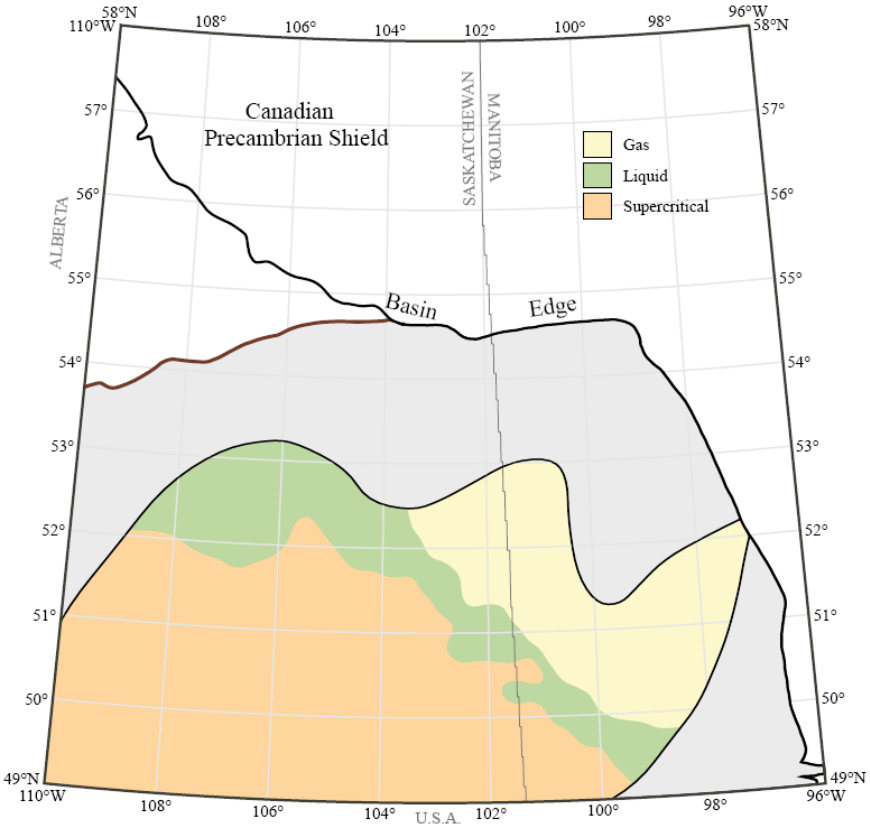

In a deep saline aquifer system, the CO_2 is immiscible with the in situ fluid, and its invasion into the pore spaces will displace the brine. The CO_2 is also more buoyant than the brine, causing any plume migration to be updip, and resulting in two distinct fluid phases contained within the pore spaces of storage units. Benson and Cole (2008) summarize important results of the subsequent multi-phase flow relationships: (1) a maximum of 30% of the pore

space can be filled during the injection and displacement stage, a limitation that is due to capillary force interactions between each of the fluids; (2) in a post-injection setting, the saturation of the medium equilibrates as the plume migration is allowed to continue; (3) capillary forces prevent the entire injected volume from migrating post-injection by retaining a fraction of the CO_2 in pore spaces; (4) the low-permeability overlying sealing rock unit has very high capillary pressures that block CO_2 from passage into the pore spaces, but allow water to migrate between layers.

There are several mechanisms for trapping the CO_2 in the basin, each of which is effective on a different time scale (Figure 2.5). The most immediate means of trapping is the stratigraphic trap in the form of the required sealing rock unit (IPCC, 2005; Benson and Cole, 2008; Smit *et al*., 2014). Residual trapping comes into effect during the post-injection stage: as the CO_2 starts to migrate upwards, the displaced brine will flow back towards the edges of the plume and fill the smaller pore spaces and pore throats. The CO_2 that is near to this water-rock interaction is then trapped by capillary forces in the larger pore spaces (Smit *et al*., 2014). The impact of residual trapping increases over time with continued plume migration. Once immobilized by residual trapping, CO_2 is susceptible to dissolution into the brine. Dissolution represents a more secure mode of storage known as solubility trapping as it eliminates a fraction of the buoyant fluid (Benson and Cole, 2008). The final possible form of trapping is conversion of the dissolved CO_2 into solid carbonates in what is known as mineral trapping. Mineral trapping occurs as silicate minerals are weathered by the CO_2 solution and release cations (Mg^{2+}, Fe^{2+}, Ca^{2+}). The aqueous CO_3^{2-} will react with the cations to form stable carbonate minerals (IPCC, 2005; Benson and Cole, 2008; Smit *et al*., 2014). Bachu *et al*. (2007) note that the time

dependence of these trapping systems complicates the estimation of the potential CO_2 storage capacity in saline aquifers.

Figure 2 5: CO_2 trapping mechanisms and effective time scales (IPCC, 2005). Copyright by IPCC. Used with permission.

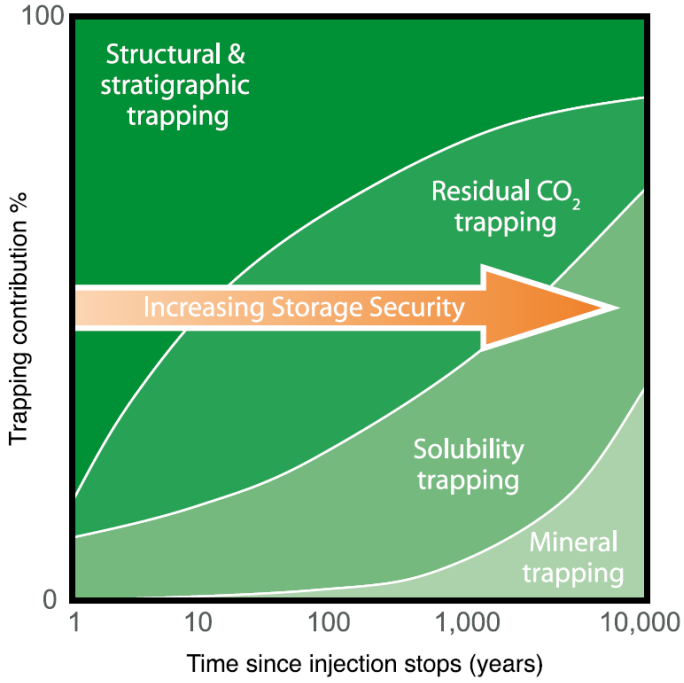

2.4 Monitoring for electrical properties of injected CO_2

Techniques for monitoring of the evolving CO_2 plume take advantage of either structural effects of injecting a fluid volume into the reservoir (e.g. deformations measured by tiltmeters at the surface), chemical changes to the constitution of the pore fluid, or observable changes to the bulk physical properties of the reservoir. In the case of a saline aquifer, the invasion of a second fluid phase will alter the electrical properties of the reservoir. Changes in the electrical resistivity are therefore the focus of EM geophysical monitoring.

Prior to CO_2 injection, the aquifer's resistivity is controlled by its porosity, fluid saturation, typical pore geometry, and the resistivities of the dry rock and pore fluid. For salt water aquifers, the resistivity of the brine is several orders of magnitude lower than the resistivity

of the dry rock (e.g. Figure 2.6), and thus the pore fluid has a volumetrically disproportionate effect on the bulk resistivity. Archie's Law is an empirical relationship that estimates the bulk electrical properties from the pore fluid characteristics (Keller, 1991):

$$\rho_b = a\rho_w S^{-n}\varphi^{-m} \tag{2.3}$$

where ρ_b is the bulk resistivity, ρ_w is the resistivity of the water, S is the fluid saturation, φ is the porosity, and a, n, and m are constants used to describe the pore geometry. The values of ρ_b and ρ_w range according to rock mineralogy and water salinity, respectively. Since a conductive fluid will dominate the electrical resistivity of the bulk volume, saline aquifers can be characterized as generally conductive relative to other geological formations.

Figure 2.6: Typical range of resistivities of geologic materials (modified from Knight and Endres, 2005). Copyright by SEG. Used with permission; http://seg.org/Publications/Policies-and-Permissions/Permissions.

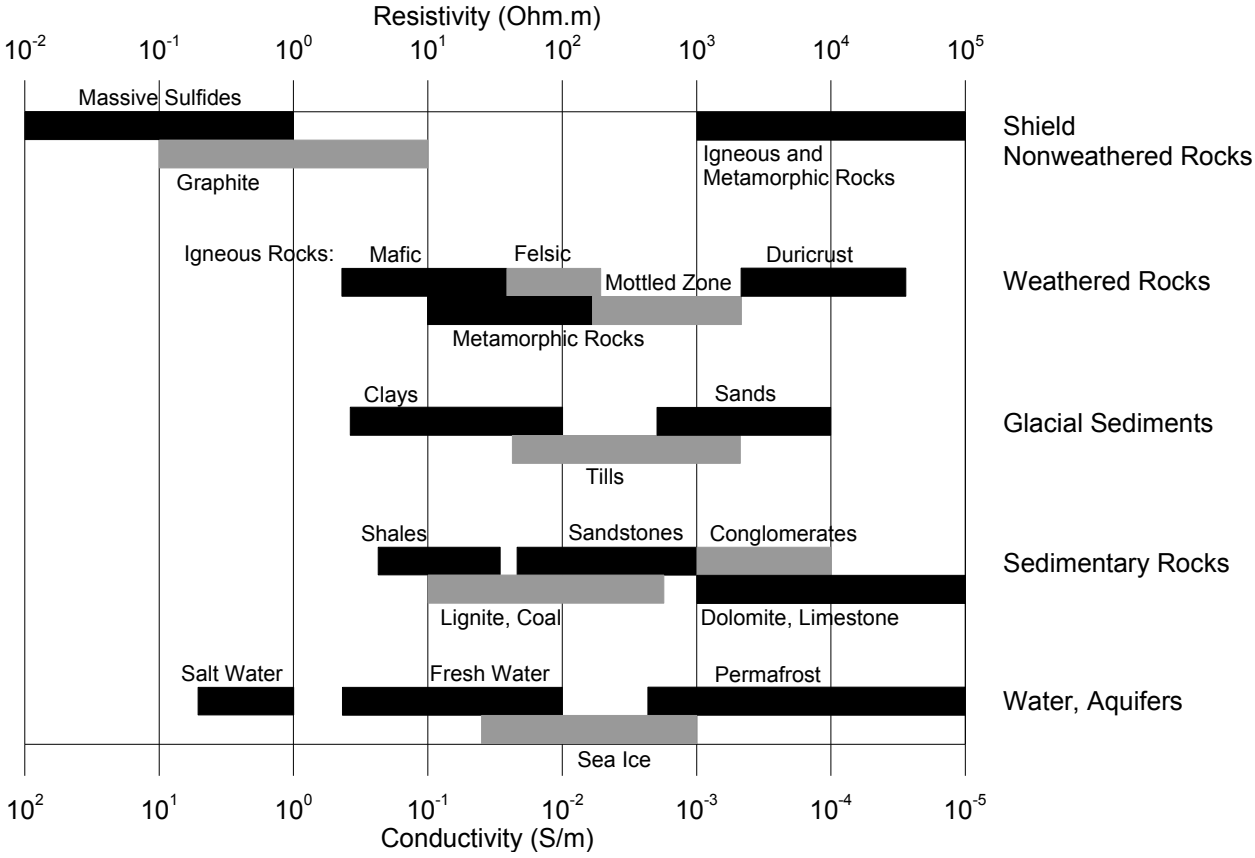

Addition of CO_2 to the pore fluid would serve to reduce the influence of the brine on the bulk resistivity of the aquifer. The change in electric properties with injected CO_2 is more significant than the change in seismic properties (Figure 2.7). In the scenario of two separate fluid phases (e.g. before residual trapping becomes significant), the CO_2 saturated portion of the aquifer will have a higher resistivity, as it lacks the electrolytic content of the brine. Bosch *et al*. (2016) demonstrate that EM methods detect higher resistivity with increasing saturation of CO_2 in a sandstone sample for a range of pressures and temperatures. However, in the solubility trapping stage, additional dissolved ions from the CO_2 will decrease the resistivity of the formation fluid. This effect depends linearly on the concentration of dissolved CO_2 (Fleury and Deschamps, 2008) and varies with temperature, pressure, and salinity of the brine (Börner *et al*., 2013; Börner *et al*., 2015). Based on this relationship, EM monitoring has the potential to both image areas of CO_2 saturation and track the evolution of the fluid trapping.

Figure 2.7: Electrical resistivity and seismic P-wave velocity vs. CO_2 saturation at the Nagaoka injection site (Nakatsuka *et al.*, 2010). Copyright by Elsevier. Used with permission.

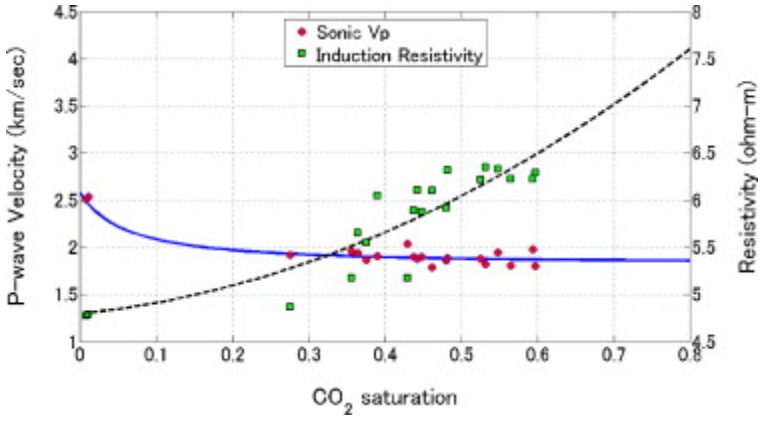

Chapter 3: Background Geology and Geophysics

3.1 The Williston Basin

3.1.1 General setting

The Williston Basin is a large intracratonic basin consisting of a Phanerozoic sedimentary succession, extending from southern Saskatchewan and southwest Manitoba, Canada southward into Montana and South Dakota, USA (Figure 3.1). Structurally, the basin forms a depression in the Precambrian basement, centred on North Dakota (Kent and Christopher, 1994). The basin covers an area of 250,000 km^2 and, at its maximum dimensions, measures 560 km in diameter and 4.9 km in thickness.

Figure 3.1: Aerial extent of the Williston Basin (Whittaker and Worth, 2011). Copyright by Elsevier. Used with permission.

The Phanerozoic sediments of the Williston Basin were deposited on several Archean and Proterozoic terranes: the Hearne craton, the Sask craton, and the Trans-Hudson Orogen. The

collision of the Hearne and Sask cratons with the eastern Superior craton during the closure of the Manikewan Ocean was the driving force of the 1.8 Ga Trans-Hudson orogeny. The Trans-Hudson Orogen is a north-south trending Paleoproterozoic domain that spans most of eastern Saskatchewan and western Manitoba and encloses the Sask craton (Figure 3.2) (Ansdell, 2005).

Figure 3.2: Major North American geological divisions (modified from Hoffman, 1988; Jones *et al.*, 2005). Copyright by NRC Research Press. Used with permission.

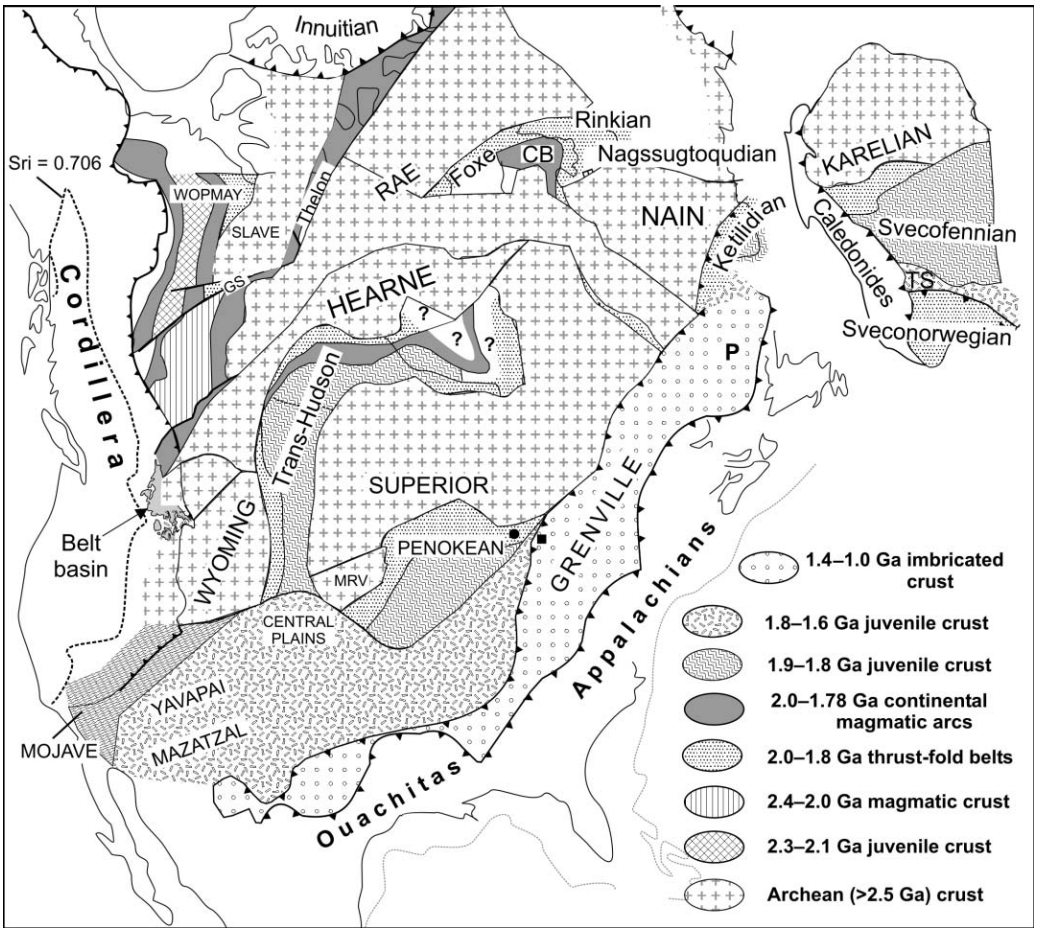

Strata of the Williston Basin are separated from formations of the Western Canada Sedimentary Basin by epeirogenic structures associated with the Laramide Orogeny such as the Sweetgrass Arch (Figure 3.3). To the north, south and east, the basin is delimited by the Punnichy, Sioux and Severn Arches, respectively. During the initial deposition of the strata, the areal dimensions of the basin were significantly greater than is observed in the present day. The

uplifting of arches surrounding the current basin extremities, and the erosion of strata are interpreted to have caused the basin's decreased lateral extent (Porter *et al.*, 1982; Kent and Christopher, 1994).

Figure 3.3: Isopach and structural elements of Williston Basin (Kent and Christopher, 1994). Copyright by AGS/AER. Used with permission; https://open.alberta.ca/licence.

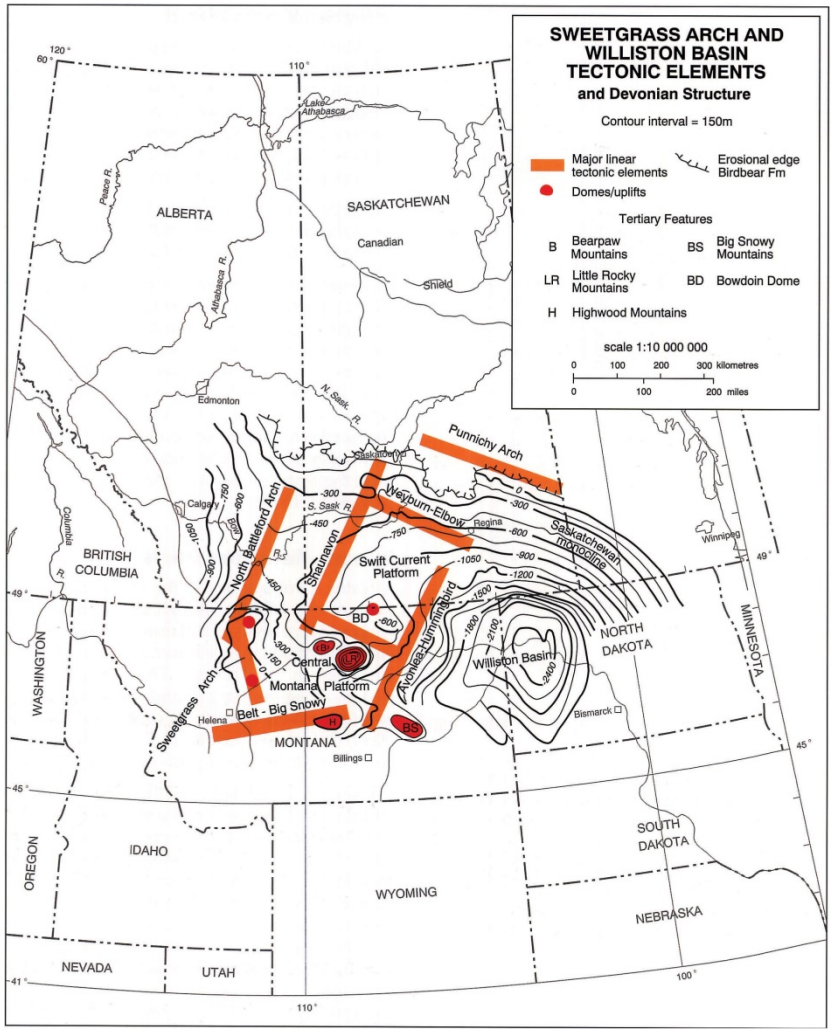

Ages of the constituent formations of the Williston Basin range from middle Cambrian to early Cenozoic. In southeast Saskatchewan, this succession has a thickness that is between 2.2 and 3 km (Vigrass *et al.*, 2007; Whittaker and Worth, 2011) (Figure 3.4).

Continuous subsidence from the Cambrian to the Jurassic is suggested as the driving mechanism of the Williston Basin's development (Fowler and Nisbet, 1985). One of the principal influences on this progressive subsidence is a phase transition of deep crustal material to eclogite facies. Following the Jurassic, tectonic forces to the West of the basin lead to more complex subsidence.

Figure 3.4: Western Canadian Sedimentary Basin isopach in km (modified from Vigrass *et al.*, 2007). Copyright by Saskatchewan Geological Survey. Used with permission; http://www.gov.sk.ca/copyright/.

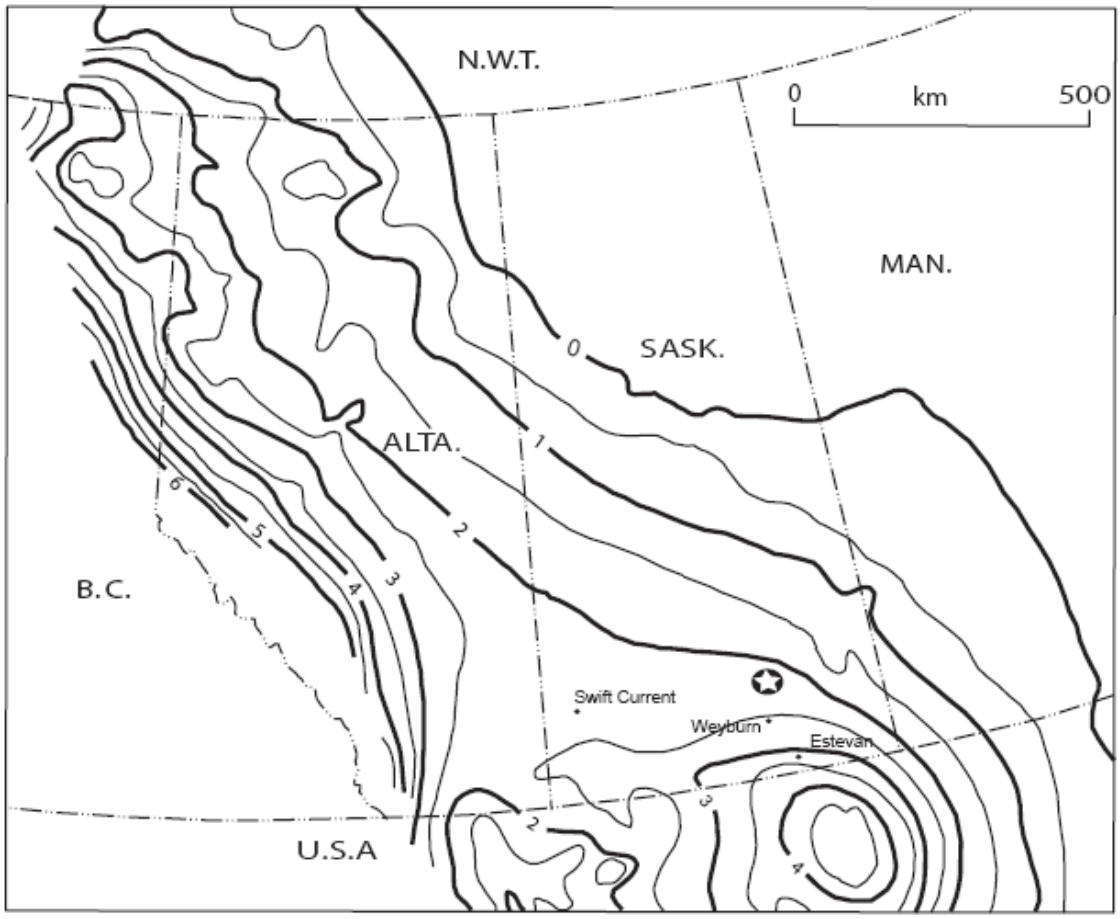

3.1.2 Depositional history

The basin's sedimentary record is notably incomplete. Unconformities associated with periods of erosion and hiatuses in deposition correlate well with eustatic changes in sea level.

Based on these correlations, deposition of strata in the Williston Basin is divided into genetically linked successions of sediment accumulation (Figure 3.5) (Porter *et al*., 1982; Fowler and Nisbet, 1984).

Figure 3.5: Regional stratigraphy of the Williston Basin in Saskatchewan (Fowler and Nisbet, 1985). Copyright by NRC Research Press. Used with permission.

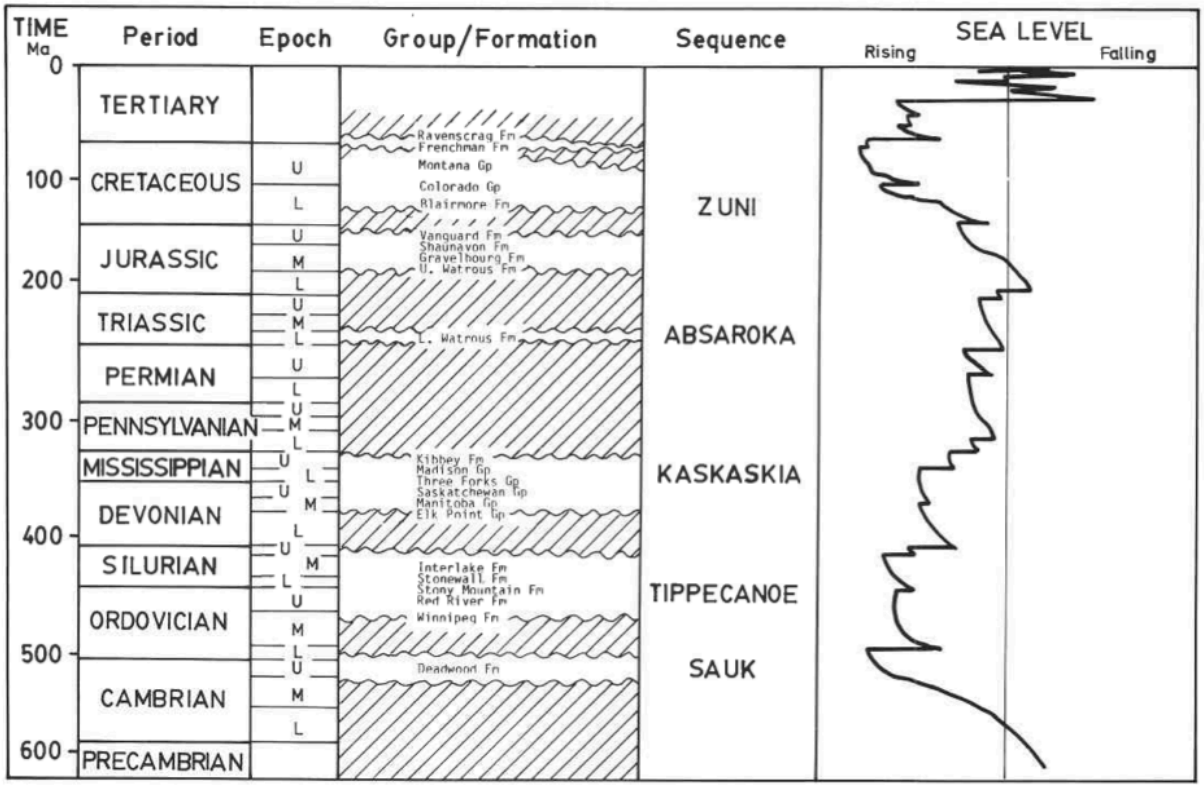

The initial Sauk sequence was formed by the deposition of clastic materials onto the Precambrian platform during the early Cambrian. This sequence includes the Deadwood Formation, which, in the northeast portion of the basin, is the deepest unit of the Phanerozoic sediments, and lies unconformably on the basement. The subsequent Tippecanoe sequence was initiated by a dramatic transgressive event in the late Cambrian and includes several carbonate formations (Porter *et al.*, 1982). Carbonates, evaporites and shale characterize the overlying Kaskaskia sequence. The Triassic shales of the succeeding Lower Watrous formation are

unconformably overlain by the Jurassic evaporites of the Upper Watrous. These units form part of the Absaroka sequence, which is defined by a period of falling sea level. This sequence is poorly preserved in Canada (Fowler and Nisbet, 1984; Osadetz *et al*., 2002). Above this interval lies the Zuni sequence and surficial glacial deposits of the Pleistocene (Porter *et al.*, 1982; Gowan *et al*., 2009).

In a broader classification, the Phanerozoic rocks of the Williston Basin can be divided into three units: a basal clastic unit, a carbonate and evaporite unit, and an upper clastic unit (Figure 3.6) (Bachu, 2002; Vigrass *et al.*, 2007). The initial deposition of clastics covers the Cambrian to Lower Ordovician interval of the geologic record. A lack of clastic input then allowed the formation of dominantly carbonate and evaporite deposits from the Middle Ordovician to the end of the Mississippian. Following this period, the style of sedimentation changed to be once again dominated by clastics. A cross-section of the eastern Williston Basin strata in Canada is depicted in Figure 3.7.

Figure 3.6: Major lithological units of the Willison Basin. Thickness values are based on core from 3-8-17-19W2 well, near Regina, SK (Vigrass *et al*., 2007). Copyright by Saskatchewan Geological Survey. Used with permission; http://www.gov.sk.ca/copyright/.

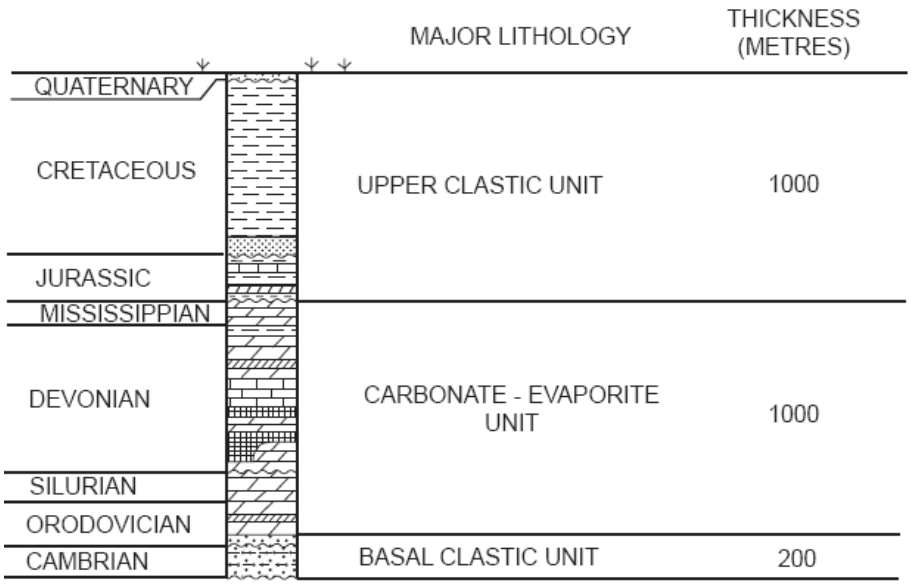

Figure 3.7: Profile of Williston Basin strata from west-central Saskatchewan to eastern Manitoba (modified from Dietrich *et al*., 1999). Copyright by Natural Resources Canada. Used with permission; http://www.nrcan.gc.ca/terms-conditions/10847.

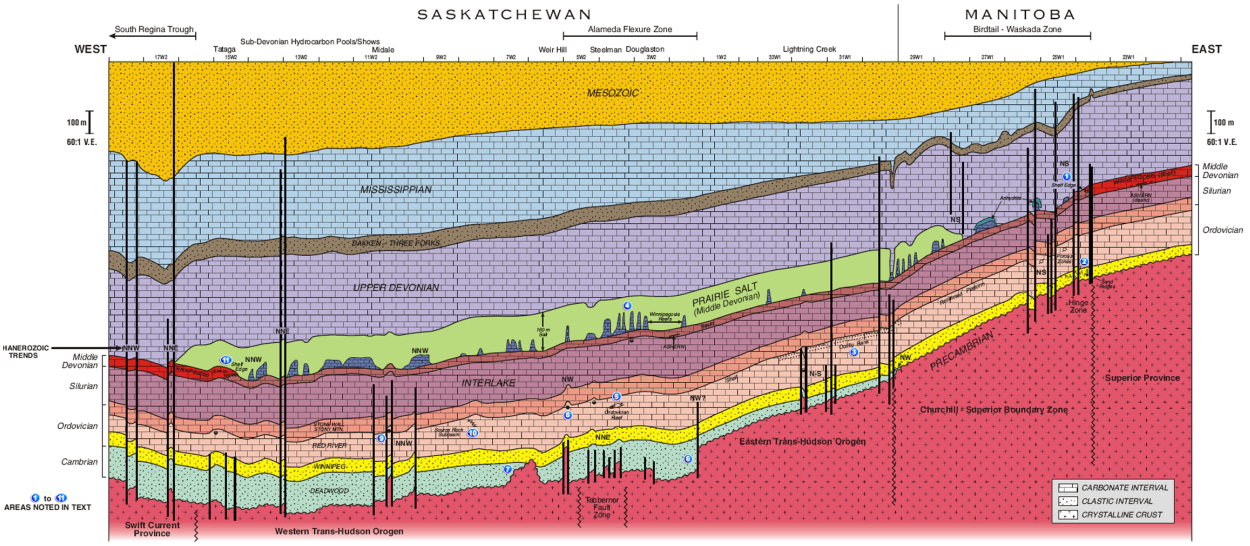

3.2 The Ordovician Winnipeg and Cambrian Deadwood Formations

3.2.1 Deadwood Formation

Deposition of Cambrian clastics predates the initiation of Williston Basin development. As such, the earliest Williston sediments were deposited over an extensive area that reaches farther west than the current basin structure (Greggs, 2000). A series of initial transgressive events as part of the Sauk sequence led to the deposition of marine clastics on the Precambrian platform. These strata are diachronous and thicken significantly to the west, the direction from which they prograded (McLean, 1960; Anna, 2013; Dixon 2008). The Basal Sandstone Unit and the Earlie Formation were deposited first, followed by the Deadwood Formation in the succeeding transgressive-regressive cycle. There is little evidence for eroded materials at the contact between the Deadwood and Earlie formations (Dixon, 2008). East of the Regina area, the lowermost sandstone units were not deposited, and the Deadwood sits unconformably overtop of the Precambrian basement (Figure 3.8).

Figure 3.8: West to East profile of Cambro-Ordovician sediments in the Williston Basin (Dixon, 2008). Copyright by CSPG (2008). Reprinted by permission of CSPG whose permission is required for further use.

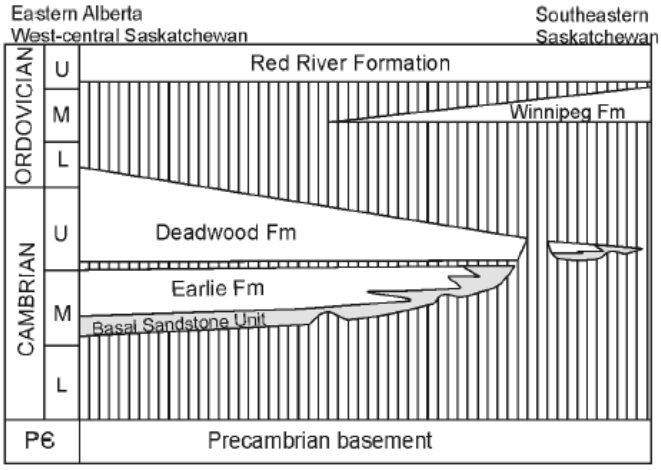

Figure 3.9: Paleogeographic map for the Late Cambrian – approximate location of present day Williston basin shown in red (Blakey, 2015). Copyright by Ron Blakey, Northern Arizona University. Used with permission; https://www2.nau.edu/rcb7/.

By the late Cambrian, the rising sea levels had forced marine incursion to the eastward bounds of the present-day Williston Basin (Figure 3.9), where relatively thinner columns of Deadwood strata are present. Deposition of the Deadwood continued into the early Ordovician.

The division of the Deadwood Formation into six sub-members (**A** through **F**) was initially based upon wire-line log characteristics observed in North Dakota (Anderson, 1988). Member **A** is the lowermost in the succession, and is characterized by a transgressive marine sandstone showing bioturbation, and accessory amounts of glauconite, pyrite, and micas. The rocks of member **B** contain some interbeds of silt and shale and reflect a deeper water environment. Prior to the deposition of member **C**, a brief regression occurred. Subsequent transgression resulted in nearshore facies sandstone deposits (with small amounts of limestone included) of member **C**, and offshore facies sandstones of member **D**. Members **E** and **F** are grouped as lagoonal sandstones with a higher amount of carbonate content. Much of member **F** has been eroded from the stratigraphic record. This classification best describes the Deadwood Formation in the region of the thickest Phanerozoic cover. Moving away from this basin centre, the upper sub-members are less prominent, and members **A** and **B** are observed closer to the contact with the overlying Winnipeg formation (Anna, 2013).

In the eastern portion of the Williston Basin, the Deadwood Formation is predominantly a sandstone unit, whereas in Alberta, the formation consists mostly of shales. Sandstones of the northern Deadwood Formation are highly glauconitic and the rocks become more quartzose and generally coarser grained to the south (McLean, 1960). In south-eastern Saskatchewan, the Deadwood Formation is a fining upward sequence with very coarse- to medium-grained, poorly sorted, well-rounded sediments at its base, grading to fine-grained, well-sorted deposits near its

top surface (Fyson, 1961; Seibel and Bend, 2000). Bioturbation and cross-bedding structures are commonly observed in core samples (Vigrass *et al.*, 2007).

3.2.2 The Winnipeg Formation

Following the termination of the Sauk sequence in the Middle Ordovician, the commencement of basin subsidence caused widespread erosion of upper Deadwood sediment and coincided with a new occurrence of eustatic sea level rise. This transgressive event led to the deposition of the Winnipeg Formation onto the erosional surface at the top of the Deadwood Formation (Smith and Bend, 2004; Anna, 2013). The Winnipeg Formation is divided into three sub-units: the Black Island, Icebox, and Roughlock members (Figure 3.10) (Paterson, 1971; Smith and Bend, 2004; Anna, 2013; Ferguson *et al*., 2007).

Figure 3.10: Stratigraphic section of the lower Williston Basin (modified from Smith and Bend, 2004). Copyright by Elsevier. Used with permission.

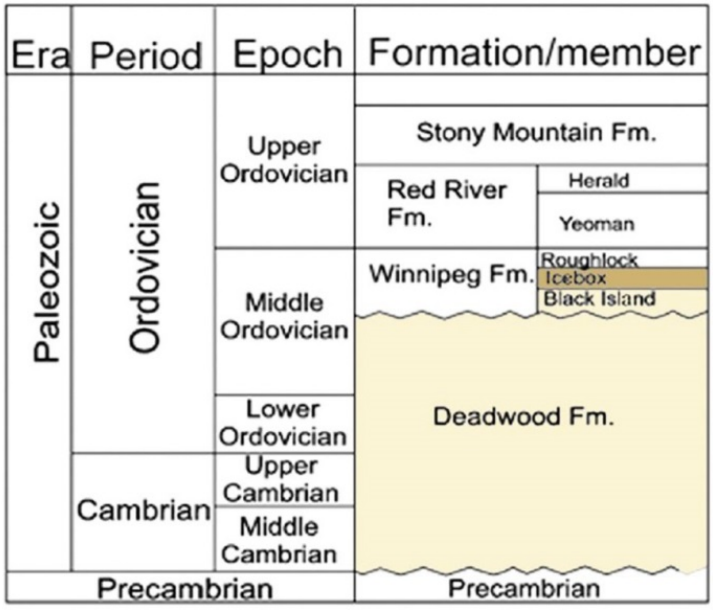

The Black Island member is a nearshore facies sandstone deposit, reflecting the early stages of the Tippecanoe transgression. This sandstone is primarily quartzose, containing

interbeds of siltstone and shale (Binda and Simpson, 1989; Anna, 2013). It is a fining upward unit of poorly- to well-sorted quartzose grains (Fyson, 1961; Vigrass *et al.*, 2007). The Black Island sandstones are differentiated from the Deadwood Formation by a higher textural and mineralogical maturity, an absence of glauconite, and lower gamma-ray log radioactivity counts (Binda and Simpson, 1989).

With continued sea level rise, the basin was then flooded allowing the deposition of the deep marine shales of the Icebox member (Smith and Bend, 2004; Anna, 2013). The Icebox is a green-coloured shale with some occurrences of arenaceous bedding (Binda and Simpson, 1989). In the northern portion of the Williston Basin, the Icebox has a siltier character (Smith and Bend, 2004).

A subsequent drop in sea level reduced the rate of clastic sedimentation permitting the formation of argillaceous limestone deposits. The influx of clastics eventually dropped to negligible levels, resulting in a dominantly carbonate lithology. This section of the geologic record is represented by the Roughlock member. It is considered a transitional period leading into the deposition of the overlying carbonate Red River Formation during the late Ordovician (Smith and Bend, 2004; Anna, 2013). The Roughlock member is not present in most of Saskatchewan, and in these areas, the contact between the Red River and Winnipeg Formations is unconformable (Smith and Bend, 2004).

In North Dakota, the Winnipeg Formation reaches a maximum thickness of over 140 m (Binda and Simpson, 1989; Anna, 2013). The maximum thicknesses for each of the sub-members are all encountered in North Dakota, and are 75 m for the Black Island sandstone, 45 m

for the Icebox shale, and 25 m for the Roughlock member (Figure 3.11). In south-east Saskatchewan, these dimensions are reduced to 45 m for the Black Island member and 20 m for the Icebox member.

Figure 3.11: Isopach (in feet) for the Black Island (A) and Icebox (B) members (Anna, 2013). Copyright by USGS Williston Basin Province Assessment Team. Used with permission.

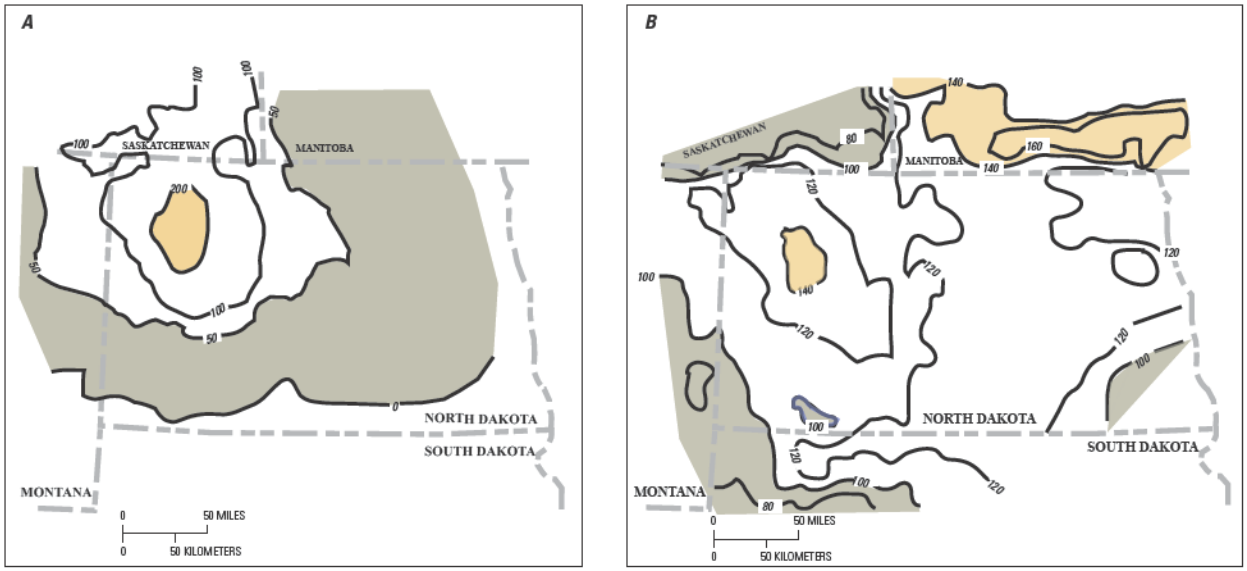

3.2.3 Hydrogeological characteristics

Collectively, the strata of the Williston Basin form alternating sequences of aquifers and aquitards (Figure 3.12), providing a natural multi-staged barrier against upward fluid leakage. The Black Island member of the Winnipeg Formation, and the Deadwood Formation, define a saline aquifer at the base of the Williston Basin. It is this aquifer that is targeted as a CO_2 storage reservoir. At the Aquistore site, the Icebox member will serve as the primary seal for the injected fluid (Whittaker and Worth, 2011).

Figure 3.12: Generalized hydrostratigraphy of Williston Basin in at Aquistore site (Whittaker and Worth, 2011). Copyright by Elsevier. Used with permission.

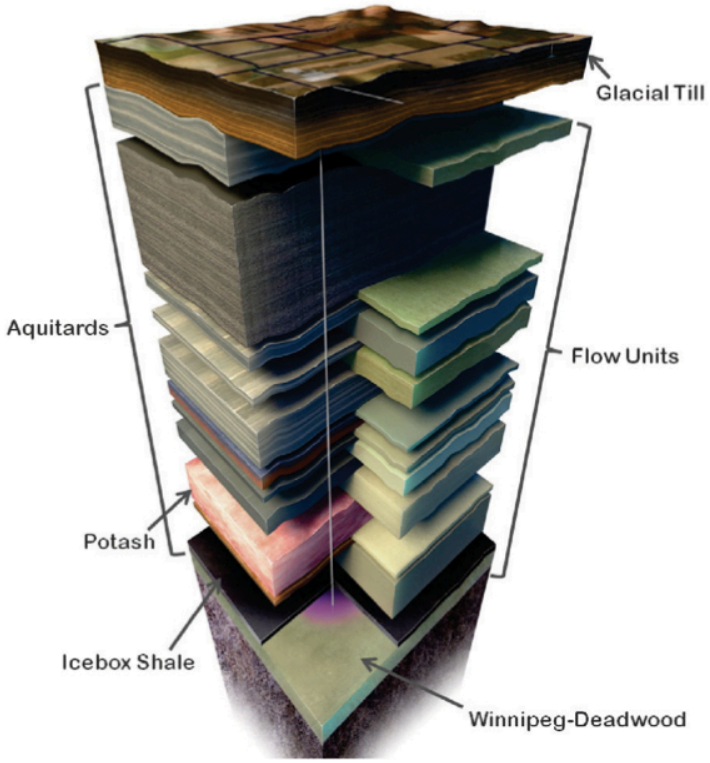

Vigrass *et al.* (2007) report on hydraulic properties of this aquifer system in the Regina area. The effective thickness of the sandstone aquifer in this region is 111 m. The porosity and permeability determined from core and log analysis, and averaged over the thickness of the unit are 13.2 % and 115 mD, respectively. Drillstem tests indicated significantly higher permeabilities than the core samples. This difference is likely due to fractures in the sandstone providing additional pathways for fluid migration. The effective permeability in this area was determined from drillstem tests to be 350 mD. The storativity of the aquifer system, that is the volume of fluid released from storage per unit hydraulic head decrease per unit area, is estimated at 5×10^{-4}.

3.3 Surficial geology

The Tertiary Ravenscrag Formation, which extends to depths of 180 m beneath the surface, is the shallowest recognized geological unit in the Estevan area. The Ravenscrag lithology varies between sand, silt, clay, and lignite compositions (Irvine, 1978; Klappstein and Rostron, 2014). Seams of lignite coal embedded in these Tertiary deposits include the Estevan seam and the Boundary seam. The Estevan seam is the shallower of the two, and has been strip-mined in the area. The deeper Boundary seam is observed at maximum depths of 40 m, on average 14 m deeper than the Estevan coals (Irvine, 1978). The lignite seams follow the regional structure of the Ravenscrag Formation, which plunges to the southeast (Irvine, 1978).

Above the Ravenscrag Formation, thin sequences of glacial till material form an unconformable contact with the Ravenscrag. This overburden has a maximum thickness of 10 m in the Aquistore region. Where strip mining is significant, mine spoil sits in place of the typical glacial overburden (Klappstein and Rostron, 2014). In some locations in the Estevan area, buried channel aquifers are present beneath the till (Klappstein and Rostron, 2014).

3.4 Regional geophysics

3.4.1 Magnetotelluric studies

Generally, MT responses over the Williston Basin indicate a one-dimensionally varying structure overlying a more resistive multi-dimensional basement (Jones, 1988; Jones and Craven, 1990; Jones 1993; Gowan *et al*., 2009). Studies of an east-west oriented MT profile across southern Manitoba and Saskatchewan (the COPROD2 dataset) reveal one-dimensional responses at periods shorter than 10 s, as well as a significant amount of static shift (Jones, 1988; Jones 1993). Changes in the MT response from the eastern margin of the basin to the centre are

attributed to the thickening of strata and gradual lateral variations. A significant difference in the eastern and western sides of the profile is the resistivity of the Upper Devonian rocks, which is greater in the west (Figure 3.13). This is due to saline fluids leaching out of the Prairie Evaporite Formation in the east, lowering the electrical resistivity (Jones, 1988).

Figure 3.13: Profile of electric laterolog information across COPROD2 profile (Jones, 1988). Copyright by SEG. Used with permission; http://seg.org/Publications/Policies-and-Permissions/Permissions.

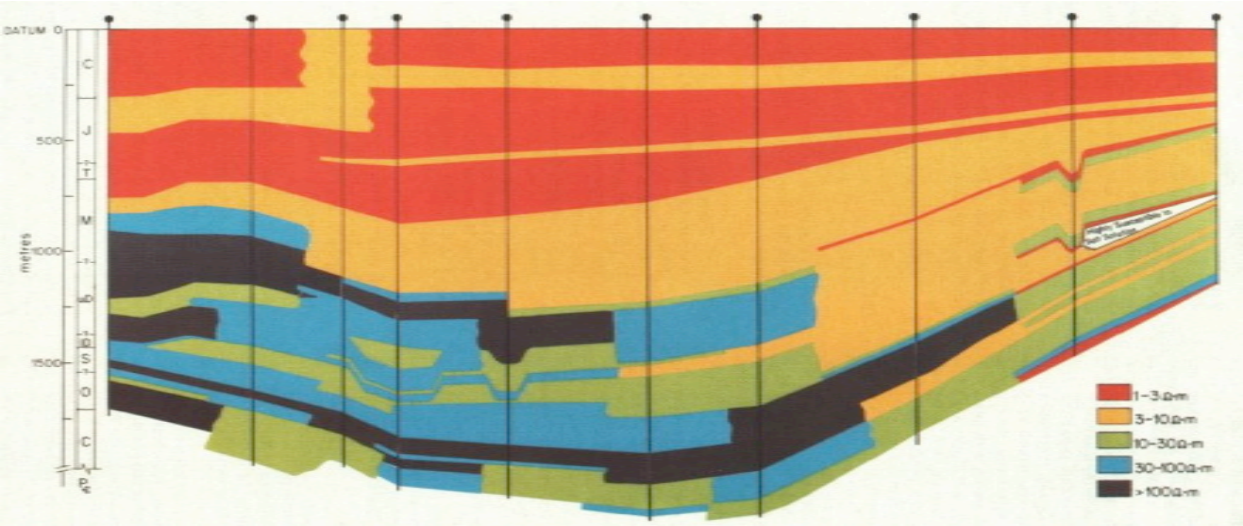

The character of the Precambrian basement MT response is dominated by the presence or absence of one of two prominent crustal features: the North American Central Plains conductor (NACP) and the Thompson Belt conductor (TOBE), which are linked to the Paleoproterozoic Trans-Hudson Orogen (Jones and Craven, 1990; Jones *et al.*, 2005; Gowan *et al.*, 2009). These north-south striking crustal bodies are important contributors to a broad range (~100-1000 s) of low-frequency responses for EM surveys. The NACP is modeled as a broad regional feature at ~10 km depth, stretching more than 10 km in the east-west direction throughout Saskatchewan, with an anomalously low crustal resistivity of ~10 Ωm (Figure 3.14). The NACP is spatially correlated with a zone of high heat flow, gravity anomalies, and a relatively low magnetic response (Jones and Craven, 1990; Dietrich *et al.*, 1999) (Figure 3.15).

Figure 3.14: Map of spatial extent of the NACP determined from MT and GDS data (Jones *et al.*, 2005). N.O.D., S, M, N, L, and X mark areas of previous MT and GDS surveys. Copyright by NRC Research Press. Used with permission.

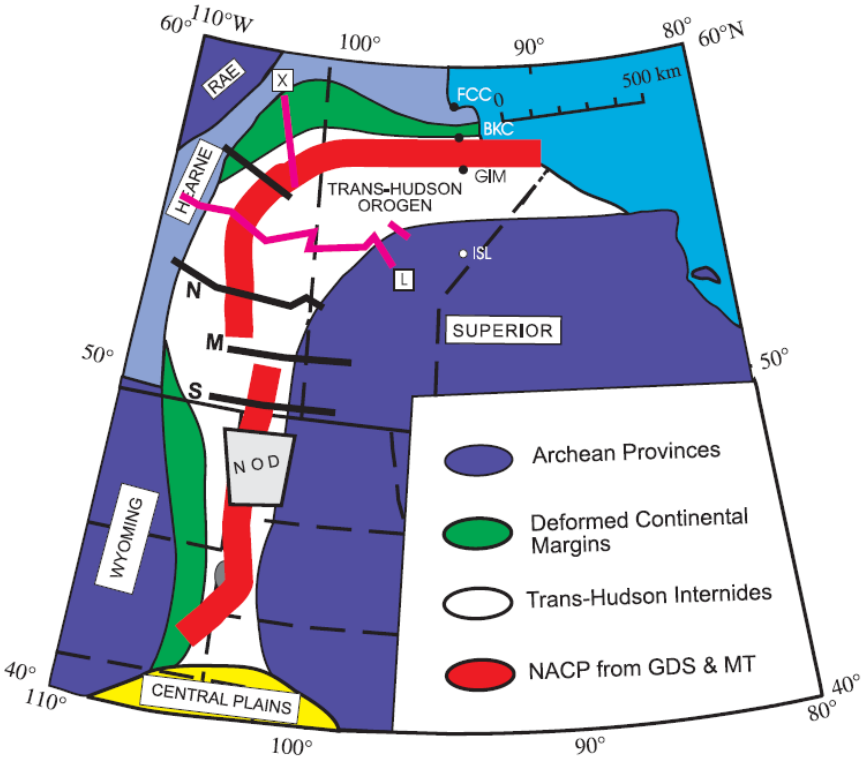

Figure 3.15: Geophysical profile (top) and integrated crustal model (bottom) of an east-west profile across the Canadian Williston Basin. Approximate Aquistore location is denoted by arrow (Dietrich *et al.*, 1999). Copyright by Natural Resources Canada. Used with permission; http://www.nrcan.gc.ca/terms-conditions/10847.

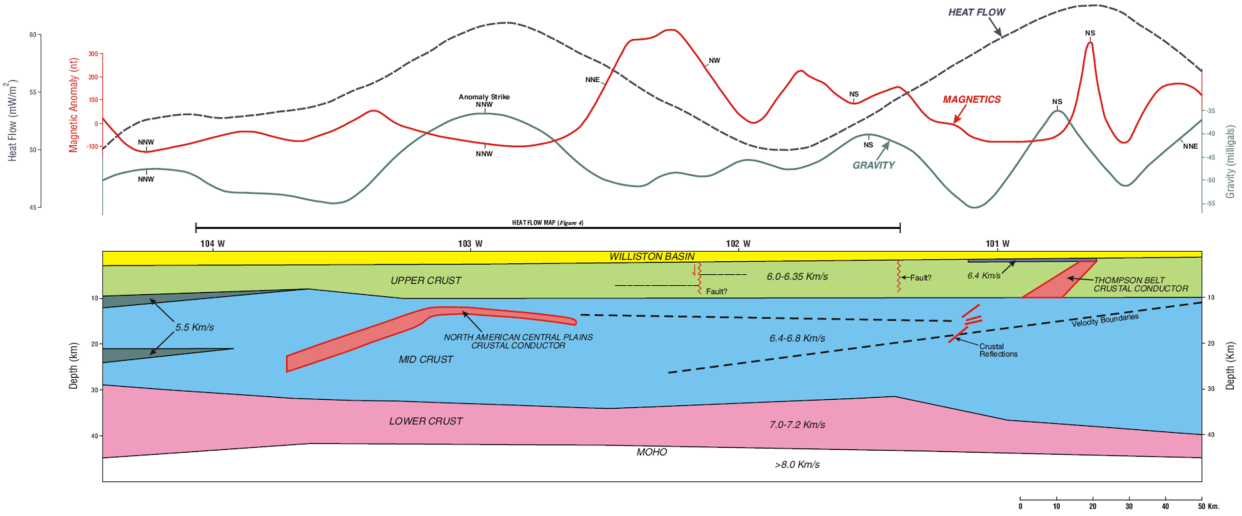

3.4.2 Seismic studies

Seismic reflection studies of the Williston Basin in Saskatchewan have permitted the reconstruction of basin development history. Zhu and Hajnal (1993) identified a series of time-stratigraphic sequences, as well as distinct instances of erosion and subsidence. Three episodes of tectonic activity are observed to have influenced the evolution of the basin: a primary period of subsidence during the deposition of Sauk sequence units, a stable period of continued deposition of sedimentary units from the Tippecanoe to Zuni sequences, and a later period of deformation. An additional study of reflection data with a focus on deeper crustal and mantle features was done by Baird *et al*. (1995). It is noted that in southern Saskatchewan, the Moho is not clearly defined. The lack of Moho reflectivity is possibly associated with a phase transition to eclogite of a deep crustal remnant of the Trans-Hudson orogen.

3.4.3 Potential fields

The Williston Basin Targeted Geoscience Initiative (TGI) produced maps of gravitational and magnetic field anomalies over the Williston Basin in Manitoba and Saskatchewan (e.g. Figures 3.16 and 3.17). The area surrounding Estevan lies within a relative gravitational high while the magnetic response is regionally low. Li and Morozov (2007) interpret the Aquistore site as being located within the Sask-Reindeer boundary zone, which is transitional between the Sask craton and the interior region of the Trans-Hudson orogen.

Figure 3.16: Bouger gravity anomaly over southern Manitoba and Saskatchewan. Study area circled in black. Erosional edge of sedimentary strata indicated by white line (Li and Morozov, 2007). Copyright by Jiakang Li and Igor Morozov, University of Saskatchewan; reproduced with permission.

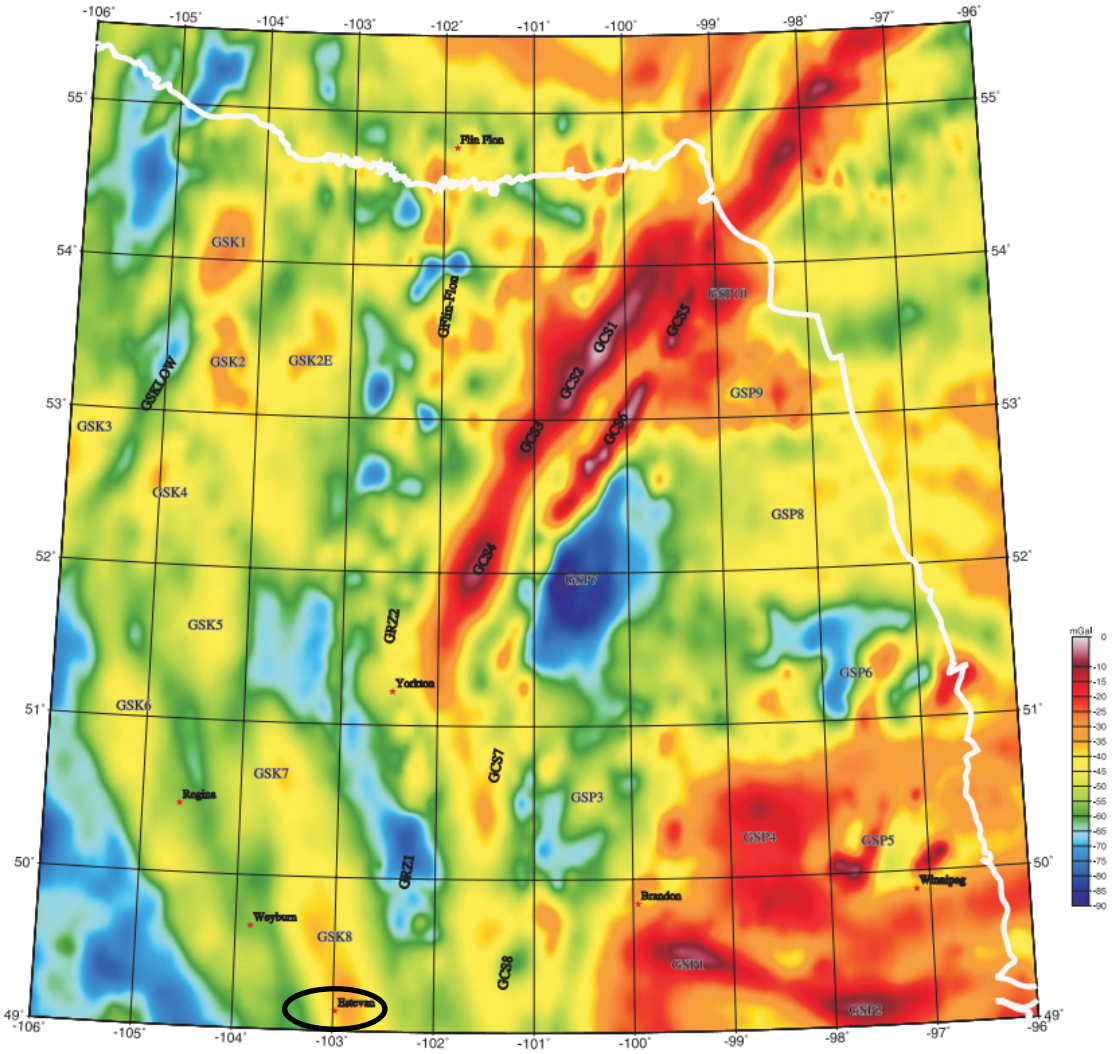

Figure 3.17: Magnetic field anomaly (band-pass filtered for 2-32 km wavelengths) with interpreted structural domains. Study area circled in black. Erosional edge of sedimentary strata indicated by white line (Li and Morozov, 2007). Copyright by Jiakang Li and Igor Morozov, University of Saskatchewan; reproduced with permission.

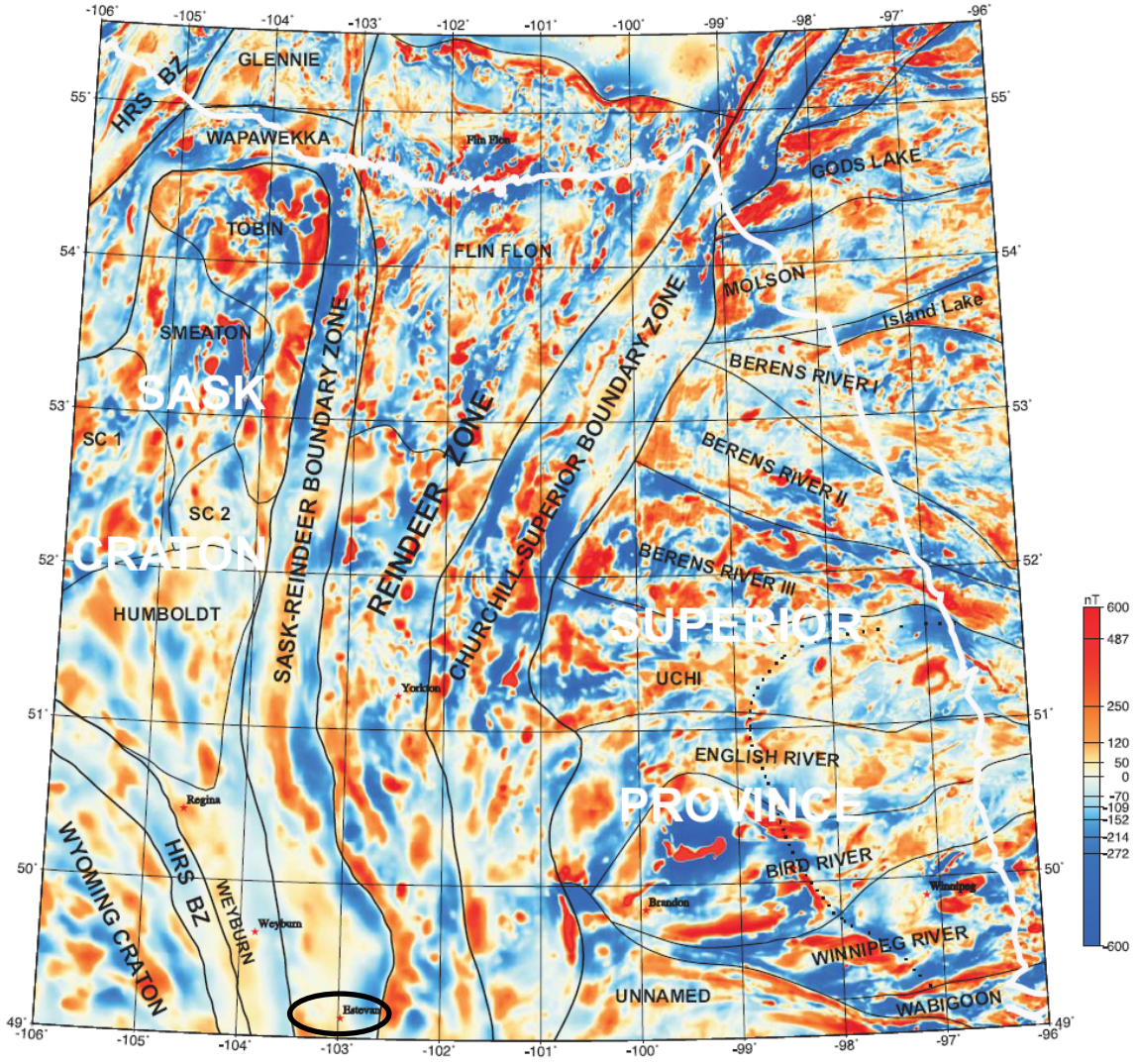

3.5 Aquistore site geophysics

A variety of geophysical techniques are being implemented at Aquistore for baseline and time-lapse characterization of the reservoir. Execution and analysis of a preliminary 3D Vibroseis seismic survey over a 30 km^2 area determined that, in the vicinity of the injection well, the targeted reservoir formations have minimal thickness variations, the Prairie Evaporite

Formation provides an unbroken seal, the reservoir is comprised largely of porous sandstones, and there are no observable vertical faults (SERC, 2013).

Surface-based geophysical monitoring techniques will include a permanent 3D seismic array, passive seismic, as well as gravity measurements. Tiltmeters, GPS, and groundwater monitoring are additional surface-based techniques being applied (SERC, 2013).

Well-based monitoring will make use of several different methods: pressure and temperature measurements, fluid tracers, cross-well seismic, vertical seismic profiling, surface to downhole electromagnetics, and gravity. A suite of logging tools is also in place and includes gamma ray, spontaneous potential, resistivity, density, neutron density, sonic compressional and dipole shear, and nuclear magnetic resonance (SERC, 2013).

3.6 Borehole resistivity data

Logging of the Aquistore injection well (PTRC INJ-5-6-2-8W2) (Figure 3.18) has offered an opportunity to study the subsurface in the immediate vicinity of the reservoir. Among the well logging tools used to examine the local rock properties is a resistivity log. This PTRC logging experiment used a Schlumberger array induction imaging tool (AIT) to collect readings every centimetre (Schlumberger, 2016).

Figure 3.18: Diagram of Aquistore injection well with formation depths and thicknesses (Aquistore, 2016). Copyright by PTRC. Used with permission.

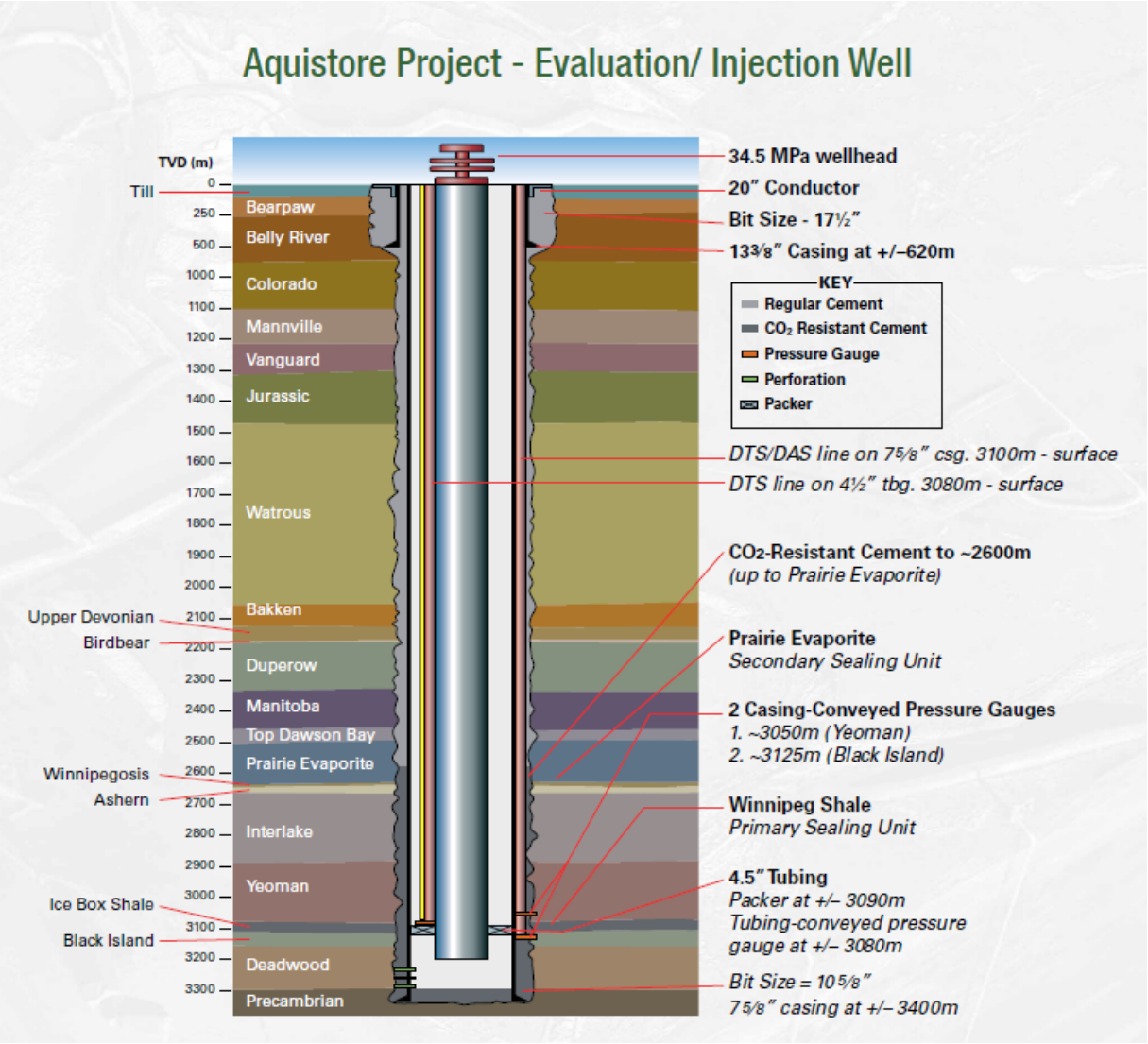

The depth range covered by the DC resistivity log data is from 0 m to 3,387 m. These readings were resampled to 3 m depth intervals (J. Craven pers comm, 2014). The uppermost 1,000 m of the log shows relatively conductive Mesozoic rocks extending from the Belly River Formation down to the Upper Watrous Formation (Figure 3.19). The resistivity is typically between 1 and 3 Ωm. This is in agreement with laterolog results reported by Jones (1988).

At greater depths, the resistivities are higher, reflecting the dominantly carbonate and evaporite lithologies of Ordovician to Mississippian-aged strata. The resistivity values in this carbonate-evaporite depth section are an order of magnitude higher than for those of the upper clastic rocks. The Prairie Evaporite Formation is particularly resistive; readings at this formation depth, from 2,600 to 2,650 m, are clipped at an instrumental maximum response of 1,950 Ωm. Some more conductive sediments in this carbonate-evaporite interval include the Upper Devonian deposits overlying the Duperow Formation (~2 Ωm), and the Interlake Formation (~3 Ωm).

The earlier interval of clastic deposition is evident at depths of ~3,080 m, and is represented by lower resistivities. The Black Island and Deadwood sandstones appear to have similar electrical properties (5-9 Ωm), differentiating this interval from the high-resistivity overlying formations and the underlying Precambrian basement.

While the above description interprets the resistivity data with respect to lithology, the readings are more strongly associated with the presence or absence of conductive formation fluids and the presence of shaly materials (Schlumberger, 2016). In this case, the high-resistivity of Paleozoic carbonate and evaporite units is due to thick sections of low porosity rock. In contrast, the Black Island-Deadwood aquifer system has a low-resistivity signature, reflective of its hydraulic properties. The characterization of the Williston Basin in terms of a series of aquifers and aquitards is therefore reflected by its electrical properties.

Based on preliminary observations of the log data, a coarse resistivity model was produced to provide a simplified representation of the basin's electrical properties at the Aquistore site (J. Craven pers comm, 2014). This model consists of 15 layers, each having a uniform resistivity, and a 1,100 Ωm half-space. The model is summarized in table 3.1.

Figure 3.19: AE90 resistivity curve (left) and simplified depth model (right) for PTRC INJ-5-6-2-8W2.

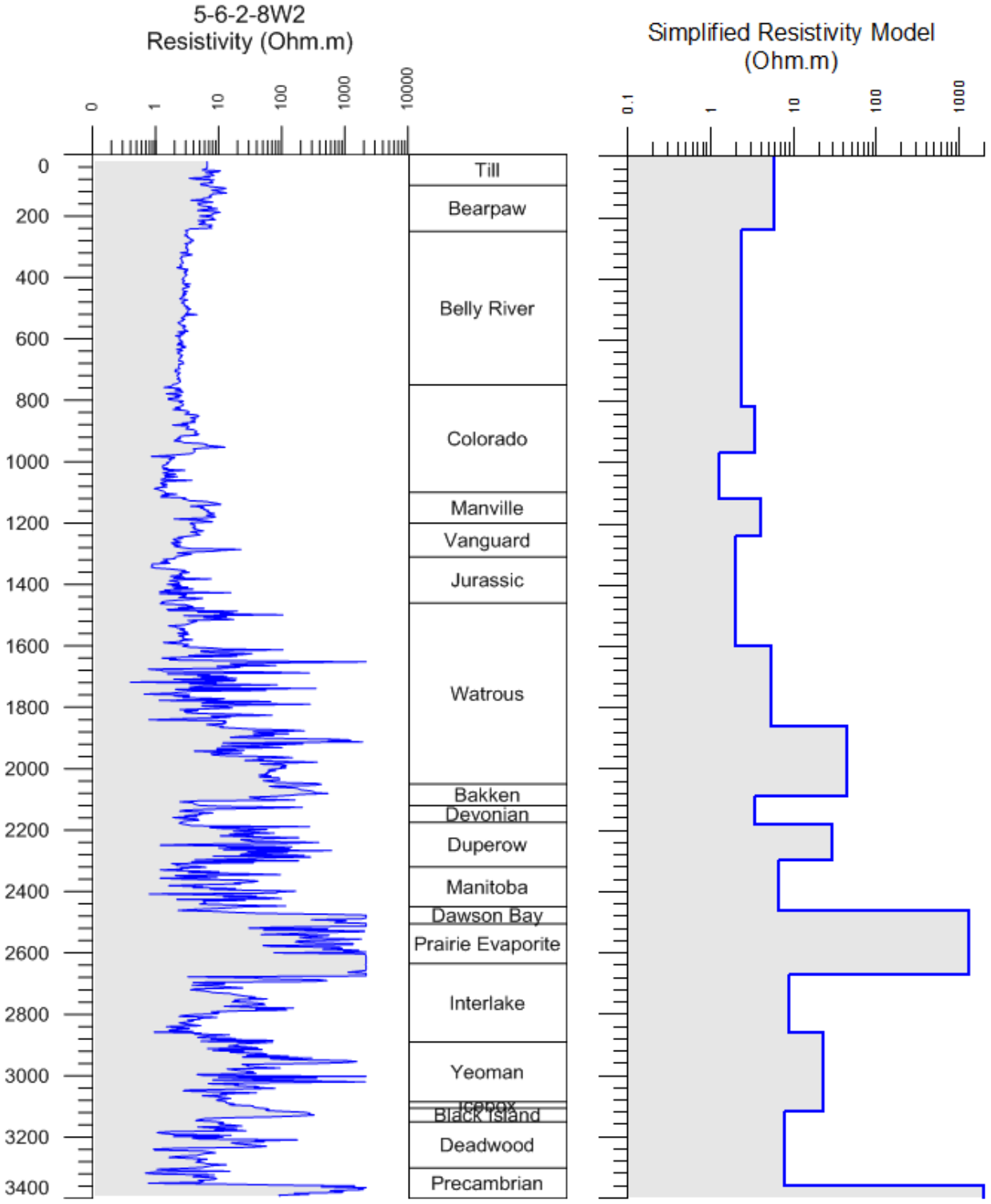

As part of the present research the coefficients of anisotropy were calculated for the units in the simplified resistivity log and are listed in Table 3.1. The coefficient of anisotropy is defined as (Edwards *et al*., 1988):

$$\lambda_a = \sqrt{\frac{\rho_\perp}{\rho_\parallel}} \tag{3.1}$$

where $\boldsymbol{\rho}_\perp$ is the resistivity perpendicular to bedding:

$$\rho_\perp = \frac{\sum_i h_i \rho_i}{\sum_i h_i} \tag{3.2}$$

and $\boldsymbol{\rho}_\parallel$ is the resistivity parallel to bedding:

$$\rho_\parallel = \frac{\sum_i h_i}{\sum_i h_i \sigma_i} \tag{3.3}$$

h_i, ρ_i, and σ_i are the thickness, resistivity and conductivity of the *i*th layer, respectively. In calculating the coefficient of anisotropy for the 5-6-2-8W2 log, the thickness of each individual 'layer' is equal to the depth sampling, 3 m. The anisotropy values represent the transverse anisotropy, which is the difference between the electrical properties in the horizontal and vertical directions.

Table 3.1: Parameters of layered resistivity model.

Layer	Thickness (m)	Resistivity(Ωm)	Coefficient of anisotropy	Geological Formations
1	240	6	1.06	Till, Ravenscrag, Bearpaw
2	580	2.4	1.04	Belly River
3	150	3.5	1.08	Upper Colorado
4	150	1.3	1.06	Lower Colorado
5	120	4	1.08	Manville
6	360	2	1.35	Vanguard, Upper Watrous
7	260	5.5	3.01	Middle Watrous
8	230	45	2.09	Lower Watrous, Bakken
9	90	3.5	1.88	Bakken
10	120	30	2.36	Duperow
11	165	6.8	2.32	Manitoba
12	205	1300	2.17	Prairie Evaporite
13	190	9	2.70	Interlake
14	260	23	2.83	Yeoman
15	240	8	5.85	Winnipeg-Deadwood

Chapter 4: Electromagnetic Theory and Methodologies

4.1 Electromagnetic induction

In geophysics, EM induction refers to the indirect generation of subsurface electrical currents using magnetic or electric sources. Secondary fields resulting from the induced currents are then measured and analyzed to gain insights into subsurface electrical properties. An understanding of the physical principles of induction begins with Maxwell's equations (Ward and Hohmann, 1988):

$$\nabla \cdot \boldsymbol{D} = \rho_e \tag{4.1}$$

$$\nabla \cdot \boldsymbol{B} = 0 \tag{4.2}$$

$$\nabla \times \boldsymbol{E} = -\partial \boldsymbol{B}/\partial t \tag{4.3}$$

$$\nabla \times \boldsymbol{H} = \boldsymbol{J} + \partial \boldsymbol{D}/\partial t \tag{4.4}$$

where $\boldsymbol{D}$ is the electric displacement current, ρ_e is the electric charge density, $\boldsymbol{B}$ is the magnetic induction, $\boldsymbol{E}$ is the electric field, $\boldsymbol{H}$ is the magnetic field, and $\boldsymbol{J}$ is the electric current density. Equations 4.1 and 4.2 are Gauss' law for electricity and magnetism, indicating the fundamental difference between the divergent flux from an electric charge and the zero-flux magnetic dipole. Faraday's law, equation 4.3, describes how time-variations in a magnetic field generate circulating electric currents. Finally, there are two mechanisms for creating circulating magnetic fields: electric currents and time changes in electric displacement currents, as shown by Ampère's law, equation 4.4. In a homogeneous non-polarizing medium, the vector fields from 4.1 to 4.4 are related by constitutive parameters of the medium (Ward and Hohmann, 1988):

$$\boldsymbol{D} = \varepsilon \boldsymbol{E} \tag{4.5}$$

$$\boldsymbol{B} = \mu \boldsymbol{H} \tag{4.6}$$

$$\boldsymbol{J} = \sigma \boldsymbol{E} \tag{4.7}$$

where ε is the electric permittivity, μ is the magnetic permeability, and σ is the electric conductivity.

To examine geophysical EM signals, first consider that propagating electric and magnetic fields are described in the frequency domain (for a positive exponential time dependence) in a uniform medium by the differential equations (Ward and Hohmann, 1988):

$$\nabla^2 \boldsymbol{E} + k^2 \boldsymbol{E} = 0 \tag{4.8}$$

$$\nabla^2 \boldsymbol{H} + k^2 \boldsymbol{H} = 0 \tag{4.9}$$

where k is the propagation constant:

$$k^2 = \mu\varepsilon\omega^2 - i\mu\sigma\omega = \mu\omega(\varepsilon\omega - i\sigma) \tag{4.10}$$

In separating the real and imaginary parts of the solutions to equations 4.8 and 4.9, we obtain the sinusoidally varying phase constant, α (real part), and the exponentially decaying attenuation constant, β (imaginary part) (Ward and Hohmann, 1988). The skin depth, the depth to which laterally uniform EM fields decay to $1/e$ of their surface value, is then defined as:

$$\delta = {}^{1}/_{\beta} \tag{4.11}$$

The induction number, B, of a particular EM method or survey refers to the ratio of the source-receiver separation to the skin depth:

$$B = {}^{r}/_{\delta} \tag{4.12}$$

When values of B are much greater than and much smaller than 1, EM methods are termed as high- and low-induction number methods, respectively. The induction number is an indication of the influence that the survey geometry and the frequency of the source field will have on the depth of investigation.

In dealing with earth materials and typical operating frequencies of geophysical surveys, it is often the case that the second term in equation 4.10 dominates ($\sigma >> \varepsilon\omega$). This scenario is called the quasi-static limit. In the quasi-static limit, the magnetic fields produced by displacement currents ($\partial \boldsymbol{D}/\partial t$ term in Ampere's Law) are neglected, and the phasing effect is eliminated (West and Macnae, 1991). Thus the wave-like propagation character of the signal is insignificant and the EM fields travel diffusively through the earth. In this case, we can neglect the $\varepsilon\omega$ term, and the skin depth then simplifies to (Ward and Hohmann, 1988):

$$\delta = \sqrt{\frac{2}{\mu\sigma\omega}} \tag{4.13}$$

Assuming that the magnetic susceptibility of earth materials does not deviate significantly from the free space value, it is clear that the depth of signal penetration depends only on the frequency and on the conductivity of the medium (Zonge and Hughes, 1991).

The dielectric limit describes the opposite extreme of EM propagation; a dielectric medium is one that is resistive ($\sigma << \varepsilon\omega$). For these materials the propagation velocity of EM signals is the speed of light, and the skin depth approaches infinity. In geophysical work, dielectrics only become relevant at very high frequencies (>20,000 Hz) and for a signal travelling through the air (Zonge and Hughes, 1991).

The determination of geophysical responses from EM methods is simplest for the case of a homogeneous earth. In this scenario, any resistivity response derived from the transfer functions between EM field components is the true resistivity. The introduction of more complex structures means that the resistivity responses represent averaged responses for the entire depth interval over which the signal penetrates. Directionally varying subsurface electric structures have different effects on the transfer functions. Geoelectric structures may be

described as 1D, 2D, or 3D, depending on the number of directions in which the subsurface resistivity characteristics vary (Figure 4.1). One-dimensional structure typically refers to vertical variations. For 2D structure, it is often possible to define a geoelectric strike in the horizontal plane. Three-dimensional characteristics may be the result of complex geologic structures such as localized bodies (Simpson and Bahr, 2005).

Figure 4.1: Schematic representation of increasingly complex geoelectric structure.

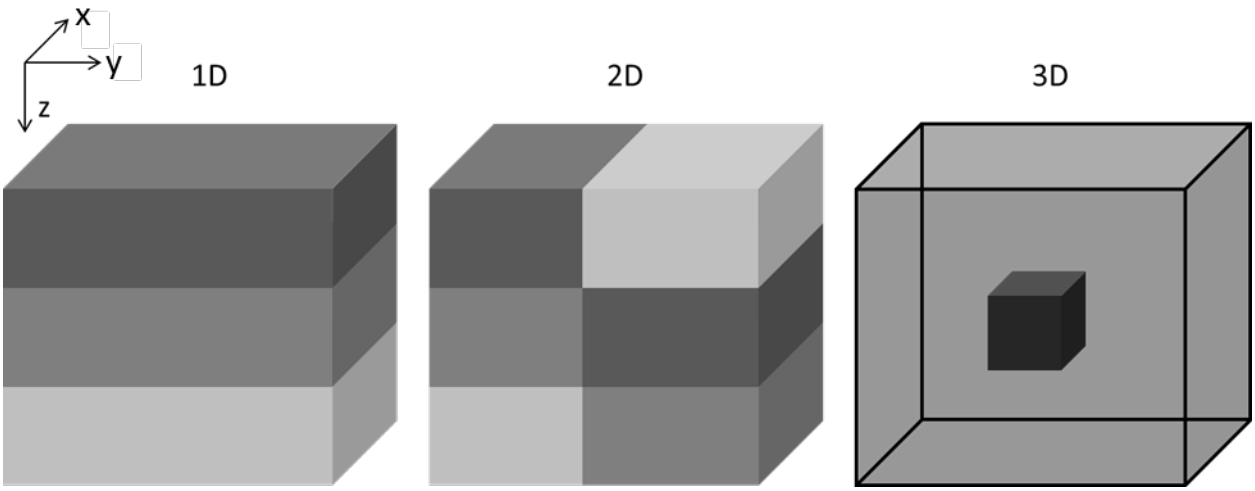

Electric currents within a 1D or 2D structure can be mathematically decoupled into independent modes of flow: transverse electric (TE) and transverse magnetic (TM). The TE mode describes current flow that is contained within horizontal planes and is characterized by the absence of a vertical electric field. For the TM mode, current loops flow in vertical planes, and there is no associated vertical magnetic field. It is often advantageous to decompose the current source into these modes to obtain a better understanding of the geometries of the source field and the earth responses (Chave and Weidelt, 2012). These two modes of current flow also provide sensitivity to different types of geoelectric structure: TE currents tend to flow preferentially

through horizontal conductive layers, while vertically flowing TM currents are more sensitive to horizontal resistive layers.

4.2 The magnetotelluric method

4.2.1 Introduction

The MT method relies on naturally-occurring geomagnetic variations to induce electric currents in the Earth's subsurface. Orthogonal horizontal components of the magnetic and electric fields arising from these sources are recorded as time series at the surface. The relationship of the magnetic fields to the induced telluric currents flowing in the subsurface allows for the determination of the electrical resistivity properties within the Earth.

4.2.2 Magnetotelluric signal source

The passive-source nature of the MT method is both an advantage and disadvantage. The strong broad-band signal provides a uniquely comprehensive range of long-period depth investigations in a manner that is not financially or environmentally prohibitive. However, the lack of control over the signal levels renders MT surveys susceptible to all types of EM noise. Vozoff (1991) classifies the MT source field as either low-frequency signal (< 1 Hz), arising from ionospheric and magnetospheric effects, or high-frequency signal (1 Hz to 10 kHz), generated by lower atmospheric processes.

The ionosphere forms as a large conductor at the top of an otherwise resistive atmosphere. The solar wind impacts the magnetic field continuously and with irregular pulses of ions and smaller magnetic fields. Time variations in the magnetic field caused by this interaction are responsible for ionospheric currents, geomagnetic storms, and resulting electric fields that are observable at Earth's surface. The source fields propagate downward into the Earth as plane

waves and are approximately vertically incident on Earth's surface. These low frequency MT signals decrease in strength regularly away from auroral latitudes to much weaker levels near the magnetic equator (Vozoff, 1991; Viljanen, 2012).

At frequencies greater than 1 Hz, the spectral energy of the EM signal is primarily sourced from lightning strikes in the lower atmosphere. It is estimated that between 100 and 1,000 lightning strikes occur every second, globally. The signals generated form these events are known as spherics. The resistive atmosphere serves as a waveguide for EM waves from distant lightning strikes. Energy from this source reflects back and forth between the ionosphere and the surface of the Earth, with a fractional amount refracting at the lower boundary, and transmitting downwards to travel diffusively through the subsurface. In contrast to the low frequency end of the spectrum, the high-frequency signal can be expected to be stronger at tropical latitudes (Vozoff, 1991).

For frequencies of approximately 1 Hz, there is no process that regularly generates strong MT signal above the noise levels of typical MT acquisition systems. As such, this part of the spectrum is considered to be a 'deadband'. Likewise, the signal at around 2 kHz is also characteristically weak (Vozoff, 1991; Viljanen, 2012).

As none of the source field mechanisms are galvanically coupled to the ground, the MT method relies primarily on TE mode currents in a 1D medium. Horizontally flowing currents generate circulating magnetic fields by Ampère's law, which, by induction, produce currents in progressively deeper subsurface bodies (Figure 4.2). A result of this induction style is that the MT method is insensitive to horizontally-oriented, high-resistivity layers (Chave and Weidelt, 2012).

Figure 4.2: Recursive induction from an external TE source field in a 1D medium.

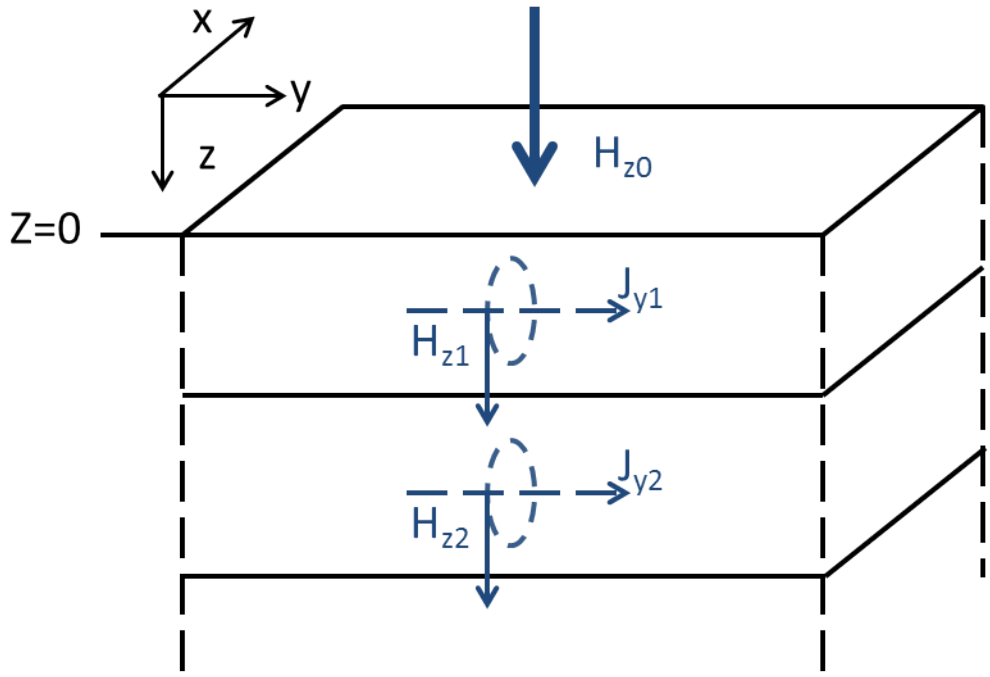

Unwanted EM signals arise from a variety of noise sources such as AC powerlines (usually 50 or 60 Hz), electric fences, railway systems, radio communication antennae, and pipelines (cathodic protection and pipeline current mapper instruments). Magnetic field noise is stronger with distance from the source over more electrically resistive terrain, but the electric fields decay less over conductive terrains. In some cases, such as for powerline noise, a simple notch filter can effectively remove the signal, but more advanced signal processing is often required. MT receiver locations need to be carefully placed to avoid or diminish noisy signals (Ferguson, 2012).

4.2.3 Transfer functions and impedance tensor

There are typically five time series of orthogonal electric (***E***) and magnetic (***H***) field components recorded in an MT survey: E_x, E_y, H_x, H_y, and H_z. By convention, the positive x and

y directions usually represent north and east, respectively, and the *z* direction is defined positive downwards. The electrical impedance (Z_{ij}) relates each of the field components lying in the horizontal plane as a function of frequency (Vozoff, 1991; Simpson and Bahr, 2005):

$$E_x = Z_{xx}H_x + Z_{xy}H_y \tag{4.14}$$

$$E_y = Z_{yx}H_x + Z_{yy}H_y \tag{4.15}$$

These equations are organized into matrix-vector form to define the impedance tensor, $\boldsymbol{Z}$:

$$\begin{pmatrix} E_x \\ E_y \end{pmatrix} = \begin{pmatrix} Z_{xx} & Z_{xy} \\ Z_{yx} & Z_{yy} \end{pmatrix} \begin{pmatrix} H_x \\ H_y \end{pmatrix} \tag{4.16}$$

$$\boldsymbol{E} = \boldsymbol{ZH} \tag{4.17}$$

As the transfer function is defined in the frequency domain, the elements of $\boldsymbol{Z}$ are complex; they will have an associated magnitude and phase (Simpson and Bahr, 2005). The dependence of the impedance tensor on the subsurface electrical structure allows the MT method to extract information on the Earth's geoelectric structure; the flow of telluric currents through a subsurface volume is influenced by the presence of conductive elements and their directional characteristics. The currents' associated secondary fields, related to the EM fields in the impedance tensor, therefore are determined not only by the bulk resistance to current flow, but by the geometrical distribution of electrical properties as well.

To determine a value of resistivity from the measured fields, first consider the relationship between fields propagating vertically downward through a homogeneous medium (Stratton, 1941; Vozoff, 1991):

$$\boldsymbol{H} = \frac{k}{\omega\mu}\mathbf{n}\times\boldsymbol{E} \tag{4.18}$$

where **n** is a unit vector pointing down and the propagation constant, k, (defined in equation 4.10) can be conveniently expressed in terms of the skin depth:

$$k = (1 - i)\frac{1}{\delta} = (1 - i)\sqrt{\frac{\omega\mu\sigma}{2}} \tag{4.19}$$

From the above expressions, we can examine the ratio E_x/H_y:

$$\frac{E_x}{H_y} = \frac{\omega\mu}{k} = (1 + i)\sqrt{\frac{\omega\mu}{2\sigma}} \tag{4.20}$$

Substituting the appropriate impedance tensor element for this ratio, we can solve for the resistivity defined by the ratio and obtain:

$$\rho_{xy} = \frac{Z_{xy}Z_{xy}^*}{\mu\omega} \tag{4.21}$$

For a more complexly structured Earth, the resistivity estimated using this equation may vary with position and frequency and is called an apparent resistivity. More generally, the apparent resistivity determined from the ij^{th} element of the impedance tensor, expressed as a function of frequency, is:

$$\rho_{a,ij}(\omega) = \frac{1}{\mu\omega}\left|Z_{ij}(\omega)\right|^2 \tag{4.22}$$

and the impedance phase is given by:

$$\varphi_{ij}(\omega) = \tan^{-1}\left(\frac{\mathrm{Im}\{Z_{ij}\}}{\mathrm{Re}\{Z_{ij}\}}\right) \tag{4.23}$$

The apparent resistivity and phase, as a function of frequency, are the typical responses obtained from the MT method. Phase responses are generally anti-correlated with apparent resistivity; a change to more conductive media will be signaled by a positive phase shift (Simpson and Bahr, 2005). In the absence of changing geoelectric structure, the phase is asymptotic to 45°. The

dispersion relationship relates the phase to the apparent resistivity mathematically. In a 1D medium this relationship can be expressed as (Vozoff, 1991):

$$\varphi(f) \approx 45° \left[1 + \frac{\partial \log \rho_a(f)}{\partial \log f}\right] \quad (4.24)$$

An effect of the dispersion relationship is that the phase response 'anticipates' changes in resistivity at higher frequencies than the apparent resistivity response (Vozoff, 1991). Due to the orthogonality of EM fields, each of the impedance elements Z_{xy} and Z_{yx} tend to represent secondary fields arising from a particular direction of induced current flow. Thus the apparent resistivities and phases derived from the off-diagonal impedance elements are given much greater emphasis in analysis of the MT responses.

The fifth field component usually measured in MT surveys, and not accounted for by the impedance tensor, is the vertical magnetic field, H_z. The tipper function, $\boldsymbol{T} = [T_x, T_y]^T$, describes the relationship of horizontal to vertical magnetic fields:

$$H_z = T_x H_x + T_y H_y \quad (4.25)$$

As with the impedance tensor, the individual tipper elements, T_x and T_y, are complex quantities. The tipper is named as such because it indicates the 'tipping' of the $\boldsymbol{H}$ vector from the horizontal; in the absence of lateral resistivity variations, the H_z component is nearly zero (Vozoff, 1991).

4.2.4 Earth response

The MT method is a high-induction number method, with signal propagation through earth materials best described by the quasi-static limit. That is to say that the source to receiver separation is very large, and that geometry of these two survey elements does not affect the depth investigation of MT soundings. Rather it is the frequency of the signal and the conductivity of

the medium that determine the propagation characteristics as the fields travel diffusively through the Earth. The skin depth for these signals is therefore defined by equation 4.13. Assuming the magnetic permeability to be that of free space ($\mu_0 = 4\pi \times 10^{-7}$ Hm^{-1}), we may express the skin depth as an approximation in terms of the apparent resistivity (ρ_a) and frequency (f) (Vozoff, 1991):

$$\delta(m) = 500\sqrt{\frac{\rho_a(\Omega m)}{f(Hz)}} \tag{4.26}$$

4.2.4.1 1D case

As the MT method relies on horizontally flowing telluric currents, a structure consisting of horizontal layers will lead to straightforward secondary field relationships. The horizontally uniform nature of the layers allows for simplification of the impedance tensor (Vozoff, 1991; Simpson and Bahr, 2005):

$$\boldsymbol{Z} = \begin{pmatrix} 0 & Z_{xy} \\ -Z_{xy} & 0 \end{pmatrix} \tag{4.27}$$

The MT responses for 1D structure will therefore be identical for the *xy* and *yx* curves, save for the phases in different quadrants.

4.2.4.2 2D case

For a multidimensional resistivity structure, the current patterns will be more complex, with resistivity boundaries represented by both horizontal and vertical planes. A geoelectric structure defined by a horizontal strike direction is considered two-dimensional, and will have a characteristic impedance tensor (Vozoff, 1991; Simpson and Bahr, 2005):

$$\begin{gathered} Z_{xx} = -Z_{yy} \neq 0 \\ Z_{xy} \neq -Z_{yx} \end{gathered} \tag{4.28}$$

If the geoelectric strike is parallel to one of the horizontal coordinate axes, then (Vozoff, 1991; Simpson and Bahr, 2005):

$$\begin{matrix} Z_{xx} = Z_{yy} = 0 \\ Z_{xy} \neq -Z_{yx} \end{matrix} \tag{4.29}$$

In practice, the geoelectric strike is not known in advance of data collection, and the coordinate *x* and *y* vectors represent cardinal directions. It is therefore advantageous to perform a rotation on the coordinate system to achieve the relationships in equation 4.29. A clockwise rotation, defined by the angle θ, is applied to minimize the off-diagonal impedance elements. The rotated tensor is given by (Vozoff, 1991):

$$\boldsymbol{Z'} = \boldsymbol{RZR}^T \tag{4.30}$$

where:

$$\boldsymbol{R} = \begin{pmatrix} \cos\theta & -\sin\theta \\ \sin\theta & \cos\theta \end{pmatrix} \tag{4.31}$$

Swift's solution is a method for determining the principle axes of a 2D subsurface. The formula seeks angles of rotation that maximize $|Z_{xy}|$ and minimize $(|Z_{xx}|^2 + |Z_{yy}|^2)$ (Vozoff, 1991):

$$4\theta = \tan^{-1}\frac{\left[(Z_{xx}-Z_{yy})(Z_{xy}+Z_{yx})^* + (Z_{xx}-Z_{yy})^*(Z_{xy}+Z_{yx})\right]}{|Z_{xx}-Z_{yy}|^2 - |Z_{xy}+Z_{yx}|^2} \tag{4.32}$$

The strike angle provided by Swift's solution contains a 90º ambiguity that may be clarified from geological constraints (Vozoff, 1991) or use of tipper information as discussed below.

In the description of decoupled current systems, there are some differences between the general EM induction terminology and the MT terminology. MT defines the TE and TM modes in terms of the two orthogonal horizontal directions of current flow with respect to the geoelectric strike (Figure 4.3). Currents flowing parallel to the strike direction belong to the TE mode, whereas currents that flow perpendicular to this boundary belong to the TM mode. The

TE mode is also known as the E-polarization, and the TM mode as the B-polarization (Chave and Weidelt, 2012). The MT and EM terminologies are formally in agreement. The MT TE current system corresponds to the EM TE system and is characterized by the absence of a vertical electric field and the MT TM current system corresponds to the EM TM system and is characterized by the absence of a vertical magnetic field.

Figure 4.3: The MT definition of TE and TM modes, A), compared to the more general definition, B). Current flows represented by dashed arrows.

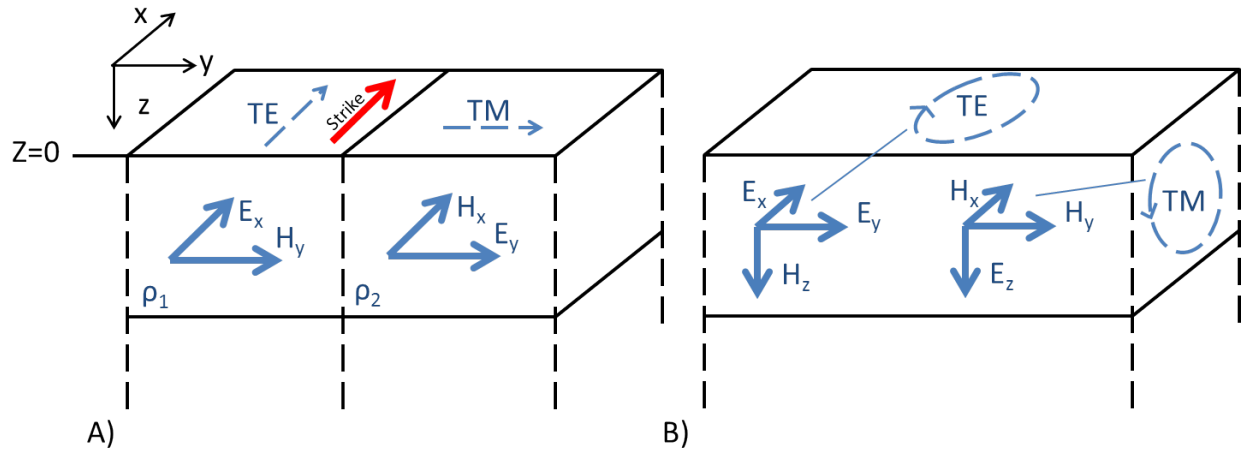

A consequence of the tensor rotation in a 2D structure is that the impedance responses may be completely separated into independent TE and TM modes:

$$\boldsymbol{Z} = \begin{pmatrix} 0 & Z_{TE} \\ -Z_{TM} & 0 \end{pmatrix} \tag{4.33}$$

As TM mode currents travel in the direction of horizontal resistivity variations and cause electric charge accumulation on resistivity boundaries, the Z_{TM} responses will resolve lateral variations more sharply than the TE mode (Simpson and Bahr, 2005).

The tipper is part of the TE mode response and may be used as an indicator of 2D structure. If geoelectric strike is in the *x*-direction, then the tipper is reduced to (Vozoff, 1991):

$$H_z = T_y H_y \tag{4.34}$$

The tipper is often represented in the form of induction arrows, which indicate the modulus and vector direction of the tipper. These arrows show the direction of lateral resistivity changes (i.e. are oriented perpendicular to strike) and, by the Parkinson convention, point towards the more conductive region (Simpson and Bahr, 2005).

4.2.4.3 3D case

The MT and tipper transfer functions become significantly more complex when earth structure varies in all three directions. For these cases, all elements of the impedance tensor are non-zero, and more advanced methods must be used to define the direction of geoelectric changes and execute subsequent inversions (Vozoff, 1991; Simpson and Bahr, 2005).

4.2.5 Distortion and noise effects

Distortion of MT responses is an effect of near-surface inhomogeneities. The accumulation of charged particles at resistivity boundaries, perpendicular to current flow, is the cause of these distortions (Vozoff, 1991). When near-surface inhomogeneities are smaller in scale than the signal wavelength, they appear to be simpler features, of a lower order of dimensionality, due to under-sampling. Effects such as these are the cause of galvanic distortion (Simpson and Bahr, 2005). Static shift is a common result of the near-surface distortion. The phase response is not subject to the effects of static shift, but the apparent resistivity curves will be shifted along the log vertical axis to values that are no longer representative of the regional resistivity structure.

Broadband EM noise is typically manifest in MT responses by apparent resistivity curves that slope at a 45° angle (on a log-log plot) and by phase responses that approach zero (Ferguson,

2012). Where signal levels are low (e.g. the MT deadband), the effects of noise on the responses is accentuated.

4.2.6 Dimensionality and strike analysis

Analyses are required to characterize unrotated, multidimensional responses; there needs to be a measure to distinguish 2D from 3D responses. The Swift skew is a simple calculation that provides a preliminary dimensional analysis (Simpson and Bahr, 2005):

$$\alpha = \frac{|Z_{xx}+Z_{yy}|}{|Z_{xy}-Z_{yx}|} \tag{4.35}$$

The skew is independent of the rotation. Swift skews greater than 0.2 are considered to indicate a 3D geoelectric structure (Simpson and Bahr, 2005). Lower orders of dimensionality will have a calculated Swift skew value near zero. However, the Swift skew may be affected by near-surface distortion, and thus the phase skew is preferred, as its calculated values are unchanged by galvanic effects:

$$\eta = \frac{\left|[Z_{xx}-Z_{yy},Z_{xy}+Z_{yx}]-[Z_{xx}+Z_{yy},Z_{xy}-Z_{yx}]\right|^{1/2}}{|Z_{xy}-Z_{yx}|} \tag{4.36}$$

where the operator $[a,b] = \mathrm{Im}(ba^*)$. For this measure, a value of 0.3 is taken to be a threshold for 3-dimensionality (Simpson and Bahr, 2005). Symmetric 3D structures will sometimes have skew values lower than the thresholds, for both types of skew calculation.

The Groom-Bailey tensor decomposition method defines the regional 2D geoelectric characteristics and 3D distortion effects separately from the initial impedance responses (Groom and Bailey, 1989):

$$\boldsymbol{Z_m = RCZ_{2D}R^T} \tag{4.37}$$

where $\boldsymbol{Z_m}$ is the measured tensor, $\boldsymbol{Z_{2D}}$ is the regional 2-D impedance tensor, and $\boldsymbol{C}$ is the real frequency-independent distortion tensor. From this decomposition, the regional 2D structure and geoelectric strike direction may be determined with greater confidence than the Swift skew. In a Groom-Bailey analysis the distortion model defined by equation 4.37 is fitted using a least-squares approach to the data at one or more frequencies. The distortion tensor may be further decomposed as:

$$\boldsymbol{C} = g\boldsymbol{TSA} = g\begin{pmatrix}1 & -t\\ t & 1\end{pmatrix}\begin{pmatrix}1 & e\\ e & 1\end{pmatrix}\begin{pmatrix}1+s & 0\\ 0 & 1-s\end{pmatrix} \tag{4.38}$$

The term g is a site gain scalar, $\boldsymbol{T}$ is the twist tensor, $\boldsymbol{S}$ is the shear tensor, and $\boldsymbol{A}$ is the anisotropy tensor. The $\boldsymbol{A}$ tensor generates distortion-based anisotropy by stretching the field components. This effect is added to the anisotropy already in $\boldsymbol{Z_{2D}}$ as the two sources are experimentally indistinguishable (Groom and Bailey, 1989). The shear tensor has the effect of rotating the vectors of the principal axes of a coordinate system. For example, if a vector on the x-axis is rotated clockwise by some angle $\phi_e = \tan^{-1}e$, then a vector on the y-axis will be rotated counter-clockwise by the same angle (Groom and Bailey, 1989). Shear values range from 0° to ± 45° for high distortion. Multiplication by the twist tensor will rotate the electric field vectors through a clockwise angle $\phi_s = \tan^{-1}t$. Extreme distortion is reflected in twist values up to ± 60°. The Groom-Bailey analysis does not solve for the site gain (static shift).

4.2.7 Data processing and impedance solutions

Raw MT data consist of time series recordings of the five different field components. The goal of MT data processing is to convert these time series into interpretable MT transfer functions, which can later be used to recover geological models. The first step in this process is to transform the raw data into the frequency domain by applying a fast Fourier transform (FFT).

The results are then segment and band averaged to smooth the spectra (Vozoff, 1991). The average auto-spectral density is:

$$\langle A(f_j)\rangle = \sqrt{\frac{1}{m}\sum_{k=1}^{m} A_k A_k^*} = \langle A_j A_j^*\rangle^{1/2} \tag{4.39}$$

where $\left\langle A_j A_j^* \right\rangle$ is the autopower for a particular segment and frequency, and *m* is the number of segments and frequencies included in the averaging. Similarly, the crosspower density of two spectra *A* and *B* at f_j is given by:

$$\langle A(f_j), B(f_j)\rangle = \frac{1}{m}\sum_{k=1}^{m} A_k B_k^* = \langle A_j B_j^*\rangle \tag{4.40}$$

The manipulation of spectra into auto- and crosspowers provides a more meaningful physical form to the frequency-domain data that emphasizes deterministic signals and permits the solution of equation 4.16 for the impedance.

Expressing each of the individual field components as either an autopower or a crosspower, we can rewrite each of the impedance relationships into pairs of equations. For a particular set of band-averaged frequencies, basic solutions for the impedance elements are determined using a least-squares method. For each window over which averaging has been applied, there is a pair of equations such as (Vozoff, 1991):

$$\langle E_x H_x^*\rangle = Z_{xx}\langle H_x H_x^*\rangle + Z_{xy}\langle H_y H_x^*\rangle \tag{4.41}$$

$$\langle E_x H_y^*\rangle = Z_{xx}\langle H_x H_y^*\rangle + Z_{xy}\langle H_y H_y^*\rangle \tag{4.42}$$

The pair of equations above contains two complex unknowns Z_{xx} and Z_{xy}. We can solve these equations simultaneously, and determine the impedance values using a least squares method. For example:

$$Z_{xx} = \frac{\langle E_x H_x^*\rangle\langle H_y H_y^*\rangle - \langle H_y H_x^*\rangle\langle E_x H_y^*\rangle}{\langle H_x H_x^*\rangle\langle H_y H_y^*\rangle - \langle H_y H_x^*\rangle\langle H_x H_y^*\rangle} \tag{4.43}$$

Similar equations are defined to solve for Z_{yx} and Z_{yy} in addition to the tipper (Vozoff, 1991):

$$\langle H_z H_x^* \rangle = T_x \langle H_x H_x^* \rangle + T_y \langle H_y H_x^* \rangle \quad (4.44)$$

$$\langle H_z H_y^* \rangle = T_x \langle H_x H_y^* \rangle + T_y \langle H_y H_y^* \rangle \quad (4.45)$$

The autospectra in the impedance solutions introduce a bias (Vozoff, 1991; Simpson and Bahr, 2005). To counteract the biasing effect of noise, all autospectra can be removed from the solutions and replaced with remote reference crosspower estimates. A remote site is chosen at a distance of 100 m to 1 km from the main survey area, and the orthogonal ***H*** fields are recorded (***E*** field receivers are used less commonly). For the case of Z_{xx}, the impedance solutions then become (Vozoff, 1991; Simpson and Bahr, 2005):

$$Z_{xx} = \frac{\langle E_x R_x^* \rangle \langle H_y R_y^* \rangle - \langle H_y R_x^* \rangle \langle E_x R_y^* \rangle}{\langle H_x R_x^* \rangle \langle H_y R_y^* \rangle - \langle H_y R_x^* \rangle \langle H_x R_y^* \rangle} \quad (4.46)$$

where R_x and R_y are the remote site's horizontal magnetic fields. Note that in order for the remote reference impedance estimate to be unbiased there should be no correlated noise between the primary MT and remote reference site.

4.2.8 The 1D forward problem

Calculation of the surface impedance for a 1D, layered model (Figure 4.4) is accomplished in a recursive manner. By matching boundary conditions at each interface, and using the impedance of the basal half-space, which can be easily derived based on the response of a uniform earth, a recursive approach is used to determine the MT response at the surface.

Figure 4.4: For 1D layered Earth structures, each layer will have its own MT impedance, defined at the top interface of the layer. The Nth layer (half-space) is used as a starting point for obtaining all other layer impedances.

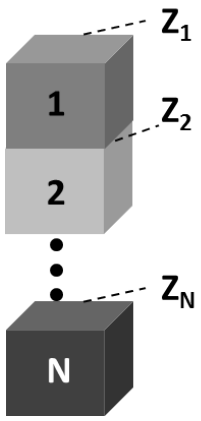

For a source field producing horizontal subsurface currents only (i.e. TE mode), the impedance at the top of the lower half-space (*N*th layer) is (Simpson and Bahr, 2005):

$$Z_{xy}^{N} = \frac{i\omega\mu}{\theta_N} \tag{4.47}$$

where θ is the vertical wavenumber, defined as:

$$\theta^2 = i\omega\mu\sigma - \omega^2\mu\varepsilon + k_x^2 + k_y^2 \tag{4.48}$$

where k^2 is the wavenumber. The relationship between the impedances at the top interfaces of successive layers is (Simpson and Bahr, 2005):

$$Z_{xy}^{j+1} = \frac{-i\omega\mu}{\theta_j}\frac{\left[\theta_j Z_{xy}^{j} - i\omega\mu\tanh\left(\theta_j h_j\right)\right]}{\left[\theta_j Z_{xy}^{j}\tanh\left(\theta_j h_j\right) + i\omega\mu\right]} \tag{4.49}$$

where *h* is the layer thickness. The surface impedances may then be used to forward calculate the apparent resistivity and phase responses for a range of frequencies (equations 4.22 & 4.23). Equivalent relationships can be derived from the physics of a source field that induces only vertical currents (TM mode):

$$Z_{yx}^{N} = \frac{\theta_N}{\sigma_n + i\omega\varepsilon} \tag{4.50}$$

$$Z_{yx}^{j+1} = \frac{-\theta_j}{\sigma_j} \frac{\left[\sigma_j Z_{yx}^{j} - \theta_j \tanh\left(\theta_j h_j\right)\right]}{\left[\sigma_j Z_{yx}^{j} \tanh\left(\theta_j h_j\right) + \theta_j\right]} \tag{4.51}$$

Manipulation of the 1D MT forward problem reveals characteristics of the MT response for some limiting cases. The surface impedance of layers that are either very thick or very conductive will approach a half-space response. The effect of very thin layers on the impedance does not depend on the resistivity or thickness separately, but on the conductance; equivalency of the conductance of a layer in two different models will result in the models having the same MT response. If a very thin layer is also very resistive, its contribution to the apparent resistivities will become negligible (Simpson and Bahr, 2005). Generally, the presence and properties of a resistive layer overlain by a much more conductive layer will be difficult to resolve using the MT method.

4.2.9 The 1D inverse problem

Representation of the resistivity structure of the Earth as a 1D model is often a drastic oversimplification of earth structure. However, there are cases where a 1D model is plausible: shallow sedimentary basins may be well approximated as a layered structure, and the geoelectric response of the mantle suggests there are minimal lateral variations in resistivity at depths exceeding 400 km (Parker and Booker, 1996). When it comes to inverting MT responses for these types of basic 1D structure in the absence of other constraints, the simplest possible model is preferred, in accord with Occam's razor. This model will consist of either a smoothly varying function, with small gradients, as would be appropriate for the lower mantle, or a series of sharp boundaries for layered basins (Parker, 1983).

Though the resulting models from 1D inversions will represent simple structures, the governing equation of the inverse problem (e.g. equation 4.49) is complex and is a non-linear

function of earth resistivity. It can be shown that solutions to the 1D MT problem exist and that for bandlimited and finite-error data, the problem is non-unique (Parker, 1983). Typically, an objective function is constructed to minimize data misfit of either the impedances, or the phase and log apparent resistivity, along with some measure of model roughness (e.g. Rodi and Mackie, 2012). The log of the apparent resistivity is often preferred as a data parameter to the linear apparent resistivity because the estimated resistivities, ρ_{est}, are distributed lognormally about the true resistivities, ρ_{true} (Jones and Hutton, 1979), and such a parameterization prevents the inversion from solving for negative resistivities. A model is judged acceptable if its misfit or objective function value falls below a prescribed tolerance level. Parker (1983) suggests a chi-squared test be used to establish the tolerance criteria. This would require that the data be unbiased and that the statistical distribution of the estimated data be known.

4.3 Controlled-source electromagnetics

4.3.1 Introduction

Controlled-source EM has some advantages over the MT method: the variety of possible sources, receivers, and survey configurations allows for different types of induction to target subsurface features otherwise unseen by the TE mode signal dominating the MT response. CSEM also offers more reliable signal to noise ratios. As with the MT method, geophysical CSEM techniques operate mainly in the quasi-static regime of EM propagation.

CSEM exploration methods may be classified as either frequency domain or time domain, based on the nature of the inducing signals. For frequency-domain EM surveys, the in-phase and quadrature components of the secondary fields produced by eddy currents induced by a periodic source are measured (Figure 4.5). The response may be expressed in terms of the in-

phase and quadrature components of the measured field or in terms of the amplitude and phase. The response may be expressed in terms of the units of the measured field or in terms of an impedance, defined as the ratio of the voltage in the receiver to the current in the transmitter. As with the MT response, the amplitude response is often expressed in terms of an apparent resistivity. This response is the resistivity of a homogeneous half-space that yields the same amplitude as the measured response.

The measured fields may be compared to a reference field. Separation of the response into in-phase and quadrature components of the signal facilitates this comparison (Figure 4.5). For magnetic sources, the reference field is usually the primary field, the corresponding field produced by the same source in free-space. For electric sources, the reference field is often the static homogeneous (uniform half-space) earth field, which is also sometimes referred to as the primary field. The response impedance from either an electric or magnetic source may be normalized to form the mutual impedance Z/Z_0, the ratio of the observed impedance to the impedance for the reference field.

Figure 4.5: Summary of EM fields contributing to a frequency domain CSEM measurement using a horizontal electric dipole source.

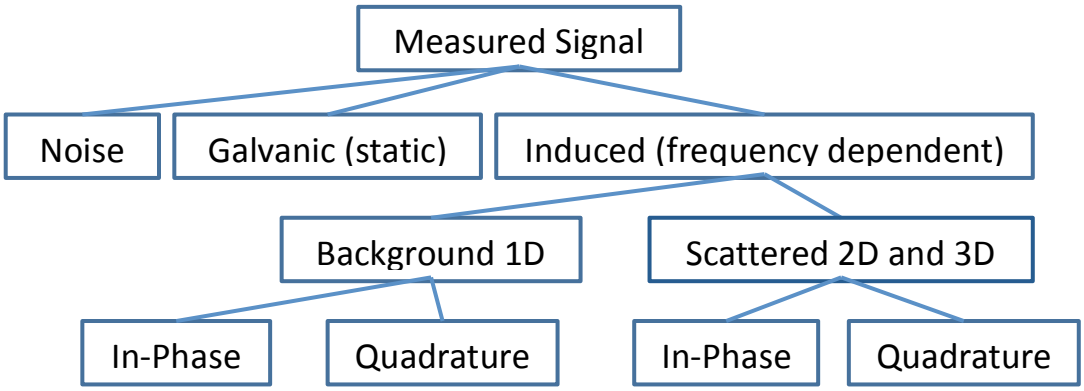

Multi-component measurement systems may record ratios of orthogonal field components or polarisation ellipsoid parameters, such as tilt angle and ellipticity. For these

alternative measured quantities, and for the phase, the transmitter source moment does not impact the measurement.

The depth of investigation in frequency domain surveys is controlled either by the frequency of the source (high induction number, $r >> \delta$) or the source-receiver geometry (low induction number) (Spies and Frischknecht, 1991).

In time-domain EM (TEM) surveys, the source current is paused so that the scattered fields may be measured without being masked by the primary field. The secondary fields are induced by the sudden change in the primary field, in accordance with Faraday's Law (Nabighian and Macnae, 1991). Common transmission waveforms are periodic step function-like pulses, triangular waveforms, and sinusoidal signals. The measured response following each of these pulses is stacked to improve the signal to noise ratio. Long-offset TEM (LOTEM) is employed in situations where the depth to the target is less than the separation of source and receiver (Strack *et al*., 1990).

Sources used in CSEM work are grounded wires and current loops. Grounded wire sources are coupled to the earth by conductive electrodes. These sources may be treated as electric dipoles for receiver sites located a distance greater than 5 times the length of the grounded wire away. Otherwise grounded wire sources must be considered as electric bipoles, with the wire length taken into account (Ward and Hohmann, 1988; Spies and Frischknecht, 1991). Likewise, loop sources located at distances away from receivers that are 2-3 times greater than the loop dimensions may be approximated as simple circular loops. For closer loop receiver pairings, the geometry of the source becomes important. Loops that are very small compared to survey dimensions may be approximated as time-varying magnetic dipoles (Spies and Frischknecht, 1991).

An important application for CSEM methods is the detection of offshore hydrocarbon deposits. Marine-based techniques are more effective as in many settings the transmitted air wave (primary field) does not figure prominently in the data recordings, and there is generally an absence of cultural noise. Performing CSEM work on land has proven to be more challenging (Streich *et al*., 2011).

Theoretical modeling of EM responses to a CO_2 saturated reservoir gives an indication of the optimized usage of a controlled-source methodology. Streich (2016) shows that to detect a thin relatively resistive layer in a more conductive background (as would be the case for CO_2 injected into an aquifer), the most sensitive survey configuration employs a horizontal electric dipole source and inline measurements of the E_x and E_z fields (Figure 4.6, panels d and e). Measurements of the vertical electric field would be ideal in this scenario, but this would require borehole sensors. For a surface-based survey, measurements of the inline E_x component will be the most sensitive to an embedded resistive layer.

Figure 4.6: Modeling of anomalous EM responses (anom) relative to background responses (bg) for an embedded resistor (0.2 Hz) or conductor (1 Hz) (Streich, 2016). Panels (b) and (c) are for a vertical magnetic dipole source. Panels (d) to (i) are for a horizontal electric dipole. Copyright by Springer. Used with permission.

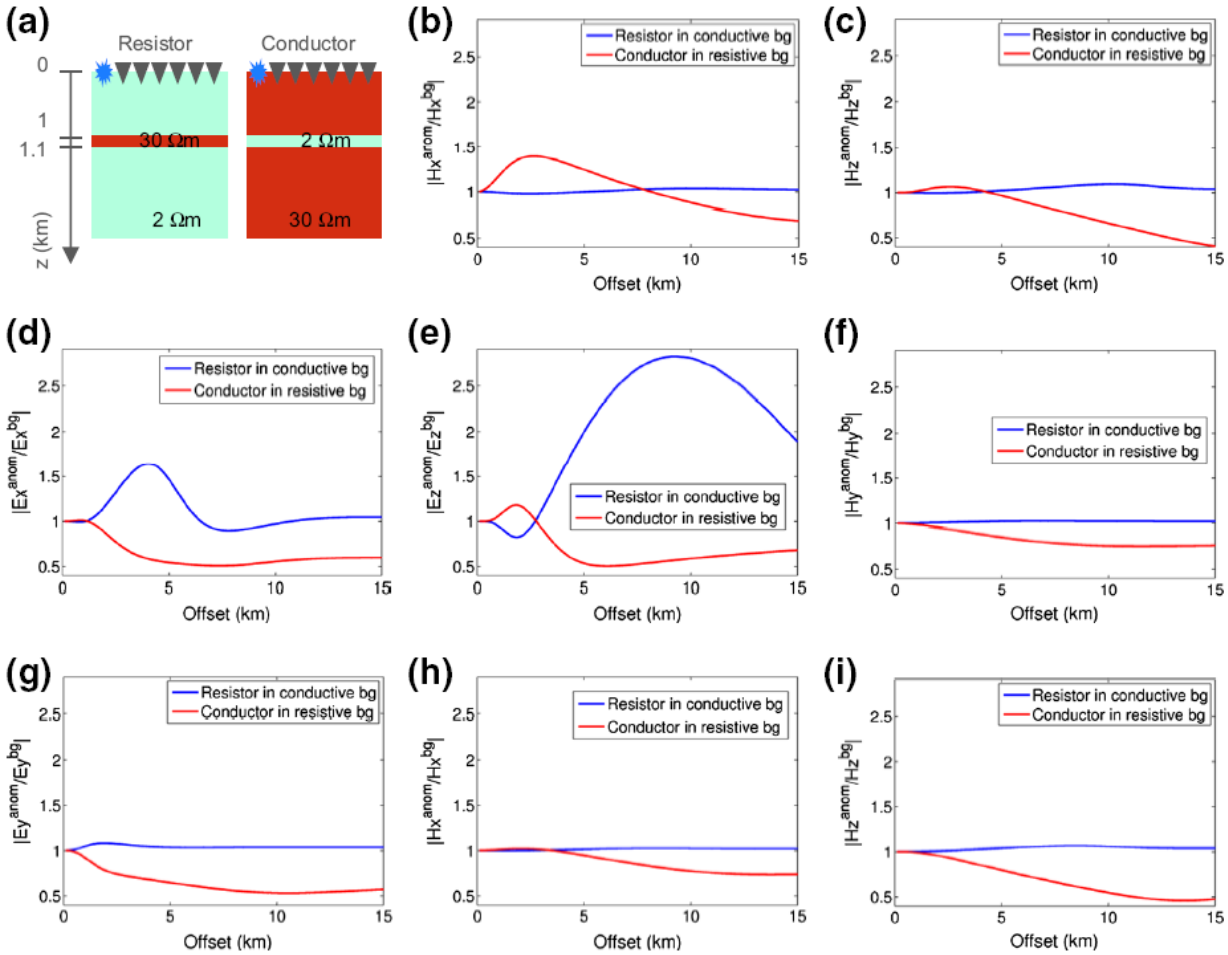

4.3.2 Horizontal electric dipole sources

Streich (2016) has shown that a horizontal electric dipole source, coupled with inline E_x measurements, form the CSEM methodology most applicable to carbon sequestration monitoring. A number of authors have presented the theory for fields of a horizontal electric dipole in a 1D setting (e.g. Chave and Cox, 1982; Kauffman and Keller, 1983; Ward and Hohmann, 1988; Key, 2009). For an *x*-directed source at the surface of a layered earth, Ward and Hohmann (1988) write the resulting fields as:

$$E_x(x,y,z) = \frac{-Ids}{4\pi}\frac{\partial}{\partial x}\frac{x}{\rho}\int_0^\infty \left[(1-r_{TM})\frac{\theta_0}{i\omega\varepsilon_0} - (1+r_{TE})\frac{i\omega\mu_0}{\theta_0}\right]J_1(k\rho)dk \qquad (4.52)$$
$$-\frac{i\omega\mu_0 ds}{4\pi}\int_0^\infty (1+r_{TE})\frac{k}{\theta_0}J_0(k\rho)dk$$

$$E_y(x,y,z) = \frac{-Ids}{4\pi}\frac{\partial}{\partial x}\frac{y}{\rho}\int_0^\infty \left[(1-r_{TM})\frac{\theta_0}{i\omega\varepsilon_0} - (1+r_{TE})\frac{i\omega\mu_0}{\theta_0}\right]J_1(k\rho)dk \qquad (4.53)$$

$$H_x(x,y,z) = \frac{Ids}{4\pi}\frac{\partial}{\partial x}\frac{y}{\rho}\int_0^\infty (r_{TM}+r_{TE})\exp(\theta_0 z)J_1(k\rho)dk \qquad (4.54)$$

$$H_y(x,y,z) = \frac{-Ids}{4\pi}\frac{\partial}{\partial x}\frac{x}{\rho}\int_0^\infty (r_{TM}+r_{TE})\exp(\theta_0 z)J_1(k\rho)dk \qquad (4.55)$$
$$-\frac{Ids}{4\pi}\int_0^\infty (1-r_{TE})\exp(\theta_0 z)kJ_0(k\rho)dk$$

$$H_z(x,y,z) = \frac{Ids}{4\pi}\frac{\partial}{\partial x}\frac{y}{\rho}\int_0^\infty (1+r_{TE})\exp(\theta_0 z)\frac{k}{\theta_0}J_1(k\rho)dk \qquad (4.56)$$

where I is the current flowing through the wire, ds is an element of dipole length, J_n are Bessel functions, and r_{TE} and r_{TM} are the reflection coefficients for the TE and TM modes:

$$r_{TE} = \frac{Y_0 - \hat{Y}_1}{Y_0 + \hat{Y}_1} \qquad (4.57)$$

$$r_{TM} = \frac{Z_0 - \hat{Z}_1}{Z_0 + \hat{Z}_1} \qquad (4.58)$$

where $\hat{Y}_1$ is the surface admittance, $\hat{Z}_1$ is the surface impedance and Y_0 and Z_0 are the free space admittance and impedance, respectively. Ward and Hohmann (1988) leave the expressions for the fields in undifferentiated form in order to concisely express the behaviour of both dipole and bipole sources. For a bipole with a long grounded wire, the differential operator vanishes upon integration, and a sign change is applied to the expression. However, in the case of a dipole, the differentiation of Bessel functions must be applied carefully. Using the relation (Dwight, 1961):

$$\frac{\partial}{\partial x}J_1(\lambda x) = -\frac{J_1(\lambda x)}{x} + \lambda J_0(\lambda x) \qquad (4.59)$$

the form of the electric and magnetic field equations can be reduced. For example, the E_x field along the axis of the source becomes:

$$E_x(x,y,z) = \frac{-Ids}{4\pi}\int_0^\infty \left[(1-r_{TM})\frac{\theta_0}{i\omega\varepsilon_0} - (1+r_{TE})\frac{i\omega\mu_0}{\theta_0}\right]\frac{J_1(k\rho)}{x}dk + \int_0^\infty \frac{\theta_0}{i\omega\varepsilon_0}(1-r_{TM})kJ_0(k\rho)dk \quad (4.60)$$

Spies and Frischknecht (1991) and Zonge and Hughes (1991) give the equations for the fields produced by a grounded horizontal electric dipole, on the surface of a homogeneous half-space. The homogeneous earth case represents a simplification of the layered earth case which is useful in illustrating the spatial behaviour of CSEM fields in limiting cases. In particular, the responses at a particular frequency depend on the position of the receiver with respect to the source i.e. the induction number. The EM responses also simplify when presented in a cylindrical coordinate system, where φ and r are the angle and the radial modulus in the horizontal plane and z is the vertical direction.

In the low induction number setting ($r << \delta$), the responses of a horizontal electric dipole are:

$$E_r \approx \frac{I\,ds\cos\varphi}{\pi\sigma r^3} \quad (4.61)$$

$$E_\varphi \approx \frac{I\,ds\sin\varphi}{2\pi\sigma r^3} \quad (4.62)$$

$$H_r \approx \frac{I\,ds\sin\varphi}{4\pi r^2} \quad (4.63)$$

$$H_\varphi \approx -\frac{I\,ds\cos\varphi}{4\pi r^2} \quad (4.64)$$

$$H_z \approx \frac{I\,ds\sin\varphi}{4\pi r^2} \quad (4.65)$$

These results show that, at low induction numbers, the fields have no frequency dependence and are affected by the distance from the source. The electrical fields are proportional to the

subsurface resistivity, but the magnetic fields are unaffected by the medium. The magnetic fields are said to be saturated, as their responses are independent of both the resistivity and the frequency. The decay of the fields away from the source is greater for the electric fields (proportional to r^{-3}) than for the magnetic fields (proportional to r^{-2}).

The high induction number ($r >> \delta$) solutions also simplify considerably:

$$E_r \approx \frac{I\, ds \cos\varphi}{2\pi\sigma r^3} \tag{4.66}$$

$$E_\varphi \approx \frac{I\, ds \sin\varphi}{\pi\sigma r^3} \tag{4.67}$$

$$H_r \approx \frac{I\, ds \sin\varphi}{\pi\sqrt{\mu\sigma\omega} r^3} e^{-i\pi/4} \tag{4.68}$$

$$H_\varphi \approx \frac{-I\, ds \cos\varphi}{2\pi\sqrt{\mu\sigma\omega} r^3} e^{-i\pi/4} \tag{4.69}$$

$$H_z \approx \frac{-3I\, ds \sin\varphi}{2\pi\mu\sigma\omega r^4} e^{-i\pi/2} \tag{4.70}$$

Note that the magnetic fields are no longer saturated, as both the frequency and resistivity now impact the response. All horizontal field components decay away from the source at a rate of r^3.

The responses in the transition zone ($r \approx \delta$, examined below) can be quite complicated, especially for non-homogeneous media.

Figure 4.7 shows the spatial variation in the responses for Cartesian coordinates. The fields exhibit symmetry about the source at both high and low induction numbers. Along the dipole axis, or in the equatorial position, the fields will either vanish or reach a maximum magnitude.

Figure 4.7: EM field responses in a 10 Ωm homogeneous earth. Field components are defined in the Cartesian coordinate system for an x-directed electric dipole with a 1 Hz frequency and 100,000 Am moment.

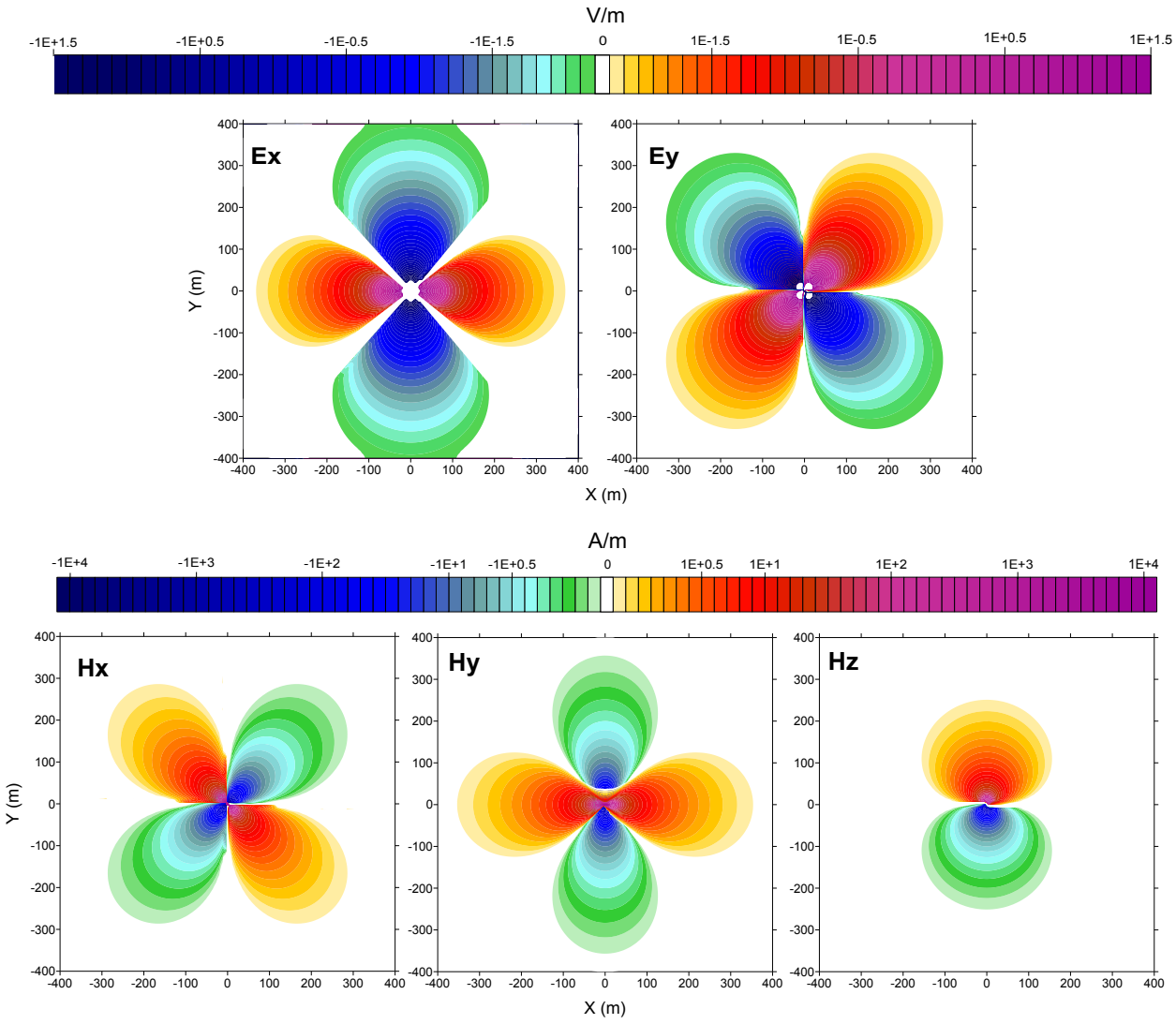

The full form of the electric field responses of a horizontal electric dipole will now be considered in more detail. The solution of equation 4.52 for a half-space is, in cylindrical coordinates, is given by (Spies and Frischknecht, 1991)

$$E_r = \frac{Ids}{2\pi\sigma r^3}\left[1 + (1 + ikr)e^{-ikr}\right] \tag{4.71}$$

$$E_\varphi = \frac{Ids}{2\pi\sigma r^3}\left[2 - (1 + ikr)e^{-ikr}\right] \tag{4.72}$$

The real part of the response is dominated by the primary field, and is independent of frequency at high and low induction numbers (Figure 4.8). The imaginary part of the response increases exponentially at low induction numbers, and decays in an oscillatory manner at high induction numbers. As the induction number approaches 1, the response undergoes a transition between the two types of asymptotic behaviour.

Figure 4.8: Inline electric field response to a 24,000 A.m horizontal electric dipole over a 1 S/m homogeneous half-space. Observation point is 1,000 m from the source.

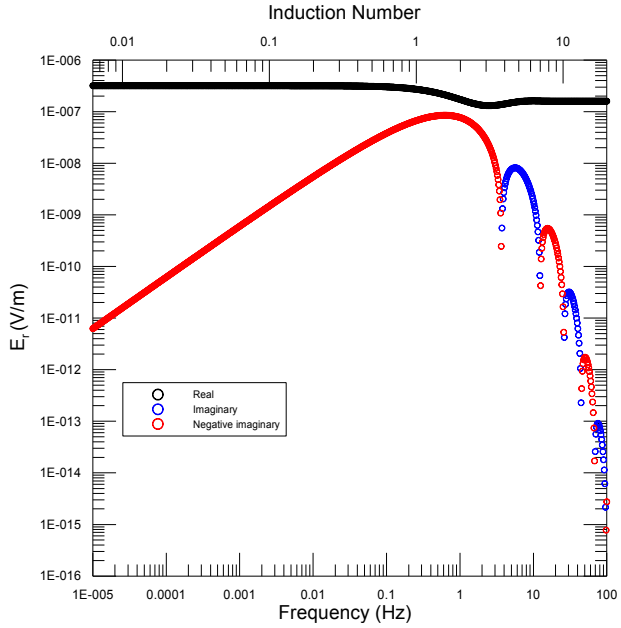

The phase and amplitude of the mutual impedance also show the transition between high and low induction number asymptotes (Figure 4.9). The transitional behaviour of the fields occurs at an induction number of ~1. The electric fields exhibit a distinct angular dependence. In the in-line position, the fields are halved at high induction number, whereas the fields are doubled in the equatorial position. At low frequency, the response is close to the DC limit, and so normalization by the static field yields a unit Z/Z_0 amplitude. The halving and doubling of the fields at high induction number are due to the increasing contributions of inductive signals. In the transition between low to high induction number, the E_r and E_φ responses each shift ~21˚ out

of phase from the source, in opposite directions, and then shift back to zero-phase with increasing induction number. The zero-phase limits at high and low inductions numbers are the result of the much smaller imaginary component, as shown in Figure 4.8.

Figure 4.9: Mutual impedance amplitude and phase responses to a horizontal electric dipole over a homogeneous half-space for the inline and equatorial positions. Observation point is 1,000 m from the source. The induction number scaling is for the 1 S/m case.

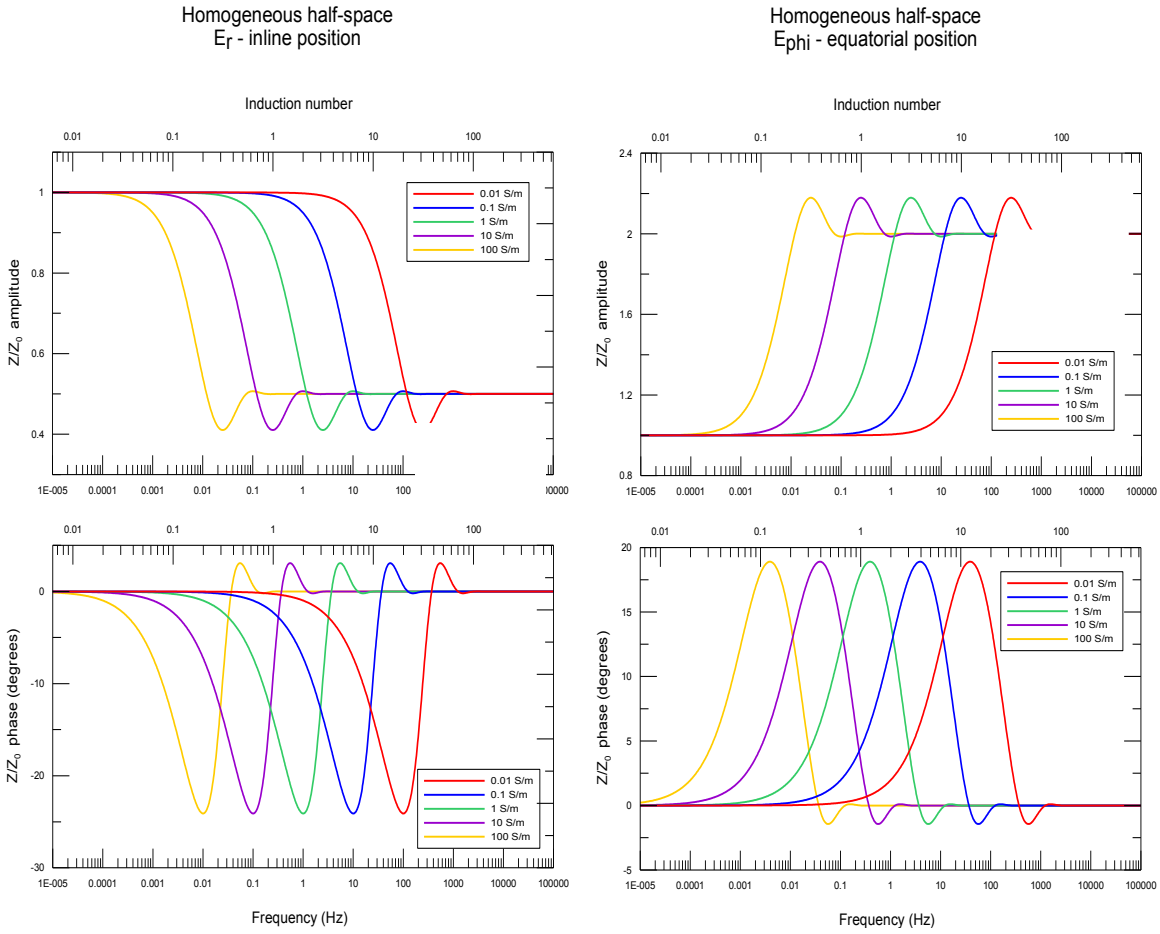

The fields created by the horizontal electric dipole source may arise from physically distinct current systems. Ward and Hohmann (1988) describe the separation in terms of vortex terms, which are frequency-dependent TE mode currents associated with the current flowing between grounding points, and grounding terms which are non-inductive, frequency-independent, currents injected at each end of the dipole and include both TE and TM currents.

For a dipole or bipole oriented in the x-direction, the E_y and H_x components do not include vortex terms, and are therefore frequency independent, whereas the H_z term contains only TE vortex terms. The E_x and H_y components will include both vortex and grounding terms and include both TE and TM currents.

A mathematical separation of source terms is also possible. Based on the full expression for a horizontal electric dipole (equation 4.60), the independent contributions of three integral terms may be considered in a half-space setting (Figure 4.10). At low induction number, there are equal contributions from the TM J_0 and J_1 terms, which both have zero phases. Through the transitional range, the J_1 TE term increases to significant amplitude while the J_0 term decreases. At high induction number, the amplitude of the J_1 TE and TM terms are equal but almost 180˚ out of phase. The response is dominated by the small difference between these terms and has a phase close to zero.

Figure 4.10: Decomposed Ex response for a 100 Ωm halfspace in terms of mutual impedance and phase.

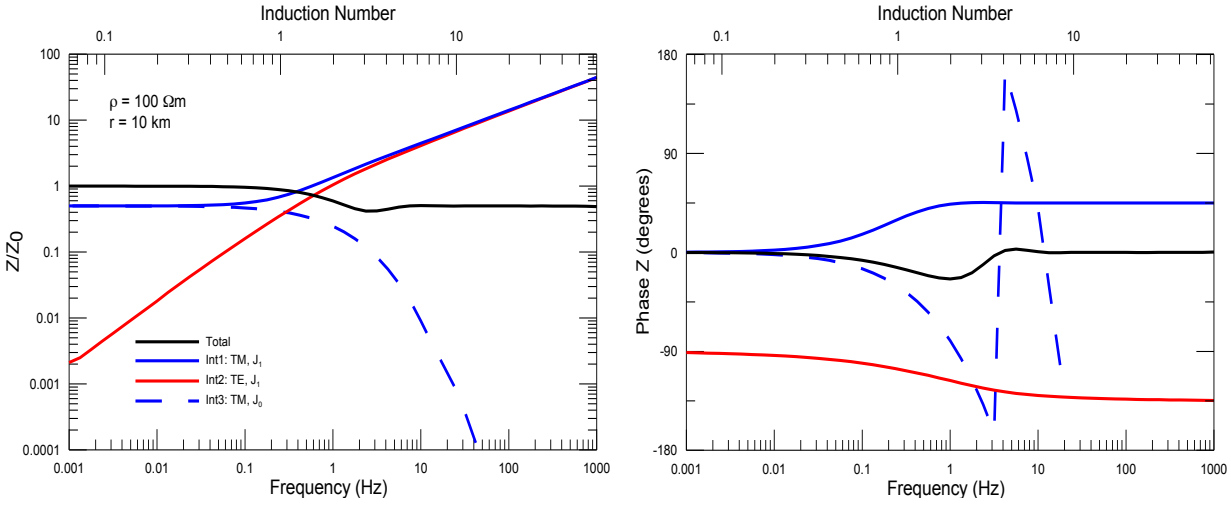

4.3.3 Controlled-source audiomagnetotellurics

Audiomagnetotellurics (AMT) is a subset of the MT method that focuses on a narrow, high frequency band of the source field between tens and tens of thousands of Hz. AMT provides data on only the shallowest depths of investigation of the MT method, but the data collection is much quicker than broad-band MT soundings due to the exclusion of long-period recordings (Goldstein and Strangway, 1975).

Though it is a controlled-source method, CSAMT retains many important characteristics of the MT method. The introduction of a controlled source to an AMT survey will change the nature of the subsurface currents and secondary fields, but the receiver configuration used to collect the data remains the same (Streich *et al*., 2010). The assumption made for the MT method that the source field is vertically incident on the earth is also used in CSAMT and requires that the measurements be made an appropriate number of skin depths away from the source. As with MT, the responses are examined in terms of their impedances. Grounded dipoles and horizontal current loops are the usual sources for CSAMT surveys (Zonge and Hughes, 1991).

From the expressions in the previous section for a horizontal electric dipole at the surface of a homogeneous earth (equations 4.61-4.70) the CSAMT impedance may be viewed in the low induction number limit as (Zonge and Hughes, 1991):

$$Z = \left|\frac{E_\varphi}{H_r}\right| = \frac{2\rho}{r} \qquad (4.72)$$

Note that there is no frequency dependence so normal MT procedures cannot be applied; only geometric soundings are possible at low induction numbers. At high induction number, satisfying the skin depth requirement mentioned above, the impedance reduces to:

$$|Z|^2 = \left|\frac{E_\varphi}{H_r}\right|^2 = \mu\rho\omega \quad (4.73)$$

This relationship is equivalent to equation 4.21.

4.4 EM methods in carbon sequestration: applications

The MT and CSEM methods have previously been used to characterize CO_2 storage complexes in Hontomín, Spain and Ketzin, Germany prior to the fluid injection. As at Aquistore, these are land-based sequestration projects that target saline aquifers.

4.4.1 Hontomín, Spain

At the Hontomín site in Spain, the injection reservoir is a 100 m interval of lower Jurassic limestones located at a depth of 1,500 m (Ogaya *et al*., 2013). The MT method was selected to characterize the geoelectric response of the injection target due to its depth penetration. Cultural noise sourced from powerlines and wind turbines at this site is characterized by 10 and 50 Hz signal (Escalas *et al*., 2013). Using constraints from nearby borehole resistivity data, both 2D and 3D inversions of MT data collected prior to injection indicate that the contrast in electrical resistivity of the reservoir rock and the primary seal is resolvable and sufficient to identify any changes in the rock properties following an injection (Ogaya, *et al*., 2013; Ogaya *et al*., 2014).

Further work at the Hontomín site included a CSEM survey using a vertical electric dipole. The dipole source was deployed from the borehole at reservoir depths, while the resulting electric fields were measured at the surface. Transfer functions for this survey were estimated and repeatability analysis indicated that the responses from the background structure are highly reproducible (Vilamajo *et al.*, 2015). Horizontal electric dipole soundings were also made using grounding points near the base of the injection and observation wells (Vilamajo, 2016).

4.4.2 Ketzin, Germany

The Ketzin sequestration project aims to inject CO_2 into the Upper Triassic Stuttgart sandstone aquifer at a depth of 635 m (Streich *et al*., 2010). Numerical modelling of the feasibility of detecting CO_2 plumes near Ketzin using CSEM methods has offered mixed results. Streich *et al*. (2010) concluded that CO_2 may be clearly identified using EM methods, but that not all source-receiver configurations will provide the resolution needed to observe growth of the plume over time. Vertical electric field sensors placed in boreholes would be ideal for CO_2 detection. The CSEM work that has since been implemented at Ketzin uses a three-phase transmitter and five-channel receiver stations that also record MT data. The transmitter is coupled to the ground by three electrodes separated by ~1 km lines and arranged such that multiple source field polarizations are achievable (Streich *et al.*, 2013). MT-based processing techniques have allowed for the recovery of superior earth responses. In executing a 3D inversion of this CSEM data, Grayver *et al*. (2014) found much of the magnetic field data to be redundant and used only small selections of this data to improve the efficiency of the inversions. It is noted that magnetic field data is only necessary for the MT portion of the survey; CSEM work needs only electric field measurements. A Gauss-Newton minimization scheme was successful in fitting a model to the data within geological constraints.

An alternative method of conducting surveys at reservoir depth is being attempted at Ketzin: surface-downhole electrical resistivity tomography (SD-ERT). For this technique, recordings are made at the surface as well as at depth, using a cross-well sensor array. The combination of surface and depth-collected data provides good constraints for modeling and inversions, and the permanent deployment of downhole electrode arrays is ideal for time-lapse monitoring (Bergmann *et al*., 2012).

4.4.3 Aquistore

At the Aquistore site, an additional EM monitoring technique is being tested. Groundmetrics Inc. is using a depth to surface EM (DSEM) approach to image resistivity changes. In this method, current injected at the surface travels to the depth of the target reservoir via the steel casing of the injection well. Electric field dipole sensors are then deployed radially around the well, providing data over a significant area (Hibbs, 2013).

A borehole to surface methodology (BSEM) has also been examined by Daley *et al.* (2014). In a numerical modeling experiment, it has been determined that a BSEM method could detect injected CO_2 volumes at Aquistore between 0.8 and 270 kt.

4.5 EM modeling for CCS applications

A 3D modeling exercise was performed to provide a preliminary understanding of the theoretical EM response for the Aquistore CCS project. A layered model based on COPROD2 dataset inversions (see section 3.4.1; Jones, 1988) is used for this modeling to simulate the Aquistore subsurface (Figure 4.11). The target was chosen to be a 10 Ωm rectangular prism, with dimensions of 5,000 m × 5,000 m × 250 m, and placed at a depth of 3,200 m within a 2 Ωm layer. The thickness of this target reflects a reservoir saturated over 50% of its vertical extent, while the lateral extent is based on, but overestimates, the extent of a plume determined in a modeling study of plume development (Whittaker and Worth, 2011). The source transmitter for this initial test is a 1 km long horizontal electric dipole operating at 1 Hz.

Figure 4.11: Simplified resistivity model of Williston Basin.

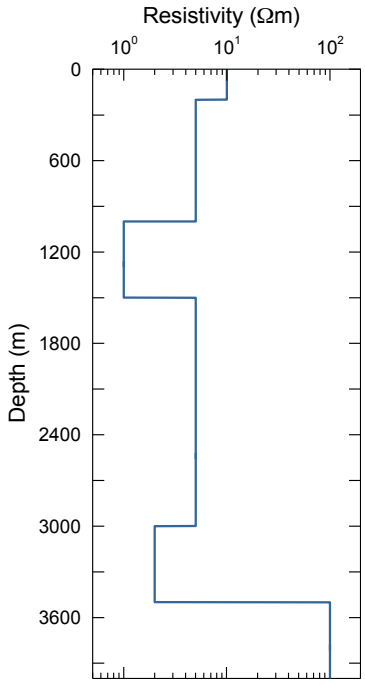

The total measured field may be subdivided into contributions from the static galvanic response and the frequency-dependent inductive responses (Figure 4.5). Of interest in this scenario are the scattered secondary fields that are due to the presence of the 2D or 3D buried resistive body. The scattered fields can be examined in terms of either the in-phase or quadrature response. The calculations were run using Emigma v8.1 software (Petros Eikon, Orangeville, Ontario).

Examining the electric field along an inline profile (Figure 4.12.), there is some indication that the response is sensitive to the position of the target; significant perturbations in the secondary fields occur over the extent of the resistive body. This pattern can be difficult to observe when the in-phase and quadrature parts of the response are considered separately, as there are sometimes complex patterns with multiple sign changes. However, the examination of

the field amplitudes makes target definition very straightforward. The front edge of the target in particular causes large perturbations in these fields.

Figure 4.12: Scattered electric field response at distance X from the source. Red is the in-phase response, blue is the quadrature response, green is the amplitude. Position of the resistive body is marked by the red rectangle.

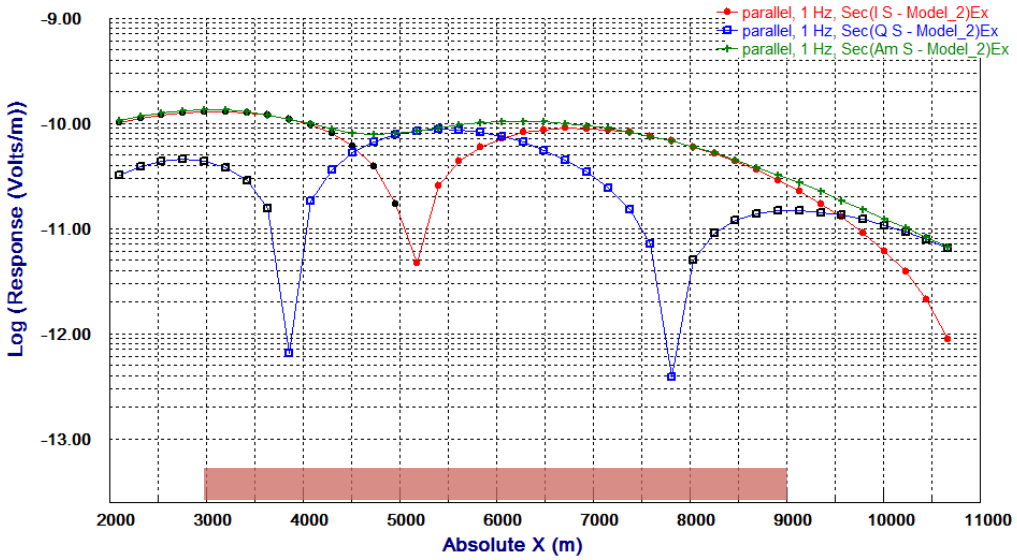

Although the modeling results show the EM fields are physically responsive to the reservoir target, they also indicate that the scattered fields are generally too small relative to the background fields associated with the host rocks to allow for resolution of the target. Electric field responses are at most 10^{-4} of the reference field for the Aquistore simulations.

In separate modeling scenarios, responses were considered for the same resistive body at depths of 1,600 m (Figure 4.13) and 200 m. It is evident from the different simulations that shallower targets are easier to detect. The fields represent a much higher proportion of the total field. A separate modeling study by Gasperikova and Hoversten (2006) demonstrate that 1,900 m deep CO_2 saturated area with a resistivity of 1 Ωm, compared to a 0.33 Ωm host rock, produces changes of the order of 8% in the response. Thus there is potential for shallower resistivity anomalies to produce measurable responses in a land-based CSEM survey.

Figure 4.13: Total (blue), background (green), and scattered (red) electric field responses for a 1,600 m deep target. Responses given in ppm of galvanic field.

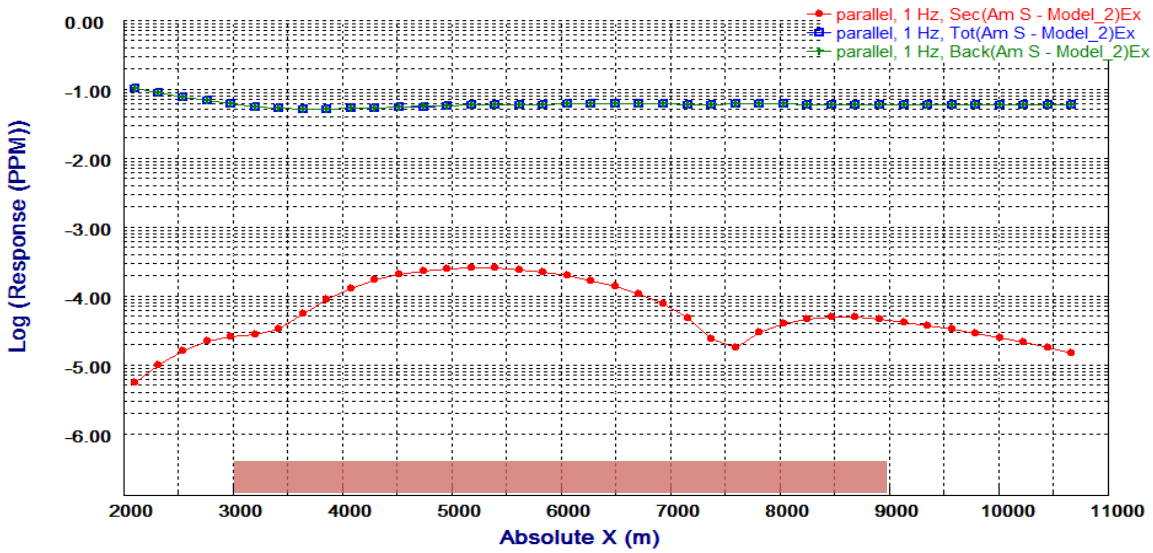

Modeling of a 3D 10 Ωm CO_2 plume within Aquistore-based layered models has shown that there is a distinct response due to the resistive plume within the reservoir. However, the relative size of this response is very small, particularly at reservoir depth. The implications of this result are that EM monitoring of a resistive CO_2 plume at Aquistore is more likely to be successful at detecting any significant upward migration of CO_2 through the cap rock to shallower depths. This would help to serve an important function for the injection monitoring.

Chapter 9 provides a description of further CSEM modeling and sensitivity studies for the Aquistore site. The additional calculations presented in Chapter 9 are based on more accurate models of the host resistivity structure of the area surrounding the Aquistore injection site than those used in the current exercise.

Chapter 5: Data Acquisition and Processing

5.1 Data acquisition

5.1.1 Overview of fieldwork

Collection of pre-injection EM data at the Aquistore site was conducted in three separate field campaigns: in August 2013, November 2014, and November 2015. MT data were acquired in all three campaigns with the aim of determining the background geoelectric responses of the basin, characterizing the local noise, and testing the accuracy and repeatability of the MT response estimation. The investigations covered an area of 2.5 km x 8.5 km immediately surrounding the Aquistore injection location (49°05'39.4" N, 103°04'42.1" W).

Detection of stored CO_2 by a surface EM method may depend on the ability to generate vertically flowing currents with a CSEM transmitter. Thus, CSEM surveys were also conducted in 2013 and 2015. The surveys employed a horizontal electric bipole transmitter and MT receiver stations. The purposes of the CSEM portion of the fieldwork were to test the capabilities and logistics of this survey method at the injection site. The application of the CSEM methodology to CO_2 monitoring was considered more experimental than the use of the MT method.

5.1.2 Site selection

The site locations were chosen to facilitate the survey objectives. Three different types of sites were installed: sites located in a cluster within ~3 km of the injection well (concentrated in the updip direction northeast of the injection well) intended for MT/AMT recordings, sites located on the axis of the transmitter dipole intended for CSEM recordings, and remote reference MT sites (Figure 5.1). A number of the on-axis CSEM sites also double as MT stations.

Figure 5.1: Initial survey layout, August, 2013.

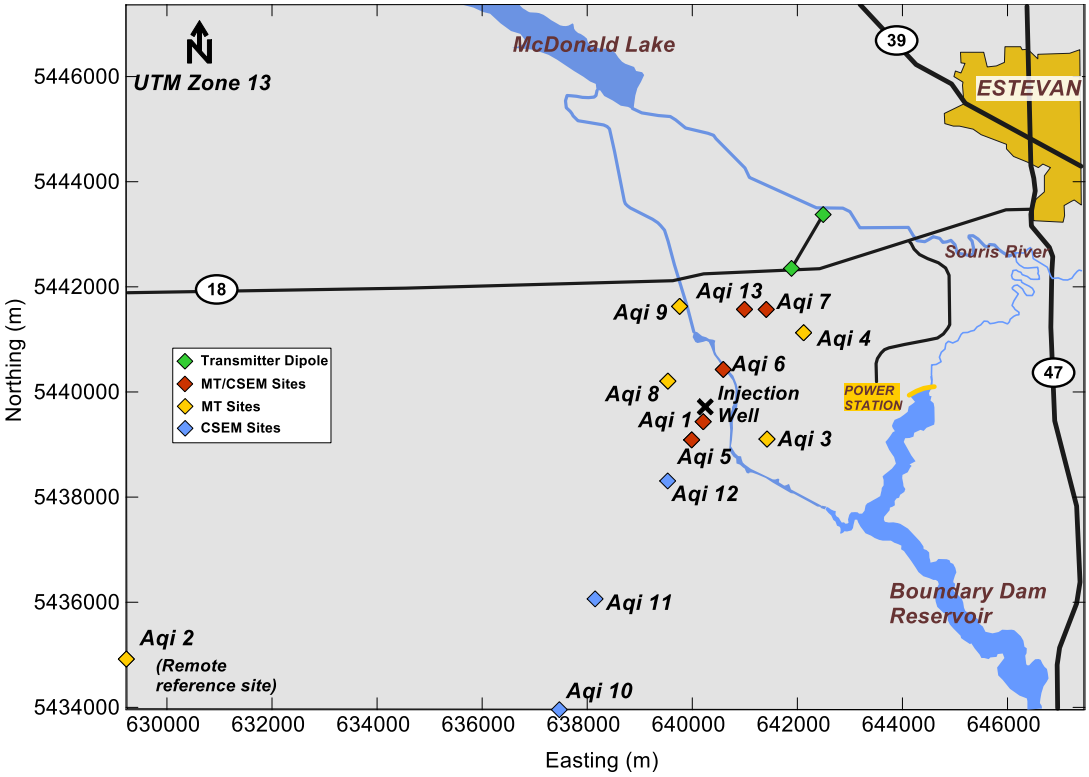

The exact site locations were chosen in part for their accessibility; most recording stations are situated a short distance from provincial roads. In some cases, it was necessary to coordinate with Sask Power Boundary Dam Power Station staff for access to gated areas near the plant or the injection well pad. Noise considerations were also important, as it was desirable to place the sites so that they are clear of cultural features, e.g. fences and powerlines. Prairie farmland areas were commonly used for the site installations (e.g. Figure 5.2). Use of these lands required permitting with local landowners. Full location details of the survey sites are provided in Table 5.1.

Figure 5.2: Typical landscape of main survey area.

Table 5.1: Aquistore survey site coordinates.

	Latitude	Longitude	UTM (13) northing (m)	UTM (13) easting (m)	Comments
aqi01	49°05'30.4"	103°04'46.2"	5439435	640208	Immediately south of injection well pad.
aqi02	49°03'12.9"	103°13'52.6"	5434919	629228	Remote reference MT site ~12 km southwest of injection well.
aqi03	49°05'18.7"	103°03'46.8"	5439104	641423	Southwest of power station.
aqi04	49°06'23.6"	103°03'09.9"	5441128	642120	Northwest of power station. AMT/MT only.
aqi05	49°05'19.4"	103°04'57.4"	5439089	639989	South of well pad.
aqi06	49°06'02.2"	103°04'26.2"	5440428	640590	West of canal.
aqi07	49°06'38.5"	103°03'44.4"	5441570	641408	South of Hwy 18.
aqi08	49°05'55.9"	103°05'18.4"	5440206	639536	West of well pad.
aqi09	49°06'41.8"	103°05'05.6"	5441628	639759	Northwest of well pad.
aqi10	49°02'35.3"	103°07'07.9"	5433956	637470	Distant inline site.
aqi11	49°03'43.0"	103°06'31.8"	5436064	638151	Distant inline site.
aqi12	49°04'54.5"	103°05'20.9"	5438308	639532	South of well pad.
aqi13	49°06'38.9"	103°04'04.8"	5441572	640994	South of Hwy 18.
aqi14	49°06'36.0"	103°03'58.1"	5441484	641131	South of Hwy 18.
aqi15	49°15'31.9"	102°50'07.6"	5458486	657494	Remote reference MT site ~26 km northeast of injection well.

5.1.3 MT instrumentation

MT recordings were made using field equipment borrowed from Carleton University, Institut Nationale de la Recherche Scientifique (INRS), and Natural Resources Canada. A Phoenix Geophysics V5 2000 system that includes porous pot electrodes and wires for electric field measurements, MT or AMT magnetic coils for magnetic field measurements, and 5-channel MT units (MTUs) was used for each of the surveys.

The function of the MTU is to sample and record GPS time-referenced measurements from both electric and magnetic field sensors. These devices include solid state memory for the firmware, processing and diagnostics tools, a memory-card recording system, and a GPS antenna (Phoenix Geophysics, 2016). There were 6 to 8 MTUs employed for each survey.

Three different types of induction coil sensors were used as magnetic field sensors for data acquisition: AMTC-30 coils for AMT recordings, and two different generations of MTC-80H coils for MT recordings. The AMT coils are designed to measure signals from 10,000 to 0.1 Hz whereas the MT coils are most sensitive to signals in the 400 to 0.00002 Hz range (Phoenix Geophysics, 2016). The differences in the frequency-dependant gain and phase response curves for the three types of coils are displayed in Figures 5.3-5.5. The field work was typically executed using a total of 10 to 14 induction coils, of which 4 to 5 were of the AMTC-30 type.

Figure 5.3: Calibration curves for AMTC 1170 magnetic field sensors. An explicit frequency-dependence inherent in an induction coil response has been removed from each of the calibration curves shown.

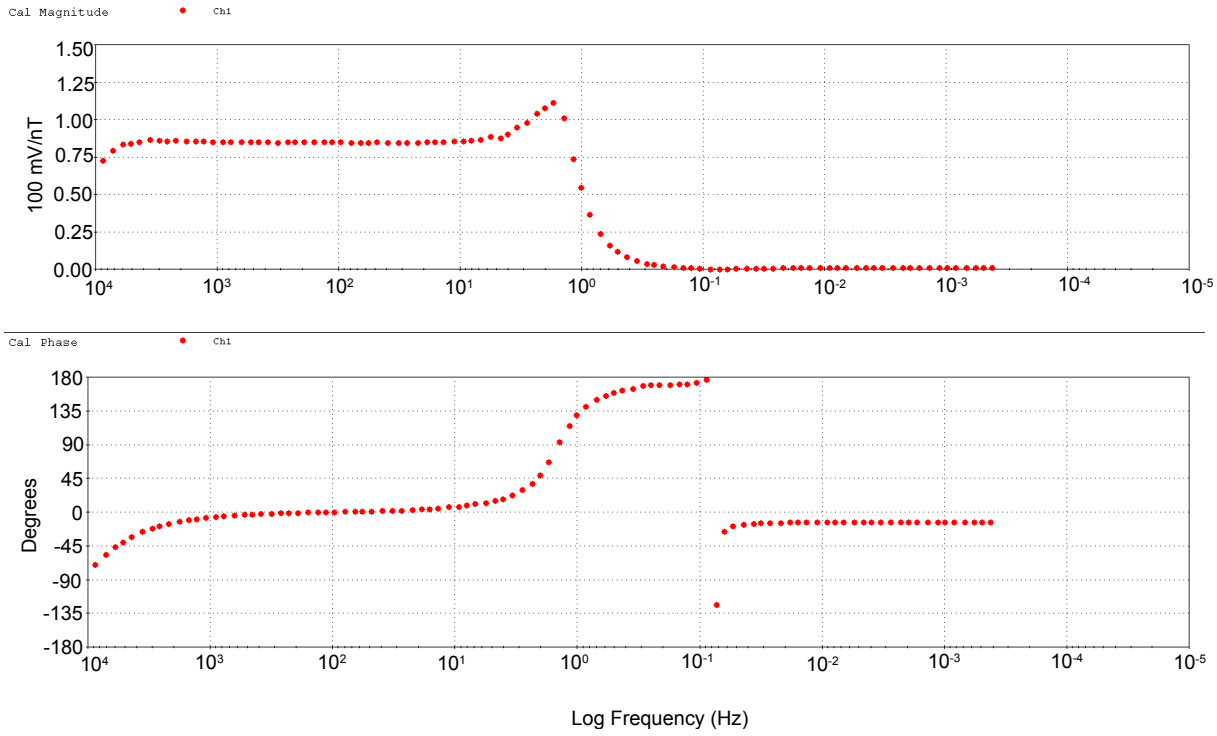

Figure 5.4: Calibration curves for MT8C 7320 magnetic field sensors.

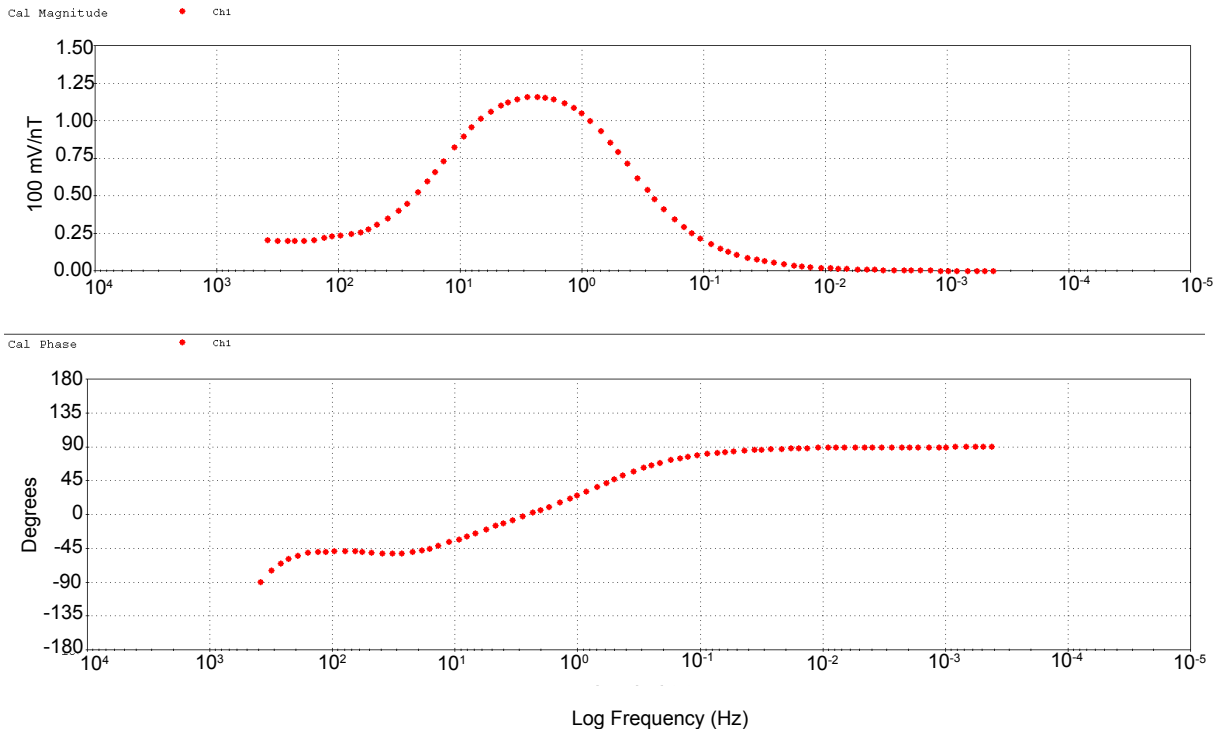

Figure 5.5: Calibration curves for MT8C 8051 magnetic field sensors.

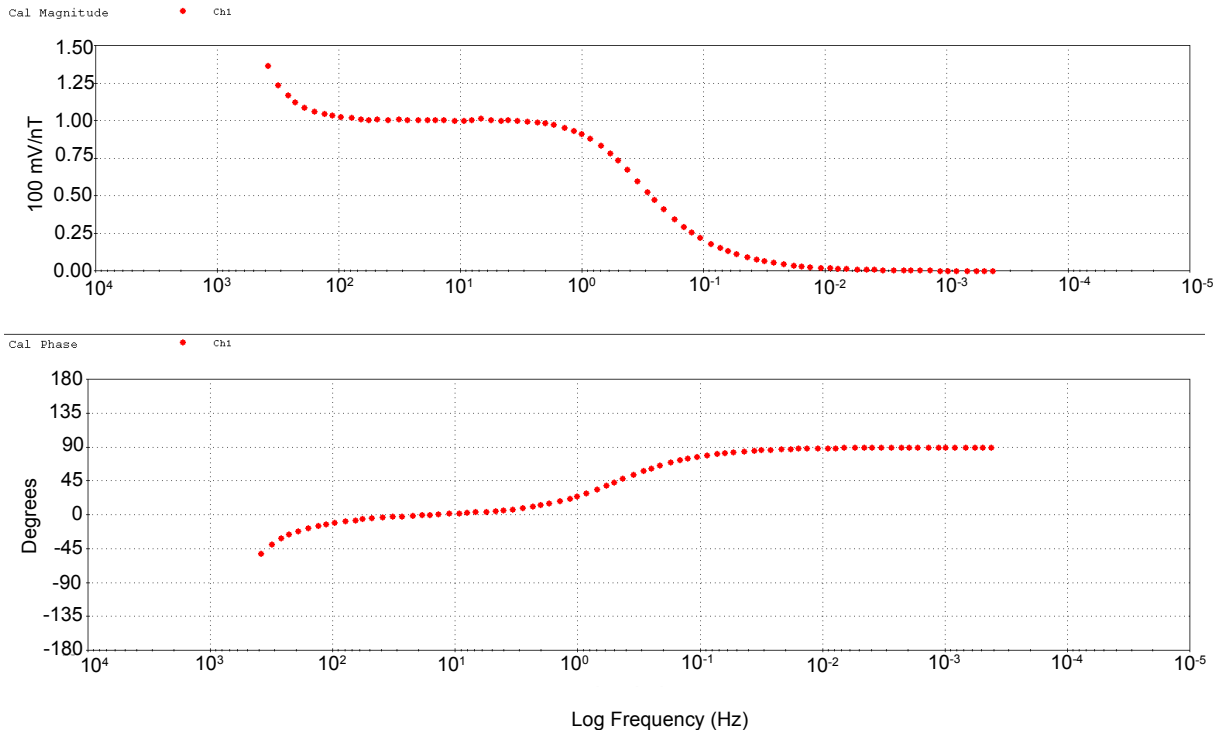

5.1.4 CSEM instrumentation

The source field equipment, including a Zonge International GGT-30 transmitter, was borrowed from the INRS in Québec. In 2013 an XMT-32 controller was provided by GMI (who in turn rented it from Zonge International). Though the controlled source was designed to be a straight electric bipole, topographic and cultural complications required a deviation in the wire connecting the grounding electrodes (Figure 5.6).

The transmitter station is located north of the Saskatchewan Provincial Highway 18, with its southern end very close to the road (Figure 5.1, Table 5.2). The two dipole ends are 1,188.6 m apart. Table 5.2 documents the coordinates of the individual straight segments of the transmitter wire. Starting from the northern grounding point, the wire juts out to the southeast from the dipole axis for several hundred metres, following a road to the power generator, and

running up a hill before returning to the path of the dipole axis. While this geometry is not ideal, it represents a compromise between using a long wire source to generate a high transmitter moment, avoiding cultural features, and remaining in appropriate proximity to the injection well.

Figure 5.6: Path of the transmitter wire connecting the terminal grounding points.

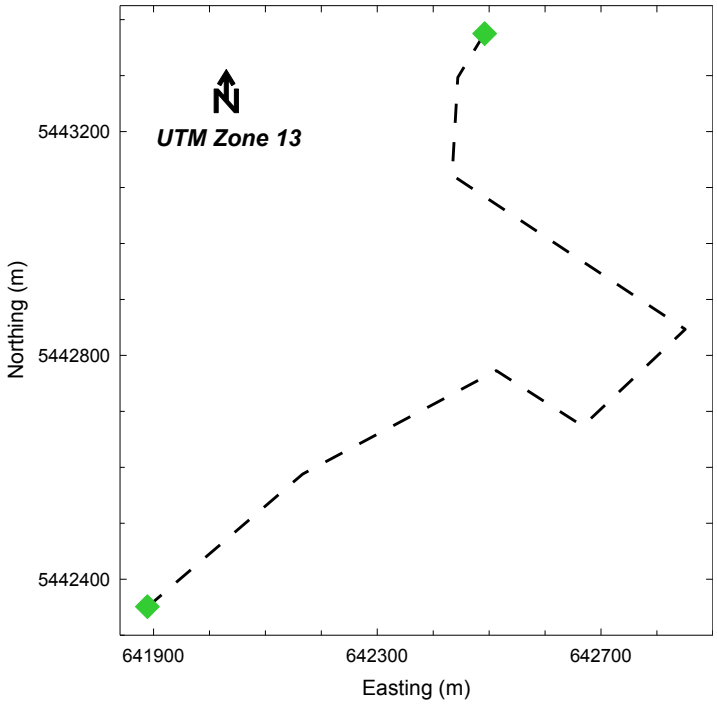

Table 5.2: Endpoints of Aquistore transmitter wire straight line segments. Dipole grounding points are Tx-N and Tx-S.

	Latitude	Longitude	UTM (13) northing (m)	UTM (13) easting (m)	Comments
Tx-N	49°07'36.0"	103°02'48.7"	5443375	642492	Access to gated area required.
Tx-1	49°07'33.6"	103°02'51.0"	5443298	642446	Located along dirt road.
Tx-2	49°07'28.0"	103°02'51.6"	5443124	642438	Located along dirt road.
Tx-3	49°07'18.7"	103°02'31.5"	5442847	642852	Generator location - base of hill.
Tx-4	49°07'13.2"	103°02'40.7"	5442673	642671	Top of hill.
Tx-5	49°07'16.5"	103°02'48.3"	5442772	642515	Next to powerline pole.
Tx-6	49°07'10.9"	103°03'05.5"	5442589	642170	Open field area
Tx-S	49°07'03.4"	103°03'19.7"	5442351	641889	Located in a field north of Hwy 18.

Figure 5.7: CSEM generator and control station. Located at a point between terminal electrodes.

5.1.5 MT recording strategy and parameters

For the MT surveys, it was desirable to record simultaneously at as many sites as possible in order to maximize data collection and increase options for remote-reference site choice. However, as there were limitations in the number of recording units available, ***H***-field coils were installed at only a select number of sites. Thus not all sites were full MT/AMT recording stations. The deployment of the available induction coils sought to use particular sites consistently as sources of AMT or MT magnetic field data. At a small number of sites a third coil was installed to enable recording of the vertical magnetic field for tipper determination and additional EM noise characterization. Telluric dipoles were employed for recordings at all sites, save for the remote reference location, and were typically 50 m long. The equipment installation at the remote reference sites remained in place for the entirety of each survey while the remaining equipment was moved to different sites within the main survey area on a daily basis. Magnetic field data collected at the remote reference locations were subsequently used for robust remote-reference processing of as much of the data set as possible (see section 5.3). Calibration of the MTUs and induction coil sensors was performed at the remote reference locations.

The MTU AMT sampling configuration (Table 5.3) was employed for almost all of the recordings. In this configuration, the MTUs were used to collect raw time series using three different sampling rates, termed bands 2, 3, and 4. The MT sampling configuration shown in Table 5.3 was given limited use during the acquisition campaigns. The instruments use a 60 Hz comb filter for band 3 and 4 sampling to minimize powerline noise. The MTUs were programed to record measurements for durations of 14 to 22 hours throughout the local evenings, nights, and early mornings.

Table 5.3: Phoenix MTU-A acquisition bands (modified from Phoenix Geophysics, 2003).

	MT acquisition	AMT acquisition
Band 2		24,000 Hz 0.1 s of data every 5 s
Band 3	2,400 Hz 1 s of data every 5 s	2,400 Hz 1 s of data every 5 s
Band 4	150 Hz Continuous sampling	150 Hz Continuous sampling
Band 5	15 Hz Continuous sampling	

5.1.6 CSEM recording strategy and parameters

The CSEM experiments were designed to measure the electric field at site locations in line with the dipole axis. Offsets from the dipole source ranged from 2.3 to 9.5 km. Acquisition of the CSEM data was performed following the completion of MT surveys using the existing installations of MT recording equipment. The CSEM transmitter was operated over the course of two days in each survey, allowing for recording of time series containing a large number of repeated signals at each of the experimental frequencies. Time series were recorded mainly in bands 3 and 4 of the AMT-type acquisition.

5.1.7 Field procedures

Field work was divided between two crews consisting of either 2 or 3 people. The initial stages of the surveys involved permitting sites, securing access to the sites, and performing instrument inventory and calibrations. Subsequent work focussed on deployment of the instrumentation at each of the sites. Sites were deployed using a magnetic north reference system following normal MT deployment procedures (e.g., Phoenix Geophysics, 2003; Ferguson, 2012). Dipole ground resistances and voltages were measured at each installation and site visit. The resistance was usually in the range of 100 to 150 Ω and the DC voltage between electrodes in the range of 10 to 70 mV. Recording parameters were input to the MTUs using pre-programmed data cards. Some manual labour was required for instrument installations: all electrode wires and magnetic sensor coils were anchored to the ground to avoid wind noise. It was also necessary to protect the MTUs against inclement weather and cattle using tarpaulins and snow fencing.

After every period of data recording, the MT stations were either reset for a subsequent recording, or packed up in order to make use of the instrumentation at another location. The site visits involved changing the pre-programmed data card and battery, checking wires for animal bites, and rechecking ground resistances and voltages.

5.2 Survey details

5.2.1 MT survey - 2013

The initial MT survey, conducted from August 21st to 26th of 2013, established 9 MT receiver stations in locations surrounding the Aquistore injection well (red and yellow symbols in Figure 5.1). A single remote reference site, aqi02, was used for the duration of the survey.

During the MT data acquisition period, DSEM trials conducted by GMI included sporadic transmission of a 0.5 Hz signal during daytime hours. Remote site magnetic field data were provided to GMI for telluric cancellation in their data. On August 21st, the first day of recording, data were collected with Phoenix's MT-style sample rates (bands 3-5 in Table 5.3). All other recordings used the AMT sample rates (bands 2-4).

5.2.2 NRCan CSEM survey - 2013

The NRCan CSEM survey overlapped with the end of the MT acquisition on August 25th, and continued on August 28th. Recordings on the second day were made at three telluric-only installations at locations more distant to the injection well (aqi10, aqi11, and aqi12). These CSEM-only sites defined the *x*-direction at an azimuth of 22˚ east of magnetic north, the same azimuth as a straight line connecting the transmitter grounding points, and recorded E_x fields only. The transmitter electrodes were 1.5 m long copper-plated steel rods driven into the soil.

The transmitted signal was a rectangular waveform at 100% duty cycle. Frequencies of transmission ranged from 0.5 to 8 Hz in one octave steps. The maximum current output was 24.75 A.

In order to save space on the written data cards, the acquisition parameters recorded data at the band 3 and band 4 AMT sample rates, but not the band 2 sample rates. A zero-length band 2 file (TS2) is written to the data card. Deletion of this file is necessary for examination of the TS3 and TS4 files with Phoenix software.

5.2.3 MT survey - 2014

The 2014 fieldwork took place from November 6th to 11th. The goal of the survey was to test the repeatability of results from the previous MT survey. For this reason all of the 2013 MT

sites were revisited, with the exception of aqi07 and aqi13. Since data quality was poor at those two locations, a new site was established in the same area, aqi14 (Figure 5.8). Sites aqi10, aqi11, and aqi12, which were previously used only for CSEM measurements, were re-occupied with full MT installations. An additional remote reference site, aqi15, was installed at a larger distance from the Aquistore injection well, approximately 25.7 km to the northeast of the well, close to the town of Bienfait. Acquisition parameters were more consistent than those of the 2013 MT survey, with AMT-type acquisition used throughout the survey. The durations of all recordings were set to 14.5 hours.

Figure 5.8: November, 2014 survey layout.

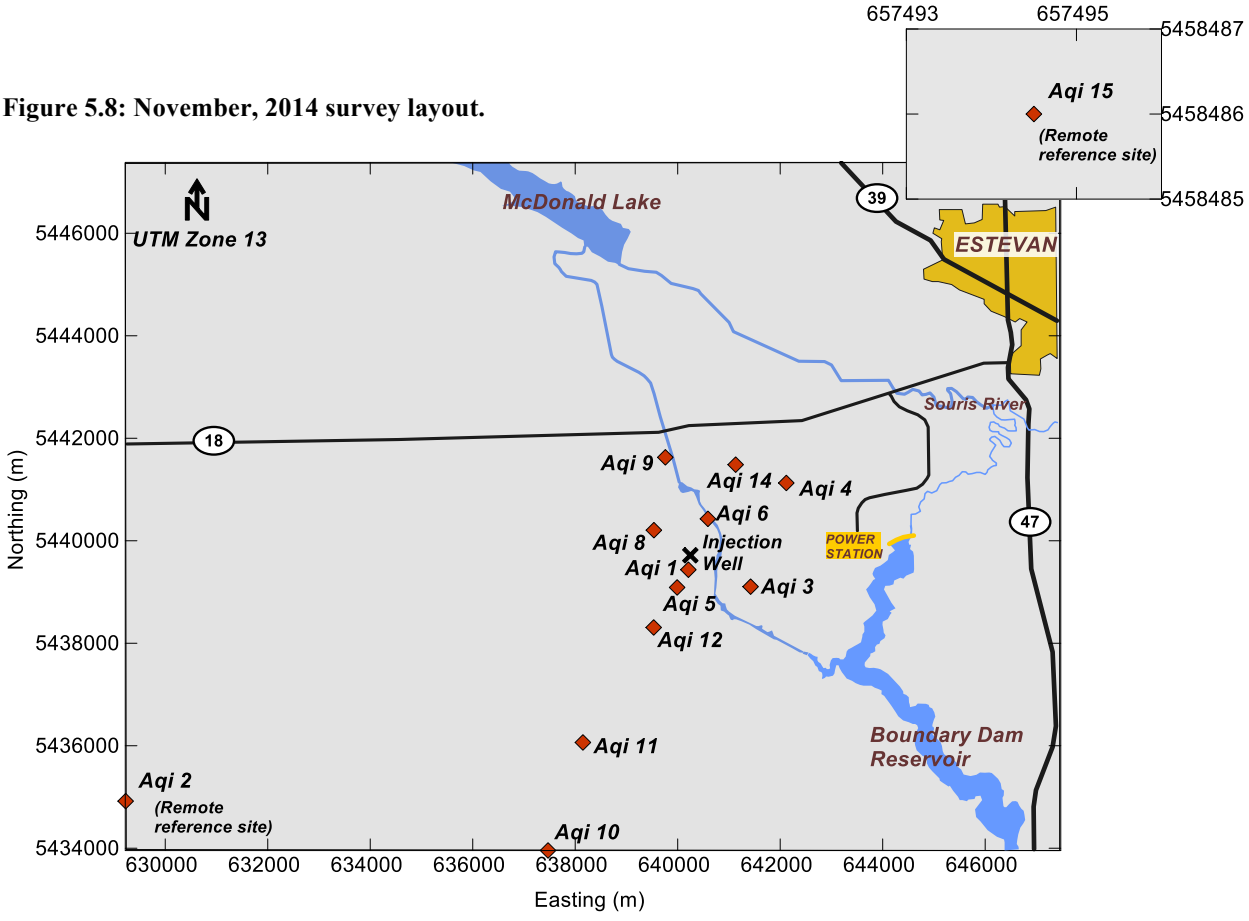

5.2.4 MT survey - 2015

A second repeat MT survey at the Aquistore site was conducted from November 2nd to 6th, 2015. Sites aqi01, aqi03, aqi05, aqi06, aqi10, aqi11, and aqi12 were re-occupied for data collection. For this field session, more emphasis was placed on the controlled-source objectives, and therefore, for the MT work, receiver stations along the transmitter dipole axis were given priority. The acquisition parameters and deployment of the MT instrumentation followed the same procedures as for the two previous years.

5.2.5 CSEM survey – 2015

On November 7th and 8th, CSEM transmissions were recorded at the Aquistore site. The transmitter setup and equipment were the same as for the 2013 work. Ground resistance was reduced by driving long brass electrodes to depths in excess of 5.5 m, in an effort to extend the electrodes to below the water table. These electrodes were wired in parallel to the 2013 electrodes, which had been left in the ground after that survey, in order to further decrease the ground resistance. The survey configuration allowed a dipole current of 30 A, successfully exceeding the level achieved in the 2013 CSEM survey.

The 2015 CSEM transmission used a rectangular waveform with frequencies descending from 32 Hz to 0.0078 Hz in 2 octave steps. A schedule of transmitter and receiver windows of operation and recording is provided in Figure 5.9. A 50% duty cycle was used for two transmissions made at 32 and 2 Hz. All other transmissions were made with a 100% duty cycle. An alternating square wave was the signal generated by the controlled source.

A CSEM site, aqi16, was established close to the end of the transmitter bipole to record the near-field response of the transmitter for signal definition. The site was located directly

across Highway 18, approximately 90 m from the southern electrode of the bipole. This site had one 10 m electric dipole oriented parallel to the transmitter axis, and a second dipole measuring 50 m in the perpendicular direction.

Figure 5.9: Log of transmissions and active receiver stations for 2015 CSEM survey. Times are GMT.

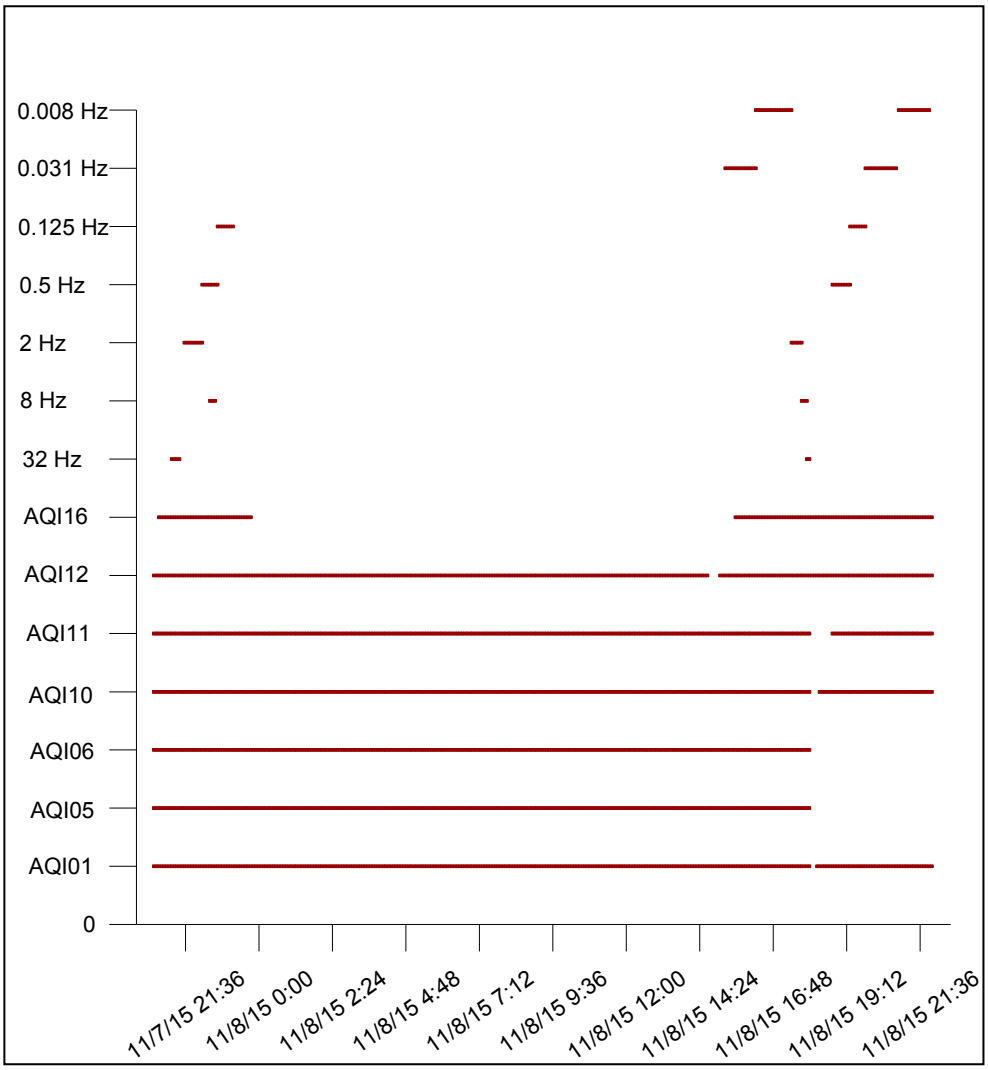

5.3 MT Data processing

5.3.1 Robust cascade decimation approach

Basic least-squares solutions for MT transfer functions using remote reference techniques (see section 4.2.7) cannot discern between the desired MT signal and correlated EM noise. The biasing effect of the correlated noise, as well as biasing of the responses due to spatial non-uniformity of MT source fields, has led to the development of robust spectral processing techniques (Jones *et al*., 1989; Egbert, 1997; Chave and Weidelt, 2012). Methods of robust processing include using coherence thresholds to reject a portion of time series and data weighting by variance or coherence.

Cascade decimation is a numerical approach for estimating power spectra that is especially effective for log-scaled low-frequency signals (Wight and Bostick, 1980). The procedure uses a low-pass filter to exclude higher frequencies from the time series, and then decimates the data by sampling every n^{th} point to create a new time series. The resulting time series are used to estimate the low frequency end of the spectra with considerably improved efficiency.

The Phoenix SSMT2000 processing software uses a robust cascade decimation code. This code uses a decimation factor of 2 to generate ministacks of harmonic estimates. These ministacks are averaged into a total stack using the inverse geometric mean of the variance of the off-diagonal elements of the impedance tensor (Jones *et al*., 1989).

5.3.2 Processing overview

The MT data were processed with a Phoenix Geophysics software package, which works together with Phoenix acquisition tools. The MT datasets from 2013, 2014 and 2015 were

processed using a consistent workflow and standard set of robust parameters. The results of the processing transformed the original time series into MT impedances, apparent resistivities, and phases, all as a function of frequency. The data processing workflow (Figure 5.10) begins with the organization of time series (.TSN) and calibration (.CAL) files into a directory, the filling out of tables (.TBL; .TBO) with relevant site-specific parameters, and the linking these tables to the associated data files. The raw time series data are then transformed to the frequency domain (.FCN) using appropriate discrete Fourier transform settings (.PFT) for the different types of acquired data, and for which the different types of processing that the data are destined. Some processing parameters are chosen (.PRM), and then a series of crosspowers are calculated so that the data are converted into their MT response. The resulting calculations are split into multiple files based on their frequency characteristics (Figure 5.11). These data are then combined in Phoenix's MT Editor software on a common-site basis, and edited to remove estimates that are either spurious, have large errors, or violate dispersion relationships. A detailed discussion of the production of final MT responses is included in Chapter 6.

Figure 5.10: Flow chart illustrating SSMT 2000 data processing steps. Relevant file types listed on the right.

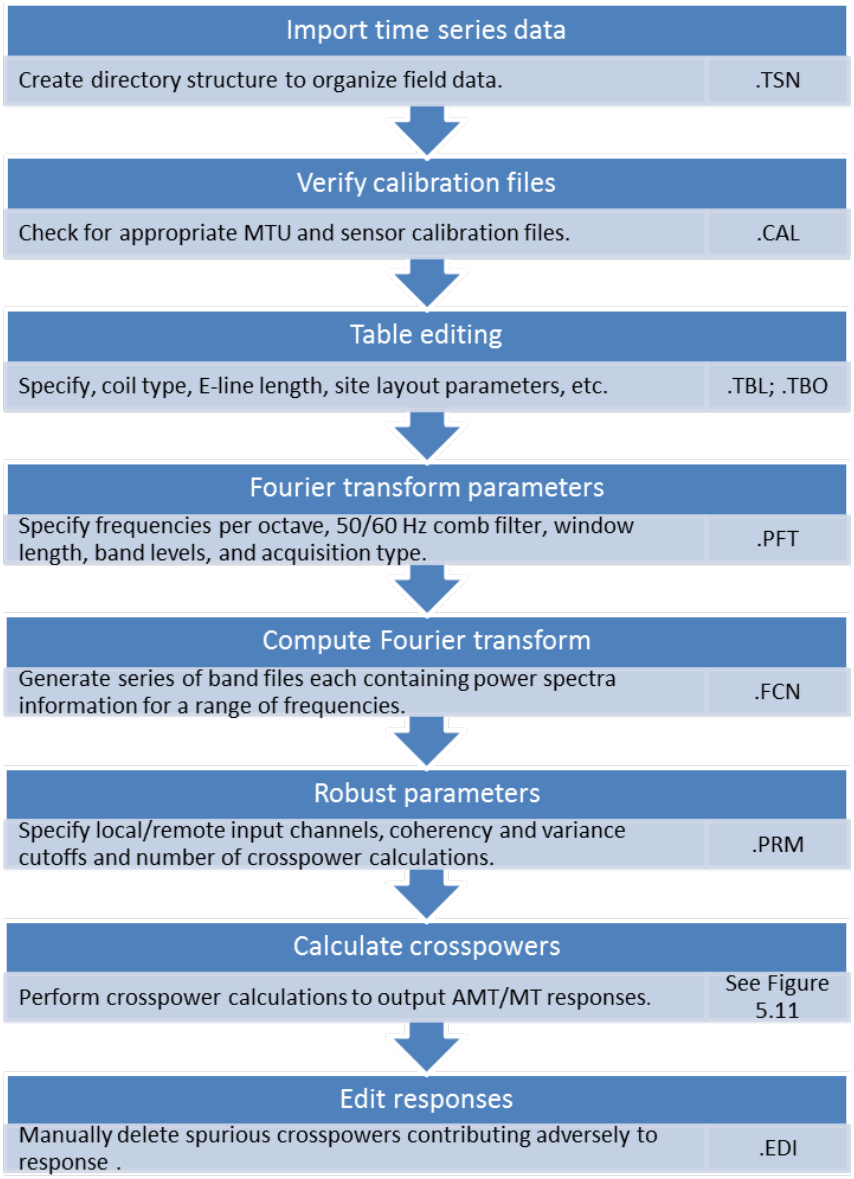

Figure 5.11: Output files for SSMT 2000 crosspower calculations (Phoenix, 2003). The current study produced mainly EMT and MMT files from AMT processing, and HMT and RMT files from MT processing. Copyright by Phoenix Geophysics Inc. Used with permission.

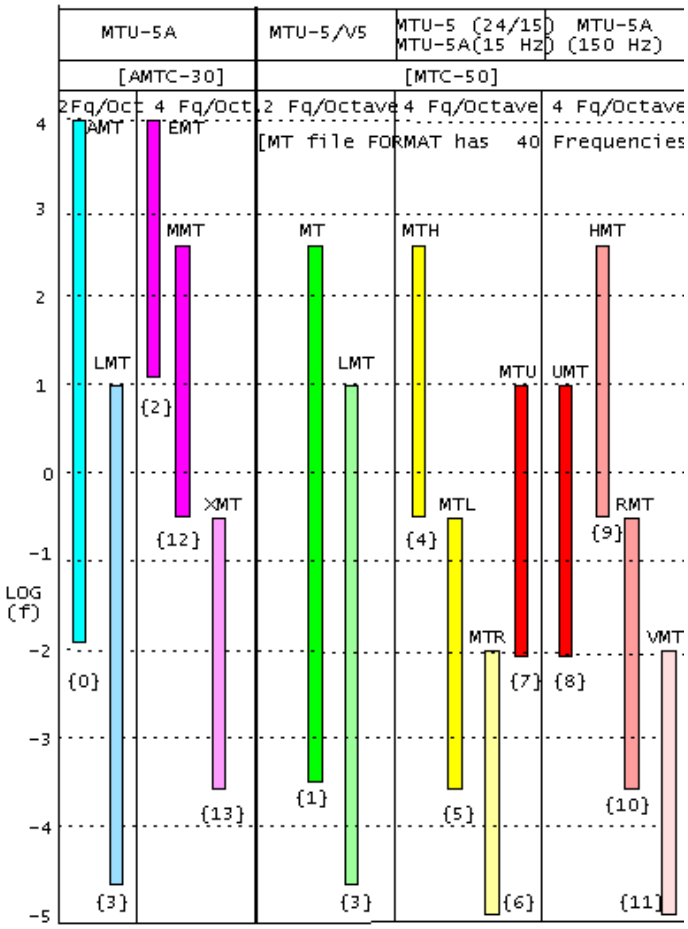

The raw time series files were processed using both AMT and MT processing configurations. To begin, these time series datasets were copied into parallel directories, one of which was destined for MT processing and the other for AMT. Each directory also required a copy of the calibration files.

The analysis of all three MT data sets used a consistent set of parameters. The Fourier transforms were computed at 4 frequencies per octave. For robust processing, the time series were divided into 20 equal length segments from which crosspowers were calculated at the selected frequencies. Crosspowers were rejected if the coherency between the local and remote

data was below a threshold of 0.35, or if the coherency between the telluric and magnetic data was below 0.25. The final responses were weighted based on their variance.

Execution of the processing scheme depended on aspects of the fieldwork and in particular on the deployment of magnetic field sensors. The band 2 to 4 (TS2, TS3 and TS4) electric field data collected using the AMT sampling configuration can be used for either AMT or MT processing. However, since there were insufficient AMT and MT ***H***-field coils to supply each site, it was often necessary to "import" magnetic field time series recorded at a nearby site to accomplish the MT or AMT processing. The imported data were used as a substitute for "local" magnetic field recordings. It is desirable to produce both MT and AMT-processed data at all locations in order to define the MT responses over a broadband of frequencies, and thus the importing of the magnetic field data was an important component of the data processing.

It was also necessary to define a second pair of AMT or MT horizontal magnetic field recordings to accomplish remote referencing processing. The remote reference sites were chosen based on their proximity to the main site in question. In AMT processing, the remote site was always located somewhere within the main survey area, in order to minimize the inter-site distance and because AMT recordings were not made at either of the true remote sites (aqi02 or aqi15). For the MT processing the magnetic data from aqi02 or aqi15 was used as the remote reference except when it was necessary to use these data for importing as the local magnetic data.

For both the importation of magnetic field data to serve as a local magnetic recording and for the selection of remote reference magnetic recordings, it was required that a sufficient time overlap exist between the recording intervals at the two or three sites involved. A summary of magnetic sensor deployment on site-by-site basis is shown for all three surveys in Table 5.4.

Table 5.4: Deployment of MT and AMT coil sensors.

	MT				AMT		
	2013	2014	2015		2013	2014	2015
aqi01	YES	YES	YES	**aqi01**	NO	NO	NO
aqi02	YES	YES	N/A	**aqi02**	NO	NO	N/A
aqi03	YES	NO	NO	**aqi03**	NO	NO	NO
aqi04	NO	NO	N/A	**aqi04**	YES	YES	N/A
aqi05	NO	NO	NO	**aqi05**	YES	YES	YES
aqi06	NO	NO	NO	**aqi06**	NO	NO	YES
aqi07	NO	N/A	N/A	**aqi07**	NO	N/A	N/A
aqi08	NO	NO	N/A	**aqi08**	YES	YES	N/A
aqi09	YES	YES	N/A	**aqi09**	NO	NO	N/A
aqi10	CSEM	YES	YES	**aqi10**	CSEM	NO	NO
aqi11	CSEM	NO	YES	**aqi11**	CSEM	YES	NO
aqi12	CSEM	NO	YES	**aqi12**	CSEM	YES	NO
aqi13	NO	N/A	N/A	**aqi13**	NO	N/A	N/A
aqi14	N/A	NO	N/A	**aqi14**	N/A	NO	N/A
aqi15	N/A	YES	YES	**aqi15**	N/A	NO	NO

As some of the CSEM data recordings include electric field data only and in some cases in 2013 data from only one channel, the CSEM recordings cannot be processed using normal MT data processing procedures. The CSEM data from both the 2013 and 2015 surveys have not been processed apart from the examination and export of uncalibrated time series. An alternative method for handling these time series, which are in a format designed for the Phoenix workflow, must be developed in order to obtain full CSEM responses from these datasets. The work falls outside the scope of the current M.Sc. thesis project.

5.3.3 2013 dataset

Complete processing of the 2013 MT data was not performed until several months after the conclusion of the fieldwork, although some preliminary processing was done in the field. Some aspects of the acquisition that limited or complicated the processing were therefore not identified until well after the survey completion. Magnetic recordings were made at sites aqi03 and aqi09 using different generation magnetic coils for each orthogonal direction with the

expectation that the different coil responses (Figure 5.4 and 5.5) would be fully corrected by the appropriate calibration files during the data processing. However, it was subsequently determined that the processing software could not handle the mismatched calibrations correctly. Thus the availability of magnetic field data for MT processing was greatly restricted for the 2013 dataset as the ***H***-field recordings at aqi03 and aqi09 could not be processed. Additionally, one of the only other pairs of MT coils was in use at the remote site (aqi02) on every day of data collection. Since this remote ***H***-field data was required to substitute for local channels, much of the MT-processed data could not be remote referenced. A second complication arose from MT-configuration acquisition parameters used at the remote site on August 22nd, which differed from other data collected on that day. The combined effect of these issues is that it was impossible to achieve full remote reference determinations for both MT and AMT processing at a number of sites and a number of days. Most of the processing of the 2013 MT data was therefore limited to local site processing only.

The Phoenix software does not allow combination of locally-processed and remote-reference data at the data merging and editing stage. This limitation means that for the 2013 data set the processing had to be split between locally-processed MT and AMT response determinations and remote-reference processed AMT response determinations. A summary of the processing on the 2013 dataset is presented in Table 5.5. Where magnetic coils have been imported, the **local/remote** convention is used to indicate the source of the coils; a response which was generated with imported magnetic field data from aqi01 and remote referenced with site aqi02 is denoted as aqi01/aqi02 in the table. If no coils were imported for the 'local' channels, the notation simplifies to /aqi02. Imported coils for non-remote referenced responses are also specified, if applicable.

There were several additional factors affecting the final data set. No processing was performed on aqi02 (remote site) data, as there were no ***E***-field sensors installed at this site; its purpose is for remote magnetic field data only. Severed coil leads due to agricultural activities at the remote site aqi02 on August 26th resulted in MT-processing problems at several sites for that particular day. For the aqi01 data from August 23rd, the processing resulted in *xy* and *yx* apparent resistivity curves that are downshifted approximately one decade. This problem was also observed after importing the magnetic coils from this site to other sites for processing. All of the MT processing from this day is therefore affected, and these data did not contribute to the final edited MT data.

Table 5.5: Summary of processing on 2013 dataset. Remote referenced data – green; non-remote referenced data – orange; failed to process – red.

		21-Aug	22-Aug	23-Aug	24-Aug	25-Aug	26-Aug
aqi01	MT			/aqi02			
	AMT		aqi05/aqi04	aqi05			
aqi03	MT		aqi01	aqi01/aqi02			aqi02
	AMT			aqi05			aqi05/aqi08
aqi04	MT		aqi01				aqi02
	AMT		/aqi05				/aqi08
aqi05	MT		aqi01	aqi01/aqi02	aqi02	aqi02	
	AMT		/aqi04		/aqi08	/aqi08	/aqi04
aqi06	MT		aqi01	aqi01/aqi02	aqi02		
	AMT		aqi05/aqi04	aqi05	aqi08/aqi05		
aqi07	MT			aqi01/aqi02	aqi02	aqi02	
	AMT			aqi05	aqi08/aqi05	aqi08/aqi05	
aqi08	MT				aqi02	aqi02	
	AMT				/aqi05	/aqi05	/aqi04
aqi09	MT				aqi02	aqi02	
	AMT				aqi08/aqi05	aqi08/aqi05	
aqi13	MT						
	AMT						

Following the MT data processing, significant data editing was required to mask to contributions of noisy or spurious crosspowers from the initial responses. A detailed description of the editing of processed results is presented in Chapter 6.

5.3.4 2014 dataset

The knowledge gained from the 2013 MT survey meant that there were fewer configuration idiosyncrasies in the 2014 dataset, leading to a more straightforward processing sequence (Table 5.6). Almost all responses were remote referenced. For the 2014 survey, there were fewer cases than in 2013 in which a lack of suitable magnetic data for importing or remote-referencing prevented full data processing. As a result, the 2014 survey yielded significantly more individual MT/AMT responses than the 2013 survey. Unlike for the previous survey, full MT recordings were made at the remote reference locations, permitting determination of MT responses for aqi02 and aqi15 data. Full MT recordings were also done at sites aqi10, aqi11, and aqi12, which were previously used only for CSEM data acquisition. A problem with one of the MTUs (1493) resulted in failed data collection on the electric field channels on three separate occasions. These issues are marked on Table 5.6 as 'failed to process'.

Table 5.6: Summary of processing on 2014 dataset. See Table 5.5 for the definition of the shading.

		6-Nov	7-Nov	8-Nov	9-Nov	10-Nov	11-Nov	12-Nov
aqi01	MT		/aqi02	/aqi02			aqi10/aqi15	aqi10/aqi15
	AMT		aqi05/aqi04	aqi05/aqi04			aqi12/aqi11	aqi12/aqi11
aqi02	MT		/aqi01	/aqi01				
	AMT		aqi05/aqi04					
aqi03	MT		aqi01/aqi02					
	AMT		aqi05/aqi04					
aqi04	MT		aqi01/aqi02	aqi01/aqi02				
	AMT		/aqi05	/aqi05				
aqi05	MT		aqi01/aqi02	aqi01/aqi02	aqi09/aqi15			
	AMT		/aqi04	/aqi04	/aqi08			
aqi06	MT				aqi09/aqi15	aqi10/aqi15		
	AMT				aqi05/aqi08	aqi08/aqi12		
aqi08	MT				aqi09/aqi15	aqi10/aqi15		
	AMT				/aqi05	/aqi12		
aqi09	MT				/aqi15	aqi10/aqi15		
	AMT				aqi08/aqi05	aqi08/aqi12		
aqi10	MT					/aqi15	/aqi15	/aqi15
	AMT					aqi12/aqi08	aqi11/aqi12	aqi12/aqi11
aqi11	MT						aqi10/aqi15	aqi10/aqi15
	AMT						/aqi12	/aqi12
aqi12	MT					aqi10/aqi15	aqi10/aqi15	aqi10/aqi15
	AMT					/aqi08	/aqi11	/aqi11
aqi14	MT			aqi01/aqi02	aqi09/aqi15			
	AMT			aqi05/aqi04	aqi08/aqi05			
aqi15	MT					/aqi10	/aqi10	/aqi10
	AMT							

5.3.5 2015 dataset

As with the 2014 MT data, the processing of the 2015 data was straightforward. The lone problem was the reoccurrence of a telluric acquisition problem with the 1493 MTU, this time at aqi05, on the first day of the survey (Table 5.7).

Table 5.7: Summary of processing on 2015 dataset. See Table 5.5 for the definition of the shading.

		2-Nov	3-Nov	4-Nov	5-Nov	6-Nov
aqi01	MT	/aqi15	/aqi15	/aqi15	/aqi15	/aqi15
	AMT		aqi05	aqi06/aqi05	aqi05/aqi06	aqi05
aqi03	MT	aqi01/aqi15	aqi01/aqi15	aqi12/aqi15		
	AMT		aqi05	aqi06/aqi05		
aqi05	MT		aqi01/aqi15	aqi01/aqi15	aqi01/aqi15	aqi01/aqi15
	AMT			/aqi06	/aqi06	
aqi06	MT			aqi01/aqi15	aqi01/aqi15	
	AMT			/aqi05	/aqi05	
aqi10	MT					/aqi15
	AMT					aqi05
aqi11	MT					/aqi15
	AMT					aqi05
aqi12	MT		/aqi15	/aqi15	/aqi15	/aqi15
	AMT		aqi05	aqi05/aqi06	aqi05/aqi06	aqi05

Chapter 6: Data Analysis

6.1 Calculated MT responses

6.1.1 Overview

There are two distinct phases of MT response determinations to consider (Figure 6.1). The first phase is the generation of preliminary responses for each site, recording period, and processing type (MT or AMT). These divisions lead to a large volume of data to consider in the early stages of the analysis. The second phase is the generation of the final responses. This step involves editing of the preliminary responses to remove inconsistent crosspower estimates and combining the data sets from different recording periods and processing types to form a combined site response. These final responses are ideally smoothly-varying functions of period that provide a measure of the geoelectric structure at a particular location. The objectives of the analyses presented below are to examine the characteristics of both the preliminary responses and the combined geoelectric response for each site.

Figure 6.1: Evolution of single site data from multiple field recordings to final response.

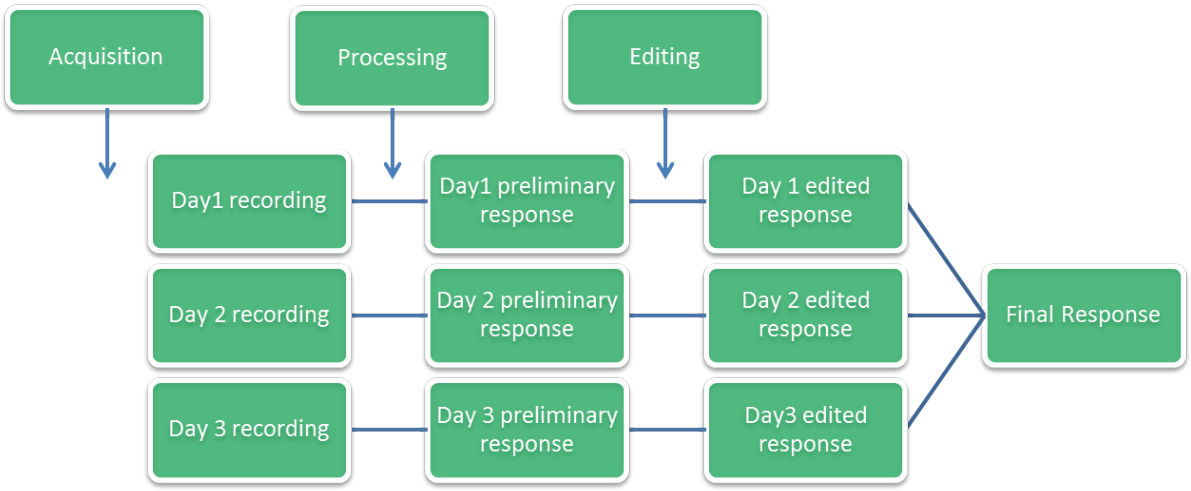

In most MT studies a consideration of the final MT responses for each site is sufficient. However, for the current study, the preliminary responses reveal important information related to the signal and noise levels, their time-evolution throughout the surveys, and their effect on the responses. Much of this information is removed in the formation of the final responses. Thus the examination of the responses in both the preliminary and final form is a valuable exercise.

An important difference between MT and AMT processed responses is the effect of bandwidth of the different coil types (see section 5.1.3). The differences in coil responses leads to less reliable crosspower estimates in the 1,000-10 Hz band for responses obtained using MT coils and at frequencies <10 Hz for responses obtained with AMT coils (see section 5.1.3) . However, there is sufficient overlap in the two types of results that final combined responses are robust over the entire range of recording periods.

As discussed in the previous chapter, there are some issues in the 2013 dataset with consequences for the impedance results. Since remote-reference MT processing was not possible for the 2013 data, the final responses for that survey must consider the locally-processed AMT-MT and remote-reference processed AMT results separately. Additionally, because of the limited number of MT magnetic recordings available, the magnetic recordings from some sites were relied on heavily for importing to other sites. This approach is generally not an issue given the spatial uniformity of the magnetic field. However, for the 2013 processing it was necessary to import magnetic data from the remote reference site (aqi02) as the local magnetic field for many of the sites. Therefore the MT-processed 2013 responses may not be as representative of the entire survey area as the subsequent years' results.

The full results of the 2015 survey will not be discussed in detail as a part of this M.Sc. study, but selected preliminary MT responses will be used for comparison with the 2013 and 2014 survey results.

6.1.2 2013 Responses

6.1.2.1 Preliminary responses

A sample of a preliminary MT response, from site aqi05, is shown in Figure 6.2. These results were locally processed (without a remote reference) using the magnetic field recordings from aqi02, which is located 11.5 km from aqi05 (see Table 5.5), as the local magnetic field. From the impedance estimates, it is evident that the 0.01 to 10 s period band is affected by noise and contains higher variance estimates than other period ranges. The off-diagonal components are affected by noise over a narrower band than the diagonal components, from 0.1 to 10 s. The coherence provides information on correlated signal and noise. In the 0.01 to 10 s band, there is a significant lack of coherence between orthogonal electric and magnetic field components, consistent with the presence of uncorrelated noise.

Figure 6.2: Preliminary MT responses from site aqi05, August 25, 2013.

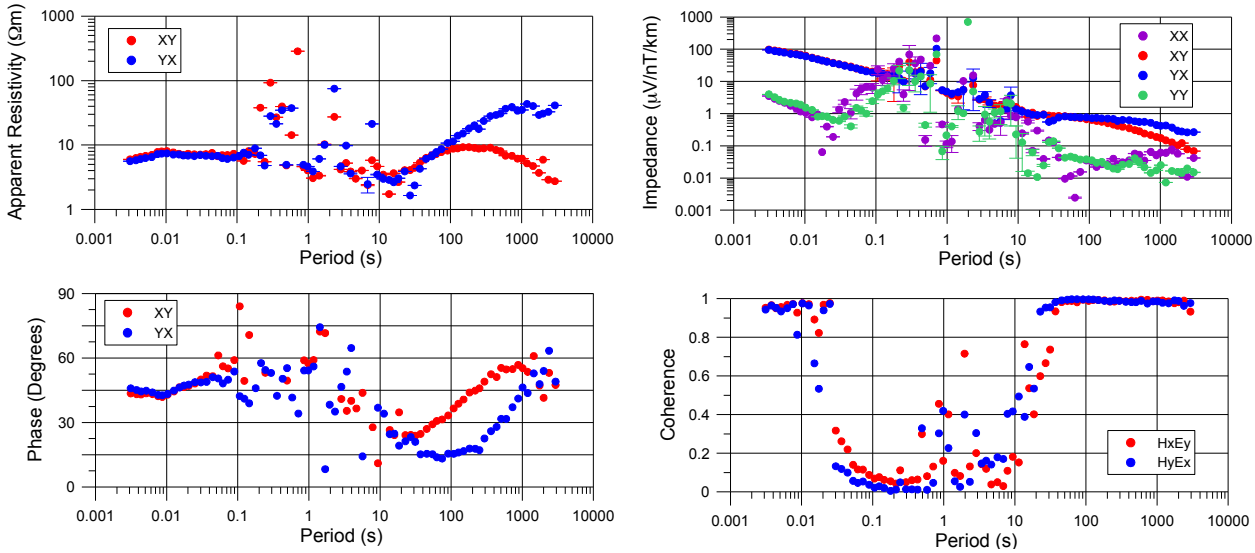

The AMT responses for the same site and day are shown in Figure 6.3. These responses were remote referenced with AMT data from site aqi08. The response is also erratic at periods larger than 0.003 s, particularly the phase response. These responses again suggest the presence of noise. At the longest periods (>1 s) the insensitivity of the AMT coils (Figure 5.4) also contributes to large variance in the responses.

Figure 6.3: Preliminary AMT responses from site aqi05, August 25, 2013.

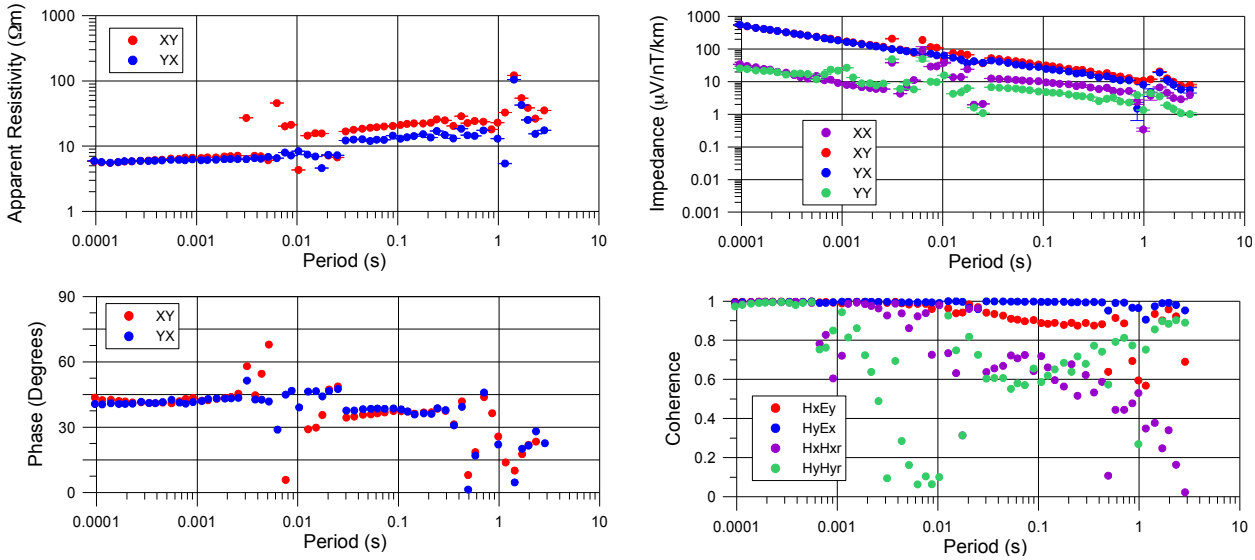

6.1.2.2 Final responses

The combined and edited results for aqi05 provide the desired site response across the entire period range (Figure 6.4 and 6.5). These final results demonstrate that despite the noise in the preliminary responses, there are enough high quality crosspower estimates within the dataset to define a smooth function. Across the band in which the preliminary responses were affected by noise, the apparent resistivity decreases smoothly from 7 to 3 Ωm between 0.03 and 6 s period. Signal coherences remain relatively low in this band (~0.83), but are much higher than for the preliminary responses (<0.1). The final AMT responses show strong agreement with the MT responses in the overlapping period range. This observation is significant, as there were no common magnetic field data between the MT and AMT response estimations. Thus the practice of importing magnetic field time series from distant sites in the processing appears justified.

Figure 6.4: Final locally processed AMT-MT responses from site aqi05, 2013 survey.

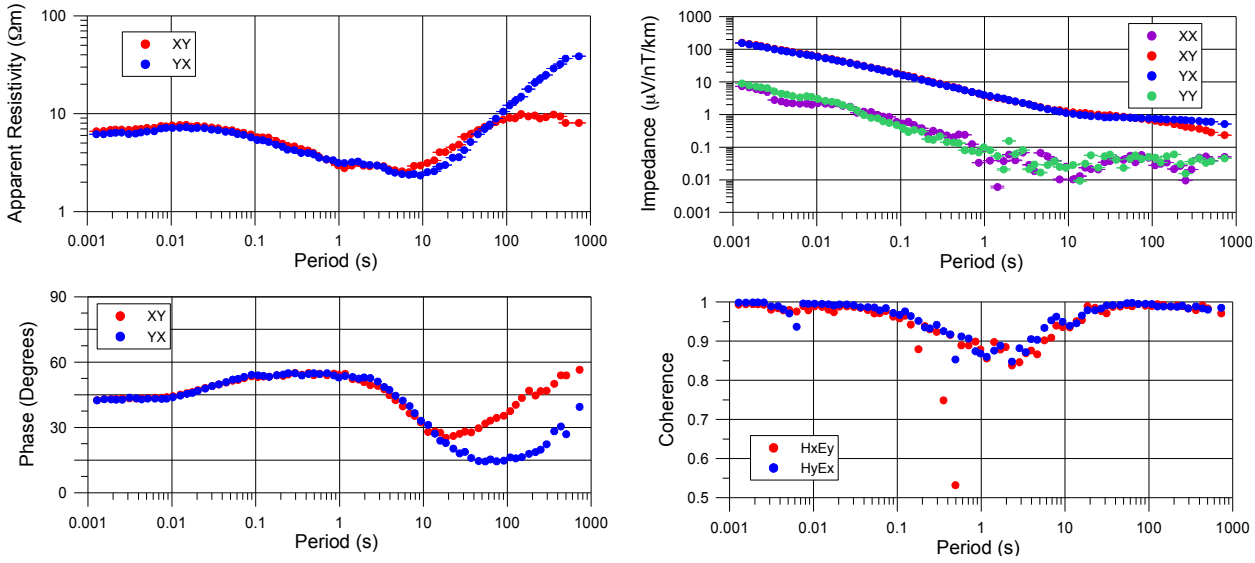

Figure 6.5: Final remote-referenced AMT responses from site aqi05, 2013 survey.

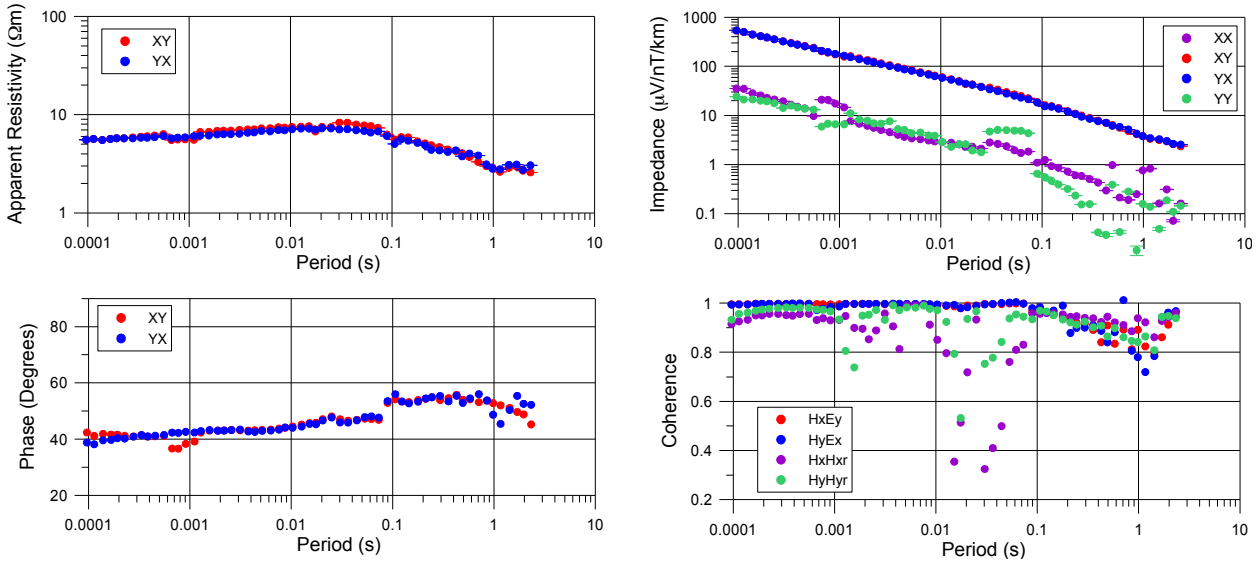

Figures 6.6 and 6.7 show the final edited and combined results for aqi09. The results match those of aqi05 closely. For aqi09, as with other sites, the final response functions are not as smooth as would be ideal, and narrow period bands were removed completely from the response due to a lack of corresponding high quality crosspower estimates. This editing is evident at long and short periods in the MT results and in the 0.0003 to 0.04 s period range of the AMT results.

Figure 6.6: Final locally processed MT responses from site aqi09, 2013 survey.

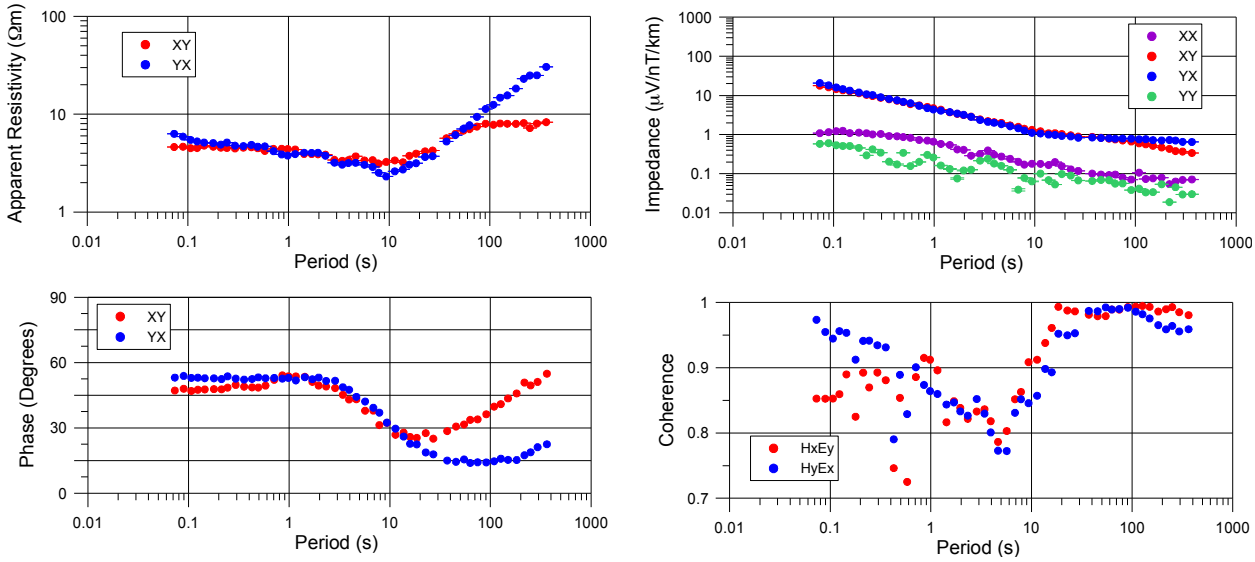

Figure 6.7: Final remote-referenced AMT responses from site aqi09, 2013 survey.

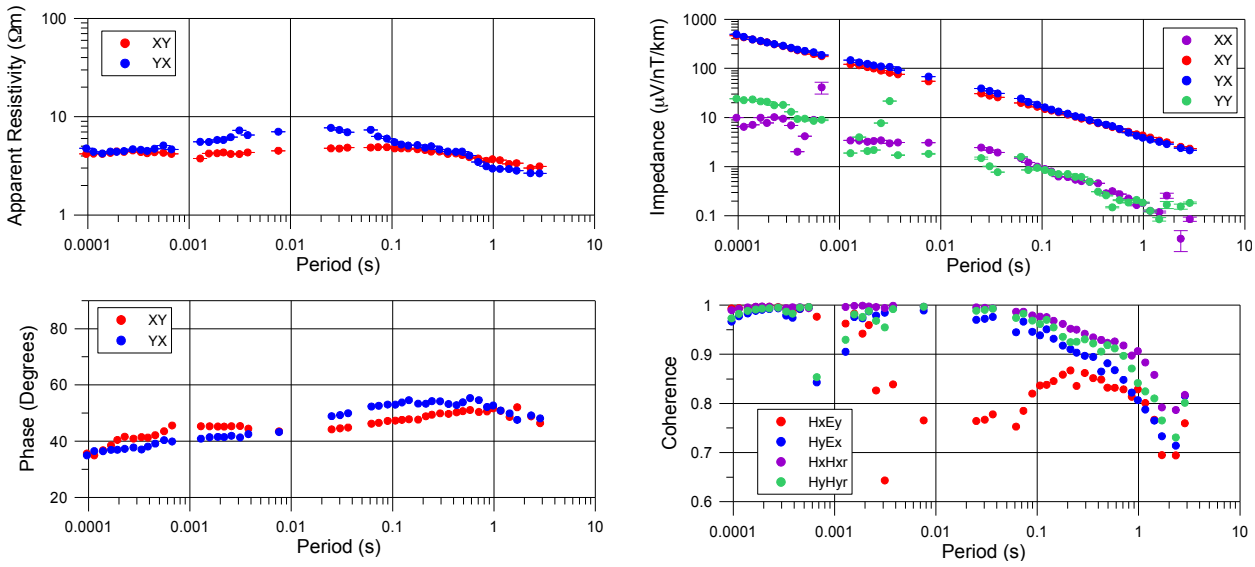

The final MT responses for sites throughout the study area are similar to those for aqi05 and aqi09. There are only minor differences in the general form of the responses and the data quality (Table 6.1). Sites aqi07 and aqi09 are the most affected by noise.

In general, the final MT responses are smoother than the AMT responses. This difference may be due to the greater consistency of the MT preliminary responses. The final

AMT results are combined from preliminary responses that were generated using multiple remote reference sites (see Table 5.5).

Table 6.1: Description of final responses for 2013 dataset.

	Comments	
	MT (local reference)	AMT (remote reference)
aqi01	Excellent data quality. Increase in noise, decrease in coherence at < 0.1 s.	
aqi03	Minor noise in narrow band response ~1-3 s.	Decrease in coherence > 0.1 s. Some noisy estimates.
aqi04	Slightly noisy responses < 10 s.	Good quality response < 0.1 s. Minor amount of noise observable.
aqi05	Excellent data quality.	Good quality response < 0.1 s. Minor amount of noise observable.
aqi06	Minor noise in narrow band response ~1-3 s.	Good quality response < 0.1 s. Minor amount of noise observable.
aqi07	Removal of response by editing from 2 to 20 s. Minor noise at all periods.	Good quality response < 0.1 s. Minor amount of noise observable.
aqi08	Minor noise in narrow band response ~2-10 s.	Good quality response < 0.1 s. Minor amount of noise observable.
aqi09	Significant removal of < 0.07 s data by editing.	Poor quality response. Significant editing around 0.01 s.

6.1.3 2014 Responses

6.1.3.1 Preliminary responses

There is a significant amount of broadband noise present in the preliminary MT responses for the 2014 dataset. Figure 6.8 shows the MT response from site aqi08 on November 10, 2014. For this response, magnetic recordings were imported from site aqi10 and the site was remote referenced with aqi15. The long period results resemble those from the 2013 survey. However, irregular behaviour of the sounding curves is present at all periods shorter than 10 s. In this period range, the estimated impedances are higher than those indicated by the 2013

calculations. In particular, the *xx* and *yy* impedance curves are shifted upwards by more than one order of magnitude and overlap the off-diagonal curves in the 0.003 to 1 s band. Coherence between the electric and magnetic fields decreases significantly in this noisy band; the H_yE_x coherence is nearly zero at all periods shorter than 1 s. The coherence between local and remote *H* fields is strong, suggesting the presence of correlated noise across the survey area.

Figure 6.8: Preliminary MT responses from site aqi08, November 10, 2014.

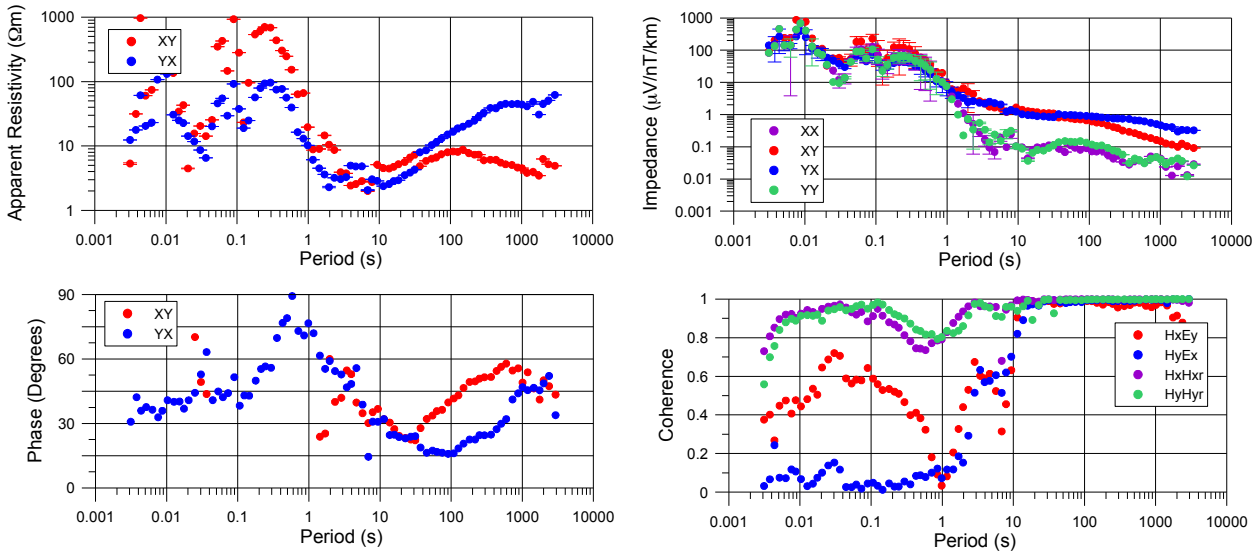

The AMT results from aqi08 on November 10th are shown in Figure 6.9. The remote reference for this response is aqi12. The impedance response for the period band from 0.3 to 30 s matches the MT results very closely. At periods less than 0.3 s, the impedance magnitude and apparent resistivity responses are less erratic. However, noise effects are observed in the phase for periods as short as 0.001 s. Coherences show different characteristics from the MT-processed results: the H_yE_x and H_xE_y coherences are near 1 for most of the reliable AMT bandwidth (< 0.1 s). Only the coherence between the local and remote magnetic fields in the *x*-direction is significantly lower than unity.

Figure 6.9: Preliminary AMT responses from site aqi08, November 10, 2014.

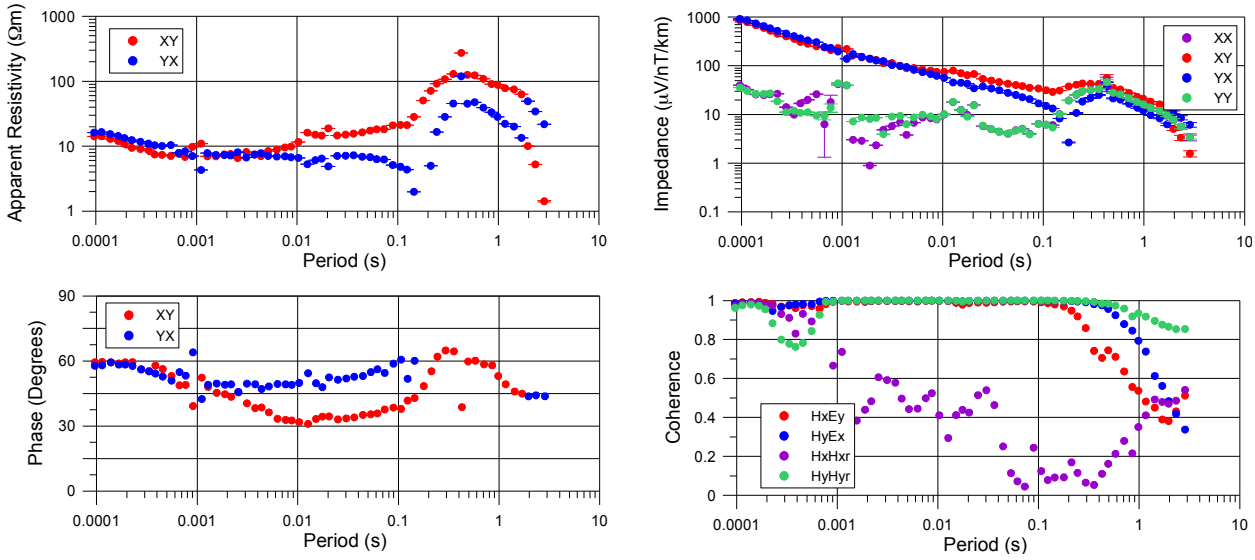

6.1.3.2 Final responses

The data editing and combination procedure was unable to recover reasonable responses in the noise band for the 2014 dataset. In the final response for aqi08 (Figure 6.10), there is a section of the impedances from 0.03 to 1 s for which all crosspower estimates were considered unsuitable, and thus the response in this band has been deleted. The short period response (< 0.001 s) has also been removed. The remaining site response matches the 2013 results for the same period bands.

The degree of editing and response deletion for aqi08 is typical of the final responses for all sites in the 2014 dataset (e.g. aqi04 in Figure 6.11). Table 6.2 describes the final responses of 2014 dataset and the extent of data editing on these responses.

Figure 6.10: Final remote referenced responses from site aqi08, 2014 survey.

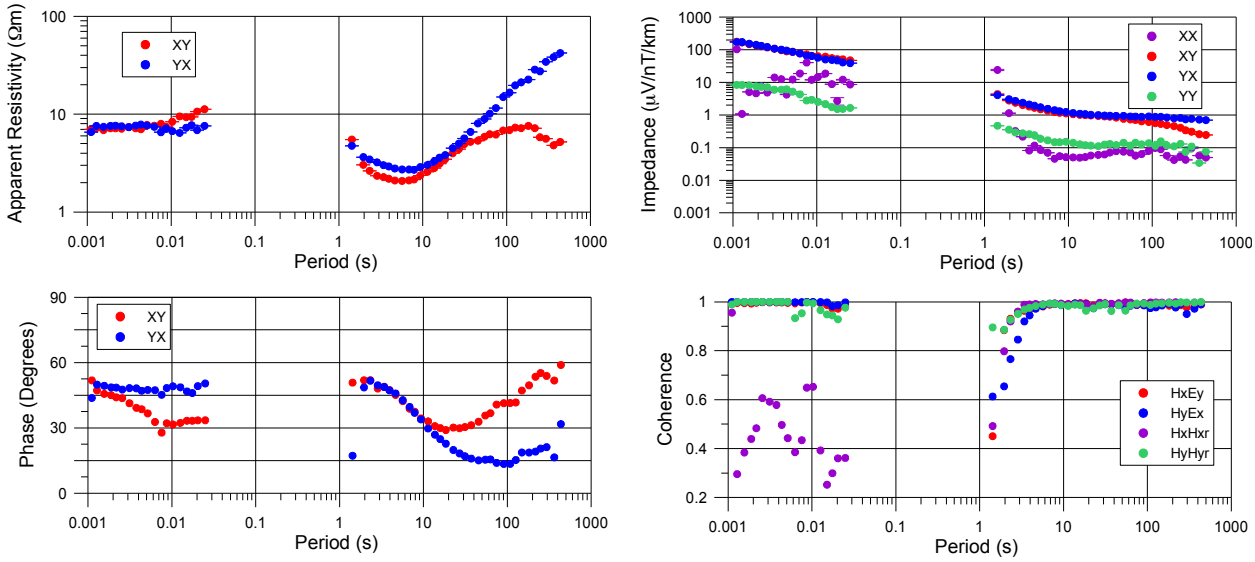

Figure 6.11: Final remote referenced responses from site aqi04, 2014 survey.

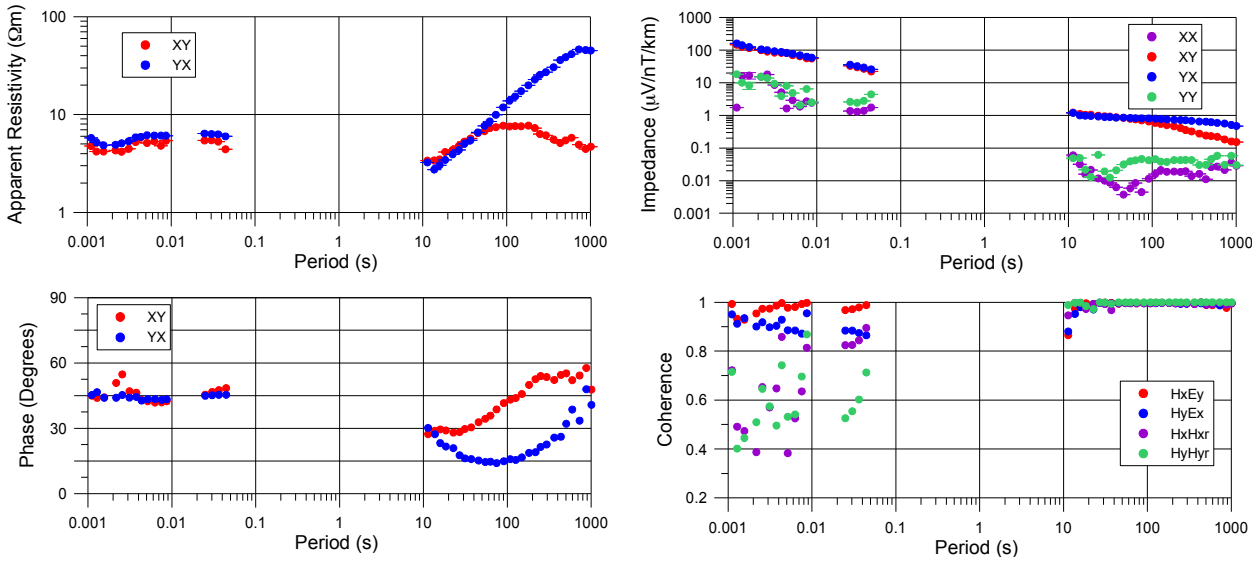

Table 6.2: Description of final responses for 2014 dataset.

	Comments
aqi01	Very noisy. Most of estimated response (0.0002 to 10 s) removed by editing.
aqi02	Very noisy. Most of estimated response (0.1 to 10 s, < 0.02 s) removed by editing.
aqi03	Very noisy. Most of estimated response (0.0002 to 10 s) removed by editing.
aqi04	Noisy. Most of estimated response (0.1 to 10 s) removed by editing.
aqi05	Very noisy. Most of estimated response (0.01 to 10 s) removed by editing.
aqi06	Very noisy. Most of estimated response (0.0002 to 3 s) removed by editing.
aqi08	Very noisy. Most of estimated response (0.02 to 2 s) removed by editing.
aqi09	Very noisy. Most of estimated response (0.1 to 10 s, < 0.002 s) removed by editing.
aqi10	Noisy. Most of estimated response (0.1 to 10 s, < 0.002 s) removed by editing.
aqi11	Very noisy. Most of estimated response (0.1 to 10 s) removed by editing.
aqi12	Very noisy. Most of estimated response (0.1 to 10 s) removed by editing.
aqi14	Very noisy. Most of estimated response (0.0002 to 2 s) removed by editing.
aqi15	Noisy. Most of estimated response (1 to 10 s, < 0.01 s) removed by editing.

The tipper responses from the 2014 survey are also dominated by broadband noise. The effect is reduced for the remote aqi15 site relative to sites in the main survey area (Figure 6.12) but even at this site it was not possible to obtain reasonable responses in the MT deadband.

Figure 6.12: Tipper responses from aqi05 (left) and aqi15 (right).

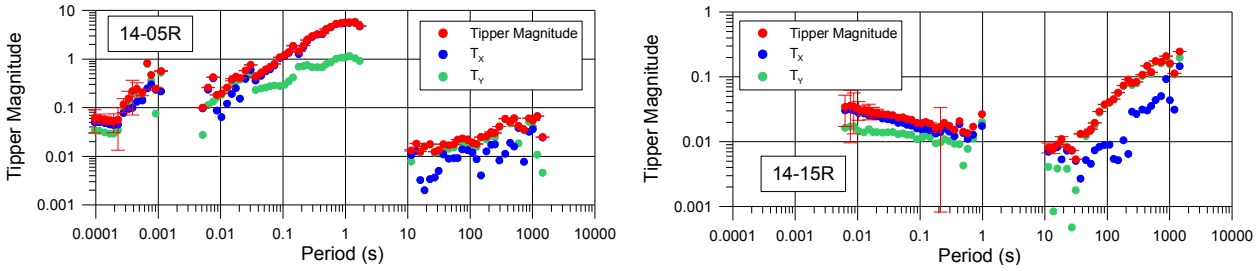

6.1.4 2015 Preliminary Responses

The preliminary 2015 MT responses are well-defined curves with minor amounts of noise at long periods. The result for aqi10 is shown in Figure 6.13. Some static shift is observed in the *xy* curve, but the resemblance to the final responses in 2013 is otherwise strong. The AMT results are noisier than for either of the previous datasets, particularly at periods less than 0.01 s (Figure 6.14). Improvement could presumably be made to the AMT results with further crosspower deletion.

Figure 6.13: Preliminary MT responses from site aqi10, November 6, 2015.

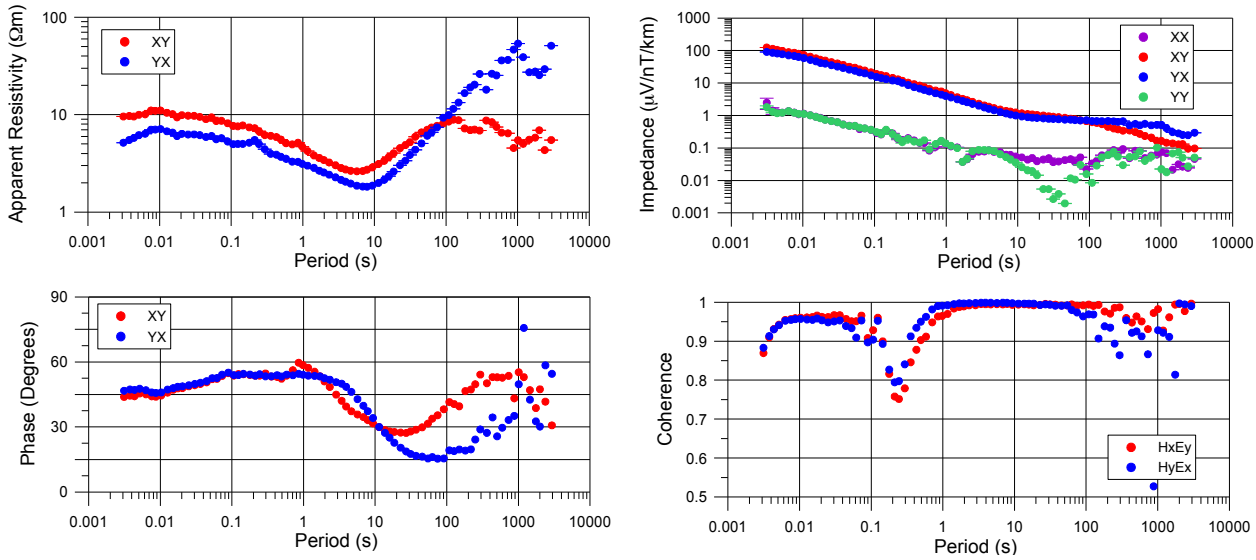

Figure 6.14: Preliminary AMT responses from site aqi10, November 6, 2015.

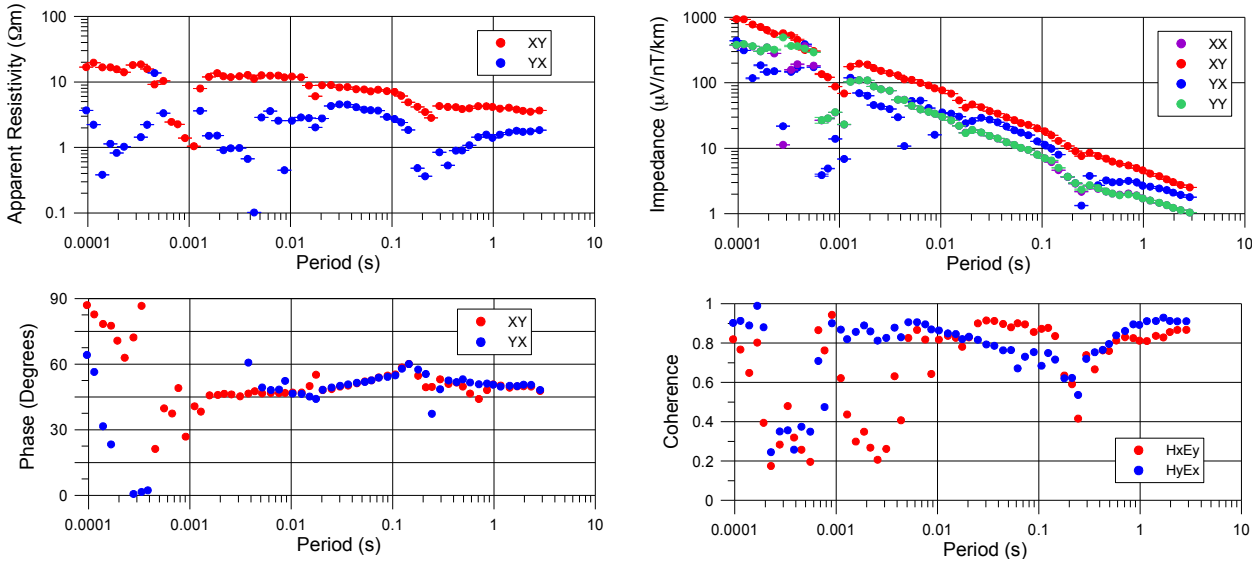

6.2 General form of MT responses

The form of the MT responses gives an indication of the geoelectric structure of the study area before inversions are used to define a resistivity model. Figure 6.15 synthesizes the 2013 MT responses from the whole study area. In the 0.001 to 60 s period range there is tight clustering of the *xy* and *yx* phase responses, and with the exception of the MT responses for aqi01 and aqi07 there is tight clustering of the *xy* and *yx* apparent resistivity responses. The responses indicate the occurrence of minimal lateral variation of the subsurface resistivity as expected for a layered sedimentary stratigraphic section. The apparent resistivities at the shortest periods (0.001-0.03 s) do not vary greatly from ~8 Ωm. At periods of 0.03 to 3 s, the apparent resistivity decreases to ~2 Ωm and the phases increase to values above 45°.

At longer periods (> 20 s for the phase and > 60 s for the apparent resistivity), the 2013 MT responses have divergent *xy* and *yx* components. The *yx* apparent resistivity and phase responses indicate higher resistivities, whereas the *xy* component has a more conductive response. This multidimensional character can be attributed to the dominant effect of the north-

south trending NACP, and, as discussed in Chapter 3, is an expected result based on previous MT soundings in the Williston Basin (Jones, 1988; Jones and Craven, 1990; Jones 1993; Gowan *et al*., 2009).

Figure 6.15: Overlay of all 2013 final MT responses.

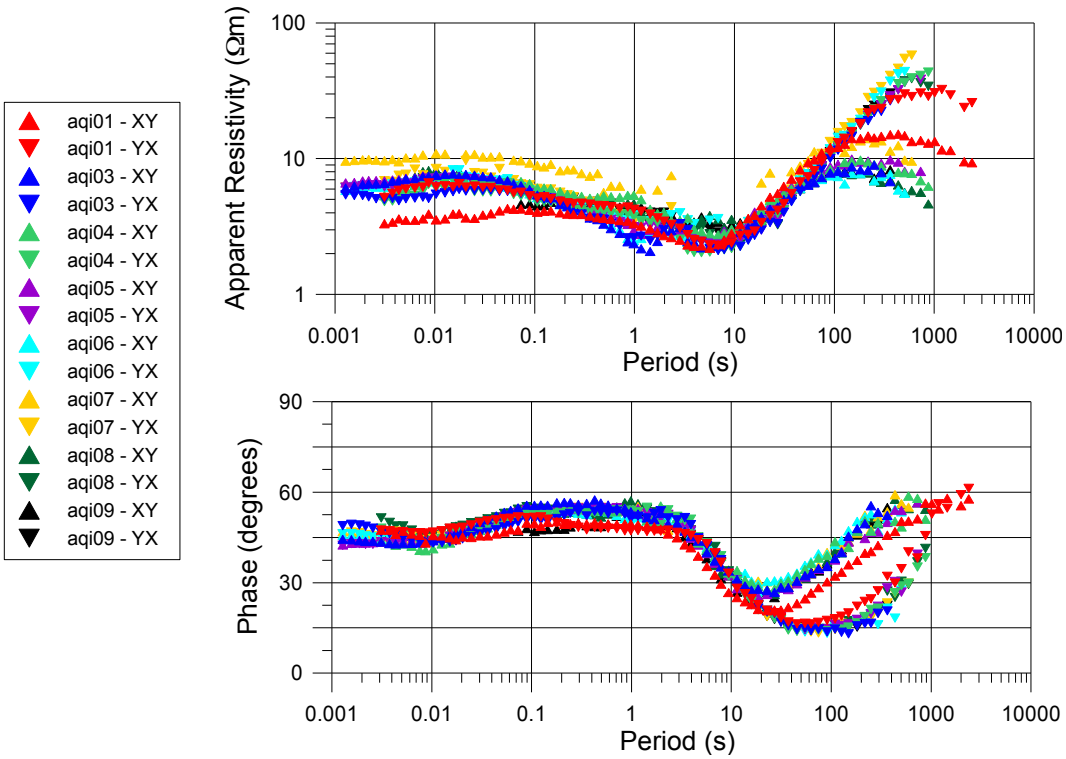

For the 2013 AMT results (Figure 6.16), there is strong agreement with the general form of the 2013 MT responses in the overlapping period range (0.001 to 1 s). From 10^{-4} to 10^{-3} s there is a greater degree of variability in the responses across the sites. The apparent resistivities range from 4 to 20 Ωm in this shortest period band, while the phases range from 35˚ to 60˚. As expected from equation 4.24, these short-period apparent resistivity and phase responses are generally anti-correlated, with an increase in phase associated with a decrease in apparent resistivity. The responses for aqi07 and aqi08 do not show this same consistency between the apparent resistivity and phase. The variation in the response is explained by near-surface

variations within the Quaternary till overlying the more uniform stratigraphy of the Williston Basin (see section 3.3).

Figure 6.16: Overlay of all 2013 final AMT responses.

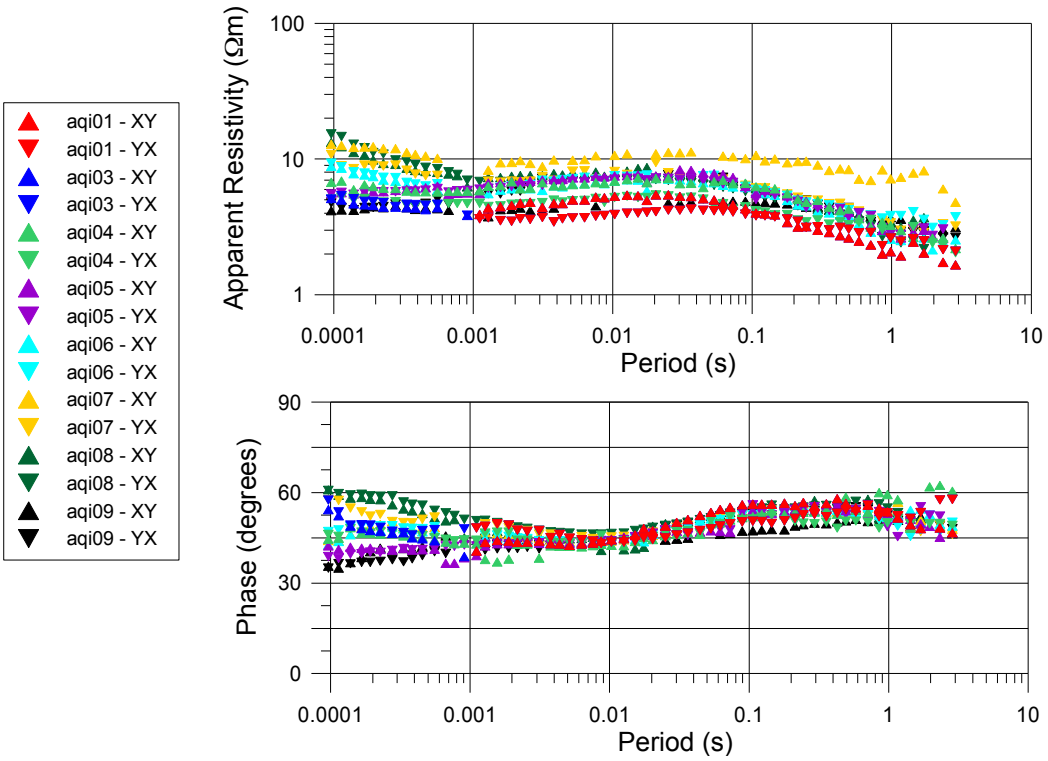

Site aqi07 displays a different apparent resistivity response from the remainder of the population for both the AMT and MT final results. The *xy* component in particular is anomalous. The cause of this effect is likely either static distortion or a bias introduced by noise that has shifted the response to a higher magnitude. High noise levels and very inconsistent crosspower estimates observed at this location often led to insurmountable difficulties in editing the preliminary responses. An attempt to relocate the site to a nearby location (aqi13; Figure 5.1), resulted in recordings that failed to process. The noise was primarily observed in the 0.001 to 10 s period band for the AMT results and the 0.1 to 100 s period band for the MT results. As a result of these issues, aqi07 and aqi13 were not revisited in subsequent surveys.

The synthesized 2014 MT results have the same form as the 2013 final responses for periods larger than 1 s (Figure 6.17). At periods less than 1 s, significant noise effects dominate the 2014 responses. The significant response editing done in this period range has not resulted in a set of plausible geoelectric responses. The spread of apparent resistivity and phase responses is large. Although the collective results are centred on the 2013 curves at each site, the responses diverge from the 2013 results. While the editing process was sufficient for overcoming noise levels in 2013, the same cannot be said of the 2014 dataset.

Site aqi14 was established a short distance (~300 m) from the aqi07 location in the 2014 survey. This site exhibited the same issues previously seen at aqi07. No effort was made to produce final responses from aqi14.

Figure 6.17: Overlay of all 2014 final responses.

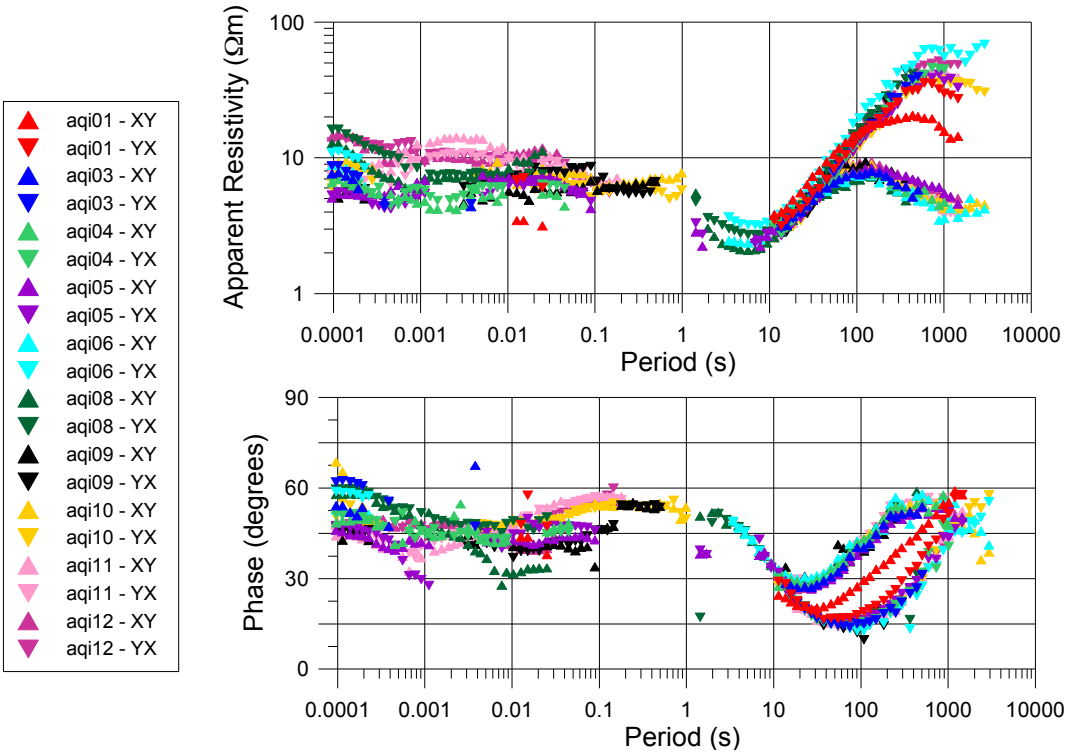

A common feature of the final responses in both the 2013 and 2014 datasets is the difference in the response at site aqi01 to that at the other sites. This discrepancy is most evident in the long-period *xy* curves, which indicate higher resistivities for aqi01. This unique site response shows differences from the other site responses at all periods for both apparent resistivity and phase, suggesting a local conductor is causing distortion of the EM response.

6.3 Noise characterization

6.3.1 Overview

Review of the calculated MT responses has indicated that the effects of noise have a strong effect on the results, particularly for the 2014 dataset. In this section the noise is examined in more detail. The available datasets include up to 15 different sites that were revisited on a day-to-day basis over two separate surveys (2015 data is excluded from these analyses).

The effects of the noise on the MT responses are to some degree controlled by the strength of the MT signal, which is variable over time. If the MT signal rises above the noise level, the response will be less affected.

Variability of noise in the time series and power spectra provides a basis for identifying the characteristic noise bands at particular locations and specific points in time. The characteristics of the EM noise such as its periodicity and its longer-term evolution over time (stationarity) may be observable in the time domain. In the frequency domain, noise may be defined by its spectral peaks and harmonics, and its bandwidth. The time-frequency content can be examined using wavelet transforms. Additionally, the spatial distribution of the noise can be evaluated from its effects on the MT impedance and tipper responses and its polarization.

6.3.2 Deadband effects

Variable levels of the natural geomagnetic signal are observed in the datasets. When signal levels are low, the MT and AMT deadbands are apparent from the spectral estimates (e.g. between 0.0003 and 0.001 s in Figure 6.18). Lower signal levels in these deadbands will lead to noise having a more significant effect on the impedance results. However, the deadbands are not always observed (Figure 6.18), and the MT responses are typically affected by a negligible to minimal amount in the deadbands.

Figure 6.18: Calculated AMT power spectra for aqi04 on August 22, 2013 (left) and August 26, 2013 (right).

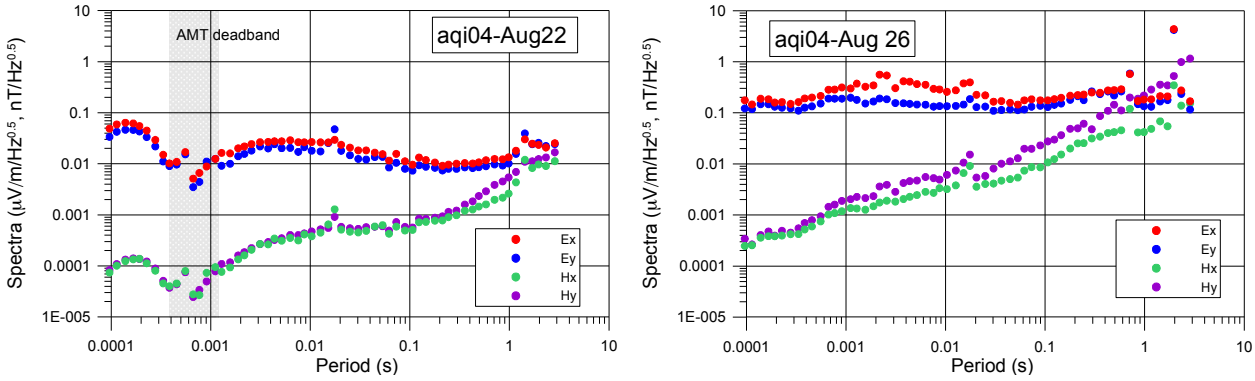

6.3.3 Signals at 60 Hz and harmonics

Powerlines are a common source of noise in EM surveys. The alternating 60 Hz signal and its harmonics are clearly visible at locations in the Aquistore survey area. Figure 6.19 shows a segment of a band 2 (TS2) H_x time series and the corresponding power spectrum calculated with the maximum taper method using Strati-signal software (Ndiaye, 2007). It is evident that as well as the fundamental 60 Hz signal, at least nine odd-numbered harmonics are contributing significant signal. These signals are strongest at aqi04, the site nearest to the power station and its associated infrastructure. However, this noise is pervasive and can be observed in the spectra derived from the TS2 time series at all survey locations. At the remote sites (e.g. Figure 6.20)

the 60 Hz noise is not identifiable in the time domain, but spectral analysis resolves multiple spectral peaks in the frequency domain. The level of noise at the remote reference locations aqi02 and aqi15 is reduced relative to the background geomagnetic signal.

Figure 6.19: TS2 HX time series segment and the calculated power spectra for aqi04 on November 8, 2014. The ninth odd harmonic is observable at 1,140 Hz. Note that the time series is uncalibrated so the units of the power spectrum are arbitrary.

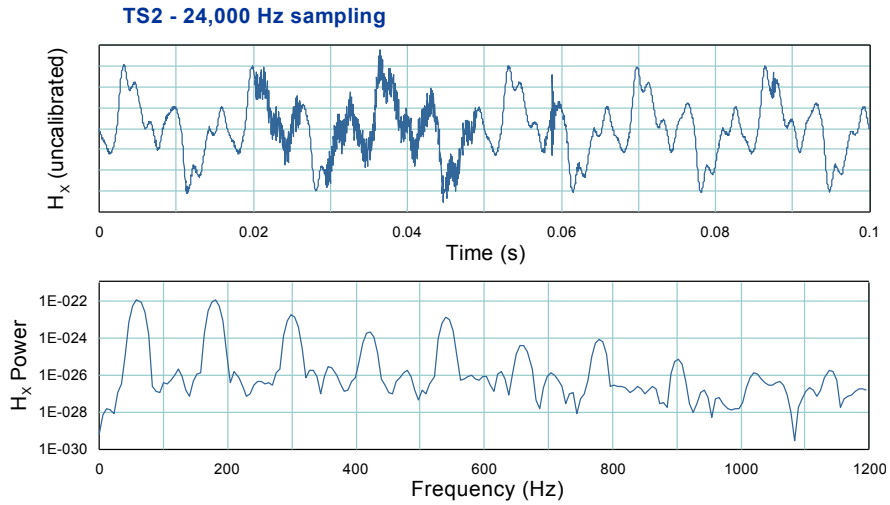

Figure 6.20: TS2 HX time series segment and calculated power spectra for aqi02 on November 8, 2014.

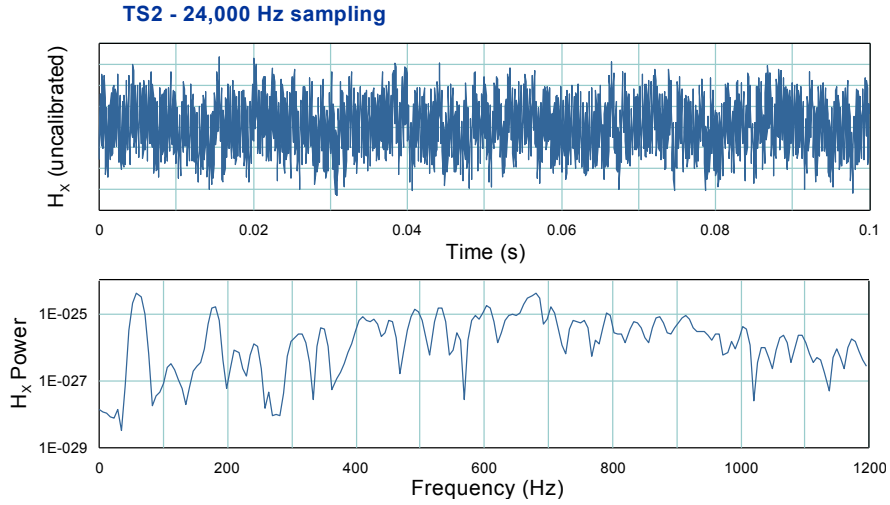

Analysis of power spectra derived from band 3 (TS3) and band 4 (TS4) recordings indicates that these time series include minimal 60 Hz noise. The Phoenix MTU instrumentation uses a comb filter to reduce the 60 Hz signal and harmonics from these time series. The

instrumentation does not use the filter on the 24,000 Hz sampled TS2 time series. In most locations this approach will not be a problem because the TS2 file data are used only to define the responses at frequencies of > 900 Hz in the .FC2 files (Phoenix Geophysics, 2003) and the power of the 60 Hz harmonics will be small at these frequencies. However, the significant power present at the higher harmonics at some Aquistore sites means that the noise can cause some degradation of the impedance responses, particularly during periods of low signal level. The impact of these harmonics is restricted to the AMT deadband at particularly noisy sites, such as aqi04.

6.3.4 Broadband noise

6.3.4.1 Time-domain, frequency-domain and wavelet analysis

Both the preliminary and final responses from the 2014 survey appear to be affected by high levels of noise in a broad band at periods less than 10 s. The effect of this noise on the impedance results is significant (e.g. Figures 6.8 and 6.9). In order to characterize this noise, we begin by examining the raw time series data. Figure 6.21 shows a sample of the H_x time series recording from aqi08 on November 10, 2014. The three types of time series provide an opportunity to inspect waveforms at different time scales. Each of the time series are dominated by continuous short-period signals.

Figure 6.21: Hx time series segments recorded on November 10, 2014 at site aqi08.

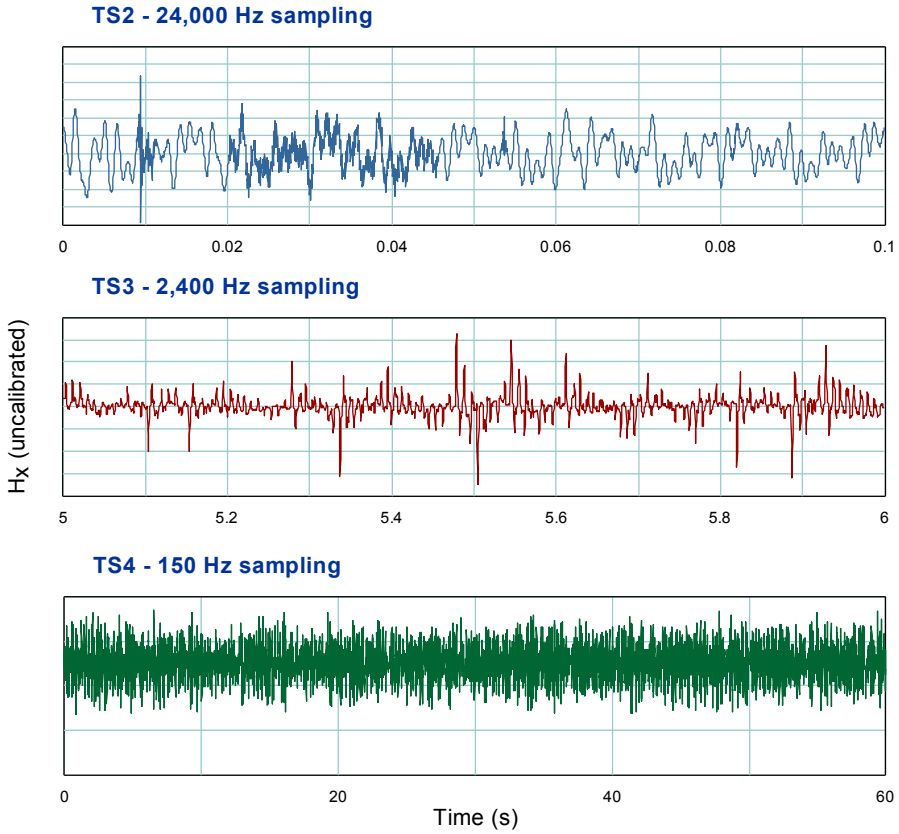

Spectra calculated from these time series segments allow for examination of detailed frequency domain characteristics (Figure 6.22). These spectra are generated from short segments of recordings for a high number of frequencies per octave using a multi-taper method in Strati-signal. Higher resolution spectral information can be examined from these plots than from the spectra generated from the complete time series at a lower number of frequencies per octave, such as those available from Phoenix processing software. Low-frequency signals (<1 Hz) are not resolved, but the impedance estimates are less affected by the noise in this range.

The spectra computed for the TS2 files are dominated by the effect of 60 Hz powerline noise and its harmonics. The time series with lower sampling frequencies give a better representation of different types of the EM noise. In the TS3 spectra, there is a band of increased

energy level between 0 and 30 Hz band, with localized peaks at 12 and 17 Hz. The signal in this band will henceforth be referred to as **B1**. There is also a second band of significant energy between ~85 and140 Hz (referred to as **B2**). For **B2**, spectral peaks are observed at 95 Hz, 110 Hz, and 130 Hz. The TS4 spectra show only the lower frequency **B1** noise. For the time series segment analysed the noise is present from ~1 to 20 Hz and is centred on 12.5 Hz. Therefore the transient noise which has been identified for the 2014 survey consists of two broadband signals centered on 12.5 Hz and 110 Hz.

Figure 6.22: Hx spectra for each of three time series types recorded on November 10, 2014 at site aqi08.

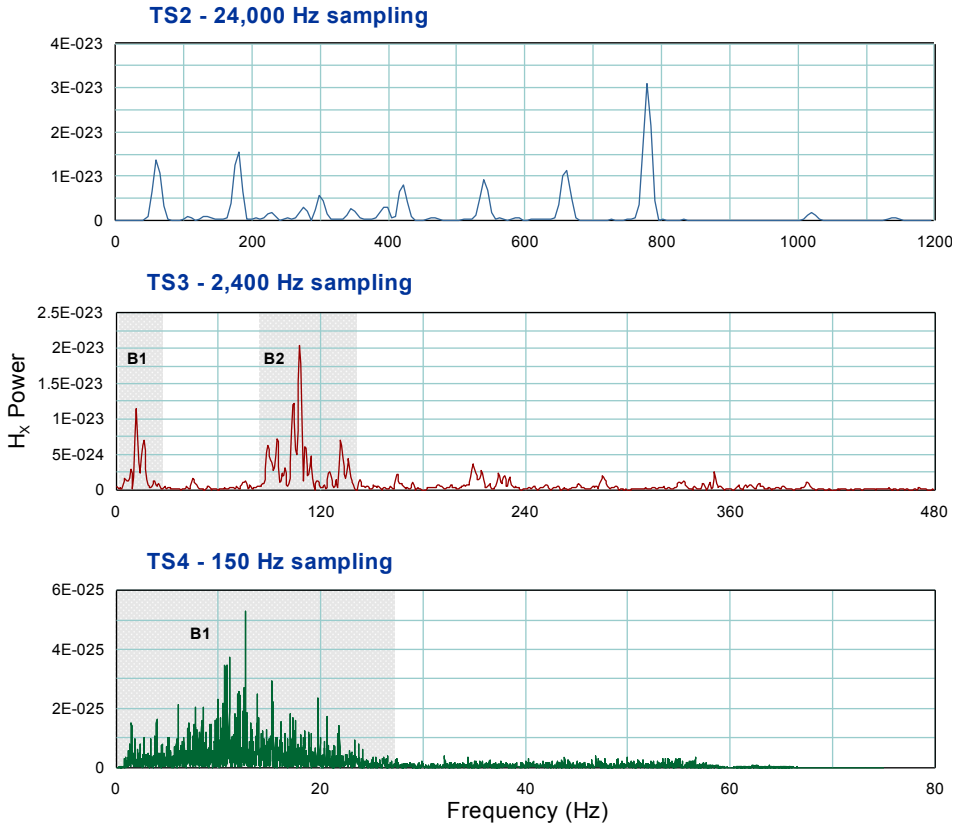

Wavelet transforms were generated from the TS3 and TS4 time series samples using a Morlet wavelet computation available in Strati signal software (Ndiaye, 2007). The resulting transforms show the time domain characteristics of the noisy signal (Figures 6.23 and 6.24). The

TS3 wavelet transform shows the noise in both bands is pulsed: the **B2** signal repeats every 0.05 seconds, and the **B1** signal repeats every 0.75 seconds. The TS4 wavelet transform shows that this pulsation is continuous over time-scales of at least one minute.

Figure 6 23: Wavelet transforms of TS3 time series for November 10, 2014 at site aqi08. The response at ~0.08 s period corresponds to the B1 band of the noise and the response at ~0.008 s corresponds to the B2 band of the noise.

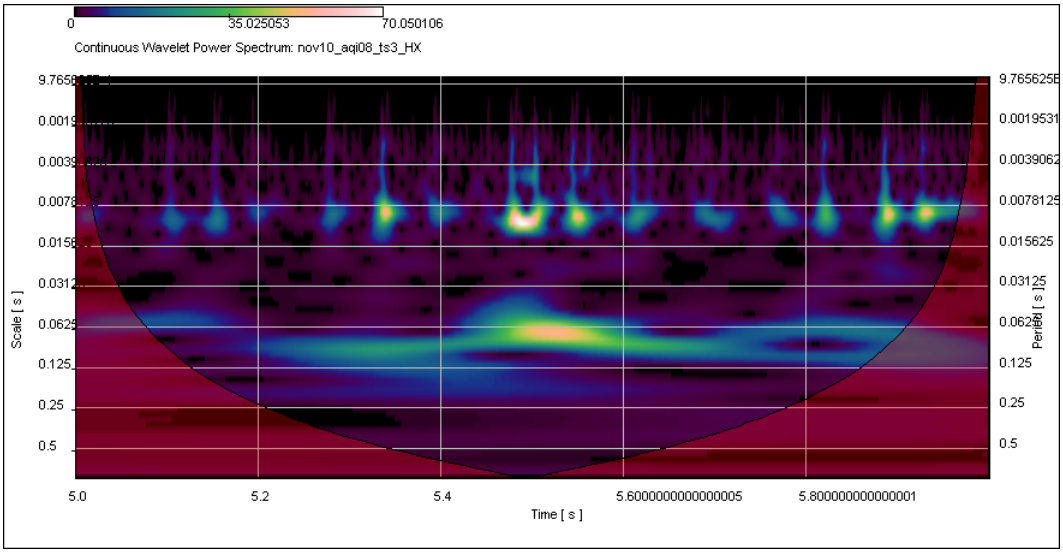

Figure 6.24: Wavelet transforms of TS4 time series for November 10, 2014 at site aqi08.

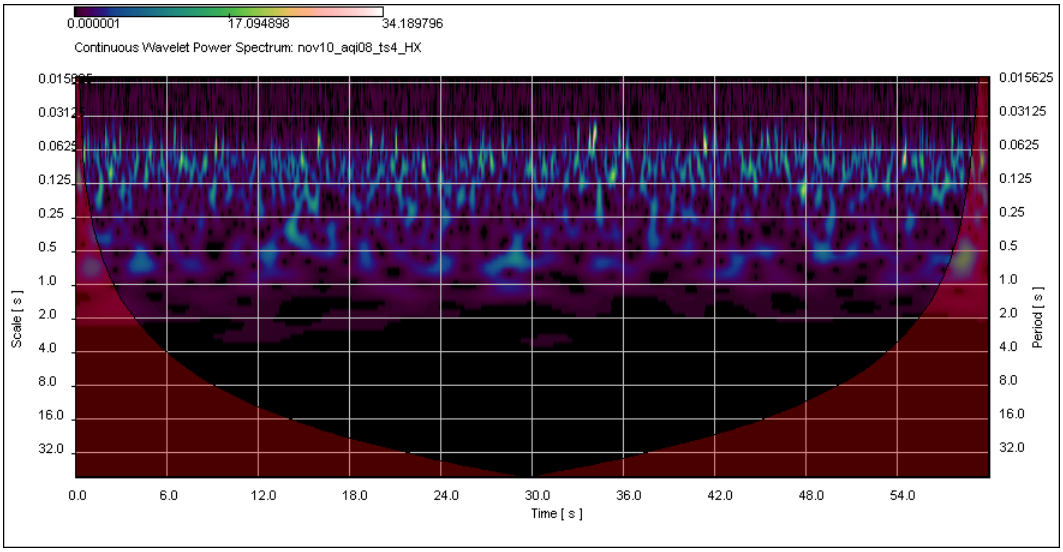

6.3.4.2 Temporal variations

Since the 2014 responses are heavily affected by noise, and the 2013 responses are not, it is worth comparing spectra from the two surveys to identify any time-evolution of the signal and noise in the study area. Differences between the two datasets could be representative of the installation of new sources of noise in the survey area following the 2013 field session. Alternatively, changes may be indicative of year-to-year variations in the strength of the inducing geomagnetic field.

The spectra shown in Figure 6.25 are representative of the differences between the two datasets. The most notable noise features in the 2014 plot are the peaks in the electric and H_y field spectra in the **B1** and **B2** bands. The broad **B1** peak in particular, with its linear sides (on the log-log plot), does not resemble a natural geoelectric or geomagnetic signal. In contrast, the 2013 spectra show none of these features. Although the geomagnetic signal levels do appear to be higher for the 2013 survey, especially for the H_x component, they are lower than the level of noise peaks observed in 2014. The peak at 2.0 s in the 2013 plot (and its odd harmonics) is associated with the CSEM transmitter.

Figure 6.25: Calculated MT power spectra for aqi01 on August 23, 2013 (left) and November 7, 2014 (right).

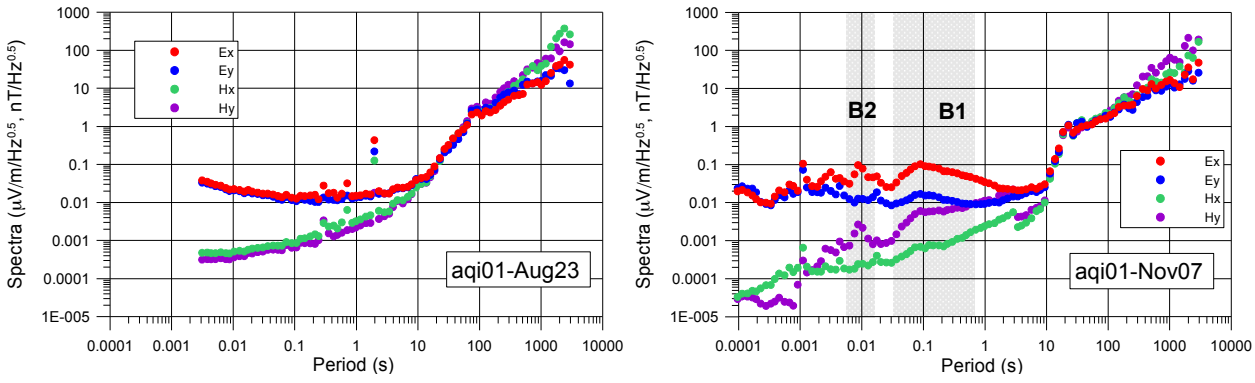

The AMT-processed data show similar results to the MT processed data. The 2014 spectra display high noise levels in both **B1** and **B2**, but the 2013 spectra do not (Figure 6.26).

Figure 6.26: Calculated AMT power spectra for aqi04 on August 22, 2013 (left) and November 8, 2014 (right).

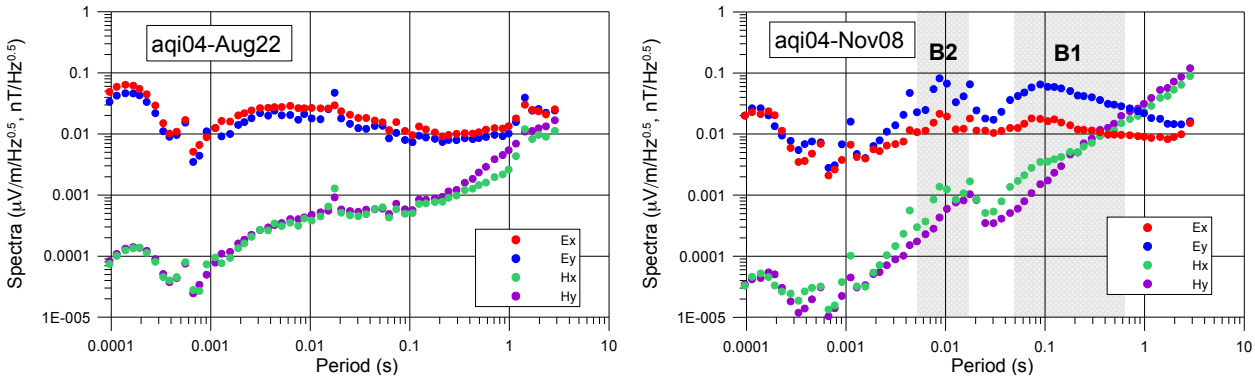

Diurnal changes in the spectra at a single site may give an indication of the level of stationarity in the noise. For aqi01 in 2014 (Figure 6.27), significant changes to the frequency content of the recordings on consecutive days are not present; the signal characteristics in the noisy bands are unchanged throughout the survey. November 12, 2014 represents a minor exception in that noise is reduced to lower levels.

Figure 6.27: Calculated MT power spectra for aqi01 on November 7, 2014 (left) and November 8, 2014 (right).

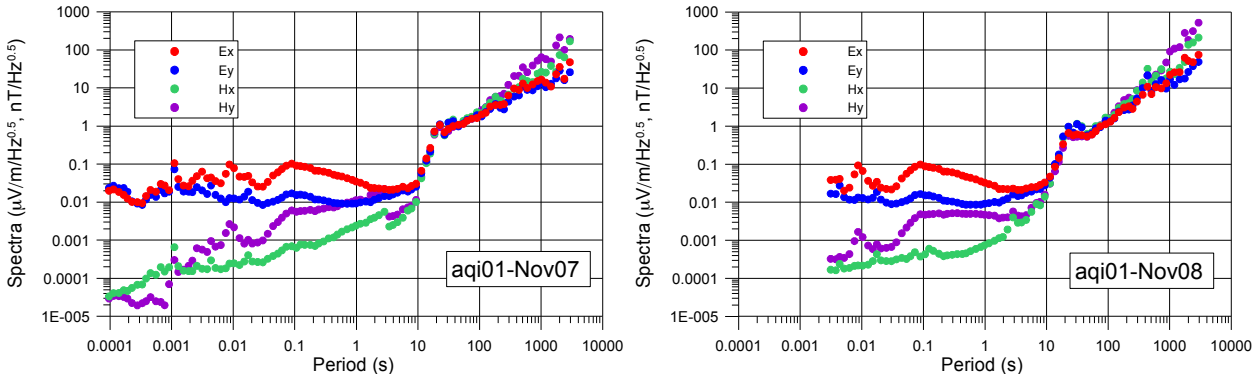

6.3.4.3 Spatial variations

Inspection of spectra from different sites in the survey area for a common recording time interval may reveal spatially localized noise. In particular, the spatial variations of the noise in the 2014 dataset may identify the source of the noise.

As an example, the relative amplitudes of E_x and E_y at sites aqi04 and aqi05 appear to be reversed between the two sites, as shown in both the MT and AMT processing (Figures 6.28 and 6.29). This is not a unique occurrence: there are differences in the relative noise amplitudes at multiple sites. Note that the magnetic spectra in Figure 6.28 are identical at both aqi04 and aqi05 as both sites have been processed using the same imported magnetic data (from aqi01 and aqi02).

Figure 6.28: Calculated MT power spectra for November 8, 2014 at aqi04 (left) and aqi05 (right).

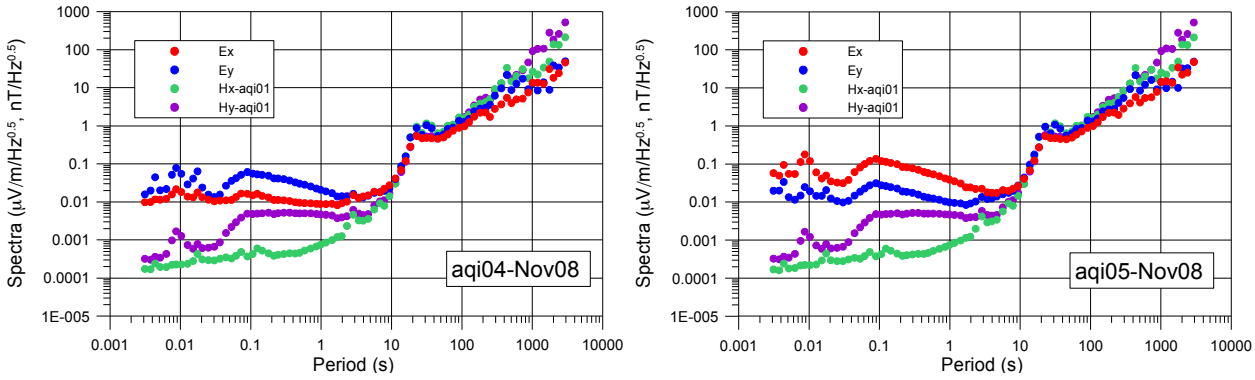

Figure 6.29: Calculated AMT power spectra for November 8, 2014 at aqi04 (left) and aqi05 (right).

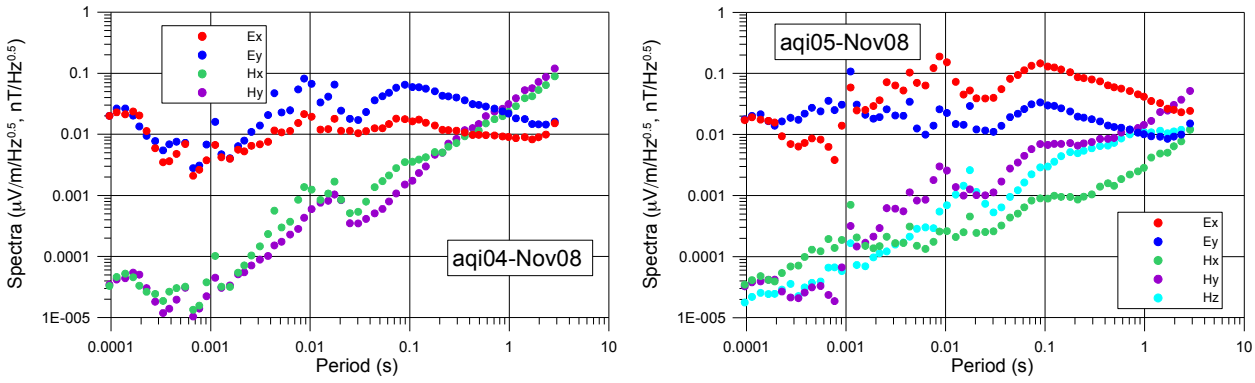

Comparing the spectra from aqi05 and aqi06 (Figure 6.30), further differences in the ***E***-field signal levels are evident. The electric fields at aqi06 do not appear to be affected by the **B1** or **B2** noise seen at aqi05. Tracing the source of the imported magnetic data, we can also observe differences in the ***H***-field at sites aqi01 and aqi09. On November 9, the aqi09 coils were imported to aqi05 and aqi06 for local magnetic field data, whereas the aqi01 coils were used on the previous day. It is clear that at aqi09 the H_x field spectra tend to follow the H_y spectra closely. This is a difference from the aqi01 site (Figure 6.28), where the H_x spectra do not have a characteristically broad peak in **B1**.

Figure 6.30: Calculated MT power spectra for November 9, 2014 at aqi05 (left) and aqi06 (right).

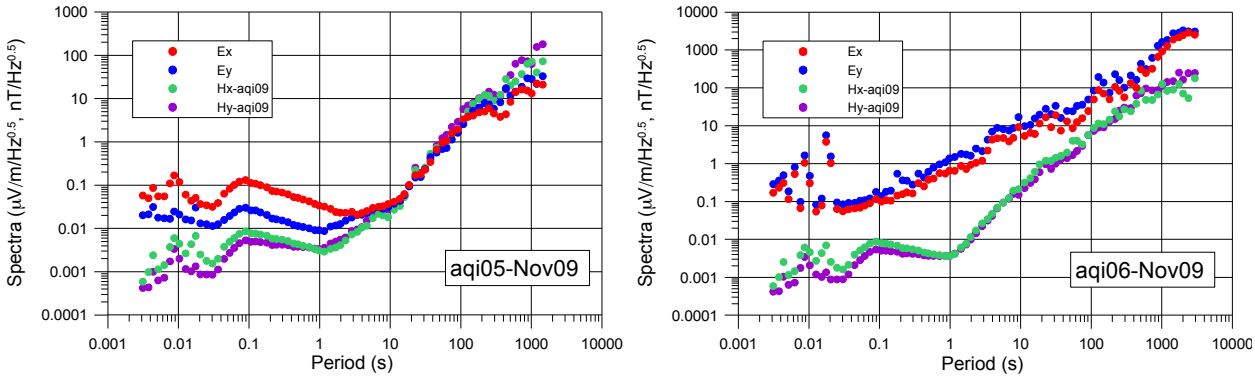

Sites aqi10, aqi11, and aqi12 show a decreasing level of noise in the **B1** and **B2** bands as the sites become more distant to the injection well. As shown in Figure 6.31, the noise level in the aqi11 spectra is less than for aqi12. The magnetic fields, imported from aqi10 and aqi15, do not exhibit the noise seen at the other sites.

Figure 6.31: Calculated MT power spectra for November 11, 2014 at aqi11 (left) and aqi12 (right).

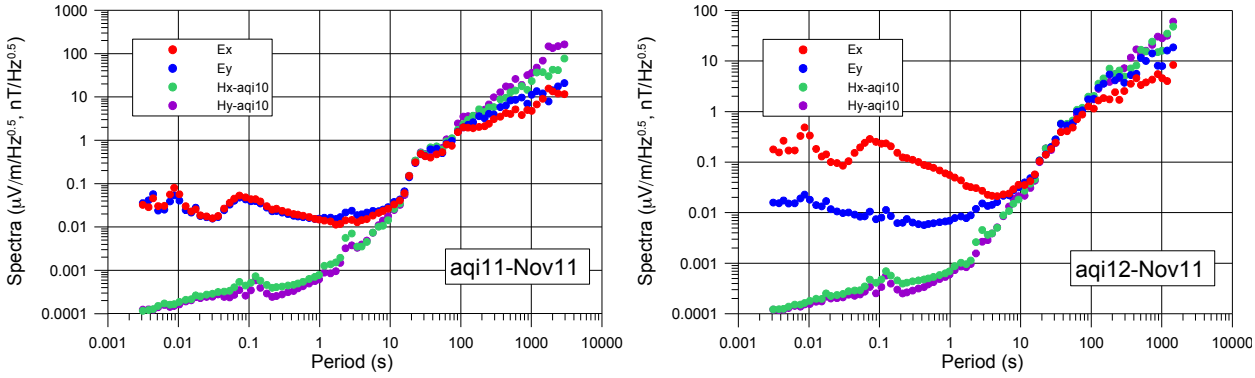

Finally, it is important to note that at the remote sites, the spectra are unaffected by the broadband noise present in the main survey area (Figure 6.32).

Figure 6.32: Calculated MT power spectra for aqi02 on November 7, 2014 (left) and aqi15 on November 9, 2014 (right).

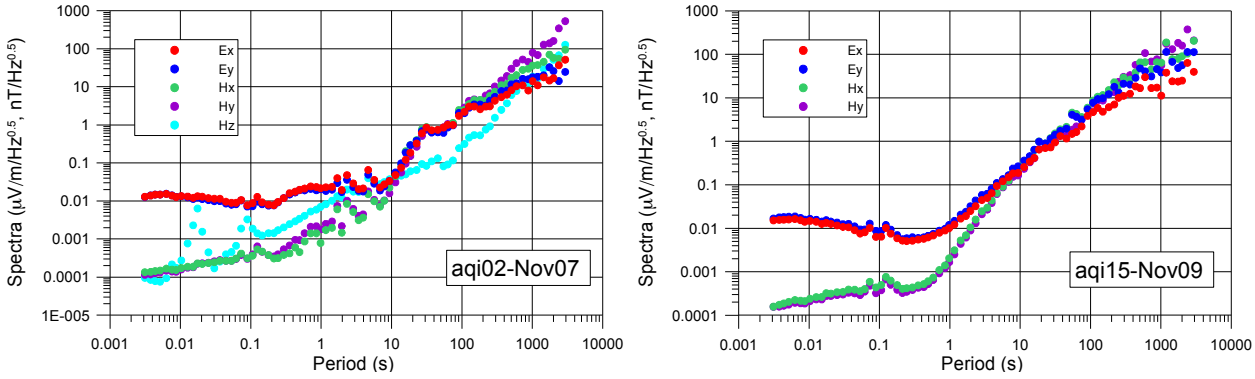

Further spatial characterisation of the 2014 noise is possible by considering the polarization of the noise at each site. At sites aqi01, aqi03, aqi05, and aqi12 the noise is significantly stronger on the E_x and H_y channels. At aqi04, and aqi14 the noise is greater on the E_y and H_x channels. Noise is present in nearly equal amounts, but at low levels, in the E_x/H_y and E_y/H_x pairs at sites aqi09 and aqi11. Sites aqi02, aqi10, and aqi15 exhibit little to no noise.

A vector map (Figure 6.33) of the noisy signal at 9.4 Hz was generated by taking the vector sum of the E_x and E_y signal levels. In order to enhance the visibility of the responses, the

vector data was gridded using the kriging method and plotted over an area that approximately corresponds to the main survey location. The plotting was done using Surfer 11 software (Golden Software Inc.).

The spatial pattern demonstrated by the vector map corresponds closely to the trend of the pipeline that transports CO_2 from the power plant to the injection site. The vectors are subparallel to the trend of the nearest segment of pipeline across the survey area. At sites more distant from the pipeline, the vector magnitude is relatively small.

Figure 6.33: Vector map of electric field signal strength at 9.4 Hz. CO_2 pipeline shown as red line. Approximate location of pipeline from White *et al.* (2014).

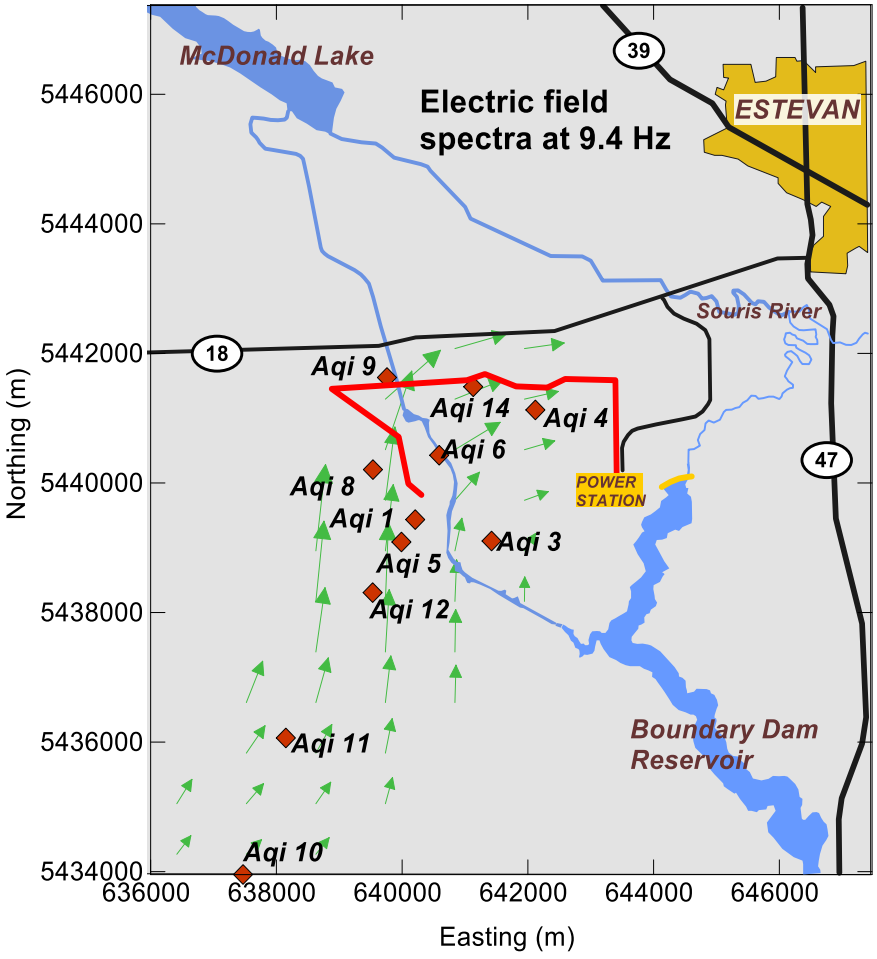

6.4 CSEM data characterization

CSEM data, collected in both the 2013 and 2015 field sessions, has yet to be processed. However, examination of the CSEM signal in the time and frequency domains is an important early step in validating the soundings carried out at Aquistore. The transmitter waveform is observable in sample time series at multiple transmission frequencies (Figure 6.34).

Figure 6.34: Two segments of E_x TS3 time series from aqi01 on November 7, 2015. 2 Hz (top) and 8 Hz (bottom) signal is observable.

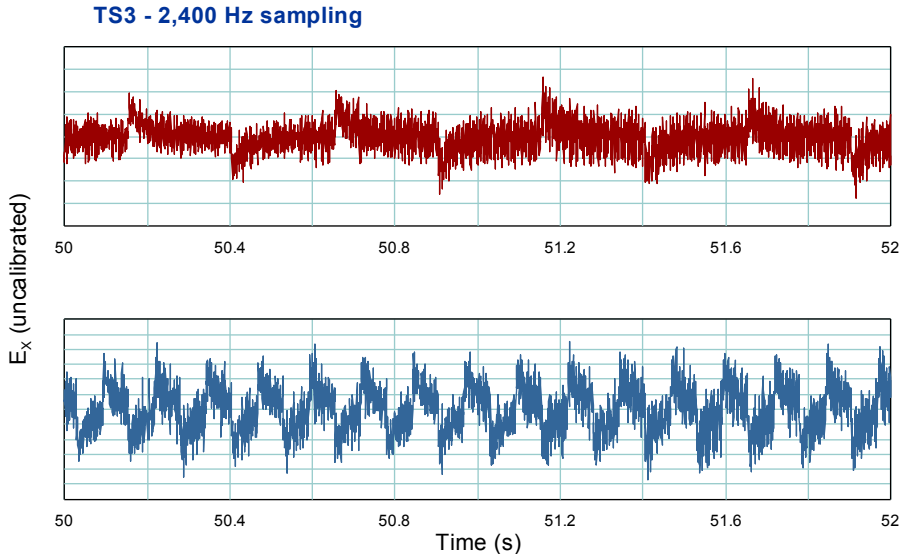

At the sites most distant from the transmitter bipole, aqi10 and aqi11 (9.5 and 7.3 km away from southernmost electrode, respectively), the waveform is not discernible in the time domain (Figure 6.35). However the transmitter contributes significant spectral energy to the recorded signal at these locations (Figure 6.36). Generally, the transmitted signal is most apparent on the H_y channel in the unrotated time domain data, perhaps due to a lack of high-energy geomagnetic signal on this channel.

Figure 6.35: Segments of H_y TS3 time series from aqi01, aqi11, and aqi10 on November 7, 2015. 2 Hz CSEM signal is visible at aqi01 only.

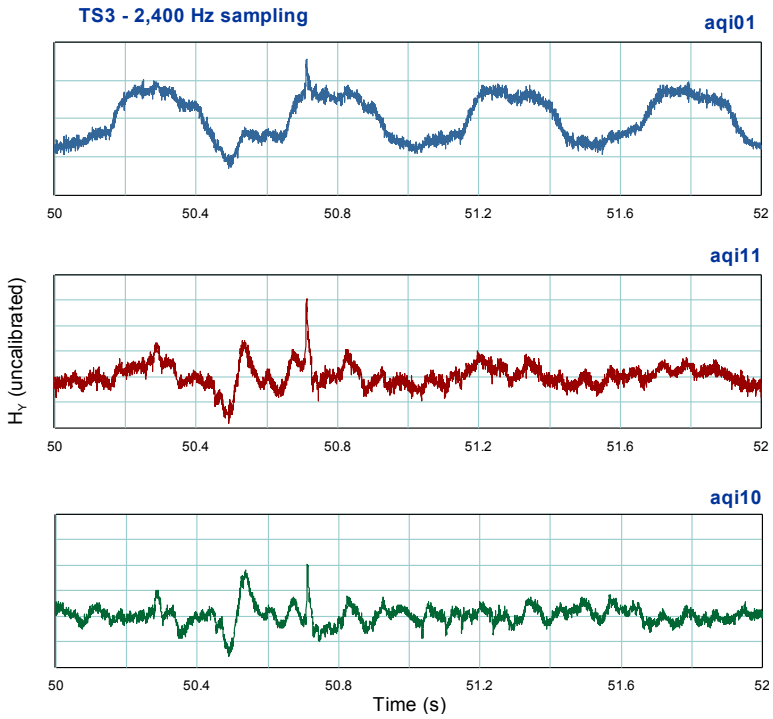

Figure 6.36: 2 Hz transmitter signal and harmonics are visible in H_yTS3 spectra at aqi01, aqi11, and aqi10 on November 7, 2015.

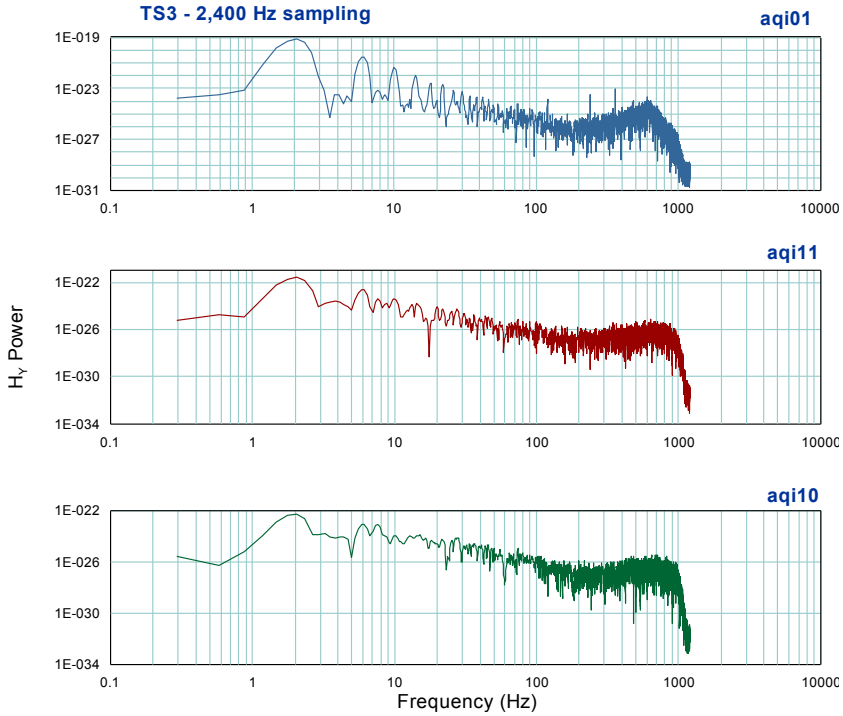

6.5 Discussion

The fully processed AMT-MT responses provide a number of insights into the resistivity structure, local noise conditions, and the feasibility of the proposed MT and CSEM methodologies at Aquistore.

6.5.1 MT responses

The processing of the 2013 data required unforeseen adaptations to deal with the limited number of useful magnetic recordings. Minor effects of noise in the preliminary responses were removed in the editing phase, and the final responses are generally smoothly varying functions of period. The resulting MT responses successfully define the geoelectric structure of the surficial sediment, the Williston Bain and underlying crust. Major inflections in the apparent resistivity curves represent the transitions from the near-surface response, to the Williston Basin response, to the Precambrian response. Final MT site responses from the 2014 dataset, though mostly reduced to long-period responses only by editing, demonstrate agreement with the earlier results. The MT responses determined for each site in the study area show strong spatial uniformity with only minor differences. In particular, the aqi01 response is consistently different from that at the other sites. The spatial similarity of the response and the expectation from the known geological constraints of a layered resistivity structure provide an initial indication that 1D inversion will be sufficient for defining a resistivity model for the Williston Basin rocks in the study area. Preliminary results from the 2015 field session also support this interpretation.

The responses at aqi01 are the exception to the general form of the response. For multidimensional part of the response in particular, the aqi01 apparent resistivities and phases deviate significantly from the typical response curves. As the MT site was completely

reinstalled at aqi01 during the 2014 field session, and both the 2013 and 2014 surveys show similar differences to the other sites, an incorrect layout of the field equipment cannot be the cause of this deviation. Considering the large scale of features resolvable in the long period MT data, and the close proximity of aqi01 to adjacent sites (e.g. aqi05) showing a different MT response, it is unlikely that the differences in the MT response at aqi01 are associated with a natural geological structure. The effect may be the result of distortion of responses near the CO_2 injection infrastructure, including the well and pipeline, which are situated within 100 m of the site. A study of the Hontomín sequestration site indicates that the distortion effect of a metallic well casing is insignificant (P. Queralt, E. Vilamajo, pers comm, 2016). Thus the observed distortion effects are more likely due to the pipeline or its combined effect with the well casing.

6.5.2 Noise impacts and source

Noise identified in 2014 dataset resulted in deletion of large sections of the MT responses. In the noisy bands, the estimates of the diagonal impedance components are biased upwards significantly. The larger off-diagonal components are not affected to the same degree. An attempt to conduct a strike or dimensionality analysis (see section 4.2.6) on this dataset will therefore be impacted by noise on the diagonal terms. Rotation of the coordinate system of the tensor is a means of minimizing, but not eliminating the noise effects. Many sites (e.g. aqi01, aqi08) have a coordinate system oriented approximately parallel to the local noise field (Figure 6.33). This favourable orientation has not prevented noisy signals from impacting the response estimation.

The stark difference in noise conditions between the 2013 and 2014 datasets suggests that the source of the two broadband signals may have been a new or temporary installation at the

Aquistore site. This is a plausible scenario as, at the time of the 2014 survey, the Aquistore and Boundary Dam locations were in a state of construction and maintenance in preparation for the initial CO_2 injections. It is also possible that a pre-existing, permanent source of noise was simply turned off during collection of the 2013 data. It is inferred from the high quality of the preliminary 2015 results that the noise source was absent confirming that the source is not in constant operation.

Polarization analysis indicates that the pipeline carrying CO_2 from the power station to the injection well is a probable source of the broadband EM noise. Anti-corrosion cathodic protection systems on pipelines and pipeline current mapping systems are potential sources of EM noise (Szarka, 1988; Junge, 1996, Ferguson, 2012). In cathodic protection systems the signal arises from pulses passed to the pipeline from a rectifier, typically at 10-50 A and 50V. However, geomagnetic disturbances can influence the amount current in the system by adjusting the potential between the pipeline and the soil, thus generating varied EM signals (Szarka, 1988). Pipeline current mapping systems measure the fields created by currents injected onto pipelines to detect pipeline location, imperfections in the pipeline or its insulating coating, and other features. The systems often inject both a low frequency (<10 Hz) signal to provide an approximately DC response and a higher frequency signal (~100 Hz) to provide an AC response (Varela *et al.* 2015). These frequencies lie within the two bands of noise observed in the 2014 data.

Junge (1996) reports that the signals related to the pipeline are inversely proportional to distance from the source in the near-field zone (low induction number), and are most evident in the vertical magnetic field. Since the majority of the Aquistore MT sites are within a comparable proximity to a single section of the pipeline and since the azimuth from the site to the nearest

section of pipeline varies from site to site (Figure 6.33), only a small number of sites are available to examine the decay of the noise with distance from the pipeline (Figure 6.37). The level of E_x noise at aqi12 is much higher than for any of the other sites examined causing a significant deviation from a monotonic linear decrease in noise levels with distance from the pipeline. This observation would not support the notion that the pipeline is generating the broadband signal.

However, if aqi12 were to be considered an outlier, the observed decay of the noisy signal in a straight line away from the pipeline would become approximately linear. Indeed the noisy signal at aqi12 is the highest observed in the entire 2014 dataset, and does not readily fit into a spatial pattern. Alternatively, the outlier may be the signal level at aqi01 – this site has already been shown to have a distinct MT response. The composite geometry of the pipeline segments is perhaps responsible for a more complex signal decay pattern.

Figure 6.37: Spatial decay of noisy broadband signal in Ex spectra with distance from aqi01 on November 11, 2014.

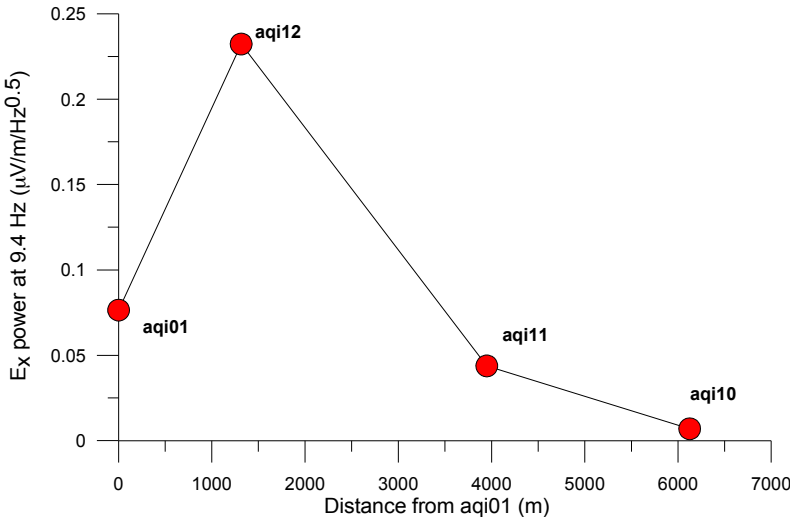

There have been a number of reported instances of powerful or intermittent EM signals from pipeline cathodic protection systems disrupting EM surveys. Ádám *et al.* (1986) describe a

low period (50-100 s) signal associated with a pipeline in Hungary. This signal was intermittent so as not to conflict with an electrified railway system. Oettinger *et al.* (2001) remark that the effects of cathodic protection are usually small, but that when maintenance tests are performed, very large voltages are applied to the pipeline resulting in a signal that was observed at distances greater than 10 km. In one example, the voltages responsible for this powerful signal were applied periodically for durations of 3s and switched off for 27 s.

Varela *et al.* (2015), describe methods for inspecting and testing a cathodic protection system. These include techniques that apply an AC signal to the pipeline, such as the alternating current voltage gradient method (ACVG). These examples show how significant pipeline noise may be temporary and related to site-specific factors, which is likely the case at Aquistore. Given that the noise was observed on five consecutive days during the 2014 survey, and not at all during the 2013 or 2015 surveys, it is most probable that very specific operations related to construction, installation or testing of new infrastructure are responsible for the unwanted signal.

From review of the coherence of all four horizontal field components, it is clear that the noise occurs on all horizontal electric and magnetic field components and is spatially correlated across the main survey area. For this reason, the robust, remote reference processing scheme was incapable of separating out the effects of the noise.

6.5.3 Noise mitigation

Should the EM noise at Aquistore prove to be recurring problem, it will be necessary to use acquisition and processing procedures to facilitate its removal. Oettinger *et al*. (2001) describe the signal-noise separation (SNS) and remote reference signal-noise separation (SNS-RR) methods as a means of overcoming the effects of correlated noise. Application of the SNS

method relies on the assumption of a noise-free remote site. This assumption is required so that a transfer function, known as the separation tensor, can be defined to relate the clean remote data to the noisy local data. The separation tensor allows for isolation of the correlated noise on magnetic field. By separating the correlated noise from the recorded data, noise-free impedance solutions may be formulated. Use of the remote site in this case does not prevent biasing of the solutions, therefore the SNS-RR approach requires a second remote reference site to generate unbiased estimates. As there are already two locations established as low-noise remote reference sites in the Aquistore area, the SNS-RR method would be a suitable noise mitigation strategy.

6.5.4 Summary

Despite the challenges encountered with respect to broadband EM noise, the MT method has capably produced background resistivity information for the Williston Basin. While the CSEM data recordings await processing and interpretation, early characterization of this data has indicated that the transmitter and receivers are operating as planned; multiple frequencies of transmitted signal are observable at inline locations and contribute a significant amount of spectral energy at distances of up to 9.5 km away from the dipole.

These pre-injection EM results are encouraging with regards to the applicability of the MT and CSEM methodologies to CO_2 sequestration monitoring at Aquistore. The acquisition configurations described in Chapter 5 to collect these data are therefore appropriate for the next phase of surface EM surveys at the site. As there is a possibility that the EM noise source affecting the 2014 response estimates could reoccur, it is recommended that both remote-reference sites aqi02 and aqi15 continue to be employed so that the SNS-RR noise reduction method could remain a processing option.

Chapter 7: Statistical analysis of spatiotemporal variations

7.1. Introduction

Long-term time-lapse monitoring of the injected CO_2 plume at Aquistore requires a consistent baseline of measurements from which changes of the response due to evolution of the storage complex may be isolated. The ability to make accurately repeated MT measurements over time depends on the extent to which a survey can be rerun in the field, and on the consistency of the determined responses in the presence of the local noise. It is therefore necessary to establish a measure of repeatability of the MT data in order to evaluate the feasibility of using EM monitoring techniques at the Aquistore site.

In addition to temporal variations in the MT responses, spatial variations are also of interest as part of a dimensionality analysis. In a 1D setting, the resistivity structure will produce identical MT soundings at different locations. Spatial uniformity of responses is therefore a requirement of 1D structure, but such uniformity does not guarantee this structure as some multidimensional features can have relatively uniform responses. Analyses that provide explicit measures of dimensionality include the phase tensor method (Caldwell *et al*., 2004), the Groom Bailey tensor decomposition method (Groom and Bailey, 1989) and the Waldim method (Martí *et al*., 2004). These methods make use of all four impedance tensor components. However, a spatial comparison of the impedances may be used as an initial test for one-dimensionality.

In this study, we divide the geological section into three depth ranges for which the dimensionality of the geoelectric structure is expected to be distinct. From the results in section 6.2, it is reasonable to expect 2D or 3D structures in the Quaternary, depending on the level of near-surface heterogeneity. However, if the lateral variations in this geological structure are

gradual, the geoelectric responses will be locally 1D. The geoelectric structure of the Williston Basin sedimentary sequence is presumed to be 1D, but this must be verified. At the depths of the Precambrian basement, 2D features are known to be present (Jones and Craven, 1990; Jones *et al.*, 2005; Gowan *et al*., 2009), but the corresponding MT responses may be relatively uniform at the scale of the Aquistore study area. A spatial comparison of MT responses will therefore provide an assessment of the dimensionality for each of these geologic domains.

In the following analysis, a method of quantitatively comparing sets of MT responses is defined to provide a measure for examining both survey repeatability and the spatial consistency of results. These calculations will be based on a normalized root mean square (RMS) misfit measure between the impedance responses in the 2013 and 2014 datasets.

7.2 Statistical comparison of MT impedances

The exercise of comparing impedance estimates from two different datasets or locations formally amounts to making a determination as to whether or not each of the sets of estimates are taken from the same statistical distribution. A common approach for such a test is to take the L_2 norm as a measure of misfit between the two sample populations, and to evaluate the significance of this misfit using a chi-squared test. The formal L_2 misfit between two datasets is:

$$X^2 = \sum_{i=1}^{N} \frac{\left|d_i^A - d_i^B\right|^2}{\sigma_i^2} \qquad (7.1)$$

where N is the number of data and σ^2 is the variance of each datum. For a statistically insignificant level of misfit, X^2 should be less than the mean of the chi-squared distribution, $E[\chi^2] = n$, for the appropriate number of degrees of freedom (Aster *et al*., 2005). Considering that X^2 will contain uncertainty, slightly larger misfit values can be defined for statistically indistinguishable data sets (Parker and Whaler, 1981):

$$X^2 < n + 2\sqrt{2n} \tag{7.2}$$

Changing the form of the normalization, an alternative measure of misfit is the RMS error:

$$E = \sqrt{\frac{1}{n}\sum_{i=1}^{N} \frac{\left|d_i^A - d_i^B\right|^2}{\sigma_i^2}} \tag{7.3}$$

which is deemed to be acceptable within the range:

$$E < 1 + \sqrt{2/n} \tag{7.4}$$

Since MT impedances are complex numbers, their comparison involves both the real and imaginary parts. These components are expected to have uncorrelated errors since the errors on the real and imaginary parts of two input transfer functions are independent (Bendat and Piersol, 1971). The comparison of the complex impedances therefore includes an independent comparison of the real and imaginary parts, doubling the degrees of freedom. Use of the L_2 norm as a comparison measure allows for simplification of the misfit calculation, as the misfit is characterized by a single real number.

The misfit calculation must be modified in the absence of reliable variance information. Because results from different impedance components may have different magnitudes, it is necessary to use an alternative normalization to ensure the terms contribute equitably to the misfit measure. One approach is to normalize the misfit by a fixed fraction of the magnitude of the data terms in order to approximate the data variance. This approach is equivalent to the relatively common procedure of using an error floor, such as 5% of the impedance magnitude, in MT inversions.

Comparison of pairs of MT responses is done on a frequency-by-frequency basis, and requires that both sets of impedance estimates have followed a reasonably consistent processing

and referencing scheme. The normalized RMS misfit between MT impedance responses *A* and *B* is given by:

$$E = \sqrt{\frac{1}{2\tau}\sum_{f=1}^{N}\sum_{i=1}^{2}\sum_{j=1}^{2}\frac{\left|Z(\omega_f)_{ij}^{A} - Z(\omega_f)_{ij}^{B}\right|^2}{\alpha^2\left|(Z(\omega_f)_{ij}^{A})(Z(\omega_f)_{ij}^{B})\right|}} \quad (7.5)$$

where $Z(\omega_f)_{ij}$ is the MT impedance data, N is the number of frequencies, and τ is the total number of terms in the summation (Nx2x2), multiplied by 2 to account for two degrees of freedom in the real and imaginary parts of the impedance. The normalization term includes the product of the two impedance terms rather than the variance. The α^2 factor is the proportional error on the data, which is used to approximate an appropriate variance estimate in the normalization term.

7.3. Misfit calculation

The application of a statistical comparison method to the datasets of the present study requires some extra consideration. As the variance estimates for these datasets are unreasonably low, on the order of 10^{-10}, the normalization of the misfit becomes important. These variance estimates and their associated standard deviations do not reflect the true error as observed in the variation between adjacent spectral estimates. The normalization type presented in equation 7.5, which is identified herein as **N1**, does not account for unequal signal/noise ratios on the individual impedance components. Two other normalization types that use only the off-diagonal tensor elements were also tested: (i) assuming the errors are coming dominantly from the electric field, the magnitude of the Z_{xy} term was used for normalizing both the Z_{xx} and Z_{xy} terms and the magnitude of the Z_{yx} term for normalizing both Z_{yx} and Z_{yy} (defined as **N2**), and (ii) for the case where the noise is assumed to be coming dominantly from the magnetic field (**N3**). For **N3** normalization, the Z_{yx} term was used for normalizing both the Z_{xx} and Z_{yx} terms and the

magnitude of the Z_{xy} term for normalizing both Z_{xy} and Z_{yy}. These alternative normalization types affect only diagonal impedance terms.

In the impedance comparison it is preferable to have a large number of impedance estimates at common periods between the two responses for the optimal calculation of the misfit. Unfortunately, due to extensive editing there is a limited amount of data available for the misfit calculations between some pairs of responses. However, in calculating the misfit for every possible pair of responses, the typical spatial and temporal variations are quantifiable at most of the available periods of response estimation.

All of the impedance calculations were executed using MATLAB (see Appendix C) and based on *.dmp* files exported from GEOTOOLS MT processing software. In addition to the cumulative RMS values, the misfits were also examined as a function of frequency.

7.4. Temporal analysis

7.4.1 Results – 2013 vs 2014 datasets

The data considered for this study are the final impedance responses from sites aqi01, aqi03, aqi04, aqi05, aqi06, aqi08, and aqi09. As the MT and AMT-processed responses could not be combined for the 2013 survey, each of these 2013 datasets is compared to the 2014 responses separately. Due to the high degree of response removal in the 0.1 to 10 s period range from the 2014 dataset, the comparison of responses is restricted mainly to the highest and lowest period bands. Depending on the particular site and the degree of editing, the remaining data may not cover the response of primary interest at Aquistore (that of the storage complex for CO_2) but it does allow an assessment of response repeatability nonetheless. In the initial calculations, the α^2 factor was set to equal 1. Subsequent calculations used a range of α^2 values to estimate error

floors. Comparisons of the temporal repeatability of the responses at sites aqi04 and aqi08 will be examined below. These are two sites for which there are a relatively high number of data points to compare in the calculation, particularly for the AMT-processed responses.

The response comparison for aqi04 is shown in Figure 7.1. It is immediately apparent that the data editing for of the 2014 response has restricted the common period data between the two surveys. For this site, there are two bands within which the data can be compared: 0.0001 to 0.04 s and 10 to 2,000 s. This section of the response does not give an indication of the consistency of the lower Williston Basin response estimation, but it does provide a measure of the repeatability of the general fieldwork and response estimation techniques. It is also clear that the off-diagonal terms, Z_{xy} and Z_{yx}, exhibit a high level of agreement between the two surveys. In contrast, the diagonal impedance terms show less agreement and contain a higher level of noise.

Figure 7.1: Comparison of impedance magnitude data at aqi04 from 2013 and 2014 surveys. Clockwise from top-left: Zxx, Zxy, Zyx, Zyy.

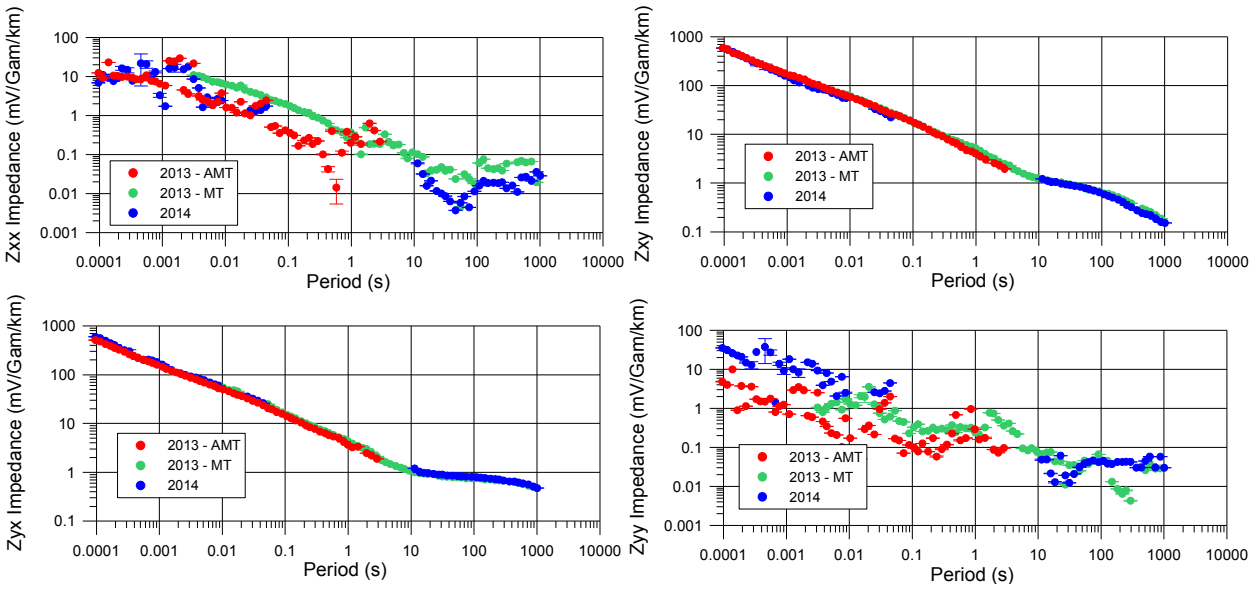

The results of the repeatability calculations using the AMT-processed 2013 data for aqi04 are shown in Figure 7.2. In the **N1** calculation, repeatability of the Z_{xy} and Z_{yx} data appears relatively high, as determined by low errors (mostly < 0.03 or 3%), but the diagonal terms have significantly larger errors (> 1 or 100%). The 2014 Z_{yy} AMT data appears to be biased upwards by about a decade from the 2013 magnitudes. This effect dominates the total **N1** RMS misfit value which is 2.099. However, the diagonal impedance terms are smaller than the off-diagonal terms by a factor of ~10, and for a 1D structure, are not representative of the subsurface geoelectric response. To counteract the dominance of Z_{xx} and Z_{yy} misfits, the **N2** and **N3** calculations normalize the misfit by electric and magnetic noise effects to emphasize the repeatability of the 1D part of the response. The **N2** and **N3** calculations are nearly identical. These alternative normalizations provide improved misfit estimates with cumulative RMS values over all periods of 12% each, but there is still a significant contribution from the diagonal terms. For each of these alternative types of misfit normalization, there does not appear to be any clear frequency dependence of the misfit, nor is there a consistent difference between the misfits of the separate impedance components.

Figure 7.2: RMS N1 (left) and N2 (right) errors for all four impedance terms at aqi04 – 2013 AMT data vs. 2014 data. The sum of the four errors terms is shown by the grey bars as an RMS misfit. RMSN1: 2.099 RMSN2: 0.120.

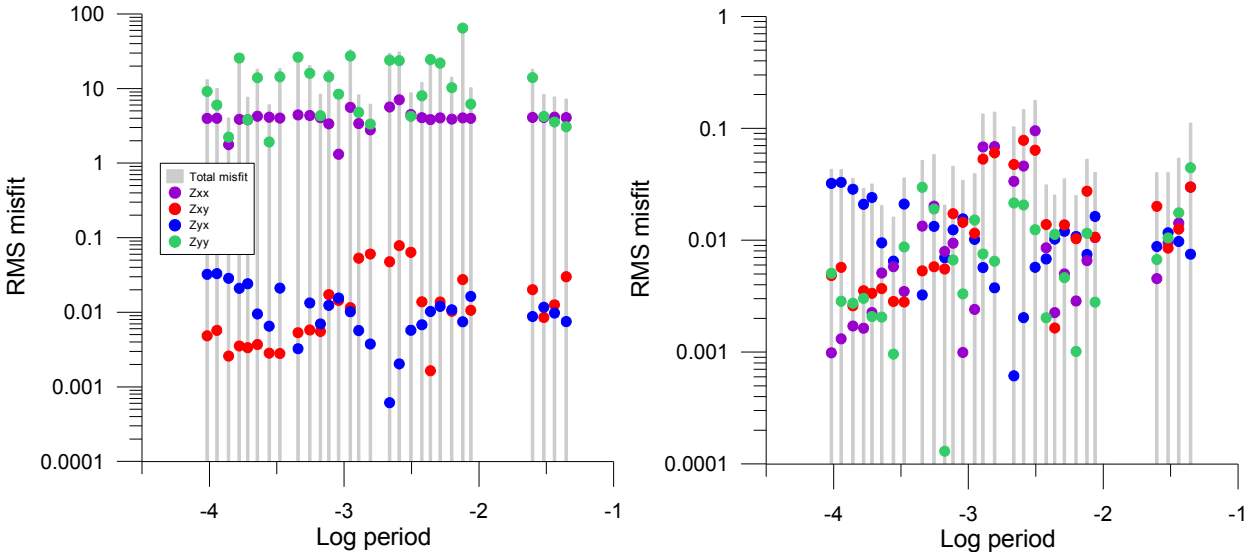

Using the MT-processed 2013 responses, we can compare the datasets at longer periods, in the 10 to 2000 s period range (Figure 7.3). The diagonal terms again lead to high misfits for the **N1** calculation. The improved misfit that results when the **N2** and **N3** measures are used does not show any systematic variation with period. The total misfit values are 0.104 (10.4%) for **N2** and 0.103 (10.3%) for **N3**, higher than desirable for survey repeatability. However, most of the contributions to this higher misfit still come from the diagonal terms and the long period Z_{xy} data. The 1D part of the response at periods shorter than 100 s has errors for individual periods in the 2-3% range, which is much more favourable. The higher misfits observed at longer periods may be due to the increased effects of noise. These misfits arise from the Z_{xy} term which has very low magnitude at long periods (associated with the conductive response of the NACP conductor). Normalization of the misfit using this small term will produce large normalized misfit values.

Figure 7.3: RMS N1 (left) and N2 (right) misfit for all four impedance terms at aqi04 – 2013 MT data vs. 2014 data. RMSN1: 1.259, RMSN2: 0.104.

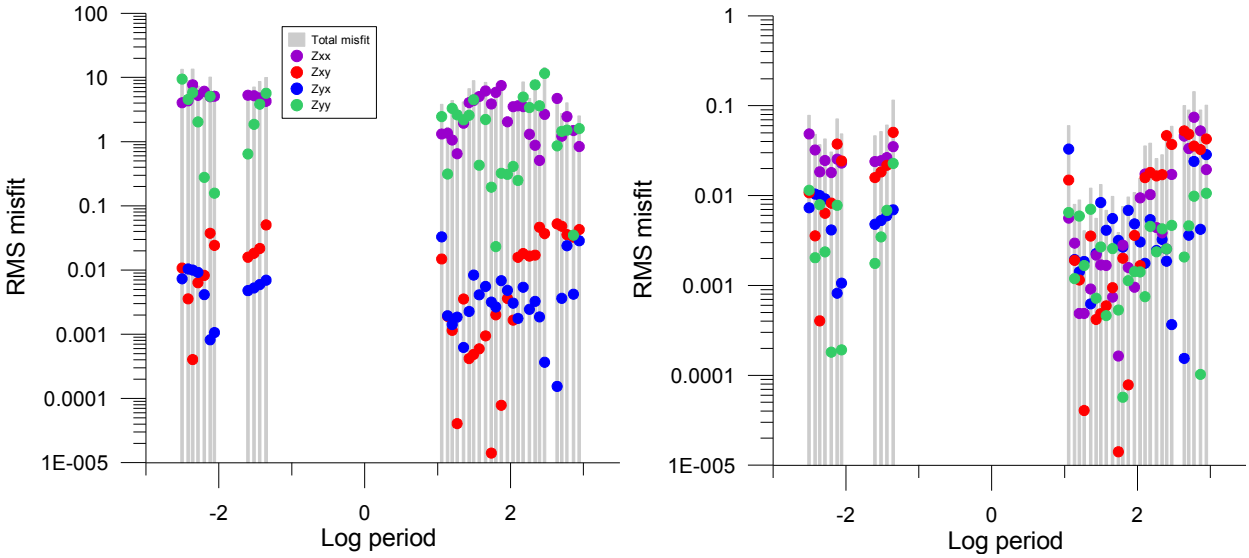

As observed for the aqi04 results, the aqi08 off-diagonal impedance components for the 2013 and 2014 surveys appear almost identical for all of the calculated response periods (Figure 7.4). For the short period range in which the 2013 remote referenced responses were compared to those from 2014, the highest misfit is attributed to the Z_{xx} term, for which both of the datasets are noisy. This result is reflected in the **N1** misfit calculation (Figure 7.5). For the subsequent **N2** and **N3** calculations, the misfits are significantly lower, but generally are still highest for the Z_{xx} term. The misfit on the Z_{xx} and Z_{xy} terms increases within, and adjacent to, the band of noise previously identified in section 6.3.4.

Figure 7.4: Comparison of impedance magnitude data at aqi08 from 2013 and 2014 surveys. Clockwise from top-left: Zxx, Zxy, Zyx, Zyy.

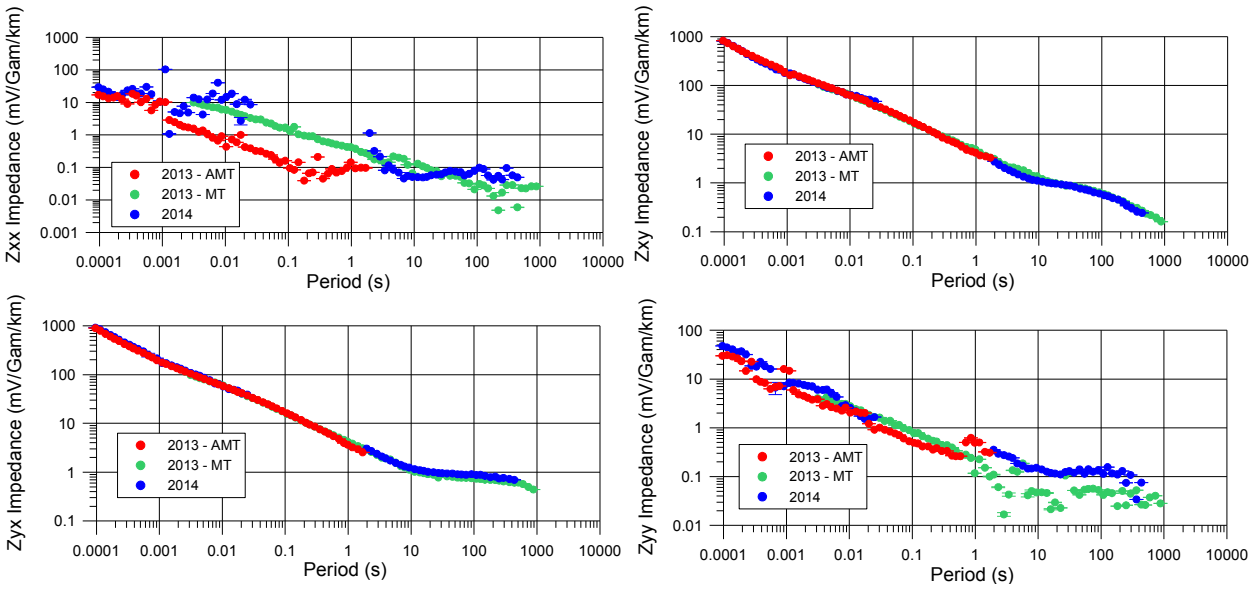

Figure 7.5: RMS N1 (left) and N2 (right) misfit for all four impedance terms at aqi08 – 2013 AMT data vs. 2014 data. RMSN1: 1.613, RMSN2: 0.124.

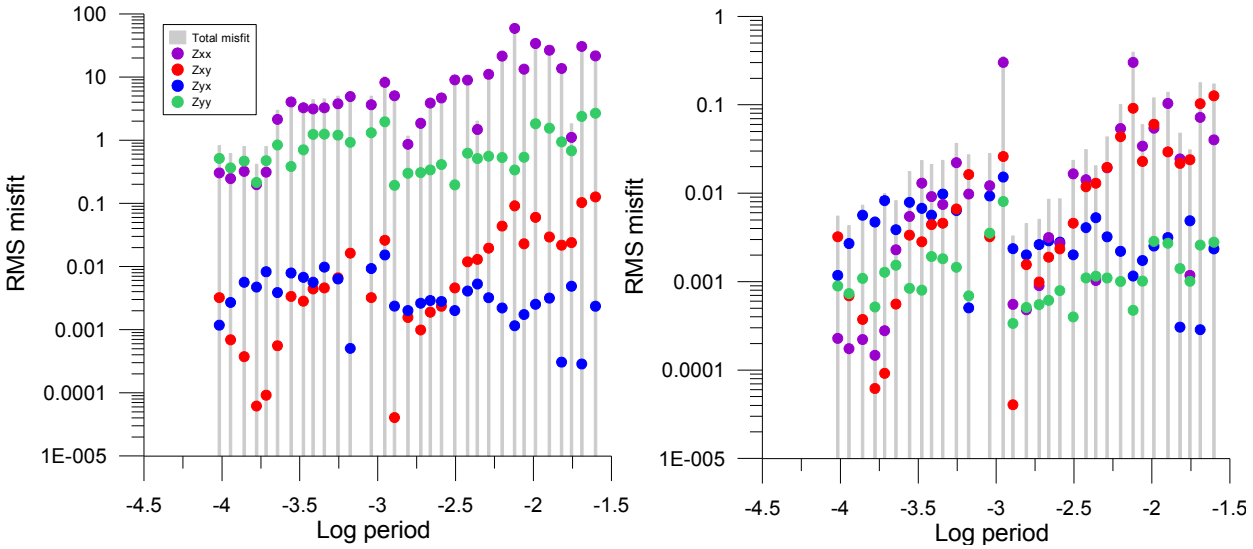

The aqi08 results are similar in the longer period range (Figure 7.6). An outlier in the 2014 Z_{xx} impedance at ~1.5 s, adjacent to the noisy band, is associated with a large error that dominates the total misfit. The misfit is larger around the 0.01 s period, indicating that broadband noise is the primary factor affecting the overall repeatability. In the parts of the

response away from the broadband noise the off-diagonal terms generally have satisfactory misfits (1-3%).

Figure 7.6: RMS N1 (left) and N2 (right) misfit for all four impedance terms at aqi08: 2013 MT data vs. 2014 data. RMSN1: 1.424, RMSN2: 0.488.

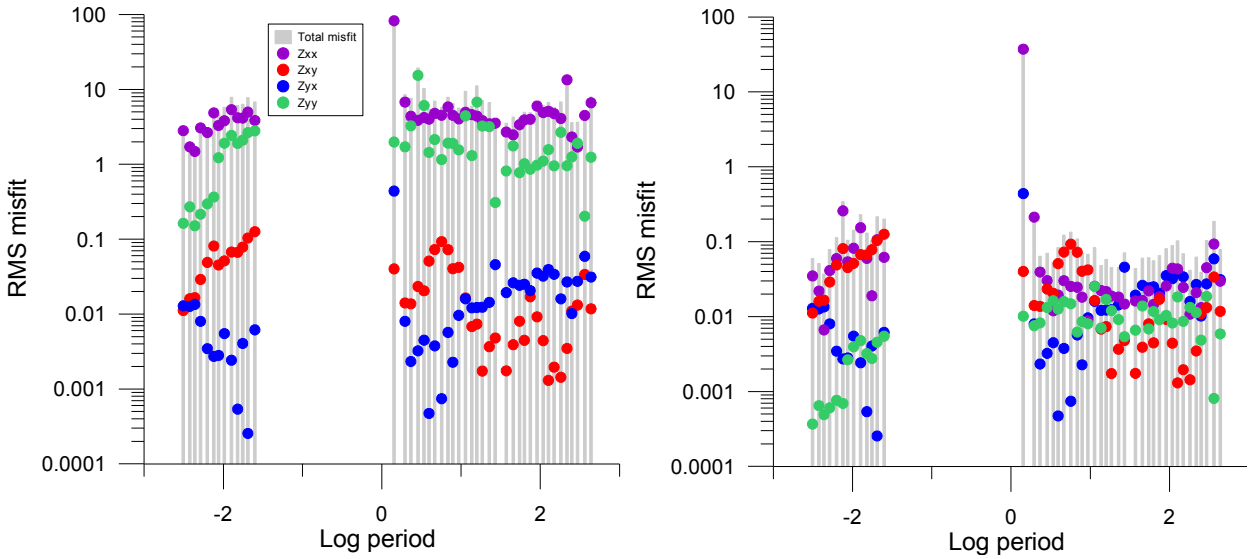

7.4.2 Summary

The impedance comparison method described here has been shown to be valuable for two purposes. The first purpose is as a noise identification tool. As shown above, the method was able to identify a noisy response in the aqi08 data. The second purpose is for statistical comparison of different MT data sets. A limiting factor in the computation of misfit values between 2013 and 2014 MT data was the small number of common frequencies available after the editing of the responses. The 0.1 to 10 s period band of the 2014 data has been consistently removed. In short, the presence of broadband noise in the 2014 survey has meant that the 2013 MT responses were not repeatable in the following year. However, by examining the misfit outside of the noise bands, an assessment of the repeatability of the 1D response was still possible.

Both visual inspection of the impedance responses and quantitative calculations indicate that the off-diagonal impedance terms were relatively consistent from survey to survey. The impedance magnitudes are similar and static shift therefore does not appear to be an issue; a static shift would result in a significant minimum misfit at all frequencies, which is not observed.

The results of the misfit calculations for all of the sites are summarized in Tables 7.1 and 7.2. Overall, the misfit values are high, consistently between 10-20% for the **N2** and **N3** normalizations. For every site, the misfits are highest for the **N1** normalization indicating the presence of large relative errors on the diagonal impedance terms. These errors persist when the **N2** and **N3** normalizations are applied, but are significantly reduced. Differences in the results between **N2** and **N3** are minimal both in terms of the cumulative RMS, and the distribution of the misfit among the separate impedance terms. The misfit values would improve considerably if normalization excluded the diagonal impedance terms. Such an approach would be preferable for future Aquistore studies if the broadband EM noise is present.

In summary, the total RMS values do not indicate strong response repeatability between the 2013 and 2104 surveys. However, away from the identified noise bands the off-diagonal components yield typical differences of 1-3% between the two surveys.

Table 7.1: Summary of RMS calculations - 2013 MT against 2014.

	aqi01	aqi03	aqi04	aqi05	aqi06	aqi08	aqi09
RMS-N1	0.737	1.377	1.259	1.084	0.975	1.424	1.570
RMS-N2	0.155	0.099	0.104	0.090	0.117	0.488	0.162
RMS-N3	0.162	0.103	0.103	0.089	0.109	0.519	0.160
Data points	28	21	36	27	27	45	30

Table 7.2: Summary of RMS calculations - 2013 AMT against 2014.

	aqi03	aqi04	aqi05	aqi06	aqi08	aqi09
RMS-N1	1.509	2.099	1.366	1.052	1.613	1.441
RMS-N2	0.199	0.120	0.113	0.128	0.124	0.169
RMS-N3	0.198	0.120	0.113	0.129	0.127	0.178
Data points	7	29	6	6	32	23

It is also possible to calculate the error floors for which the observed misfit between the 2013 and 2014 datasets is statistically insignificant. This calculation was done for the AMT responses using the sites for which the **N2** 2013 vs. 2014 calculations have a satisfactory number of overlapping data points (Table 7.3). In general, the error floor calculations were not affected by the longer period AMT responses due to the high level of data editing in this band. These additional calculations used the weighting factor α^2 in equation 7.5 to the scale the value of the denominator in the **N2** normalization to some fraction of its original value. The value of the weighting factor is determined assuming the threshold of statistical significance of the RMS response is 1 (e.g. equation 7.4). The results suggest that for ~12% errors on the impedances, the data from the two surveys would not statistically different. Based on standard propagation of error methods the impedance error is related to the apparent resistivity error and phase error by:

$$\Delta\rho_a = 2\Delta Z \tag{7.6}$$

$$\Delta\varphi = \sin^{-1}(\Delta Z) \tag{7.7}$$

Using these equations, the error floor result corresponds to a phase error of 7˚ and an apparent resistivity error of 24% or 0.106 decades. Such high errors are a definitive indication of poor overall repeatability of the two surveys. However, these results are based on the full AMT data sets. If the calculations were restricted to only off-diagonal impedance responses away from the broadband EM noise, much smaller impedance error floors would have resulted.

Table 7.3: Error floor calculations – N2.

	aqi04	aqi08	aqi09
RMS - 15%	0.798	0.825	1.129
RMS - 12%	0.997	1.031	1.411
RMS - 9%	1.330	1.375	1.882
RMS - 6%	1.994	2.062	2.822
RMS - 3%	3.989	4.125	5.645

7.5. Spatial analysis

7.5.1 Results

From the final Aquistore MT results across the survey area (see Figures 6.15-6.17), the responses have been characterized as spatially uniform and dominantly 1D. The spatial uniformity of the responses will now be assessed quantitatively. The spatial analysis compares the response at pairs of sites for both the MT- and AMT-processed components of the 2013 data and for combined MT-AMT 2014 responses. Based on the results of the repeatability analysis, the calculations were restricted to the **N2** normalization in order to appropriately balance the contribution of the diagonal terms and limit the number of calculations. The spatial variations between pairs of sites in the main survey area are expected to be less than for the remote reference sites. The 2014 impedances from remote sites aqi02 and aqi15 are therefore included in the examination of the results given below as a test of more laterally variable earth responses.

Figure 7.7 compares the impedance estimates from aqi02 and aqi10. The similarities in the data editing patterns for the two 2014 responses are clear. In the two overlapping period ranges of the responses, the Z_{xy} and Z_{yx} curves are almost identical for the two sites. The main differences in the responses are for the noisier Z_{xx} and Z_{yy} curves.

Figure 7.7: Comparison of impedance magnitude data at aqi02 and aqi10 from the 2014 survey. Clockwise from top-left: Zxx, Zxy, Zyx, Zyy.

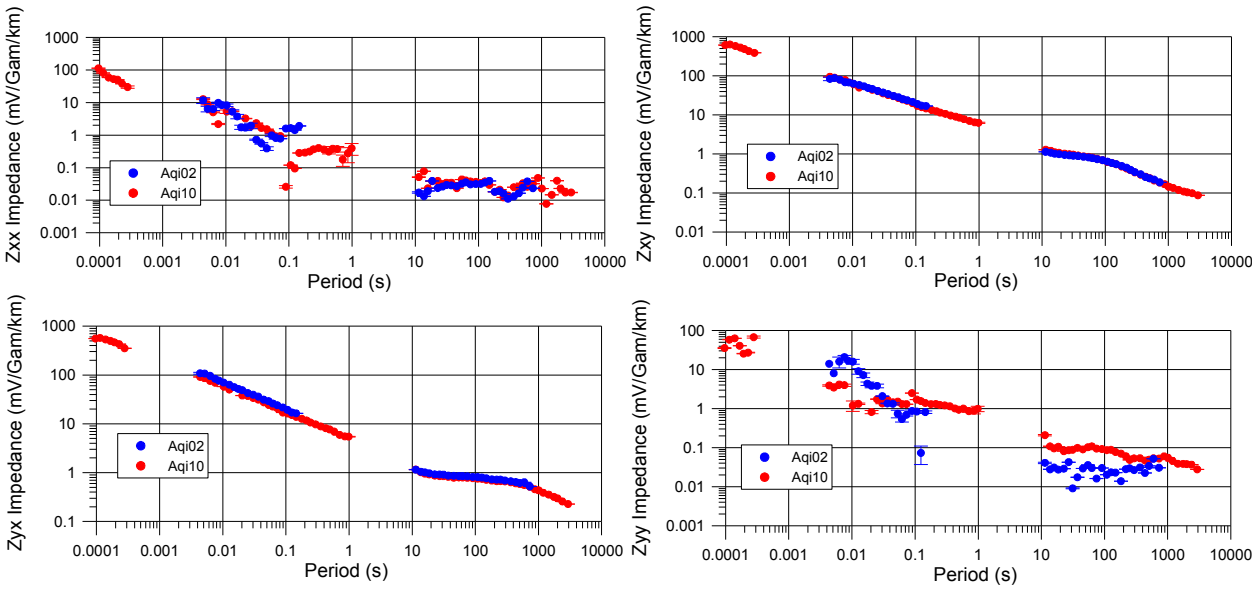

In the misfit calculations, the total **N2** RMS misfit between sites aqi02 and aqi10 is 0.108 (Figure 7.8). The lowest misfit values are for the longest periods. This result is explained by the longer wavelength responses of deeper structures (e.g. the TOBE conductor) affecting the MT response in a similar way over large distances. Greater lateral variations in the surficial geology are more likely to produce larger differences in the MT response at shorter periods. There is indeed an increased variation for periods less than 0.1 s, with the Z_{yx} values around 5%. While the comparison for these two sites did not allow for calculations of misfit values in the 10^{-3} to 10^{-4} s period band, the misfit does appear to be increasing towards shorter periods. Noise effects are once again observed in the form of increased misfit adjacent to the edited band.

Figure 7.8: RMS N2 misfit for all four impedance terms between sites aqi02 and aqi10, 2014 data. RMSN2: 0.108.

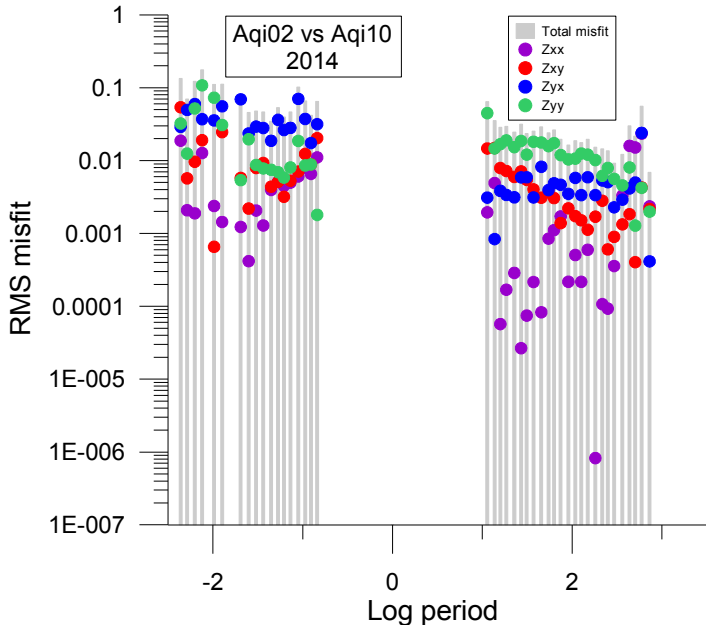

Figure 7.9 shows the comparison of 2014 responses from sites aqi03 and aqi08, two sites in close proximity in the main survey area. There are more significant shorter-period differences than for the previous example. The off-diagonal impedance terms produce much higher misfits (by approximately a factor of 10) at shorter periods than for long periods. These differences are interpreted to be caused by variations in the surficial geology and are an example of a relatively thin geologic unit having a large effect on the spatial variation of the geoelectric responses.

Figure 7.9: RMS N2 misfit for all four impedance terms between sites aqi03 and aqi08, 2014 data. RMSN2: 0.145.

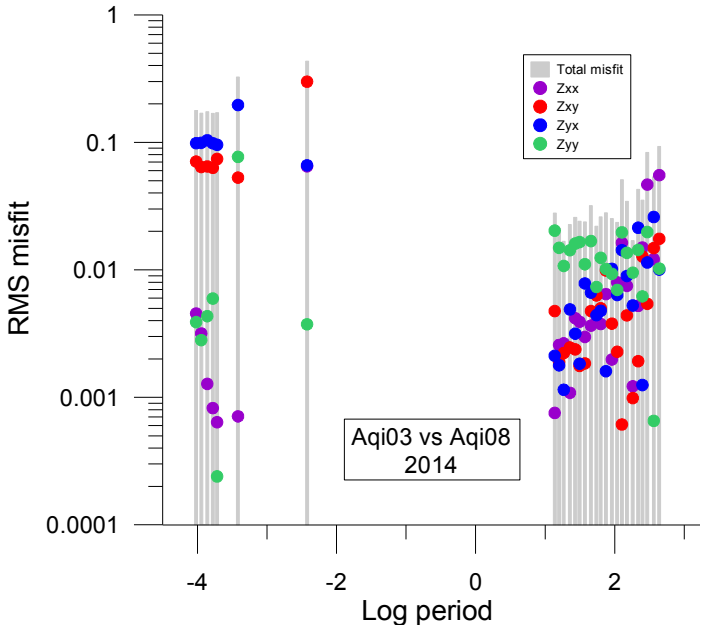

The most extreme difference in spatial location in the 2013 and 2015 datasets is between sites aqi02 and aqi15, a distance of 36.8 km. The total misfit between these two sites is 0.112 or 11.2%. The Z_{xy} term at periods greater than 100 s has the highest misfit values (~0.1) (Figure 7.10). The result shows that the effects of the NACP are of the order of 40 km in spatial scale; the aqi15 site is closer to the edge of the conductive body. At shorter periods, the errors on the off-diagonal terms are mostly less than 2%.

Figure 7.10: RMS N2 misfit for all four impedance terms between sites aqi02 and aqi15, 2014 data. RMSN2: 0.112.

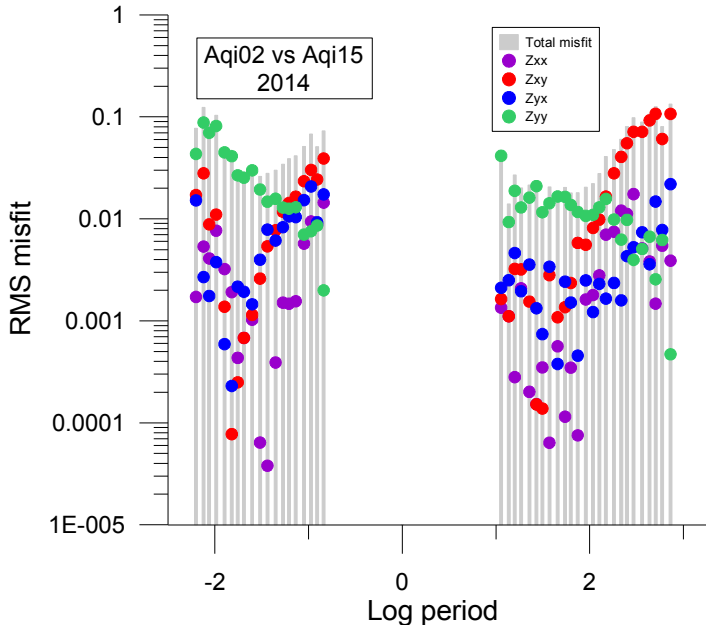

A spatial comparison of data in the 0.1 to 10 s band can only be done using the 2013 MT data. The MT soundings in this period range will give a better indication of the spatial uniformity of responses corresponding to the Phanerozoic sedimentary sequence. Some noise was observed in this band for the 2013 responses (see section 6.1.2), but not nearly to the same extent as for 2014. Comparing the aqi05 and aqi09 responses (Figure 7.11) indicates that the misfits for the off-diagonal terms are significantly higher from 0.1 to 10 s than for the longer period section of the responses. However, these misfits are mostly at a level of 1-2%, indicating a high level of uniformity in the responses despite the presence of some noise.

Figure 7.11: RMS N2 misfit for all four impedance terms between sites aqi05 and aqi09, 2013 data. RMSN2: 0.109.

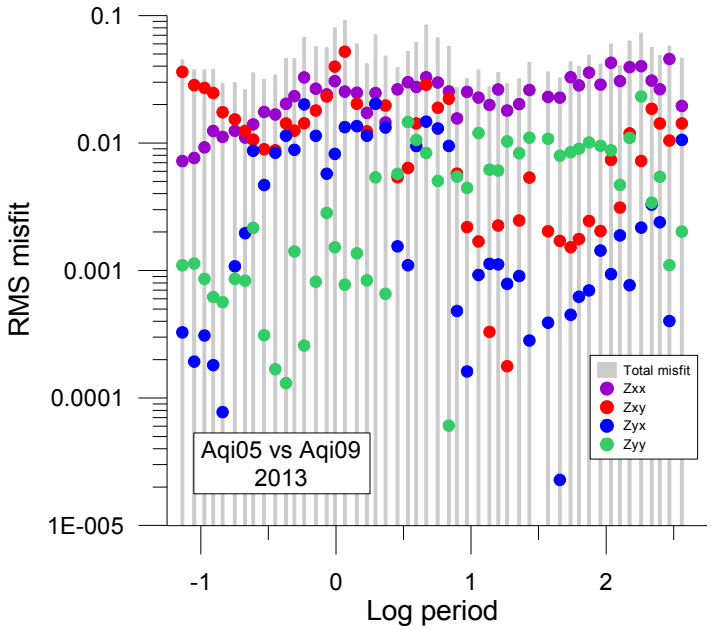

7.5.2 Summary

A summary of the results of N2 misfit calculations for all pairs of sites is provided in Tables 7.4, 7.5, and 7.6. For all sites and both surveys, the total misfit values fall consistently between 0.1 and 0.2. The misfit for each site pair tends to be more representative of noise conditions and the variations in the near-surface sediments than it is of variations in the part of the response related to the Williston Basin rocks. This result is reflected by the systematically lower total misfit values for the 2013 MT responses compared to the 2013 AMT or 2014 equivalents. Misfits are unusually high for aqi01 in the 2014 survey and aqi07 in the 2013 survey. The high aqi01 misfit is an expected result, as the responses at this site have been shown to differ from the other responses (see section 6.2). The aqi07 response in 2013 was also shown to differ from the response at other sites. This site was also particularly noisy, and was abandoned following the 2013 campaign. Due to the misfit associated with the surficial geology

and noise, the effect of intersite distance on the misfit is not clear; misfits associated with the remote sites are not necessarily greater than those for pairs of sites in the main survey area.

Table 7.4: 2013 MT RMS misfit results.

	aqi03	aqi04	aqi05	aqi06	aqi07	aqi08	aqi09
aqi03		0.117	0.071	0.101	0.224	0.107	0.138
aqi04	0.117		0.096	0.135	0.173	0.079	0.105
aqi05	0.071	0.096		0.092	0.195	0.084	0.109
aqi06	0.101	0.135	0.092		0.207	0.111	0.105
aqi07	0.224	0.173	0.195	0.207		0.194	0.170
aqi08	0.107	0.079	0.084	0.111	0.194		0.083
aqi09	0.138	0.105	0.109	0.105	0.170	0.083	

Table 7.5: 2013 AMT RMS misfit results.

	aqi01	aqi03	aqi04	aqi05	aqi06	aqi07	aqi08	aqi09
aqi01		0.190	0.202	0.175	0.186	0.309	0.194	0.135
aqi03	0.190		0.125	0.166	0.173	0.300	0.206	0.157
aqi04	0.202	0.125		0.116	0.125	0.210	0.161	0.134
aqi05	0.175	0.166	0.116		0.098	0.209	0.160	0.121
aqi06	0.186	0.173	0.125	0.098		0.184	0.123	0.143
aqi07	0.309	0.300	0.210	0.209	0.184		0.166	0.256
aqi08	0.194	0.206	0.161	0.160	0.123	0.166		0.227
aqi09	0.135	0.157	0.134	0.121	0.143	0.256	0.227	

Table 7.6: 2014 RMS misfit results.

	aqi01	aqi02	aqi03	aqi04	aqi05	aqi06	aqi08	aqi09	aqi10	aqi11	aqi12	aqi14	aqi15
aqi01		0.306	0.282	0.313	0.294	0.368	0.307	0.256	0.316	0.325	0.317	0.281	0.300
aqi02	0.306		0.059	0.128	0.105	0.118	0.176	0.185	0.108	0.134	0.097	0.155	0.112
aqi03	0.282	0.059		0.093	0.139	0.127	0.145	0.141	0.110	0.166	0.155	0.151	0.101
aqi04	0.314	0.128	0.093		0.105	0.120	0.184	0.100	0.113	0.218	0.246	0.145	0.140
aqi05	0.294	0.105	0.139	0.105		0.177	0.190	0.115	0.124	0.127	0.188	0.186	0.139
aqi06	0.368	0.118	0.127	0.120	0.177		0.125	0.161	0.174	0.156	0.139	0.143	0.174
aqi08	0.307	0.176	0.145	0.184	0.190	0.125		0.194	0.164	0.207	0.166	0.169	0.155
aqi09	0.256	0.185	0.141	0.100	0.115	0.161	0.194		0.151	0.193	0.197	0.188	0.156
aqi10	0.316	0.108	0.110	0.113	0.124	0.174	0.164	0.151		0.122	0.128	0.184	0.117
aqi11	0.325	0.134	0.166	0.218	0.127	0.156	0.207	0.193	0.122		0.171	0.192	0.142
aqi12	0.317	0.097	0.155	0.246	0.188	0.139	0.166	0.197	0.128	0.171		0.150	0.101
aqi14	0.281	0.155	0.151	0.145	0.186	0.143	0.169	0.188	0.184	0.192	0.150		0.166
aqi15	0.300	0.112	0.101	0.140	0.139	0.174	0.155	0.156	0.117	0.142	0.101	0.166	

Contour maps of the total **N2** misfit results are shown in Figure 7.12 and 7.13. These maps were generated in Surfer 11 software using a kriging gridding method. It is apparent that the misfit results are lower for the MT-processed 2013 responses than for the AMT-processed responses providing an indication that the RMS calculations are a reflection of the lateral changes in the geoelectric structure. The results do not indicate any consistent large-scale patterns that are reflective of spatial variations (Figures 7.12-7.13). However, there are groups of closely spaced sites that tend to show similar responses, e.g., aqi07 and aqi13 and aqi01 and aqi05.

Figure 7.12: Contoured spatial patterns of total misfit values for 2013 AMT data. Contour interval = 0.02.

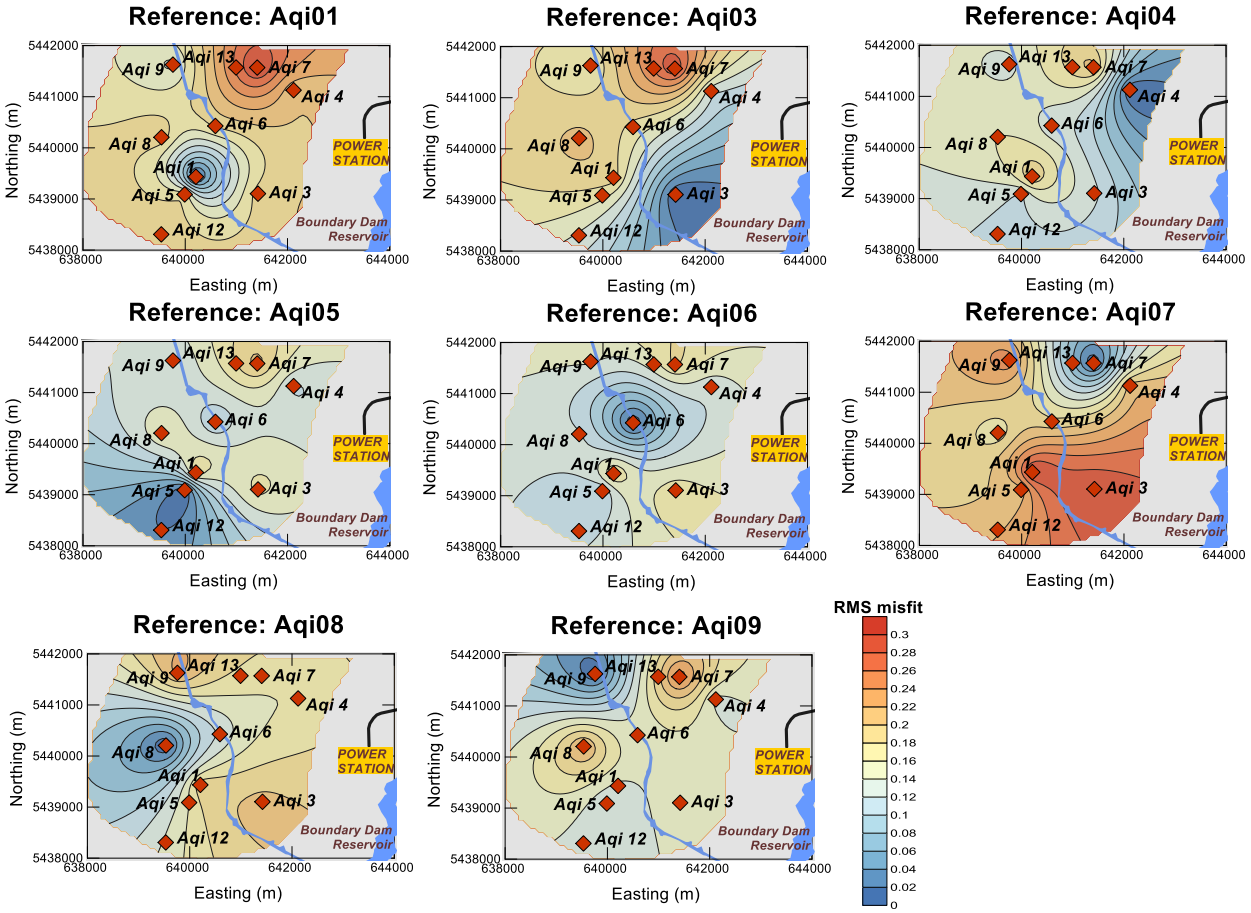

Figure 7.13: Contoured spatial patterns of total misfit values for 2013 MT data. Contour interval = 0.02.

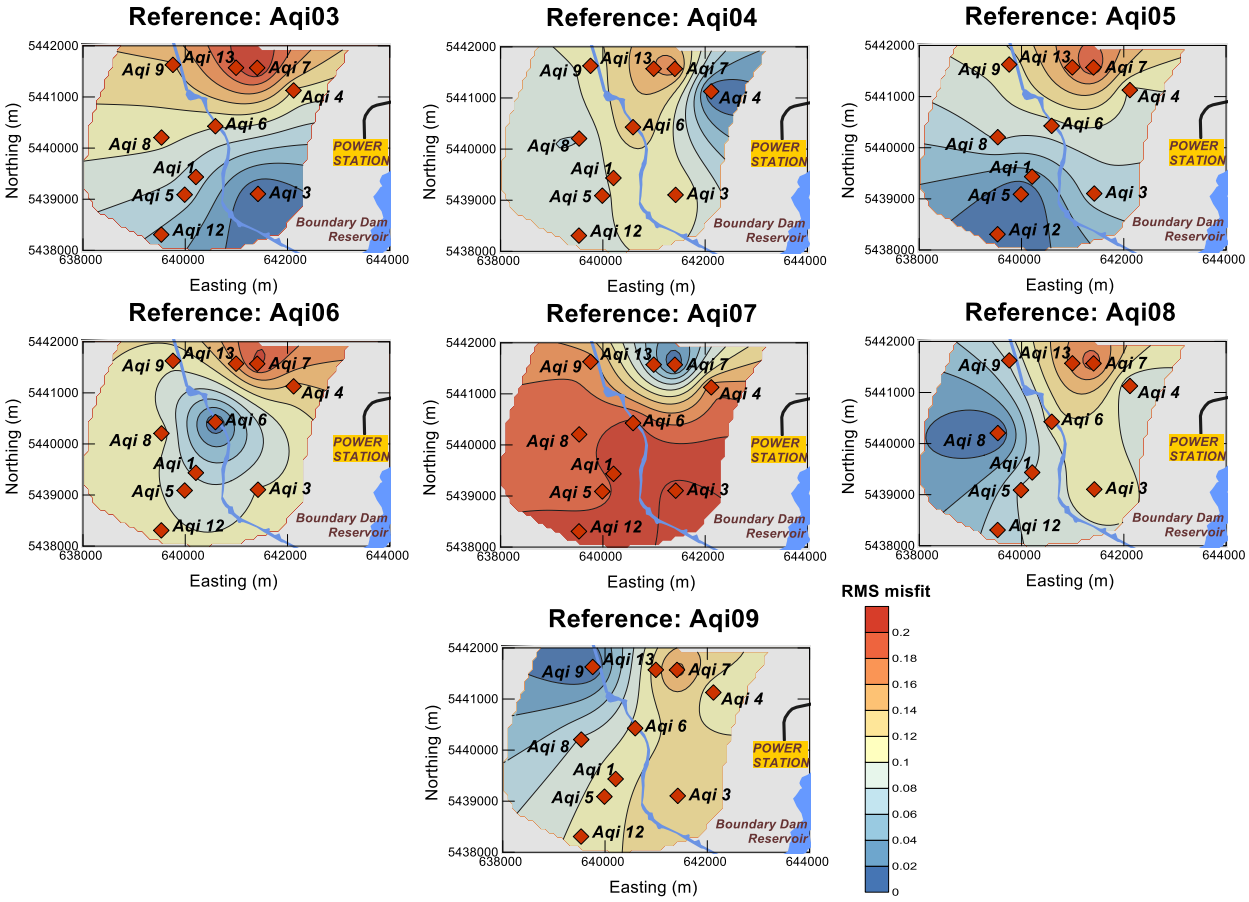

An estimate of the error floor for which the response at pairs of sites become statistically insignificant was made using five examples, chosen for the high number data points contributing to the final RMS number (Table 7.7). The methodology for determining the error floor is the same as is described in section 7.4.2. The results indicate that most of the sites in the study are statistically indistinguishable at error floors of 12-15%. However, there is a disproportionately large error contribution from near-surface materials and noise effects. Based on these results, the MT response of the Williston Basin rocks within the study area is characterized as spatially uniform.

Table 7.7: Error floor calculations – N2.

	aqi02 vs. aqi15	aqi06 vs. aqi12	aqi04 vs. aqi09	aqi14 vs. aqi15	aqi04 vs. aqi08
RMS - 15%	0.747	0.925	0.669	1.109	1.224
RMS - 12%	0.934	1.157	0.836	1.387	1.530
RMS - 9%	1.245	1.542	1.115	1.849	2.041
RMS - 6%	1.867	2.313	1.672	2.773	3.061
RMS - 3%	3.735	4.626	3.345	5.546	6.122
Data Points	44	35	32	28	47

Chapter 8: MT Inversions and Modeling

8.1 Overview

The MT data obtained in the Aquistore project can be used, with additional constraints from borehole data, to determine a reference pre-injection resistivity model for the Williston Basin rocks in the study area. This reference model will provide a basis for time-lapse comparison with post injection models. The definition of a high quality pre-injection model is thus a crucial step in the sub-surface CO_2 monitoring.

Borehole resistivity data represents *a priori* information on the subsurface electrical properties at Aquistore. While this data is valuable, it cannot serve to characterize the site on its own. For example, electrical resistivity may be partially scale-dependent (Jones, 1995) with measurements at increasingly small-scale being increasingly more resistive. Such responses may arise from fracture networks (Jones, 1995). Thus, the borehole resistivity log may not be fully representative of the larger-scale resistivity structure. In addition, the borehole resistivity log results may be affected by fluid invasion into the surrounding sedimentary formations and other borehole effects. However, the combined use of the borehole resistivity log and the surface MT response will result in a superior model of the site-scale resistivity structure. The borehole log provides critical information on small-scale vertical variations in resistivity. Thus the inversion of the MT responses, using the borehole measurements as constraints, will be more successful in defining a resistivity model for the Willison Basin rocks in the study area. The results in Chapter 7 indicate that there is a high level of spatial uniformity in the MT responses corresponding to the Williston Basin rocks, and therefore little justification for a 2D inversion. Thus the approach to the MT inversions will focus on defining a 1D model that is representative of the sedimentary layering across the Aquistore site.

In typical 1D inversions, an arithmetic or geometric average of the *xy* and *yx* MT responses would be inverted. However, in this project, the *xy* and *yx* mode responses will be inverted separately. Any differences between the two types of responses, and the 1D models used to explain them, could indicate electrical anisotropy of basin strata.

The chapter will continue with a description of the mathematical formulation of the optimization procedure. The inputs to the inversion are then specified. The main results are presented in terms of progressively refined inversions, first for the *yx* data and then for the *xy* data. Additional 1D modeling focussing on the near-surface data and theoretical CO_2 injections is then presented to complement the inversion results.

8.2 1D inversion

8.2.1 Formulation of the constrained non-linear inverse problem

The starting model for the Aquistore inversions, constructed from the borehole resistivity data, is expected to be close to the true model. As such, it is desirable to carry out the inversion in a manner that minimizes the departures from the starting model in addition to the misfit between predicted and observed data. This objective requires that the inverse problem be formulated with added constraints from the reference model.

Aster *et al*. (2005) present an explicit regularization formulation of a general optimization problem. The basic objective function we wish to minimize is the data misfit. For a non-linear inversion, this function is commonly presented as an L_2 norm, written as:

$$\phi_D = \|\mathbf{W}_D(\mathbf{d} - \mathbf{A}(\mathbf{m}))\|^2 \qquad (8.1)$$

where **d** is the data, **m** is the model, and $\mathbf{W}_D$ is the data weighting matrix. The **A**(**m**) term represents the forward predicted data. Following linearization of the solution, **A** is approximated

by the Jacobian matrix of sensitivities. A second objective function which fulfills the requirements of the model constraint is defined to be:

$$\phi_M = \|\mathbf{W}_M(\mathbf{m} - \mathbf{m}_0)\|^2 \tag{8.2}$$

The combined objective function becomes:

$$\phi = \|\mathbf{W}_M(\mathbf{m} - \mathbf{m}_0)\|^2 + \mu\|\mathbf{W}_D(\mathbf{d} - \mathbf{A}(\mathbf{m}))\|^2 \tag{8.3}$$

where μ is the relative weighting between the data misfit and model structure objectives, $\mathbf{m}_0$ is the base model, and $\mathbf{W}_M$ is a measure of model regularization (e.g. damping or smoothing).

The solution to equation 8.3 is written:

$$\mathbf{m} = (\mathbf{W}_M^T\mathbf{W}_M + \mu\mathbf{A}^T\mathbf{W}_D^T\mathbf{W}_D\mathbf{A})^{-1}\,(\mathbf{W}_M^T\mathbf{W}_M\mathbf{m}_0 + \mu\mathbf{A}^T\mathbf{W}_D^T\mathbf{W}_D\mathbf{d}) \tag{8.4}$$

It may be desirable to incorporate multiple types of model regularization into the model structure objective. The regularization types allow for manipulation of the manner in which the recovered model is constrained by *a priori* information. These regularization types might include damping, flattening, smoothing, or other higher order derivatives that exert control over the level of deviations from the base model e.g.:

$$\mathbf{W}_M^{damp} = \begin{pmatrix} 1 & 0 & \cdots & 0 \\ 0 & 1 & \cdots & 0 \\ \vdots & \vdots & \ddots & \vdots \\ 0 & 0 & \cdots & 1 \end{pmatrix} \tag{8.5}$$

$$\mathbf{W}_M^{flatten} = \begin{pmatrix} -1 & 1 & 0 & \cdots & 0 & 0 \\ 0 & -1 & 1 & \cdots & 0 & 0 \\ \vdots & \vdots & \vdots & \ddots & \vdots & \vdots \\ 0 & 0 & 0 & \cdots & -1 & 1 \\ 0 & 0 & 0 & \cdots & 0 & 1 \end{pmatrix} \tag{8.6}$$

$$\mathbf{W}_M^{smooth} = \begin{pmatrix} 1 & -2 & 1 & 0 & \cdots & 0 & 0 & 0 \\ 0 & 1 & -2 & 1 & \cdots & 0 & 0 & 0 \\ \vdots & \vdots & \vdots & \vdots & \ddots & \vdots & \vdots & \vdots \\ 0 & 0 & 0 & 0 & \cdots & 1 & -2 & 1 \\ 0 & 0 & 0 & 0 & \cdots & 0 & 1 & 0 \\ 0 & 0 & 0 & 0 & \cdots & 0 & 0 & 1 \end{pmatrix} \tag{8.7}$$

To make use of these additional regularizations, we reformulate the inverse problem as:

$$\begin{pmatrix} \mathbf{W}_D\mathbf{A} \\ \alpha_1\mathbf{W}_M^{(1)} \\ \alpha_2\mathbf{W}_M^{(2)} \\ \vdots \\ \alpha_L\mathbf{W}_M^{(L)} \end{pmatrix}\mathbf{m} = \begin{pmatrix} \mathbf{W}_D\mathbf{d} \\ \alpha_1\mathbf{W}_M^{(1)}\mathbf{m}_0 \\ \alpha_2\mathbf{W}_M^{(2)}\mathbf{m}_0 \\ \vdots \\ \alpha_L\mathbf{W}_M^{(L)}\mathbf{m}_0 \end{pmatrix} \tag{8.8}$$

where the α terms are relative weights between the different regularization types and the data misfit objective. Linearizing the problem, one obtains a relationship between the model update $\delta\mathbf{m}$ and the misfits between the predicted and observed data $\delta\mathbf{d}$. Combining the regularization and weighting terms into augmented matrices **M** and **B**:

$$\begin{pmatrix} \mathbf{W}_D\mathbf{A} \\ \alpha_1\mathbf{W}_M^{(1)} \\ \vdots \\ \alpha_L\mathbf{W}_M^{(L)} \end{pmatrix}(\mathbf{m}-\mathbf{m_0}) = \begin{pmatrix} \mathbf{W}_D\mathbf{A} \\ \mathbf{M} \end{pmatrix}\delta\mathbf{m} = \mathbf{B}\delta\mathbf{m} = \begin{pmatrix} \mathbf{W}_D(\mathbf{d}-\mathbf{A}(\mathbf{m}_0)) \\ \mathbf{0} \end{pmatrix} = \begin{pmatrix} \mathbf{W}_D\delta\mathbf{d} \\ \mathbf{0} \end{pmatrix} \tag{8.9}$$

Solving for the required perturbation to the current model at each iteration:

$$\delta\mathbf{m} = (\mathbf{B}^T\mathbf{B})^{-1}\mathbf{B}^T\begin{pmatrix} \mathbf{W}_D\delta\mathbf{d} \\ \mathbf{0} \end{pmatrix} = (\mathbf{B}^T\mathbf{B})^{-1}(\mathbf{A}^T\mathbf{W}_D^T\mathbf{M}^T)\begin{pmatrix} \mathbf{W}_D\delta\mathbf{d} \\ \mathbf{0} \end{pmatrix} \tag{8.10}$$

$$= (\mathbf{B}^T\mathbf{B})^{-1}(\mathbf{A}^T\mathbf{W}_D^T\mathbf{W}_D\delta\mathbf{d} + \mathbf{M}^T\mathbf{0}) = (\mathbf{B}^T\mathbf{B})^{-1}\mathbf{A}^T\mathbf{W}_D^T\mathbf{W}_D\delta\mathbf{d}$$

The model is updated iteratively using this perturbation:

$$\mathbf{m_{n+1}} = \mathbf{m_n} + \delta\mathbf{m} \tag{8.11}$$

We can also define the model resolution matrix **R**, which describes how well the recovered model, $\mathbf{m}_R$, matches a given true model, $\mathbf{m}_T$:

$$\delta\mathbf{m}_R = (\mathbf{B}^T\mathbf{B})^{-1}\mathbf{A}^T\mathbf{W}_D^T\mathbf{W}_D\mathbf{A}\delta\mathbf{m}_T = \mathbf{R}\delta\mathbf{m}_T \tag{8.12}$$

Ideally, **R** is an identity matrix. The above calculations were coded in MATLAB (see Appendix D).

8.2.2 Data and base model

The data selected for the 1D inversion are the 2013 aqi05 response estimates. This response is a set of smooth *xy* and *yx* curves that are less affected by noise than the response at alternative sites (e.g., Table 7.1). To balance the contributions of the data terms in the inversion, the apparent resistivity data were converted to log apparent resistivity (yielding data values with an absolute range of about 2) and the phase data were converted from degrees to radians (yielding values with an absolute range of about 1.5). The AMT and MT-processed data were combined to generate the data used in the inversion. The MT responses were given precedence in the overlapping frequency range of the results (from 0.43 to 780 Hz) since the AMT responses in this band are noisier.

The starting model for the inversion is the 15-layer model described in section 3.5 (Table 3.1). Forward calculated data from this base model are plotted in Figure 8.1. The agreement between the forward data and the real data is reasonable. Responses with higher data misfit include the short-period phase, the long-period apparent resistivity and phase, the AMT deadband, and the 0.01 to 1 s band. Some of these problematic bands are affected by noise and are manually downweighted in the $\mathbf{W}_D$ term of the inversion. In many inversions, data are weighted by the inverse of their variance estimates. However, since the variance estimates are very poor for the robust remote-referenced Aquistore MT data, a relative data weighting scheme is established.

In the 0.01 to 1 s band, the model generates a response that is generally more conductive than the data. The differences between the predicted and real data in this range are consistent in the apparent resistivity and phase so it appears to represent a true geological response. It is

therefore expected that the inversions will be able to improve the level of data misfit in this section of the response.

Figure 8.1: Comparison of aqi05 data with forward data from base model. Shaded bands are downweighted in the inversions.

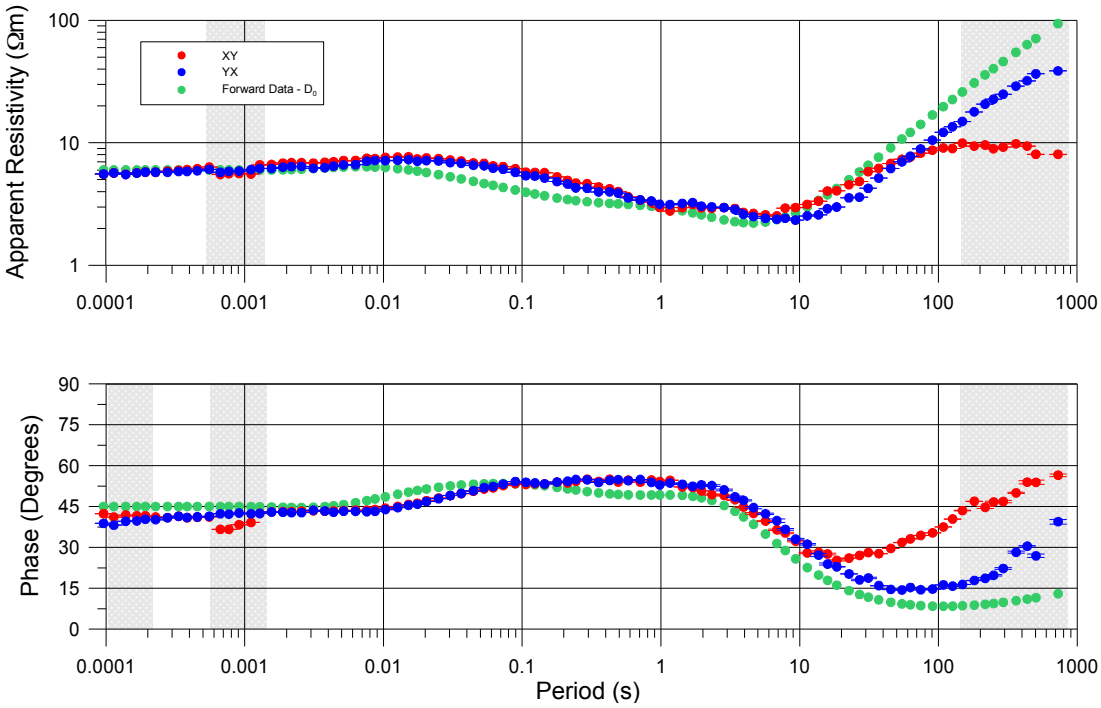

The resistivity log model is clearly more suitable as an explanation for the *yx* MT response than for the *xy* MT response. This is in part due to a lower signal-to-noise ratio observed in the *xy* response, which is particularly evident in the AMT deadband, and makes for a more challenging fit to the data. The effects of the NACP on the *xy* response are also much more significant, since the base model includes a resistive half-space below the deepest basin strata, whereas the NACP causes a conductive *xy* response at depth.

Since the sequestration reservoir sits directly above the Precambrian basement, it is difficult to establish how much of the multidimensional long-period data could be excluded from the inversion without affecting the resolution of this layer. Thus, to simplify matters, all of the long-period data is used in the model recovery and the response of the Precambrian is eventually

represented by a set of deep layers (with different resistivities for the *xy* and *yx* mode inversions). The inclusion of the long-period data is not expected to have an impact on definition of the overlying 1D structure. Furthermore, the data weighting and model constraints serve to emphasize resolution of the sedimentary strata over deeper features.

8.2.3 Inversion strategy and procedures

The model parameters for the inversions are the log resistivities of each of the layers. The layer thicknesses are held fixed and are based on the detailed information available from the borehole data which provides a robust indication of the layer thicknesses. Setting fixed thicknesses also allows for higher resolution recovery of the layer resistivities. During the inversion process some reparameterization of the model is done in order to compensate for deficiencies of the *a priori* information and improve the data misfit.

The final model for each inversion is expected to be similar to the reference model and therefore the sensitivity matrix for the reference model is expected to provide a good approximation for the sensitivity matrix **A**(**m**) for each iteration. The inversions reported here were therefore based on a constant sensitivity matrix. However, this approach could be easily modified in subsequent studies to allow for more extreme non-linearity. The sensitivity matrix, **A**, is generated by calculating the change in the response when each model parameter in the reference model is perturbed by 5% of its value. A forward modeling code based on the recursive relationships of equations 4.47 to 4.49 is used to calculate **A**.

Three types of model regularization are included: damping, flattening, and smoothing. These different model regularizations were given equal weighting in the initial inversions. An exploratory approach is taken to determine the appropriate regularization parameters, with

damping to ultimately be emphasized over flattening and smoothing, and a successful weighting scheme judged by the geological plausibility of the recovered model as much as by the data misfit.

In the data weighting matrix, data in the shaded bands in Figure 9.1 were downweighted by a factor of 2; $\mathbf{W}_D$ is a diagonal matrix with values of 1 to represent unweighted data and 0.5 to represent downweighted data. Conditions for termination of the inversion were specified thresholds of a maximum of 100 iterations, an RMS misfit of less than 1, or a successive improvement in misfit of less than 0.0001.

8.2.4 Results – yx data

The first inversion (**M1-1**) emphasizes the fit to the *yx* data by setting the weight of the regularization terms (each of the α factors in equation 8.8) to 0.05. After the maximum of 100 iterations, the resulting model (Figure 8.2) significantly improves the misfit in the 0.01 to 1 s band. However, the lower half of the model has unrealistic resistivity values.

Figure 8.2: M1-1 results. Final misfit: 1.4013. Iterations: 100. Fit of predicted data to real data of apparent resistivity (top-left) and phase (bottom-left); comparison of starting model and final model (right).

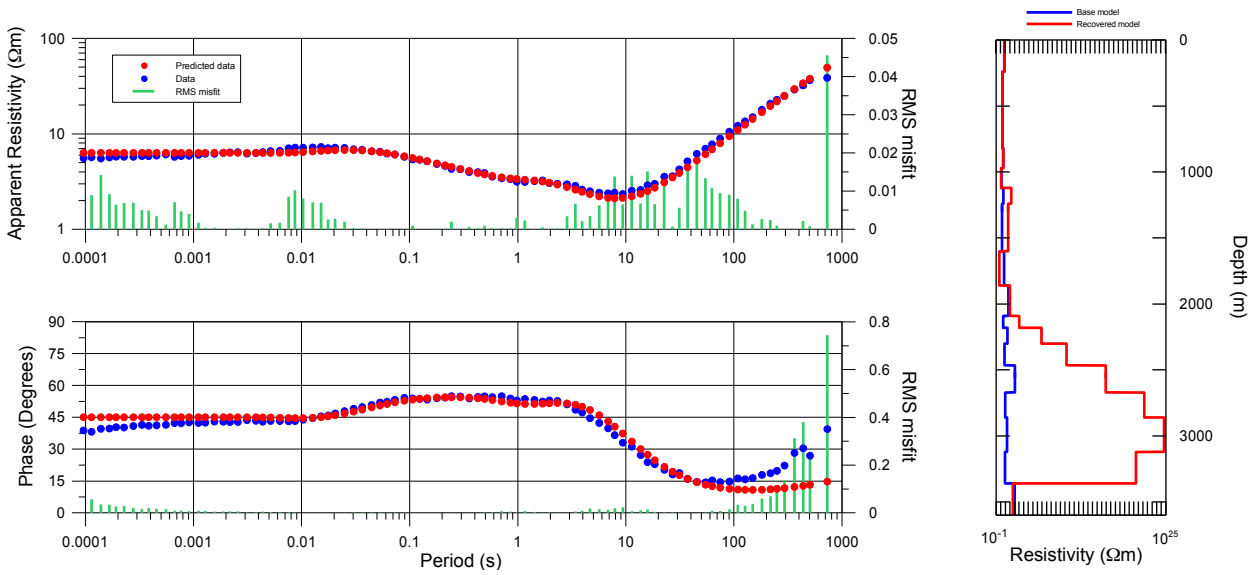

In the next inversion, **M1-2**, the fit to the data and the model regularization terms were given equal weighting (α=1). This inversion yielded a final model that is far more geologically plausible, and an improved data misfit (Figure 8.3). The observed improvement in both the model and the data misfit for the **M1-2** inversion suggest that during the **M1-1** inversion the model reached a point for which the constant sensitivity matrix no longer adequately approximated the exact sensitivity values. The recovered **M1-2** model is slightly more conductive than the base model, particularly for the deepest layers. High levels of misfit remain for the short period apparent resistivities and the long period phase.

Figure 8.3: M1-2 results. Final misfit: 0.8912. Iterations: 4.

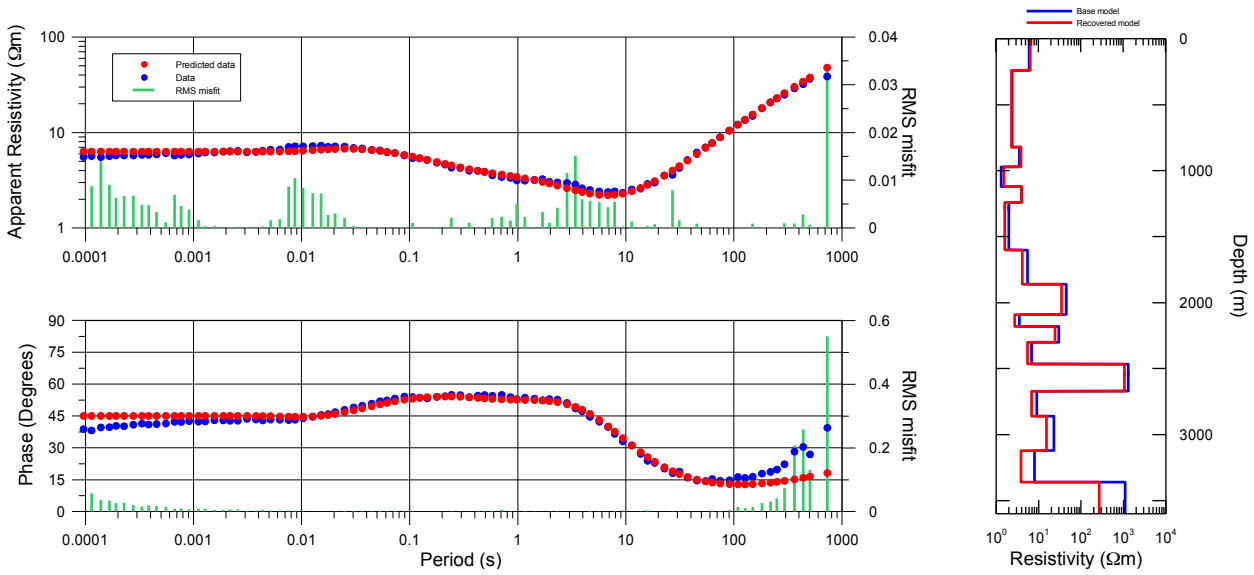

The **M1-2** inversions appear to have established an appropriate balance between data misfit and model recovery. Because of the desirability this result, the equal weighting of each of the regularization types, which was initially adopted as a trial weighting scheme, was retained for subsequent inversions. To verify the relative model weighting versus the data weighting, the inversion was repeated for a range of α values (where α is the same for all types of regularization). The results in terms of data misfit (listed in Table 8.1, Figure 8.4) indicate that

the best choice of the α value is between 0.1 and 1. This range of values yield a data fit that is close to the optimum value while allowing a maximum contribution from the model regularization. The misfit results for $\alpha = 0.1 - 1$ are all slightly less than 1; each of these inversions appears to have terminated after overshooting the convergence threshold by varying amounts.

Table 8.1: Inversion results for different regularization weights

α	Iterations	Misfit
0.1	14	0.9781
0.3	1	0.8893
1	4	0.8912
3	27	0.9935
10	100	1.5392
30	100	2.0375

Figure 8.4: Model misfit against regularization weighting.

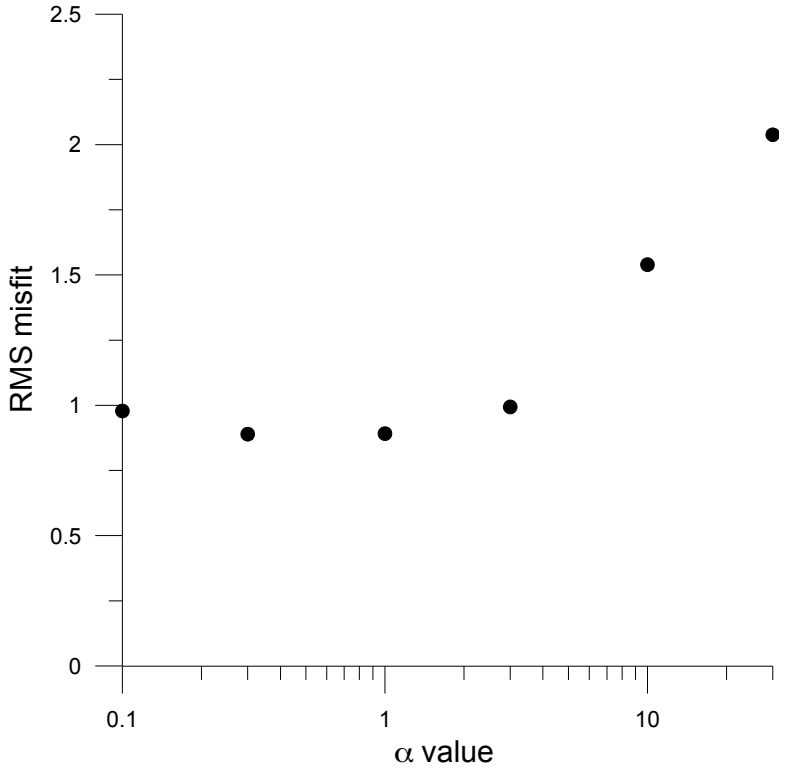

Examining the models recovered from each these runs (Figure 8.5), the most notable differences occur near the base. While the Precambrian structure is expected to be under-represented by the base model, the overlying layer, which represents the interval of interest at Aquistore, should be well-constrained by the borehole data. For this reason, the deviations from the base model recovered with α=0.3 are considered too large. The value of α chosen for subsequent inversions is 1.

Figure 8.5: Recovered model for different regularization weights.

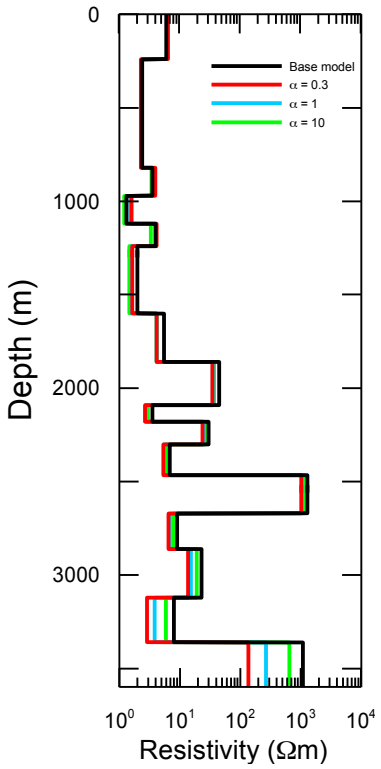

As the highest data misfits and base model deviations of the **M1-2** inversion are at the level of the basal half-space, modifications need to be made to the parameterization at the base of the model in order to obtain additional improvement. Three 1,000 Ωm and 100 m thick layers were therefore added between the 15th model layer (representing the base of the Williston Basin)

and the basal half-space. These modifications are beyond the range for which borehole constraints are available, and so do not conflict with any additional geological information.

Using this updated base model, a new inversion **M1-3** was run. For this inversion, the threshold for RMS data misfit was reduced to 0.5. The resulting model produced an improved fit to the long period phase data (Figure 8.6). The recovered Precambrian structure is progressively more conductive with depth, but remains significantly more resistive than most of the overlying strata. Despite the misfit improvement, the long-period phase data remains the worst-fitted component of the data. One way to correct this misfit is to continue to add more layers to the base of the model. However, since this increased misfit occurs at periods larger than 200 s, where the resistivity of the Phanerozoic rocks has minimal influence, the existing model is considered an adequate representation of the Phanerozoic structure.

Figure 8.6: M1-3 results. Final misfit: 0.7253. Iterations: 18.

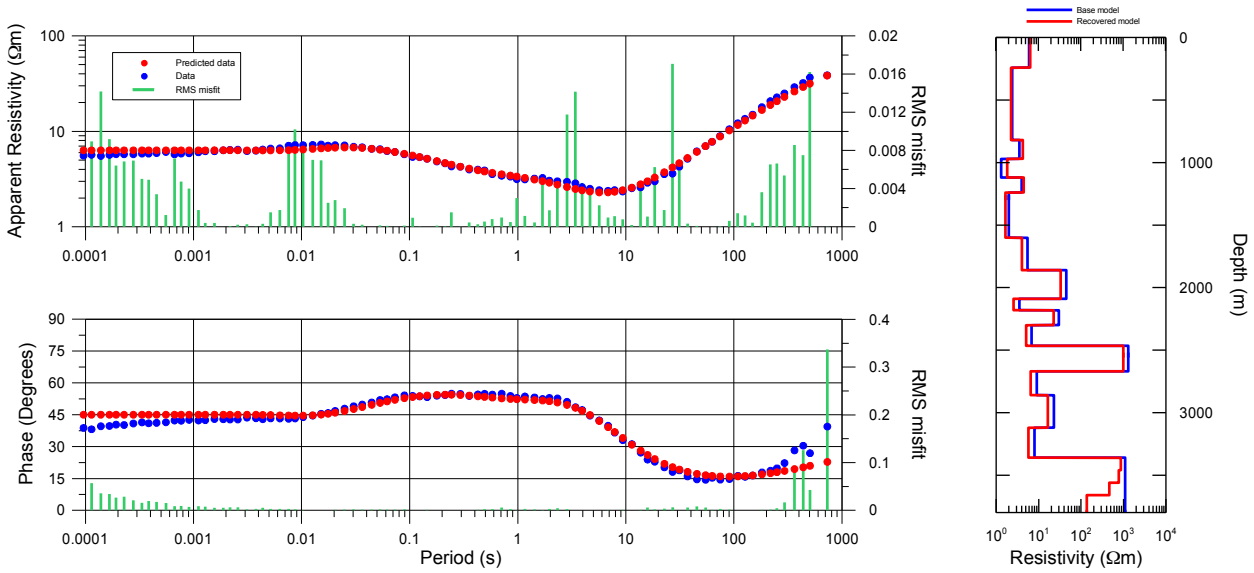

A final area in which the model could improve is related to the short-period phase. Theoretically, if the shallowest materials have uniform resistivity, the shortest period phases will be 45˚ (e.g., Figure 8.6). This is not the case in the *yx* data. The Quaternary sediments may be

better represented in the model if the top layer of the model is subdivided to yield higher model resolution at shallow depths. Thus the inversion model was reparameterized using four layers with thicknesses of 10 m, 50 m, 80 m, and 100 m in place of the original 240 m top layer. These layers were assigned a resistivity of 6 Ωm in the starting model.

The **M1-4** inversion uses this new starting model to produce the results shown in Figure 8.7. The fit to the *yx* data is excellent for both the apparent resistivity and phase.

The final model (Table 8.2) is generally more conductive than the starting estimate derived from of the borehole data, with layers 2, 3, 6, 7, and 8 being the exceptions. It is these relatively shallow layers at the level of the Ravenscrag, Colorado and Manville Formations that are fitting the predicted data in the 0.01 to 1 s band; initially, the predicted data in this period range was too conductive (Figure 8.1). The inversion has recovered a resistivity of 5.70 Ωm for the reservoir layer. This value is smaller than the initial estimate (8 Ωm) and provides a large contrast between the reservoir and the overlying (16.29 Ωm) and underlying (867.36 Ωm) layers.

Figure 8.7: M1-4 results. Final misfit: 0.4637. Iterations: 6.

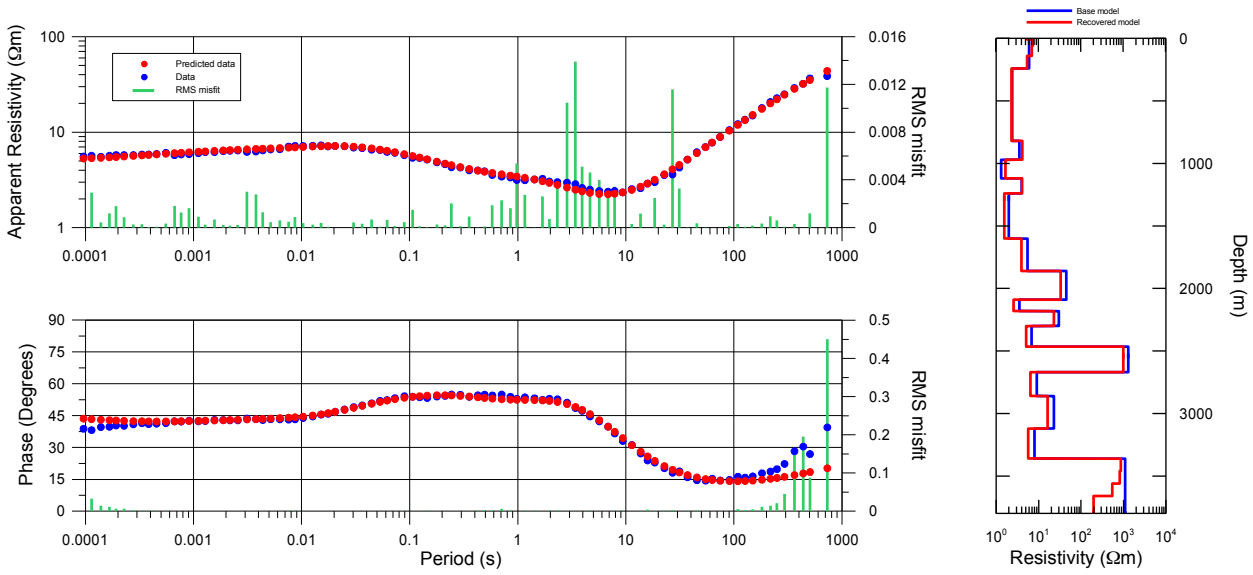

Table 8.2: Comparison of base model with M1-4 model.

Layer	Thickness (m)	Base model resistivity (Ωm)	M1-4 resistivity (Ωm)	Geological formations
1	10	6	5.34	Till
2	50	6	7.19	Ravenscrag
3	80	6	6.97	Ravenscrag
4	100	6	5.36	Bearpaw
5	580	2.4	2.31	Belly River
6	150	3.5	4.17	Upper Colorado
7	150	1.3	1.66	Lower Colorado
8	120	4	4.10	Manville
9	360	2	1.55	Vanguard, Upper Watrous
10	260	5.5	3.91	Middle Watrous
11	230	45	33.01	Lower Watrous, Bakken
12	90	3.5	2.58	Bakken
13	120	30	22.80	Duperow
14	165	6.8	5.09	Manitoba
15	205	1300	986.28	Prairie Evaporite
16	190	9	6.47	Interlake
17	260	23	16.29	Yeoman
18	240	8	5.70	Winnipeg, Deadwood
19	100	1000	867.36	Precambrian
20	100	1000	815.27	Precambrian
21	100	1000	540.01	Precambrian
Half-Space		1000	198.15	Precambrian

The resolution matrix resulting from inversion **M1-4** is shown in Figure 8.8. The matrix relates the model changes defined by the inversion process to corresponding changes to the true model. The resistivities of the shallowest and most conductive layers are best resolved in the inversion. The ninth model parameter, a 360 m thick 1.55 Ωm layer that covers the depth interval of the Vanguard and Upper Watrous Formations, is the deepest layer for which there is significant resolution. As this layer is much thicker and more conductive than the layers immediately above and below, it has a dominating effect on the surrounding parameters which are also sensitive to changes in this interval. The rows and columns of the matrix, which are ideally delta functions, are smeared about the ninth parameter. Figure 8.8 shows that the MT response has some sensitivity to the resistivity 18th layer, which represents the Winnipeg-

Deadwood sandstones. However, the sensitivity is not localized around the layer itself, so the resolution of the layer will be poor.

Figure 8.8: Resolution matrix of model M1-4.

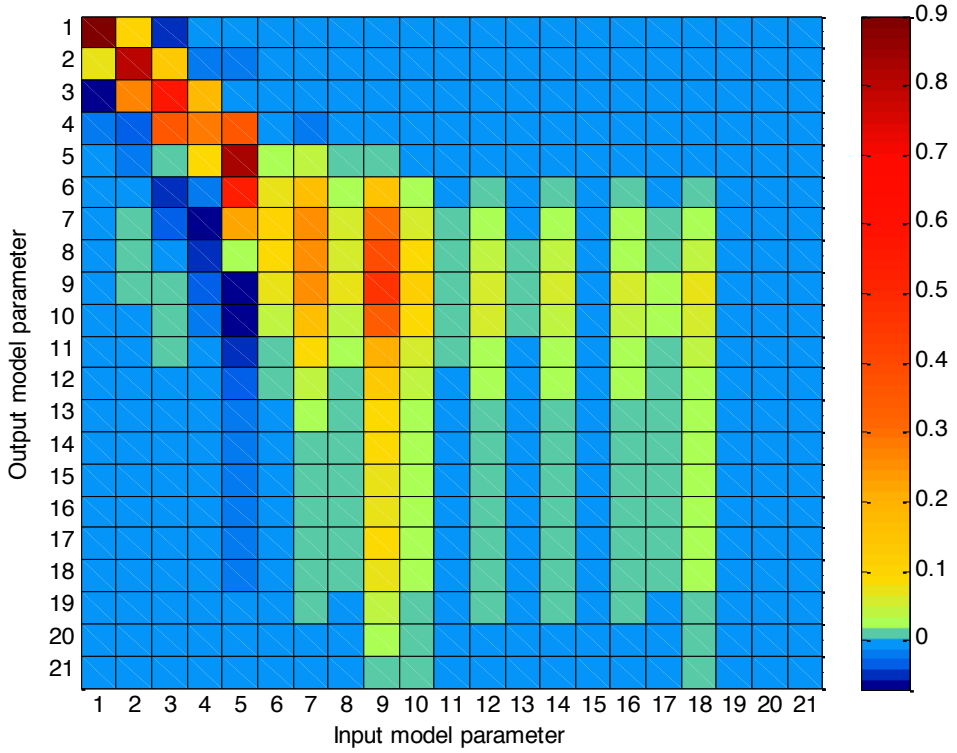

8.2.5 Results – xy data

The starting model for the *xy* 1D inversions was the final model from the *yx* inversions, **M1-4**. The additional layers added to the top and bottom of this model provide a superior parameterization than the original 15 layer model. It was expected that the noisier *xy* response would be more difficult to fit than the *yx* data. Despite this challenge, the data weighting was held constant from the previous inversions in order to avoid having to make too many assumptions on the reliability of the data in the absence of reasonable variance estimates. The regularization weights were held at α =1.

The resulting model from the initial inversion, **M2-1** (Figure 8.9), is much more resistive than the starting model. The high misfit in the AMT deadband was expected and was subsequently neglected. However, at periods longer than 1 s, the fit to the data is poor. Although this misfit is partially related to noise effects, its systematic variation with period indicates that it is largely related to a poor fitting of the response by the deeper layers in the model.

Figure 8.9: M2-1 results. Final misfit: 1.0761. Iterations: 56.

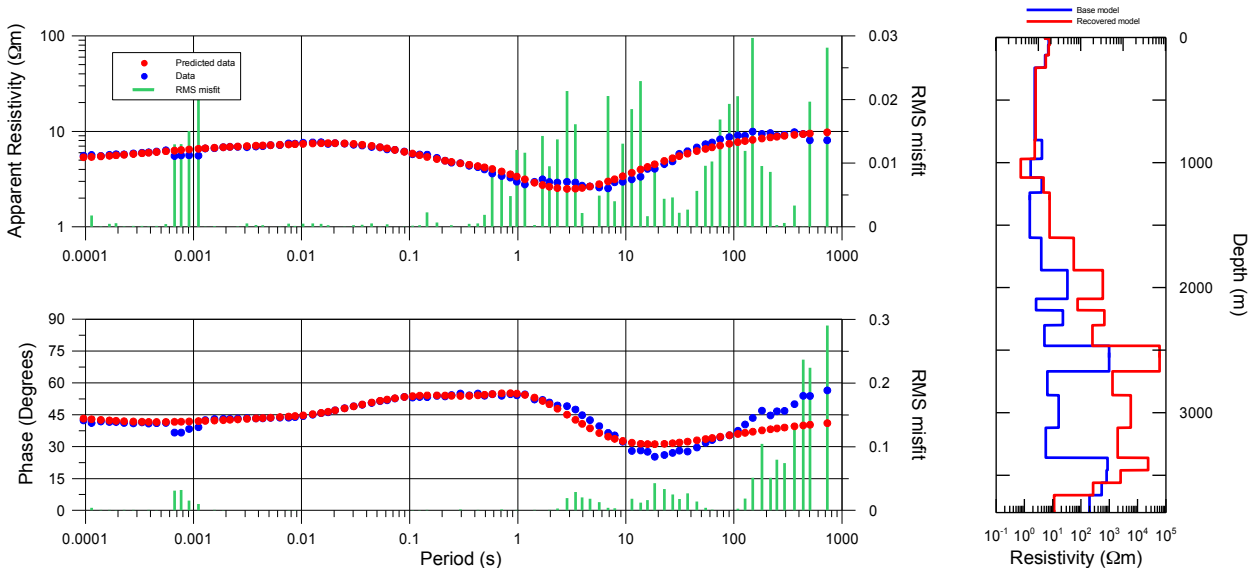

It is clear that the inversion needs to be constrained more closely by the starting model. For the subsequent inversion, **M2-2**, the damping factor on the first 18 layers of the model was increased by a factor of 5 in order to preserve the Williston Basin structure while allowing the model to vary at the Precambrian level. The recovered model (Figure 8.10) achieves a similar fit to the data as the **M2-1** inversion, but with far more realistic resistivity values. The model is again more resistive than the results of the *yx* inversions, particularly from 1250 to 1750 m. At the base of the model, there is a steeper increase in conductivity with depth from the top Precambrian layer to the basal half-space.

Figure 8.10: M2-2 results. Final misfit: 1.1441. Iterations: 100.

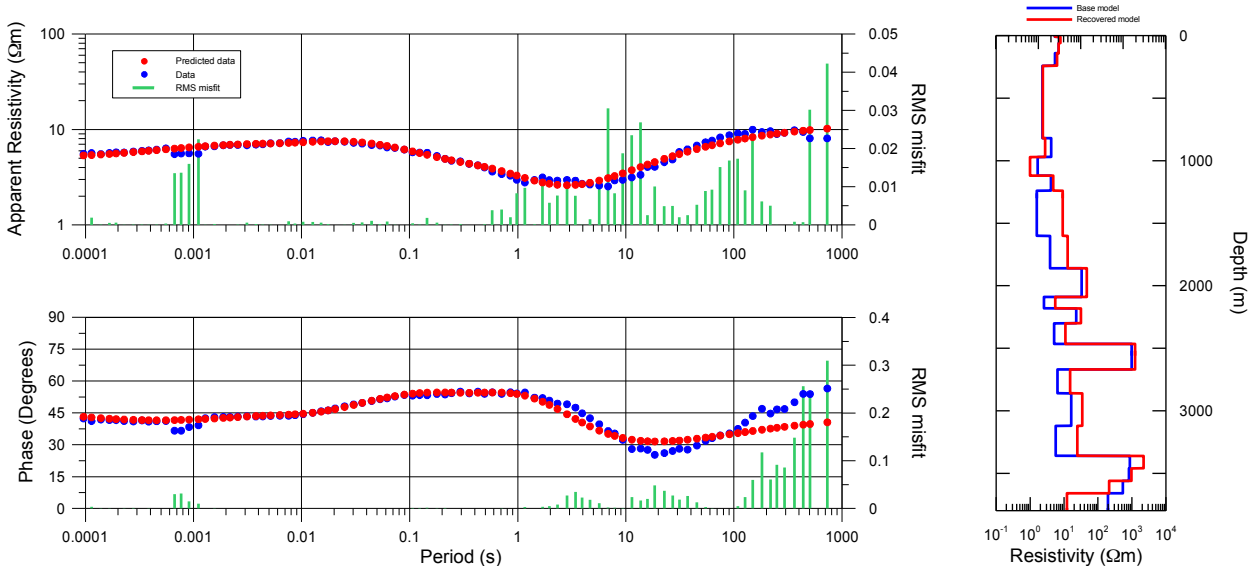

Due to the low resolution of the MT inversion in the deeper parts of the model, it is desirable to obtain a realistic Precambrian model, even though this section of the model is not the focus of the inversions. It is possible that the more resistive basin layering in model **M2-2** is a form of compensation for inadequate parameterization at Precambrian depths. To verify this idea, the **M2-3** inversion further increases the number of layers at the base of the starting model by adding 2 more 100 m thick layers (with resistivity of 1,000 Ωm in the starting model). The damping factor on the Williston Basin parameters was also increased from 5 to 20. The resulting model fits the data nearly equally as well as the previous two inversions (Figure 8.11). The model deviates very little from the **M1-4** result, with the most significant changes occurring in the shallower layers. The deeper layers are slightly more resistive than the base model, which is in line with the small differences in the *xy* and *yx* response curves in the 0.01 to 1 s band. For example, the recovered resistivity of the 16th layer is 7.37 Ωm compared to 6.47 Ωm for the base model, an increase in resistivity of 14%.

In the **M2-3** inversion, the resistivity of the reservoir layer increased 21.5%, from 5.70 Ωm in the base model to 6.93 Ωm in the final model. This layer remains relatively conductive in relation to the overlying layer (17.16 Ωm).

Figure 8.11: M2-3 results. Final misfit: 1.2639. Iterations: 100.

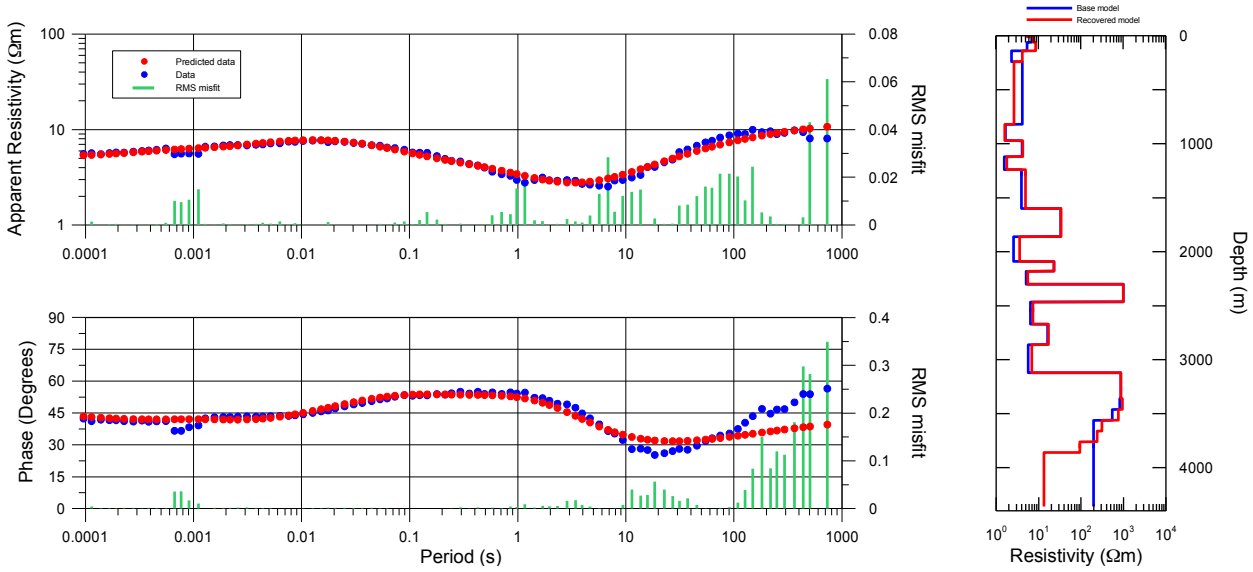

8.3 Additional modeling

8.3.1 Near-surface response

A feature in the MT responses that is not well represented in the 1D inversions is the variability of the short-period apparent resistivity and phase in the AMT processed data (10^{-4} to 10^{-3} s in Figure 8.6). Noting the range of short-period AMT responses (Figure 8.12), it is possible that lateral overburden variations across the site are not adequately explained by a 1D model. The AMT responses in this period range can be fit adequately with a D+ model of delta functions (Parker, 1980; Weidelt and Chave, 2012), suggesting they are true geoelectric responses. As there are insufficient Aquistore MT sites to allow for construction of a 2D model

of the near-surface resistivity structure, a forward modeling approach is used to examine the effect of the overburden on the AMT responses.

Figure 8.12: Final short-period AMT processed responses, 2013 dataset.

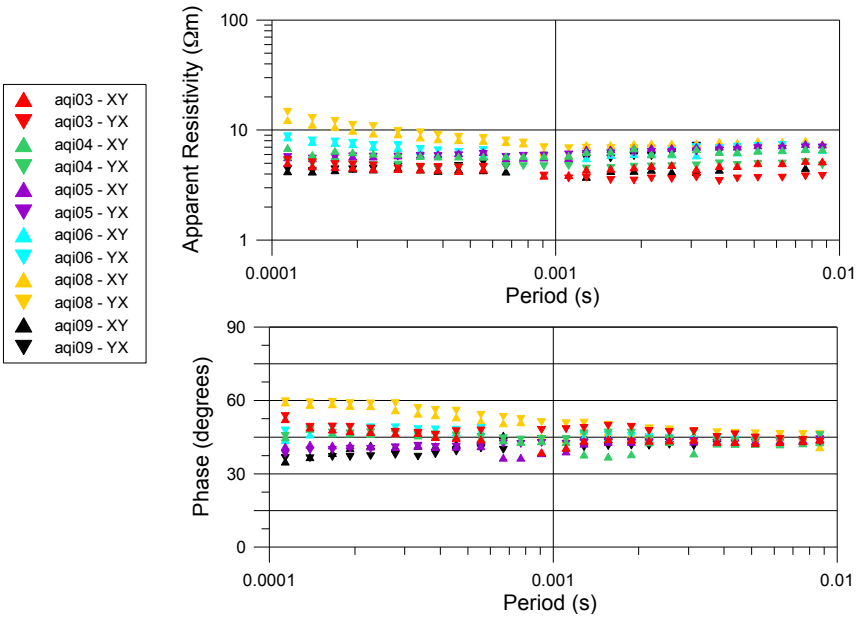

The AMT responses were examined for cases in which the overburden layer at the top of the **M1-4** model has different values of thickness and resistivity (Table 8.3). The resulting theoretical AMT responses (Figure 8.13) demonstrate that the differing values of apparent resistivity observed at short periods could plausibly be the result of lateral variations in the overburden. The observed variability in the short-period phase data was not adequately reproduced in this modeling exercise. In order to explain the phase change it would be necessary to consider surface resistivity structures with resistivity variations over depth scales comparable to the skin depth of the signal at the shortest period (from 3.95 to 7.90 mm).

Table 8.3: Overburden test cases.

	Thickness (m)	Resistivity (Ωm)
Thick resistive	30	10
Thin resistive	1	10
Thick conductive	30	5
Thin conductive	1	5

Figure 8.13: Theoretical AMT response to overburden variations.

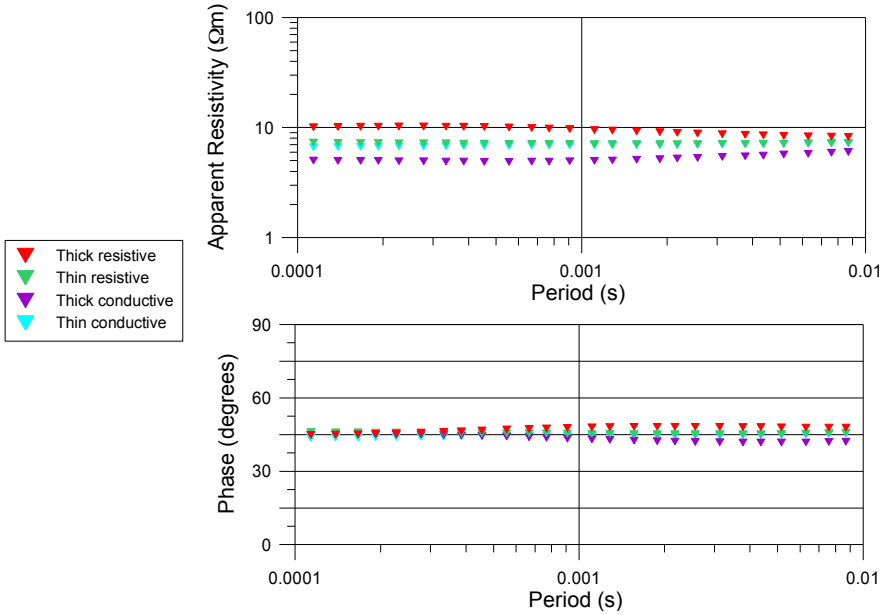

8.3.2 CO_2 injection scenarios

From the **M1-4** inversion result, it is apparent that sensitivity to the resistivity change caused by injected CO_2 may exist for a range of depths within the Williston Basin (e.g., Figure 8.8). Assuming that any resistivity changes in the basin are due to CO_2 injection at the level of the reservoir, this sensitivity effectively becomes resolution of the Winnipeg-Deadwood layer.

To provide greater context for these results, the 1D MT responses were forward calculated for different CO_2 injection scenarios: a pre-injection setting with a relatively conductive 5.7 Ωm reservoir layer, and two post-injection settings with reservoir resistivities of

20 Ωm and 50 Ωm. These values represent a range of layer saturations and injected CO_2 volumes. Differences between the pre-injection background responses and the CO_2 saturated responses were then calculated.

The MT responses for high resistivity reservoir layers are compared to the pre-injection MT response in Figure 8.14. The difference between the pre- and post-injection log apparent resistivity response becomes evident at 1 s period and reaches a broad maximum at ~40 s. This anomaly is small for both the 20 and 50 Ωm reservoir cases. It is on the order of 0.1 to 1 Ωm, which is equivalent to 3.5% impedance errors. The phase anomaly may be more useful for detecting the effects of CO_2 as the differenced phase response has a sharper maximum at a particular period related to the injection depth. For the reservoir layer, the peak phase anomaly is at 10 s. The effect of the change in resistivity on the phase is also small, 1.35˚ for the 50 Ωm case. A phase difference of this magnitude corresponds to an error of 2.4% on the MT impedance estimates. These error levels are comparable to the estimated MT repeatability errors and so the anomalies would be difficult to measure accurately (section 7.4).

Figure 8.14: Change in MT response due to CO_2 at reservoir depth. Background response (left); difference in response (right).

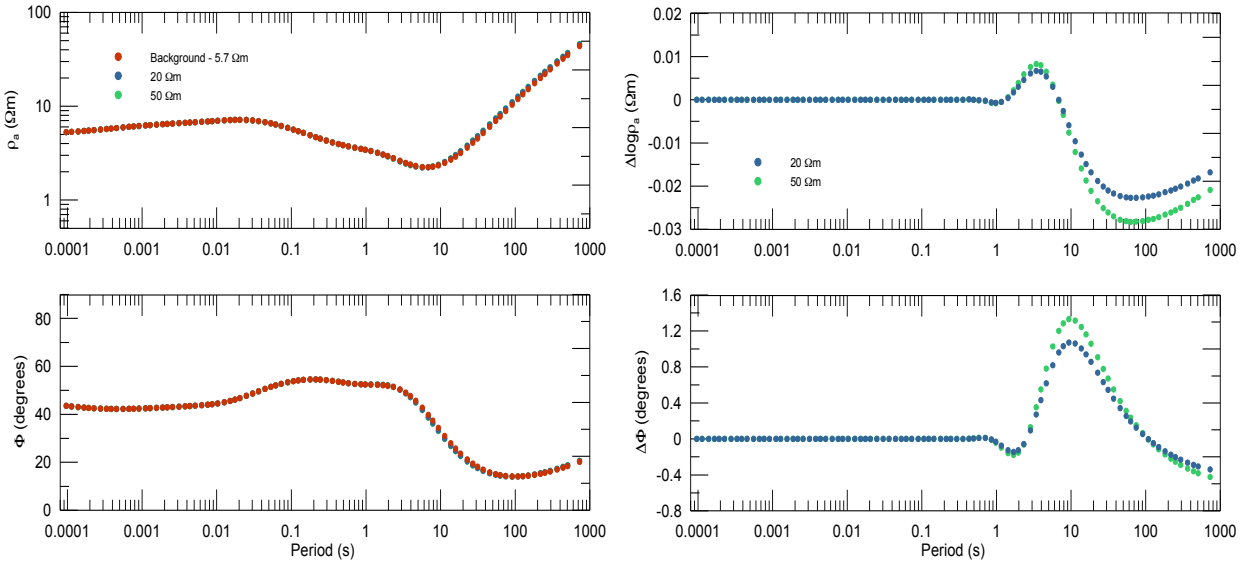

The **M1-4** resolution matrix indicates that for model layers as deep as the Vanguard-Upper Watrous interval (1240-1600 m), there is a high level of sensitivity (Figure 8.8). Figure 8.15 shows the results of the CO_2 saturation modeling exercise for the hypothetic situation of CO_2 leakage into this model layer. The anomalies produced in these scenarios are similar in form to those generated from the injection of CO_2 at reservoir depth, but they occur at a shorter period (10-40 s for the log apparent resistivity, 5-6 s for the phase) and are larger in magnitude. Differences in the responses from the pre-injection values are apparent in both the apparent resistivity and phase data. The maximum log apparent resistivity anomaly is 0.206 and the maximum phase anomaly is 8.2˚, corresponding to MT impedance errors of 30.3% and 14.3%, respectively.

Figure 8.15: Change in MT response due to CO_2 at in Vanguard-Upper Watrous Formation. Background response (left); difference in response (right).

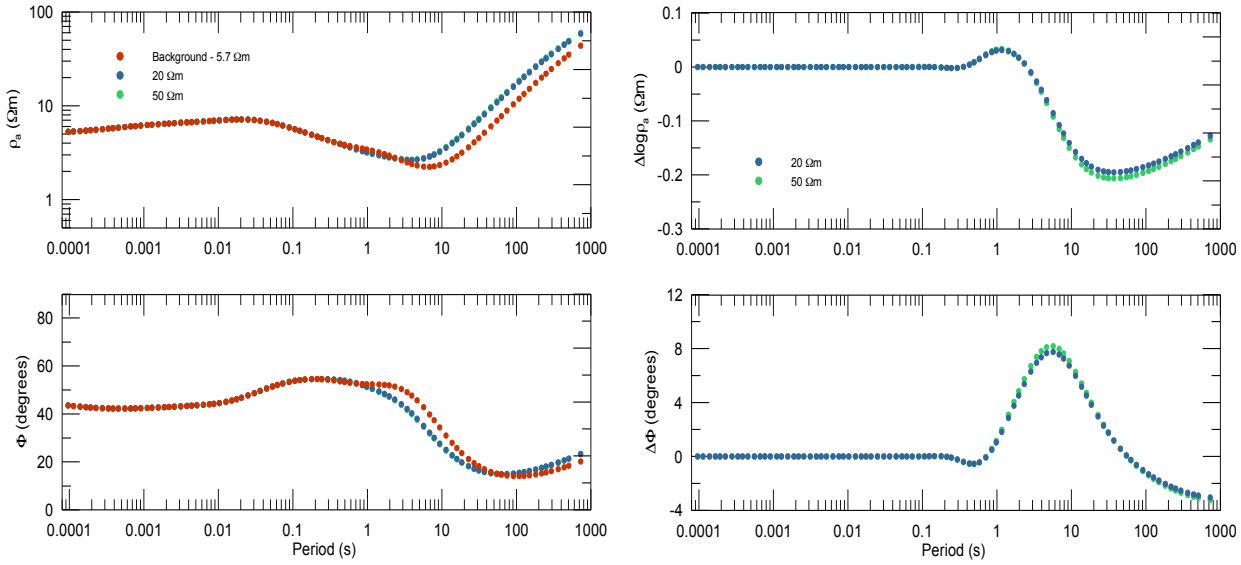

8.4 Discussion

The **M1-4** model satisfies the goals of fitting the *yx* MT data while respecting the borehole resistivity data. The results indicate that model parameterization used in the inversions

was suitable. Confidence in the **M1-4** model as a representation of the resistivity structure of the Williston Basin in the study area is therefore high. Minimal manipulation of data weighting and model regularization matrices was required to achieve this result.

Although a close fit to the *xy* data was not achieved, the increased misfit is explained in large part by the lower signal/noise ratio on this response, which is undoubtedly presenting an obstacle to the optimization process. The **M2-3** result demonstrates that the differences between models that fit the *xy* and *yx* data are found primarily at Precambrian depths. As such, the confidence in the final Williston Basin part of the *yx* model remains high.

The Aquistore area has been subject to lignite strip-mining (Klappstein and Rostron, 2014), so it is reasonable to expect significant local variations in overburden thickness and composition. The forward modeling presented in section 8.3.1 suggests such variations may be responsible for the spatial variations in the short-period responses at the Aquistore site.

Differences in the results for the *xy* and *yx* inversions could be influenced by anisotropy within the horizontal plane. This type of anisotropy would be caused by complex geoelectric structures (e.g. fractures). These features are at a scale that is not resolvable in the presented inversions, however the minor differences in final models for the *xy* and *yx* inversions is suggestive of their presence, particularly in shallower layers.

The transverse anisotropy may be useful in explaining the differences between the final models and the initial base model that was simplified from a resistivity log. The effect of internal layering on the generated base model will not be the same as for the MT response, which is sensitive to the integrated conductance of a layer. From Table 3.1, the layers with the lowest coefficients of anisotropy are typically in the shallower section of the Basin, from the Ravenscrag to the Upper Watrous. The recovered resistivities for these layers in **M1-4** match the

resistivities of the starting model more closely than the deeper layers. The highest calculated coefficient of anisotropy is for the Winnipeg-Deadwood storage complex (5.85). Both the **M1-4** and **M2-3** inversions recovered a more conductive reservoir layer than the initial base model estimate.

The inversion and modelling results have provided some insight into the use of MT for the direct detection of subsurface CO_2. While changes to the reservoir layer are measurable to a small degree, this sensitivity is not of any use in a practical time-lapse survey since the errors associated with response estimation and repeatability will likely mask the changes in the MT response for this depth. Also, the anomalies associated with a more realistic 3D plume will be smaller than those presented in the above modeling study. However, detection of CO_2 at shallower levels of the Williston Basin is possible due to high sensitivity of conductive layers such as the Vanguard-Upper Watrous interval. Thus the MT method has the potential to monitor for leaks into overlying strata. Low resolution of these shallow layers requires that assumptions be made about the localization of resistivity changes in the basin.

The 1D inversion has been successful in producing a reference model of the background, pre-injection resistivity structure at Aquistore. This model should prove useful for future post-injection EM studies performed at the Aquistore site.

Chapter 9: CSEM Sensitivity Analysis and Modeling

9.1 Introduction to sensitivity analysis

It was shown in Chapter 8 that the MT method provides limited sensitivity to the resistivity changes associated with CO_2-saturation of the Winnipeg-Deadwood reservoir and low resolution of the depth of resistivity changes. It is therefore important to examine the capabilities of the CSEM method to detect injected CO_2 and resolve the deeper basin structures in order to more fully assess the potential of surface EM monitoring methods at Aquistore. A key attribute that differentiates the CSEM methodology from MT is the generation of TM-mode currents in the subsurface. Theoretically, the TM response resolves thin resistors or resistive layers underlying a conductor more capably than the predominantly TE response of the MT method. The following analyses have the purpose of verifying that the CSEM configuration used at Aquistore can potentially detect resistivity changes at the target depth and to examine the depth range at which the CSEM response has greatest sensitivity. These objectives will be accomplished by calculating CSEM response sensitivities to small perturbations in layered models. Specific questions to be answered by these calculations include:

- How do changing offsets and operating frequencies affect the CSEM sensitivities?
- What is the effect of layering on the CSEM sensitivities?
- Which depth range within the Williston Basin at the Aquistore site has the greatest sensitivity to changes in resistivity?
- Which of the apparent resistivity or phase responses is more likely to detect changes due to injected CO_2?

- What are the implications of the sensitivity analysis for the Aquistore CSEM configuration?

9.2 Fréchet derivatives

The Fréchet derivative, that is the change in the response due to a perturbation of a parameter at a particular depth, is defined as (Chave, 1984):

$$\delta R(\omega) = \int_0^\infty F(z,\omega)\delta a(z)dz \; + \|\delta a\|^2 \tag{9.1}$$

where δR is the change in the response as a function of frequency, δa is the change in a physical property at a given depth, and F is the Fréchet derivative. If the higher order derivatives, represented by the $\|\delta a\|^2$ term, are negligible, the sensitivity can be approximated by the Fréchet derivative. For a particular frequency, the Fréchet derivative is approximately the response sensitivity as a function of model depth. The Fréchet derivative may be calculated for either the absolute or relative changes in the response. Since the model parameter of interest in EM is usually the electrical conductivity or resistivity of the subsurface, it is convenient to study the sensitivity functions in terms of perturbations to the log of these parameters:

$$\frac{\delta \ln(a(z))}{\delta z} = \frac{1}{a}\frac{\delta a(z)}{\delta z} \tag{9.2}$$

The corresponding sensitivity function is herein denoted $F_{ln\sigma}$. The logarithmic parameterization allows for a simple transformation from conductivity to resistivity in the form of a sign change:

$$\delta \ln(\sigma(z)) = -\delta \ln(\rho(z)) \tag{9.3}$$

The Fréchet derivative for the 1D MT uniform-source field response (TE) is given by Oldenburg (1979) as:

$$F_{\ln\sigma}(z,\omega) = -Z_{xy}^2 \left[\frac{E_x(z)}{E_x(0)}\right]^2 \sigma(z) \tag{9.4}$$

The sensitivity depends on the electric field as a function of depth, and the magnitude of this field has a maximum at the surface and decreases with depth. Thus the Fréchet derivative decays with depth, but is scaled by the *σ(z)* term. Oldenburg (1978) presents an equivalent expression for the Fréchet derivative of the DC resistivity response (TM) for a uniform half-space in a configuration that employs a single electrode for current, and a single electrode at distance *r* from the source for measuring potential:

$$F_{\ln\rho}(r,z) = \frac{I\rho}{\pi}\left(\frac{2z}{(r^2+2z^2)^{3/2}}\right) \tag{9.5}$$

It is evident that this sensitivity function depends on the geometry of the sounding. The sensitivity is zero at the surface and increases to a maximum at a depth that depends on *r* before decreasing at greater depth. In a layered structure, the DC resistivity sensitivity function will have a more complex form (e.g. Gomez-Treviño and Edwards, 1983).

As described above, a CSEM sounding using an electric dipole source will involve both TE and TM currents and the resulting sensitivity function will contain contributions from both of these components. The sensitivity will vary as a function of both offset and transmission frequency.

As the EM response is a complex impedance, and may be expressed as an apparent resistivity and phase, there are numerous expressions of the sensitivity functions that allow for examination of the sensitivity of a particular component of the response:

$$F_{\ln\sigma}(\mathrm{Re}(Z)) = \mathrm{Re}(F_{\ln\sigma}) \tag{9.6}$$

$$F_{\ln\sigma}(\mathrm{Im}(Z)) = \mathrm{Im}(F_{\ln\sigma}) \tag{9.7}$$

$$F_{\ln\sigma}(\rho_a) = 2\rho_a \mathrm{Re}(\frac{1}{Z} F_{\ln\sigma}) \tag{9.8}$$

$$F_{\ln\sigma}(\varphi) = \mathrm{Im}(\frac{1}{Z} F_{\ln\sigma}) \tag{9.9}$$

For practical purposes, a numerical calculation of the sensitivity functions is sometimes preferred. The numerical approach consists of inserting a perturbing layer of thickness *h* into the model at a series of depths (Gomez-Treviño and Edwards, 1983):

$$F_{\ln\rho}(z) = \frac{\Delta R}{h\Delta(\ln\rho)} \tag{9.10}$$

9.3 Overview of sensitivity calculations

The calculations of Fréchet derivatives done here are meant to mirror the CSEM survey configuration employed at Aquistore (Figure 9.1). Three of the offsets chosen for these analyses correspond to sites aqi01, aqi11, and aqi10 (3.5, 7.5 and 9.5 km away from the nearest bipole terminal). An additional offset considered in the analyses, 1 km from the source, has no equivalent at Aquistore. The receivers for this experiment are 50 m dipoles oriented parallel to the source, which is a 1 km long dipole/bipole. Source-field frequencies reflect the highest (32

Hz) and lowest (0.008 Hz) transmission frequencies used in the two Aquistore surveys, as well as an intermediate value (0.5 Hz).

Figure 9.1: Configuration of transmitter and receivers for TM-mode sensitivity calculations.

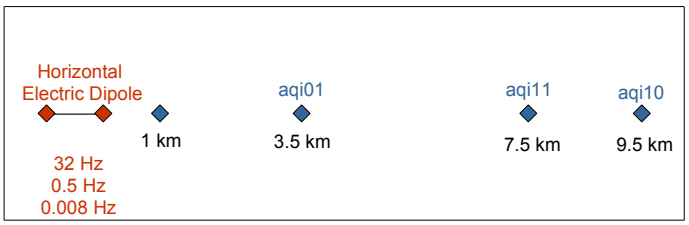

In order to more clearly examine the effects of varying offsets and frequencies on the sensitivities, the calculations will begin with a simple uniform half-space model. The effect of layering will then be examined as the input resistivity model is modified to increasingly resemble the structure observed at Aquistore as defined by the borehole resistivity readings (Figure 9.2). A simple layered case that represents the Williston Basin as a two-layer structure overlying a half-space will be tested, followed by the fifteen-layer model described in Table 3.1. In summary, Fréchet derivatives as a function of depth will be calculated for three different models, at three test frequencies, and four survey offsets. The results are viewed in terms of the apparent resistivity and phase response sensitivities for absolute changes in log resistivity.

Figure 9.2: Test case resistivity models for sensitivity calculations.

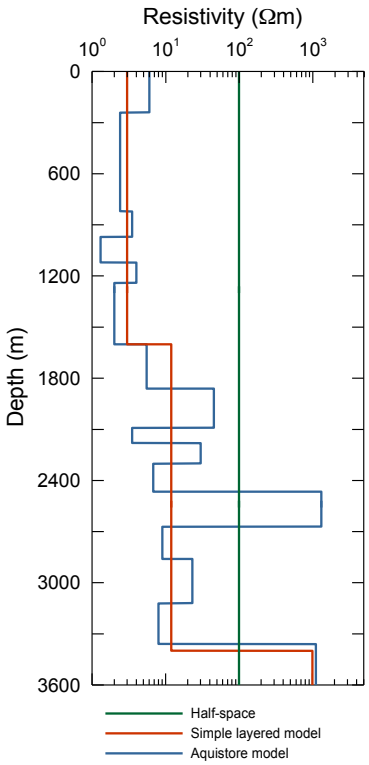

The calculations were performed in MATLAB using a modified version of the CR1Dmod forward modeling code (Ingeman-Nielsen and Baumgartner, 2006) to calculate numerical estimates of the Fréchet derivatives. Original alterations to the code were made by Hayward (2014) to allow for the calculation of DC resistivity sensitivities using a numerical perturbation technique (e.g. equation 9.9) (see Appendix E). In the present study, corresponding modifications were made to the frequency-domain EM case. A perturbation of magnitude $\ln(0.01\rho)$, and perturbing layer thickness of $(2.9\times10^{-4})z$ were used in the calculations.

9.4 Results

9.4.1 Half-space sensitivities

The task of separating the effects of geometric- and frequency-related variations in the initial half-space sensitivity calculations is a challenging endeavour. However, the combined effects of these two types of variations may be examined as a function of the induction number, and, when viewed in terms of this parameter (Table 9.1), some aspects of the sensitivity curve behaviour become more apparent. For the purposes of this exercise, the intermediate induction number range is defined to be 0.5-1.5.

Table 9.1: Induction numbers for the 100 Ωm half-space calculations. HIN (red); LIN (blue); and IIN (green).

	32 Hz	0.5 Hz	0.008 Hz
1 km	1.124	0.14	0.018
3.5 km	3.933	0.492	0.061
7.5 km	8.428	1.053	0.132
9.5 km	10.675	1.334	0.167

The apparent resistivity sensitivities for the half-space model are plotted in Figure 9.3. The sensitivity curves calculated in the high induction number (HIN) range are very similar. At 32 Hz, the HIN curves have a maximum sensitivity at the surface, and decay to zero at ~1,000 m. This is the form of the decay expected for the uniform field MT response (equation 9.4). The shorter offset 3.5 km curve has a marginally larger sensitivity at shallow depths, indicating a gradual departure from the HIN range.

The forms of the low induction number (LIN) and intermediate induction number (IIN) curves are similar and indicate that survey geometry exerts a primary control over the results. There is no frequency dependence in in this range of induction number; the results at 0.5 and 0.008 Hz are identical. The 1 km offset results have the same form at all frequencies, peaking at

a depth of ~350 m. It is observable in the 0.5 and 0.008 Hz panels that, as the offset increases, the form of the curves gradually become flatter and have a deeper, broader peak. The distinction between IIN and LIN responses is not clear.

Figure 9.3: Sensitivity curves for absolute changes in apparent resistivity responses over a 100 Ωm half-space. High induction number – HIN; low induction number – LIN; intermediate induction number – IIN.

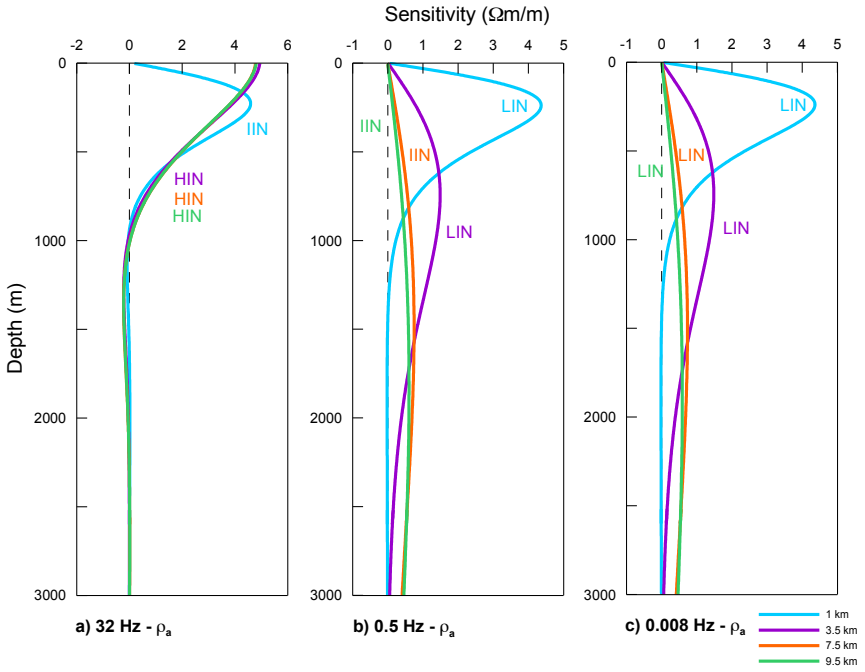

The three defined ranges of sensitivity curves (HIN, LIN, and transitional) are better understood when the independent current contributions from different components of the source field are viewed. Recall from section 4.3.3 that the E_x field from a horizontal electric dipole is the sum of three integral terms (Figure 9.4).

Figure 9.4: Decomposed *Ex* response for a 100 Ωm halfspace at an offset of 10 km in terms of mutual impedance. Three ranges of induction number are identified based on the dominance of contributions from different modes of current.

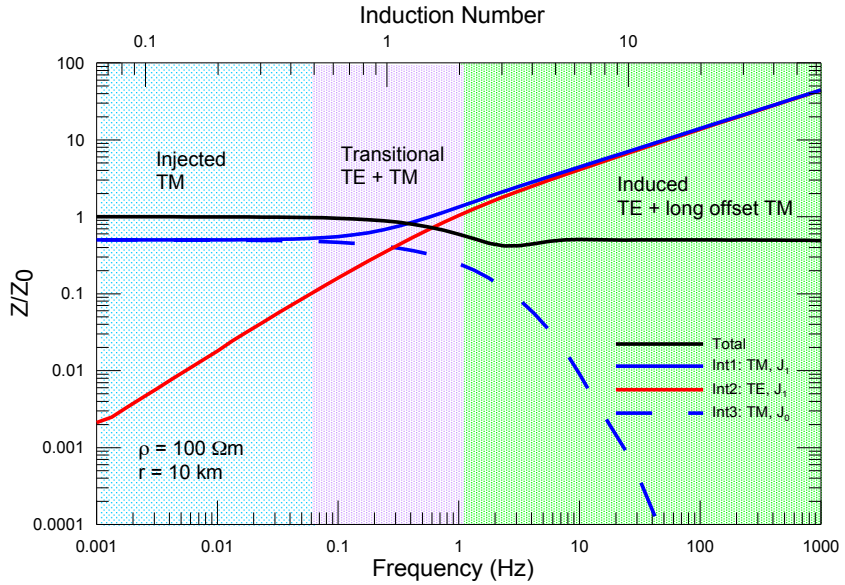

At LIN, the apparent resistivity sensitivity curves reflect a response that is dominated by the injected TM-mode currents. The maximum depth of sensitivity for the apparent resistivity response is ~0.35 of the offset, a result that is predicted by differentiating the theoretical expression for the DC resistivity Fréchet derivative in a half-space (equation 9.5) with respect to depth. The transitional zone could be redefined as the range for which the J_1 TE term exceeds the J_0 TM term but is slightly less than the J_1 TM term. Thus both TE and TM current modes are significant in this range. At HIN, the J_1 terms become equal, and both TE and TM mode currents contribute to the response sensitivity. The sum of these terms produces both frequency independent galvanic currents and frequency dependent inductive currents. In the long offset limit, both of these terms will involve approximately horizontal current flow. For this reason, the shape of the large offset HIN sensitivity functions is the same as that of the inductive uniform-source field MT current system sensitivity functions.

Boerner and West (1989) also present EM sensitivity results separated into induced (TE) and injected (TM) components (Figure 9.5). While the form of the injected kernel sensitivity function is similar to the calculated results, the induced component sensitivity curve shows some differences. Unlike the induced curves calculated here, the induced components for the Boerner and West (1989) study have a maximum sensitivity at depth rather than at the surface. This difference is because the earlier results were not generated at HIN; for the configuration considered by Boerner and West (1989) the induction numbers at 200, 500, and 1000 m are 0.397 0.993, and 1.990, respectively. Also, Boerner and West (1989) define the sensitivity using a relative measure. The decreasing sensitivity at the surface is due to the effects of a DC component of the response that plays an increasing role as the offset decreases.

Figure 9.5: Fractional sensitivity of the injected kernel (left) and induced kernel (right, 100 Hz) for a 100 Ωm halfspace. Observations distances are 200 m (solid), 500 m (dotted) and 1000 m (dashed) (Boerner and West, 1989). Copyright by Oxford Journals. Used with permission; http://www.oxfordjournals.org.uml.idm.oclc.org/our_journals/gji/rights_permissions.html.

The phase sensitivities for the same half-space simulations are shown in Figure 9.6. As with the apparent resistivity, the HIN phase sensitivity curves are similar to one another and

distinct from the rest of the results. These curves have a maximum value at the surface, and then decay to zero with increasing depth. There is a slight overshoot into negative values at greater depth. At lower induction numbers, there is greater variability in the sensitivity functions than for the apparent resistivity calculations. The 32 Hz, 1 km offset curve behaves similarly to the HIN sensitivities but with a sharper decay and less overshoot. For the 0.5 and 0.008 Hz calculations, there is a subtle frequency dependence superimposed upon more obvious geometric effects. Thus the phase sensitivities are more complex than the apparent resistivity sensitivities in the LIN range. The 1 km offset phase sensitivity curves decay from a surface maximum to zero and show slight variations depending on frequency – the 0.5 Hz curve is flatter than its lower frequency counterpart. Longer offset calculations show a comparable level of dependence on frequency and offset, and again demonstrate a transitional behaviour. The orange and green curves in the 0.5 Hz panel decay asymptotically from their surface value to zero whereas in the 0.008 Hz panel the curves decay slowly at first, and then more rapidly with greater depth. The 9.5 km offsets have larger sensitivity values than the 7.5 km offsets.

Figure 9.6: Sensitivity curves for absolute changes in phase responses over a 100 Ωm half-space.

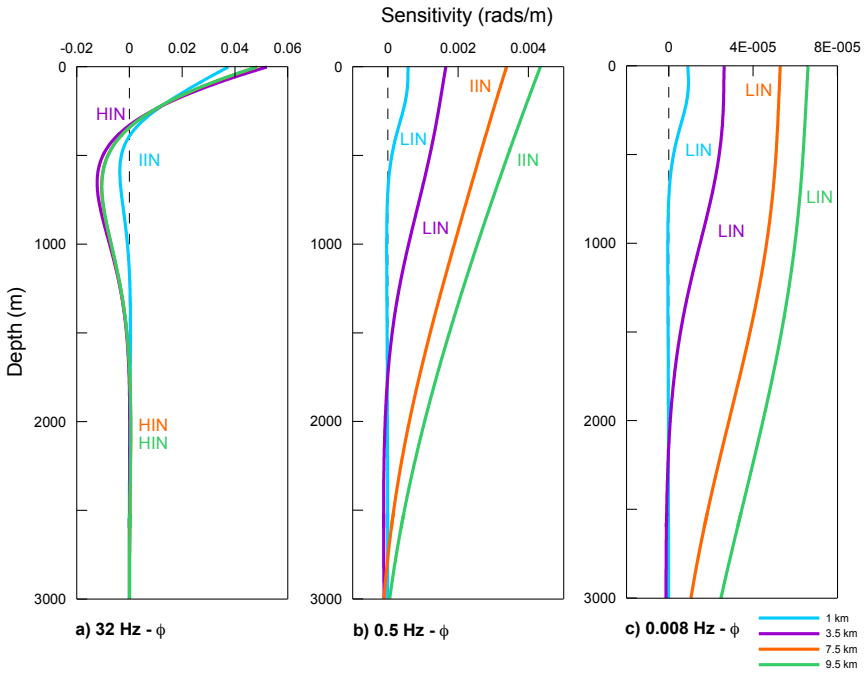

The complexity of the phase Fréchet derivative arises because of the contribution from both in-phase and quadrature components to the response. Whereas the apparent resistivity sensitivity depends almost entirely on the largest integral component (Figure 9.4) the phase response may include a significant contribution from the smaller integral terms that have an imaginary component (Figure 4.10). At LIN the in-phase response will come from the larger TM responses whereas the quadrature response will come from the smaller inductive TE response (Figure 4.10, 9.4).

9.4.2 Embedded layers

To examine the effect of layering on the Fréchet derivatives, first consider the case of a thin, embedded conductor or resistor within a half-space. Gómez-Treviño and Edwards (1983) calculated Fréchet derivatives for a 500 Ωm resistor within a 100 Ωm half-space at 100 Hz for an offset of 1,000 m (induction number: 1.990). This calculation, reproduced in Figure 9.7, verifies

that the present calculations using CR1Dmod are correct. Relative to the half-space apparent resistivity result, the sensitivities within the conductor and resistor are increased and decreased, respectively (indicating non-linearity of the responses). In the case of the conductor, there is diminished sensitivity above and below the embedded layer as the currents are more concentrated within the conductor. The embedded resistor causes the opposite effect: the resistive layer deflects more current flow into the surrounding layers and particularly the overlying layer, leading to increased sensitivity in those layers.

The sensitivity of the phase response to the conductor is similar to the apparent resistivity except that the Fréchet derivative, which is negative immediately above the layer, becomes more negative (increases in magnitude) within the layer. At the depth of the resistor, the phase sensitivity goes to zero.

Figure 9.7: (a) Apparent resistivity and (b) phase sensitivity responses to an embedded conductor or resistor in a half-space at 100 Hz. 1,000 m source receiver separation.

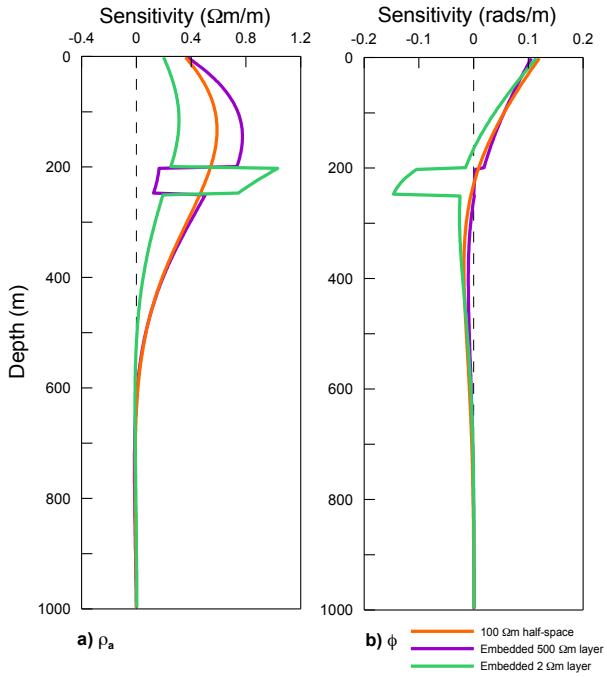

For the Aquistore survey, the effects of layering need to be considered in terms of the induction number. The depth of the embedded layer will also influence these sensitivity functions as it represents an extra distance scale (in addition to the offset and skin depth in the overlying layer) controlling the responses. For the following calculations, the thin conductor/resistor is emplaced at 1,000 m depth. In the case of the layered medium the skin depth becomes dependent on frequency and the meaning of the induction number is less clear. Here, the skin depth is approximated using the 100 Ωm resistivity of the upper layer. The induction number is thus a nominal value in these scenarios. However, the descriptive usage of this term serves to classify the responses based on the characteristic behaviours defined in section 9.4.1. For example, HIN responses exhibit strong frequency-dependence and LIN responses still exhibit strong geometrical dependence.

In a HIN setting, the apparent resistivity sensitivity to the resistor is similar to the half-space result (Figure 9.8). For this configuration the embedded layer occurs within the negative overshoot depth interval of the curve because the depth of the layer is comparable to the skin depth (~890 m). The conductive layer generates an increased negative sensitivity interval for both the apparent resistivity and phase responses, representing an increase in the magnitude of the sensitivity. The apparent resistivity and phase responses are insensitive to the resistor; the sensitivity goes toward zero within this layer.

Figure 9.8: Sensitivity responses for the cases of an embedded resistor and conductor at 1000 m depth. 9.5 km offset, 32 Hz, B = 10.675.

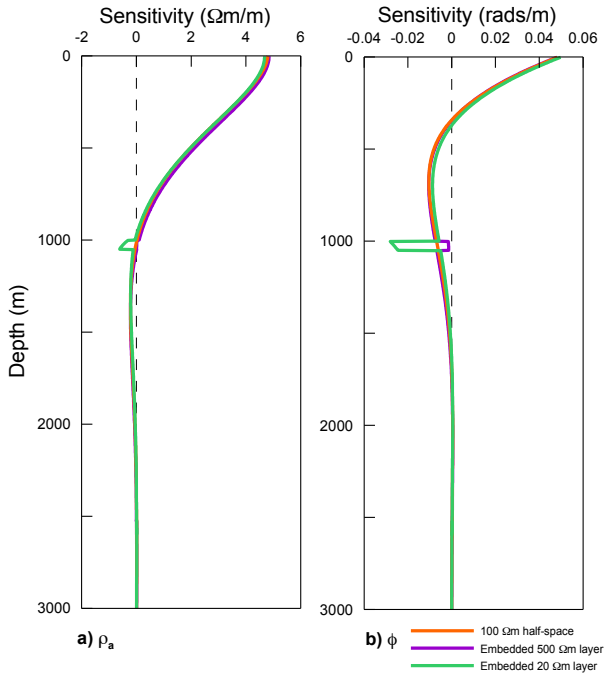

Figure 9.9 shows the effect of the embedded layer for LIN responses. At the depth of the embedded layer, the sensitivities are again low (and much less than the maximum sensitivity) since in this case the depth to the layer and the offset are comparable. For the apparent resistivity curves, the sensitivity increases within a conductor, and decreases to zero for the resistor. Above the embedded resistive layer, the apparent resistivity response is slightly more sensitive than the half-space result. The phase calculations show very little sensitivity to the conductive layer. Unlike the apparent resistivity or the HIN curves, the phase sensitivity at LIN increases within the resistive layer, and goes to zero within the conductive layer.

Figure 9.9: Sensitivity responses for the cases of an embedded resistor and conductor at 1000 m depth. 1 km offset, 0.008 Hz, B = 0.018.

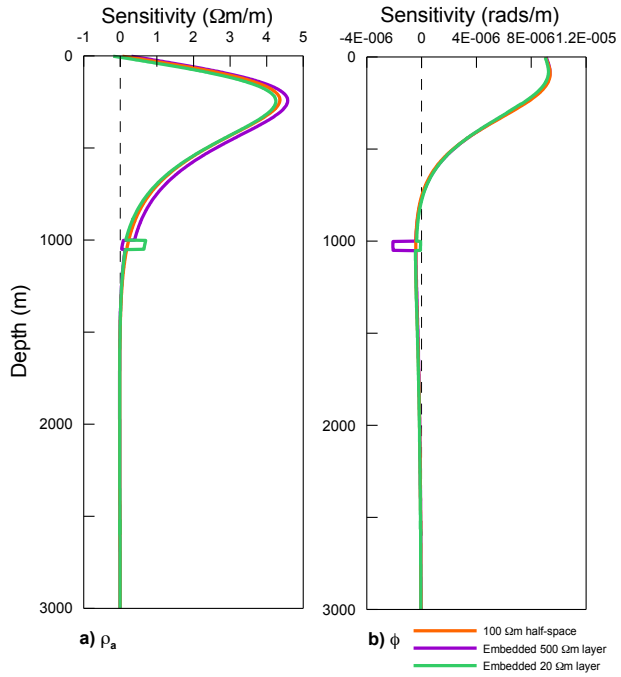

For the transitional induction number range example shown in Figure 9.10, the depth of the embedded layer coincides with the approximate depth of maximum sensitivity. The sensitivity within the conductor is greatly increased from the half-space result for both the apparent resistivity and phase. In contrast, within the thin resistor the sensitivity is greatly decreased.

Figure 9.10: Sensitivity responses for the cases of an embedded resistor and conductor at 1000 m depth. 7.5 km offset, 0.5 Hz, B = 1.053.

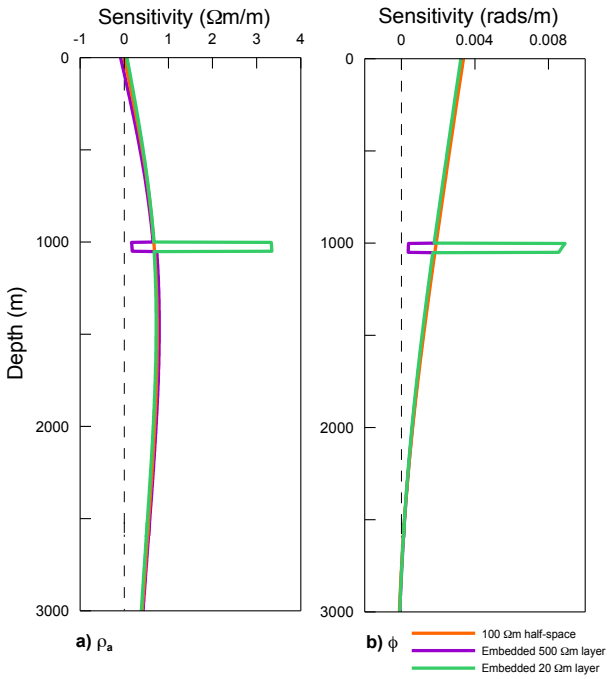

9.4.3 Simple layered model

With some fundamental behaviour of the CSEM Fréchet derivatives now established, the next stage of the analysis examines a test case with a simple layered model that bears a resemblance to the Aquistore setting. The resistivity model considered consists of two thick layers above a half-space, and is meant to represent the Williston Basin in terms of a thick succession of relatively conductive clastic sedimentary rocks overlying more resistive carbonate and evaporite rocks. The 1 km offsets are eliminated from the calculations, as these are not reflective of the Aquistore CSEM surveys. Without this shortest offset, the remaining responses are mainly IIN to HIN.

The results of the Fréchet derivative calculations demonstrate the previously established patterns: the HIN curves have a maximum at the surface and the sensitivity decreases with depth

(Figures 9.11 and 9.12). With decreasing induction number (decreasing frequency and/or decreasing offsets), the responses transition to curves with a maximum at depth. In the HIN case, there is essentially no sensitivity to the deep layering of the basin, as at all offsets the curves go to zero within 500 m of the surface. Sensitivity to the layering in the IIN range varies with frequency as much as with offset. Both the 0.5 and 0.008 Hz responses are more sensitive to the top layer for both apparent resistivity and phase; there is a ~75% decrease in apparent resistivity and phase sensitivities for the lower layer. The 0.5 Hz responses at 7.5 and 9.5 km have a maximum sensitivity at the surface. High negative sensitivity values occur just above the interface between the two layers. With a maximum sensitivity at depth, the 0.5 and 0.008 Hz 3.5 km curves have a form corresponding to those of the injected TM current modes at LIN. Interestingly, the 0.5 Hz 3.5 km curve appears to be more characteristic of injected currents than its lower frequency counterpart. In this case, the effect of the layering on skin depth and induction number calculations is fairly complex, and thus the behaviour of the sensitivity curves is less predictable than for the simpler models presented above.

Figure 9.11: Sensitivity curves for absolute changes in apparent resistivity responses over a simple layered model.

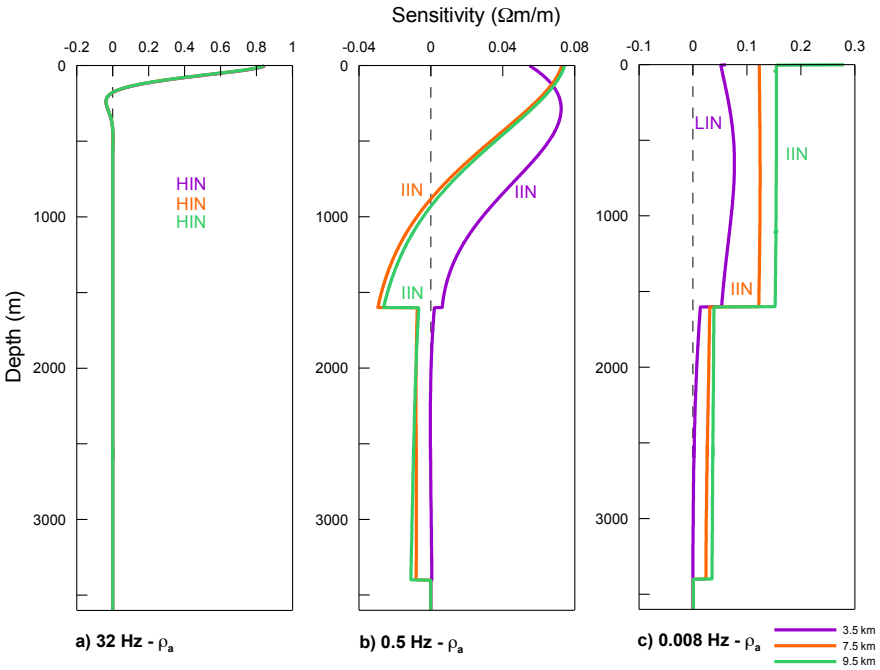

Figure 9.12: Sensitivity curves for absolute changes in phase responses over a simple layered model.

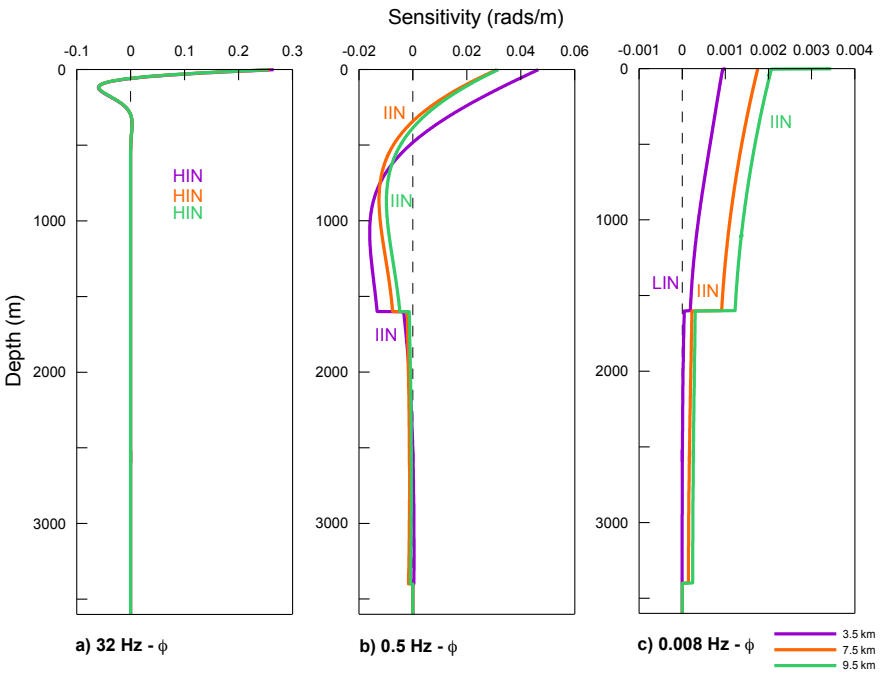

9.4.4 Aquistore model

When the CSEM Fréchet derivatives are calculated for the full Aquistore resistivity model, the results resemble those calculated in the previous section, in that there are significant changes between the generally more conductive shallow layering and the deeper more resistive layers. Detailed and complex relationships between the successive layers are superimposed on the general trend of the simpler two-layer results. The induction numbers shown in Figure 9.13 and 9.14 are once again calculated using the conductivity of the top layer to approximate the skin depth.

The HIN calculations (not shown) are nearly identical to those from the previous section; the maximum sensitivity is at the surface, and decays to near zero very quickly.

At the middle transmission frequency of 0.5 Hz, the long offset responses are sensitive to both shallow and deep basin layers (Figure 9.13). The sensitivity to deeper structures is attributed to a combination of injected and induced current effects at this frequency. In the deeper section of the basin, sensitivities are particularly high for the Interlake and Winnipeg-Deadwood units. These are layers that are significantly more conductive than their overlying strata. Other relatively conductive layers such as the Bakken and Manitoba Formations have negative sensitivities. The shorter offset, 3.5 km curves do not provide the same deep-basin sensitivity.

Figure 9.13: Apparent resistivity (a) and phase (b) response sensitivities for an Aquistore resistivity model at 0.5 Hz.

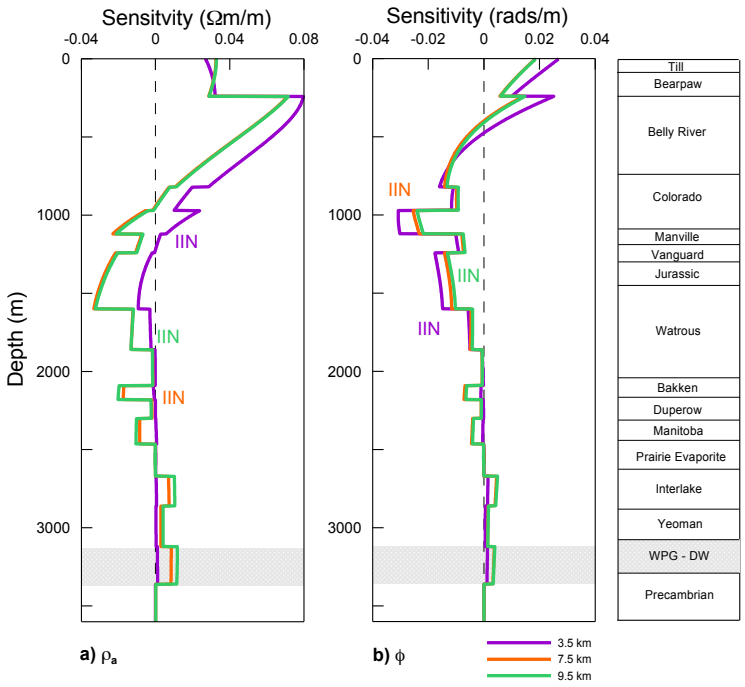

At the lowest frequency (0.008 Hz – Figure 9.14) for which the responses are closer to LIN, there is greater sensitivity to the shallower structures, in particular the layers associated with the Belly River Formation, the lower Colorado Formation, and the Upper Watrous/Jurassic. Each of these layers is more conductive than the overlying materials. At the depths of the Aquistore storage complex, the sensitivity is near zero. The depth range of reduced and negative sensitivities in the 0.5 Hz results corresponds approximately to a region of increased sensitivity in the 0.008 Hz results (from 800 to 2500 m). CSEM transmissions made at these two frequencies are therefore complementary. The fact that the 0.5 and 0.008 Hz results offer sensitivity to conductors at different depth ranges was predicted in the embedded layer calculations (see differences between Figures 9.9 and 9.10).

Figure 9.14: Apparent resistivity (a) and phase (b) response sensitivities for an Aquistore resistivity model at 0.008 Hz.

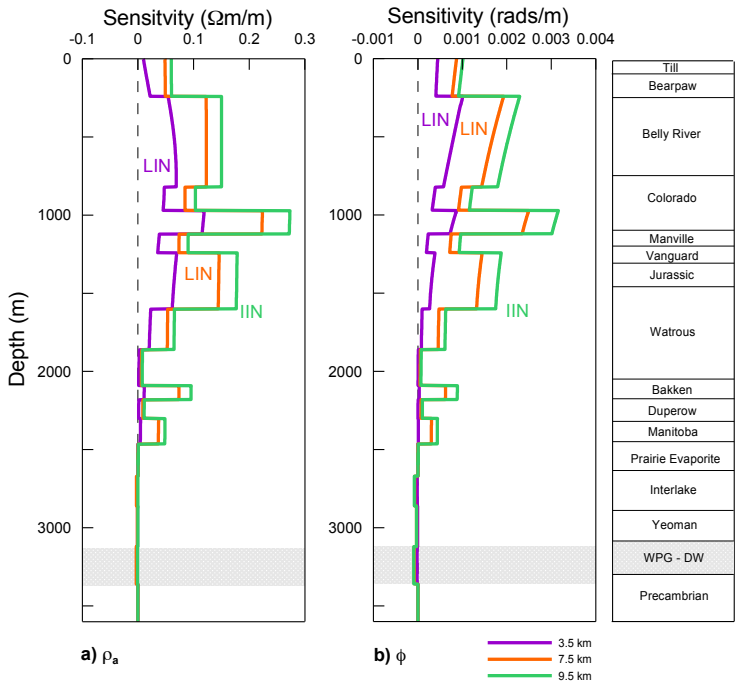

9.5 1D modeling

While the Fréchet derivative calculations are useful in predicting the sensitivity of the CSEM response to changes in the reservoir, they do not provide an immediate sense of whether or not the deviations in the response are measurable in an actual survey in the presence of EM noise and experimental error. As shown by the preliminary 3D modeling (section 4.5), the effect of the CO_2 plume on the EM fields is distinct, but it may not necessarily result in a detectable response. A similar forward modeling exercise to that described in section 8.3.2 is used here to examine the detectability of injected CO_2 using CSEM. The calculations were performed using the original CR1Dmod code (Ingeman-Nielson and Baumgartner, 2006).

The accuracy and repeatability of CSEM measurements at the Aquistore site has not yet been established. The exact values will depend on the ambient EM noise levels at the sites,

receiver sensitivity, signal strength at the receiver, duration of the recordings, and ability to replicate the exact survey configuration. However, results from other CSEM surveys can be used as a general guide to the expected accuracy of the CSEM responses. For CSEM surveys at the Hontomín sequestration site in Spain, for both vertical and horizontal electric dipole sources Vilamajo (2016) (Section 5.2.3 and 5.3.3) determined CSEM responses for frequencies of 4 to 32 Hz at most sites had repeatability of better than 1% in the amplitude and 1^{o} in the phase. Despite differences in the survey configurations and presumably the noise levels between the Hontomín and Aquistore experiments, this example serves to illustrate the expectation for achievable repeatability and measurement errors using a land-based CSEM methodology.

At the 3.5 km offset (e.g. aqi01), the background response shows a broad transition between LIN and HIN, from 0.01 to 100 Hz (Figure 9.15). Changes in the apparent resistivity response are observable at all frequencies less than ~3 Hz; there is some sensitivity to CO_2 injection in the LIN range. Phase sensitivity appears to be more limited at this offset, and is most significant from 0.02 to 2 Hz. The maximum changes in the response occur at 0.2 and 0.7 Hz for the apparent resistivity and 0.5 Hz for the phase. These maximum changes are small: 0.012-0.017 Ωm for the apparent resistivity (0.9% impedance error) and 0.57˚- 0.86˚ for the phase (1.5% impedance error). The $\Delta\rho_a$ values are constant at LIN. The changes in the LIN range are due to galvanic effects, while the changes in the transitional frequency range are the result of both galvanic and inductive effects.

Figure 9.15: Change in CSEM response at 3.5 km due to CO_2 at reservoir depth. Background response (left); difference in response (right).

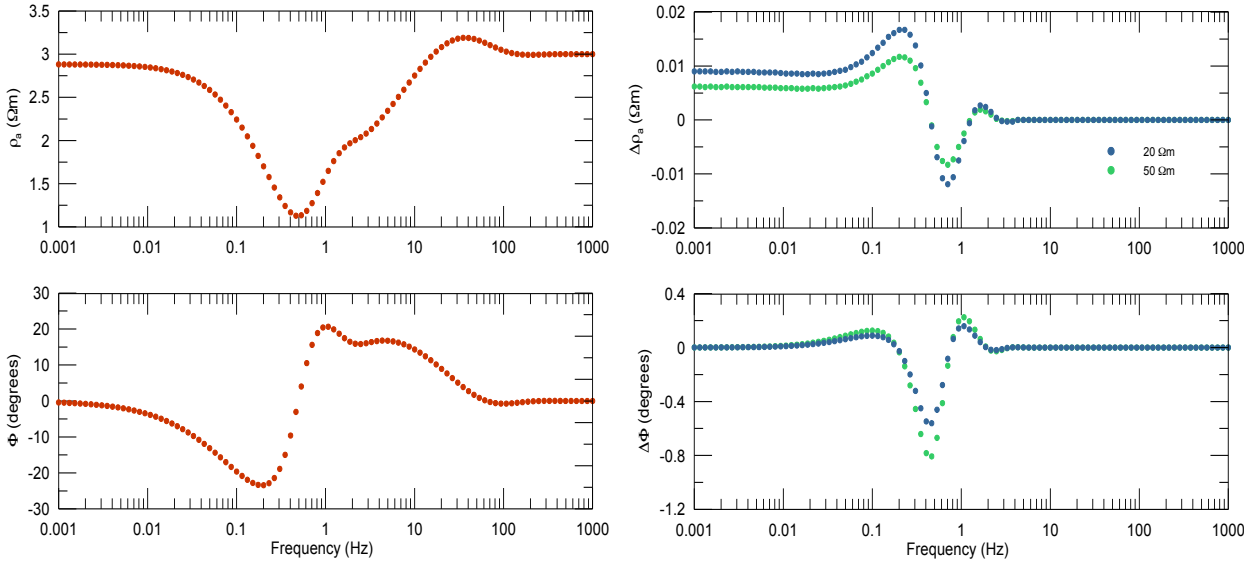

At the longer offsets, the induction number is higher, and there is a slight shift of the maximum sensitivities to lower frequency (Figure 9.16). The observed changes in the responses are greater at this offset with maximum $\Delta\rho_a$ and $\Delta\phi$ values at 0.045 Ωm and 2.87˚ for the 20 Ωm case, and 0.07 Ωm and 4.30˚ for the 50 Ωm case. The equivalent maximum impedance errors are 2.9% for the apparent resistivity and 7.5% for the phase. This frequency range of maximum change is from 0.2 to 0.6 Hz for the apparent resistivity and 0.3 to 0.4 Hz for the phase.

Figure 9.16: Change in CSEM response at 7.5 km due to CO_2 at reservoir depth. Background response (left); difference in response (right).

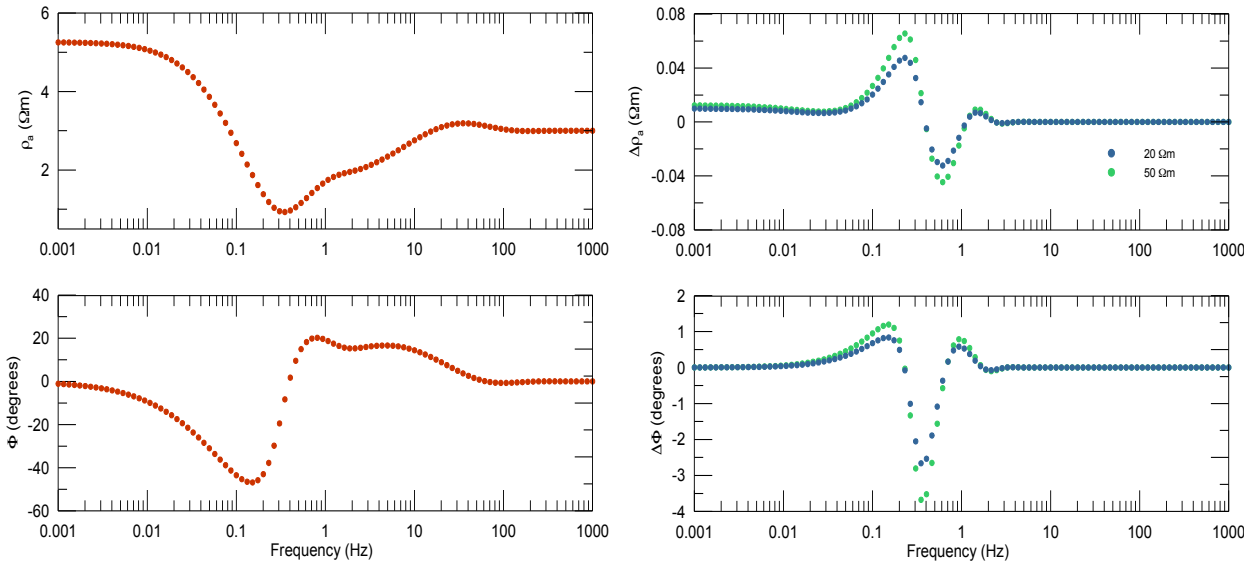

The 9.5 km results do not differ significantly from the 7.5 km results in terms of the frequency range within which the maximum changes occur (Figure 9.17). However, the sensitivities are larger than for the shorter offsets; 0.06 Ωm and 3.43˚ for a 20 Ωm reservoir and 0.08 Ωm and 4.58˚ for a 50 Ωm reservoir. The impedance errors for the maximum apparent resistivity and phase anomalies are 4.1% and 8.0%, respectively. Thus, as predicted from the Fréchet derivative calculations, the best chance of detecting changes at the reservoir level is the longest offset CSEM response at 0.5 Hz.

Figure 9.17: Change in CSEM response at 9.5 km due to CO_2 at reservoir depth. Background response (left); difference in response (right).

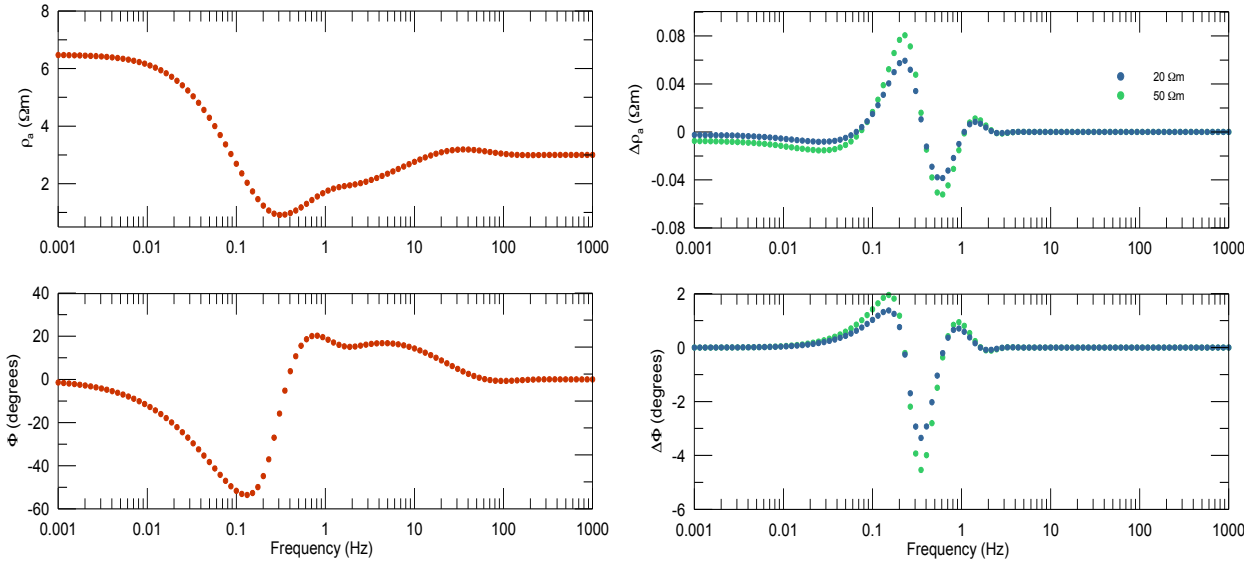

9.6 3D modeling

The 1D modeling results are representative of scenarios where the injected plume is large enough to be approximated as a locally continuous horizontal layer. A 3D test will now be presented to examine the effect of the plume dimensions on the response sensitivity.

The theoretical configuration used only the 0.5 Hz transmission frequency and the 9.5 km offset that have been shown to maximize the sensitivity. The source and receiver are unchanged from the 1D analyses. The CO_2 plume is represented by a 50 Ωm rectangular prism with a thickness of 240 m (the same as the reservoir layer), and variable lateral dimensions. This target is emplaced at the top of the reservoir layer, and centered at an offset of 3.5 km. A fully 1D model with a 50 Ωm reservoir layer was also tested.

Modeling calculations were executed in Emigma v8.1 software. A limitation of this modeling code restricts the number of layers in the model to 8, including the air layer and basal half-space. Thus a new simplified version of the Williston Basin resistivity model was

constructed (Figure 9.18). The Emigma calculations for the background 1D responses were verified against the equivalent CRmod1D results. Resulting apparent resistivity and phase responses were differenced from the pre-injection 1D response.

Figure 9.18: Simplified pre-injection resistivity model of the Williston Basin.

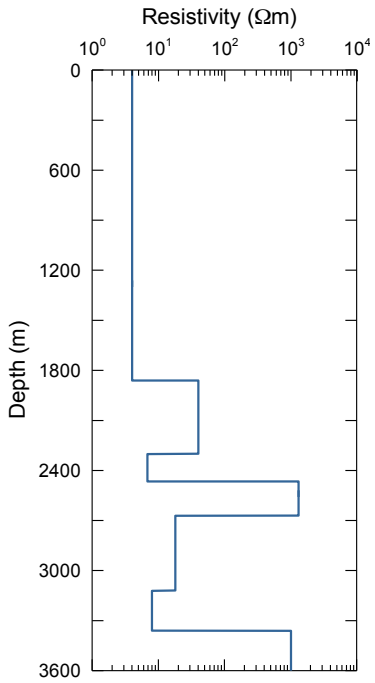

The results of the calculations are summarized in Figure 9.19 and Table 9.2. Pre-injection values of apparent resistivity and phase are 1.25 Ωm and 20.7 ˚, respectively. The effects of large plumes (10 × 10 km and 20 × 20 km) are similar to the 1D case, and demonstrate measurable differences in the phase response. Based on the modeling of Whittaker and Worth (2011), the intermediate sizes (5 × 5 km, 3 × 3 km, and 2 × 2 km) are more realistic estimates of the potential Aquistore plume dimensions, and are therefore of greater interest. These plumes generated anomalies that are from 6 to 33% different from the 1D phase response, and from 20 to 60% different from the 1D apparent resistivity response. The smaller plumes (1× 1 km and 0.5 × 0.5 km) result in negligible anomalies.

Figure 9. 19: Change in apparent resistivity (left) and phase response (right) for different sized 50 Ωm CO_2 plumes. Lateral plume dimensions are shown. The 1D case is also included. The accuracy of a measured CSEM response is expected to be around 1% in magntude ($\Delta\rho_a$=0.02 Ωm) and 1° in phase.

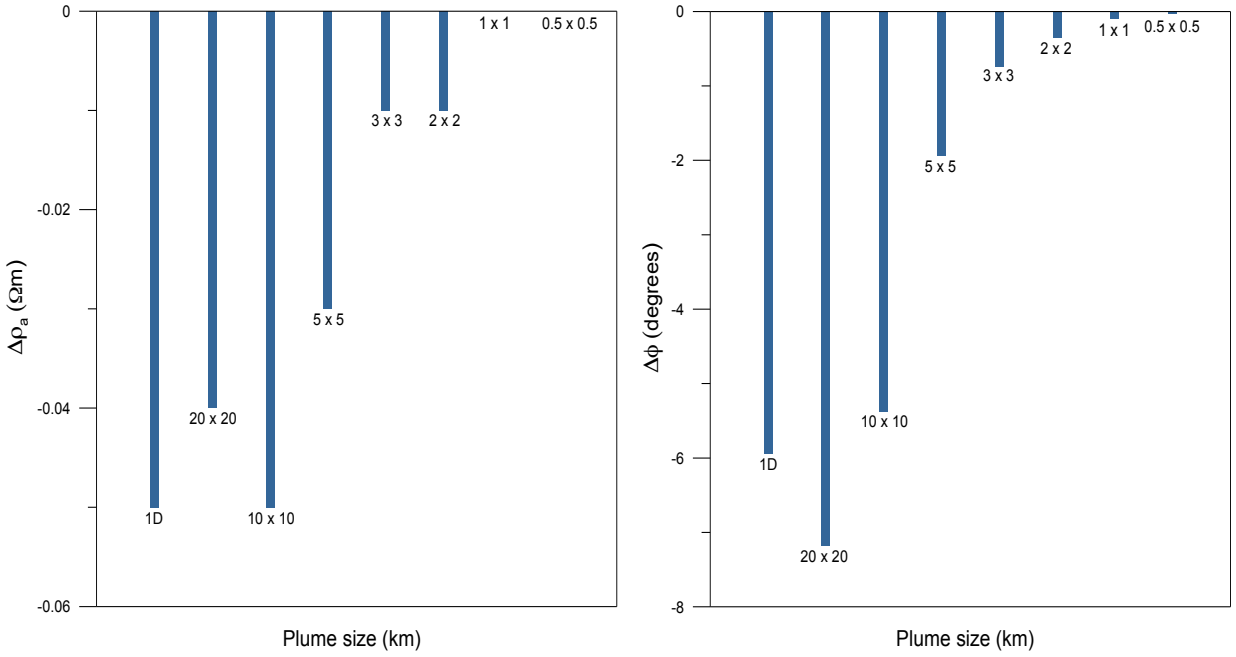

Table 9.2: Apparent resistivity and phase anomalies from 50 Ωm CO_2 plumes.

	$\Delta\rho_a$ (Ωm)	Δϕ (degrees)
1D (saturated)	-0.05	-5.94
20 km x 20 km	-0.04	-7.18
10 km x 10 km	-0.05	-5.38
5 km x 5 km	-0.03	-1.94
3 km x 3 km	-0.01	-0.75
2 km x 2 km	-0.01	-0.35
1 km x 1 km	0	-0.1
0.5 km x 0.5 km	0	-0.03

9.7 Discussion

Fréchet derivatives for the CSEM method provide useful information relating to the EM surveys at Aquistore. The effects of frequency and geometric scaling on the response are quite complex and not always easily separable. The HIN response is an endmember setting for which

the sensitivity results are independent of offset, and at the relatively high frequencies involved, the responses are generally only sensitive to shallow geological layers. These HIN sensitivities are similar to those expected in MT soundings, where the source field is approximated as uniform. Thus the insensitivity of the MT method to deeper features (e.g. the modeling results of section 8.3.2) is reflected in the CSEM HIN results.

At intermediate and low induction numbers, the effects of scaling in the frequency and spatial domains are discernable, but difficult to predict in the presence of complex layering. For some combinations of transmission and recording parameters (e.g. 3.5 km, 0.008 Hz), the soundings mostly represent injected current systems, leading to sensitivity curves with definable and predictable characteristics. A transitional range of parameters lead to complex current patterns that may be exploited to achieve higher sensitivities to deep basin structures. For the most part, the apparent resistivity and phase responses are sensitive to the same structures for a particular pair of CSEM parameters.

In the case of a thin embedded layer in a half-space, there is increased sensitivity within the depth range of conductive anomalies compared to decreased sensitivity within resistors. A control on the size and sign of the sensitivity to conductors is where the layer occurs relative to the sensitivity curve for the half-space e.g., whether it occurs below the depth of maximum sensitivity in a LIN type response or in a zone of negative sensitivity in an HIN type response. For CSEM transmissions that include both inductive and injected components, there is greater sensitivity to the more conductive sections at large depths. This is apparent in both the two-layer and full Aquistore model scenarios.

Based on the results of the Aquistore calculations, the depth range and geological units for which the CSEM response is most sensitive to changes in electrical resistivity depend on the

frequency of the source field. CSEM transmissions at 0.5 and 0.008 Hz should jointly provide the sensitivity required to detect CO_2 injection in the deep sections of the Williston Basin and possible leakage of CO_2 into aquifers at more shallow depths. In both cases, there is a clear differentiation between successive layers based on their relative conductivities. In this sense, the CSEM methodology will not be responsive to CO_2 flooding in relatively resistive strata, e.g. the lower Watrous or Prairie Evaporite Formations.

Changes in the electrical properties of the CO_2 storage complex would be best detected at sites aqi10 and aqi11, with the dipole source transmitting at 0.5 Hz. The aqi01 offset appears to have limited value in actual sequestration monitoring; the sensitivity curves at this location are at best lower sensitivity versions of the longer offset curves, and at worst provide zero sensitivity at important depth ranges. However, to balance these limitations, the aqi01 results will be valuable for constraining the resistivity structures in the upper 500 m in the study area. Within the experimental confines presented by previous Aquistore CSEM surveys, there is sufficient sampling using varied transmission frequencies and survey offsets to provide sensitivity to structure in both shallow and deep sections of the Williston Basin.

These analyses have demonstrated that the CSEM methodology's primary advantage for sequestration monitoring is the capacity to detect changes in relatively conductive layers over a range of basin depths using the inductive component of the dipole source field. This is in part due to the reservoir layer being relatively conductive in a pre-injection setting and in early stages of the injection. The injected TM currents serve to increase the depth range in which there is sensitivity to these conductive strata, and would be useful for determining the reservoir layer resistivity in a post-injection setting. Thus designing a sounding in the intermediate induction number range is of high importance in this application of the CSEM method.

While both the apparent resistivity and phase demonstrate similar types of sensitivity in most scenarios, changes to the phase response are far more likely to be at a detectable level. The 4.58˚ phase difference for a 1D 50 Ωm CO_2-saturated layer detected at an offset at 9.5 km and 0.5 Hz transmission frequency is the most significant deviation from the background response. Given sufficient stacking, a successful CSEM experiment should be able to operate within this limit; for EM surveys at the Hontomín sequestration site, Vilamajo (2016) reports phase measurement errors of 0.38˚ to 1.00˚ using a horizontal electric dipole transmitter. The apparent resistivity changes are less significant, on the order of hundredths of Ωm.

Compared to the results from the equivalent 1D MT modeling, the optimal CSEM results demonstrate greater sensitivity to the reservoir layer. The minimum required error levels in the MT impedances for detection of the anomalies are 3.5% for apparent resistivity and 2.4% for phase, whereas for the CSEM impedance errors, these thresholds are 4.1% and 8.0%. The maximum MT anomalies occur in the 40-100 s period range compared to 1-5 s for the CSEM anomalies.

The above considerations are based on a 1-D model of the CO_2 plume. For a 10 km offset this situation would require a reservoir with a lateral extent of at least 5 km to achieve a potentially measurable phase anomaly of 1.94˚. This anomaly would be detectable provided that the experimental error on the measurements is less than 3.4%. A smaller 3D reservoir may have a substantially smaller response; the more realistic scenario of a plume that measures 3 km in diameter requires an error level of less than 1.3% to detect a 0.75˚ phase anomaly. In order to establish a final detectability threshold for these phase anomalies, a repeatability study must be completed for the experimental CSEM setup.

Chapter 10: Summary and Conclusions

10.1 Summary

The goal of this thesis project has been to conduct a rigorous pre-injection study of the potential for EM surface-based methods to monitor the resistivity change associated with CO_2 injection at the Aquistore site. This research has included a breadth of topics covering both data-driven and theoretical investigations of the MT and CSEM methodologies. Studies of the MT data have extended from the acquisition of three full datasets through to processing, analyses, and inversions. Two CSEM datasets have also undergone a preliminary characterization. The focus of the theoretical studies has been to examine the effectiveness of the CSEM method at detecting injected carbon.

As reported in Chapter 5, the repeated EM acquisition surveys have been successful in establishing a procedure for the collection of MT and CSEM data at Aquistore which may be useful in future work. Analyses of the data have led to characterization of the CSEM and MT signals, calculation of the MT response, and characterization of local sources of EM noise in the time, frequency, and spatial domains. Quantitative comparisons of final MT results define the levels of spatial variability, noise and repeatability of the responses. The 1D inversion of the MT response, constrained by a borehole resistivity log, have produced a reference 1D model of the resistivity structure of the rocks of the Williston Basin in the study area. Finally, sensitivity analysis and 1D and 3D modelling have yielded greater understanding of CSEM responses, allowing optimization of future CSEM studies at the Aquistore site.

10.2 Synthesis

While the research has examined varied aspects related to the EM monitoring objectives at the Aquistore site, the combined implications of these findings have yet to be discussed in this thesis. From the perspective of applying EM methodologies to continued CO_2 monitoring, there are many positive results from the research that suggest that the approach used for the pre-injection EM surveys is suitable for additional surveys. Over three separate surveys, the strategies for recording and processing MT data have become refined to allow for the relatively straightforward generation of high quality site responses. These responses are well understood and provide a definition of the background geoelectric structure. Both the fieldwork and the resulting impedance estimates are shown to have a high level of potential repeatability; in the absence of strong noise sources, the responses have been shown to be repeatable to within errors of 1-3% on the MT impedances.

The likelihood of any future surveys being adversely affected by pervasive broadband noise, as in 2014, appears low, considering that the best explanations for the source of this noise are related to temporary construction or maintenance operations. Regardless, complications related to potentially high noise levels should be anticipated. As a means of mitigating noise effects, the SNS-RR method could be incorporated into the processing workflow, provided that the aqi02 and aqi15 pair of sites continues to be installed for remote reference purposes. This technique is untested on the Aquistore data, but its potential application to correlated noise in the main survey area is promising. Coordination with Boundary Dam staff on operations near to the injection well and pipeline to ensure any active noise sources are temporarily turned off during MT acquisition could also serve to avoid problems from unnecessary noise sources.

The 1D inversions that have been employed to define the structure of the Williston Basin made significant use of the *a priori* resistivity log information. In addition to defining a resistivity model, this approach has successfully demonstrated the value of using a high quality starting model and *a priori* model constraints. A single-site 1D approach to the MT inversion was justifiable in the pre-injection setting; the calculations of spatial variability of responses show that the Phanerozoic response is generally uniform, with 1-2% variations in impedances across the study area. However, in the next stages of the project, a 3D CO_2 plume contained within the reservoir will require multidimensional inversions. In turn, this approach would benefit significantly from a greater number of sites with high quality MT responses than were available in the 2013 and 2014 surveys. However, early indications from the 2015 dataset suggest that consistent and robust estimation of MT responses at multiple sites is achievable now that the field procedures are established, as long as the strong broadband noise is not present. The constrained inversion methodology presented in Chapter 8 has proven to be effective. Future 2D or 3D inversions would benefit from the similar use of the *a priori* resistivity model. Further modelling is also required to understand the distorting effect of metallic infrastructure on the MT response at aqi01.

A 1D modeling exercise has demonstrated that the MT method has limited sensitivity to the reservoir layer. Resolution of this layer is also poor. Given reasonable expectations for the measurement errors and response repeatability, CO_2 injected into the reservoir will not be detectable from MT responses, and thus the CSEM method is necessary to the sequestration monitoring goals.

It has been shown that the design of CSEM surveys at Aquistore was appropriate for the target and that the implementation of the CSEM surveys has been successful. Resistivity

changes to the Winnipeg-Deadwood storage complex associated with a large plume are theoretically observable in the phase response at the large offset sites aqi10 and aqi11 for a 0.5 Hz transmission. In the next stages of this project, a priority will be the testing and development of data processing techniques for the CSEM recordings.

Limiting factors in the effectiveness of these CSEM monitoring techniques are the injection schedule and total volume of sequestered CO_2. Based on the preliminary modeling of Whittaker and Worth (2011), it would take 25 years to produce a plume that is 3 km in diameter working on a theoretical injection schedule that is already ahead of the on-site operations. A plume of this size would be at the limit of CSEM detectability, with 0.75˚ phase anomaly at site aqi10. Therefore, detection of the plume at reservoir depths appears to be a challenging assignment even in the most optimistic modeling scenarios.

A more effective application of these surface EM methodologies would be monitoring focussed on potential CO_2 leakage into shallower rock formations. Sensitivity to deviations from the baseline response in relatively conductive Mesozoic formations is observable at the low induction number range of the experimental setup (e.g. 0.008 Hz transmission at aqi01). The 3D modeling exercise described in section 4.5 also indicates that shallower resistive targets produce larger and potentially more measurable signals. Finally, the 1D MT inversion methods have demonstrated that the MT responses are highly sensitive to changes in the electrical properties of some of these shallower layers, such as the Upper Watrous.

10.3 Conclusions

The key findings of this study are:

- The background MT response at the Aquistore site consists of a dominantly 1D response over the period range from 10^{-4} to 10^{1} s, defining the resistivity structure of the Quaternary and Phanerozoic sediments. At longer periods, Precambrian structures, including the NACP conductor, result in a multidimensional response. The Phanerozoic and Precambrian parts of the response are spatially uniform at the scale of the survey area except for an area adjacent to the injection well, where the responses are distorted by metallic infrastructure.
- The field work and processing procedures used to produce the MT responses show a high level of repeatability outside of a broad band noise source. Outside the frequency range where significant noise is present, the impedance responses from 2013 and 2014 surveys are repeatable to within 3% of one another. The MT method is therefore well suited for time-lapse monitoring.
- Based on frequency domain, spatial coherence, and polarization analysis, the broadband noise (1-140 Hz) is attributed to pipeline monitoring or cathodic protection operations taking place during the 2014 MT fieldwork. Despite robust and remote reference processing, and significant data editing, the noise prevented determination of reliable MT responses over much of the < 1 s period range. This noise appears to have been temporary, as it was absent or present at much lower levels during the 2013 and 2015 MT surveys, and it therefore may not impact future EM surveys.
- 1D MT inversion constrained by borehole log resistivity data has successfully defined a reference resistivity model for the study area. This model consists of 18 layers

representing the electrical properties of the sedimentary formations of the Williston Basin.

- Injection of CO_2 into the Winnipeg-Deadwood sandstones theoretically produces a measurable change in the phase response for a 0.5 Hz transmission at sites aqi10 and aqi11 or at similar offsets, assuming a large plume and high level of gaseous CO_2 pore saturation.
- The proposed CSEM methodology is unlikely to detect a small volume of CO_2 at reservoir depth. There is greater potential for monitoring upward leakage of CO_2 into shallower formations using CSEM.

10.4 Recommendations

The following recommendations are made for the continued study of surface-based EM monitoring at Aquistore:

- The procedures defined here for fieldwork, data processing, and MT inversions are deemed to have been successful and should be taken advantage of in order to expedite the workflow for producing future MT responses.
- Potentially noisy conditions should be anticipated. Processing methods for dealing with coherent broadband noise, such as the SNS-RR technique, need to be prepared as a contingency for the potential presence of noisy signals. Coordination with SaskPower staff prior to fieldwork should aim to avoid the concurrence of data acquisition and pipeline maintenance.
- A multi-dimensional approach to MT inversions will be required in the post-injection stage.

- Processing methods for CSEM responses need to be developed and tested on the 2013 and 2015 datasets. This research will define the background CSEM response and provide insights into the effectiveness and repeatability of the survey procedures e.g. the number of stacks required.
- Further 1D and 3D CSEM modeling of shallow resistive targets should be explored in order to gain a better understanding of the effectiveness of leakage monitoring.
- Following the generation of the CSEM responses, the compatibility of the MT and CSEM methods needs to be tested. Joint inversions of these datasets will determine the degree to which these methods are complementary.

References

Ádám, A., Szarka, L., Verö, J., and Wallner, Á. (1986): Magnetotellurics (MT) in mountains – noise, topographic and crustal inhomogeneity effects; *Physics of the Earth and Planetary Interiors*, Volume 42, pages 165-177.

Anderson, D.B. (1988): Stratigraphy and depositional history of the Deadwood Formation (Upper Cambrian and Lower Ordovician), Williston Basin, North Dakota; unpublished MSc thesis, *University of North Dakota*, 330 pages.

Anna, L.O. (2013): Geologic assessment of undiscovered oil and gas in the Williston Basin province, Montana, North Dakota, and South Dakota; *U.S. Geological Survey Digital Data Series DDS-69-W*, Chapter 3 *in* Assessment of undiscovered oil and gas in the Williston Basin province, Montana, North Dakota, and South Dakota, 2010, 56 pages.

Ansdell, K.M. (2005): Tectonic evolution of the Manitoba-Saskatchewan segment of the Paleoproterozoic Trans-Hudson Orogen, Canada; *Canadian Journal of Earth Sciences*, Volume 42, no. 4, pages 741-754.

Aquistore (2016): Aquistore web page. http://aquistore.ca/, accessed 02 April, 2016.

Aster, R.C., Borchers, B., and Thurber, C.H. (2005): Parameter estimation and inverse problems, Elsevier Academic Press, Burlington, MA, 301 pp.

Bachu, S. (2002): Suitability of the subsurface in Saskatchewan and Manitoba for geological sequestration of anthropogenic carbon dioxide; *Alberta Geological Survey*, Alberta Energy and Utilities Board, 81 pp.

Bachu, S. (2003): Screening and ranking of sedimentary basins for sequestration of CO_2 in geological media in response to climate change; *Environmental Geology*, Volume 44, pages 277-289.

Bachu, S., Bonijoly, D., Bradshaw, J., Burruss, R., Holloway, S., Christensen, N.P., and Mathiassen, O.M. (2007): CO_2 storage capacity estimation: methodology and gaps; *International Journal of Greenhouse Gas Control*, Volume 1, pages 430-443.

Baird, D.J., Knapp, J.H., Steer, D.N., Brown, L.D., and Nelson, K.D. (1995): Upper-mantle reflectivity beneath the Williston basin, phase-change Moho, and the origin of intracratonic basins; *Geology*, Volume 23, pages 431-434.

Bendat, J.S. and Piersol, A.G. (1971): Random data: analysis and measurement procedures. Wiley-Interscience, New York, 407 pp.

Benson, S.M. and Cole, D.R. (2008): CO_2 sequestration in deep sedimentary formations; *Elements*, Volume 4, pages 325-331.

Bergmann, P., Schmitt-Hattenberger, C., Kiessling, D., Rücker, C., Labitzke, T., Henninges, J., Baumann, G., and Schütt, H. (2012): Case history: Surface-downhole electrical resistivity tomography applied to monitoring of CO_2 storage at Ketzin, Germany; *Geophysics*, Volume 77, pages B523-B267.

Binda, P.L. and Simpson, E.L. (1989): Petrography of sulphide-coated grains from the Ordovician Winnipeg Formation, Saskatchewan, Canada; *European Journal of Mineralogy*, Volume 1, pages 439-453.

Blakey, R., Late Cambrian paleogeography (500 Ma): Colorado Plateau Geosystems. Website accessed December 17, 2015, http://cpgeosystems.com/images/NAM_key-500Ma_LCam-sm.jpg.

Boerner, D.E. and West, G.F. (1989): A spatial and spectral analysis of the electromagnetic sensitivity in a layered earth; *Geophysics Journal International*, Volume 98, pages 11-21.

Börner, J.H., Herdegen, V., Repke, J-U., and Spitzer, K. (2013): The impact of CO_2 on the electrical properties of water bearing porous media – laboratory experiments with respect to carbon capture and storage; *Geophysical Prospecting*, Volume 61, pages 446-460.

Börner, J.H., Herdegen, V., Repke, J-U., and Spitzer, K. (2015): The electrical conductivity of CO_2-bearing pore waters at elevated pressure and temperature: a laboratory study and its implications in CO_2 storage monitoring and leakage detection; *Geophysics Journal International*, Volume 203, pages 1072-1084.

Bosch, D., Ledo, J., Queralt, P., Bellmunt, F., Luquot, L., and Gouze, P. (2016): Core-scale electrical resistivity tomography (ERT) monitoring of CO_2-brine mixture in Fontainebleau sandstone; *Journal of Applied Geophysics*, Volume 130, pages 23-36.

Caldwell, T.G., Bibby, H.M., and Brown, C. (2004): The magnetotelluric phase tensor, *Geophysics Journal International*, Volume 158, pages 457-469.

Chave, A.D. (1984): The Fréchet derivatives of electromagnetic induction; *Journal of Geophysical Research*, Volume 89, pages 3373-3380.

Chave, A.D. and Cox, C.S. (1982): Controlled electromagnetic sources for measuring electrical conductivity beneath the oceans 1. Forward problem and model study; *Journal of Geophysical Research*, Volume 87, pages 5327-5338.

Chave, A.D. and Weidelt P. (2012): The theoretical basis for electromagnetic induction. *Chapter 2 in* The Magnetotelluric Method: Theory and Practice, *edited by* Chave, A.D. and Jones, A.G., Cambridge University Press, pages 19-49.

CO2CRC (2008): Storage capacity estimation, site selection and characterization for CO_2 storage projects, Report No. RPT08-1001, page 52.

Daley, T.M., Smith, J.T., Breyer, J.H., and LaBrecque, D. (2014): Borehole EM monitoring at Aquistore: Final report to the carbon capture project (CCP), 30p

Dietrich, J.R., Majorowicz, J.A., and Thomas, M.D. (1999): Willison basin profile, southeast Saskatchewan and southwest Manitoba: a window of basement-sedimentary cover interaction; *Geological Survey of Canada*, Open File 3824, 2 pages.

Dixon, J. (2008): Stratigraphy and facies of Cambrian to Lower Ordovician strata in Saskatchewan; *Bulletin of Canadian Petroleum Geology*, Volume 56, pages 93-117.

Dwight, H.B. (1961): Tables of integrals and other mathematical data, Fourth Edition, MacMillan Publishing, New York, NY, 336 pp.

Edwards, R.N., Wolfgram, P.A., and Judge, A.S. (1988): The ICE-MOSES experiment: mapping permafrost zones electrically beneath the Beaufort Sea; *Marine Geophysical Researches*, Volume 9, pages 265-290.

Egbert, G.D. (1997): Robust multiple stations magnetotelluric data processing; *Geophysics Journal International*, Volume 130, pages 475-496.

Escalas, M., Queralt, P., Ledo, J., and Marcuello, A. (2013): Polarisation analysis of magnetotelluric time series using a wavelet-based scheme: a method for detection and characterisation of local noise sources; *Physics of the Earth and Planetary Interiors*, Volume 218, pages 31-50.

Ferguson, A.G., Betcher, R.N., and Grasby, S.E. (2007): Hydrogeology of the Winnipeg Formation in Manitoba, Canada; *Hydrogeology Journal*, Volume 15, pages 573-587.

Ferguson, I.J. (2012): Instrumentation and field procedures. *Chapter 9 in* The Magnetotelluric Method: Theory and Practice, *edited by* Chave, A.D. and Jones, A.G., Cambridge University Press, pages 421-479.

Fleury, M. and Deschamps, H. (2008): Electrical conductivity and viscosity of aqueous NaCl solutions with dissolved CO_2; *Journal of Chemical and Engineering Data*, Volume 53, pages 2505-2509.

Fowler, C.M.R. and Nisbet, E.G. (1985): The subsidence of the Williston Basin; *Canadian Journal of Earth Sciences*, Volume 22, pages 408-415.

Fyson, W.K. (1961): Deadwood and Winnipeg stratigraphy in south-western Saskatchewan; *Saskatchewan Department of Mineral Resources-Petroleum and Natural Gas Branch-Geology Division*, Report no. 64, 33 pages.

Gasperikova, E., and G. M. Hoversten (2006): A feasibility study of nonseismic geophysical methods for monitoring geologic CO_2 sequestration; *The Leading Edge*, Volume 25, pages 1282–1288.

Gibbins, J. and Chalmers, H. (2008): Carbon Capture and Storage; *Energy Policy*, Volume 36, pages 4317-4322.

Global CCS Institute (2015): Aquistore: Project summary report; *Global CCS Institute*, 140 pages.

Goldstein, M.A. and Strangway, D.W. (1975): Audio-frequency magnetotellurics with a grounded electric dipole source; *Geophysics*, volume 40, pages 669-683.

Gómez-Treviño, E. and Edwards, R.N. (1983): Electromagnetic sounding in the sedimentary basin of southern Ontario – a case history; *Geophysics*, Volume 48, pages 311-330.

Gowan, E.J., Ferguson, I.J., Jones, A.G., and Craven, J.A. (2009): Geoelectric structure of the northeastern Williston basin and underlying Precambrian lithosphere; *Canadian Journal of Earth Sciences*, Volume 46, pages 441-464.

Grayver, A.V., Streich, R., and Ritter, O. (2014): 3D inversion and resolution analysis of land-based CSEM data from the Ketzin CO_2 storage formation; *Geophysics*, Volume 79, E101-E114.

Greggs, D.H. (2000): The stratigraphy, sedimentology, and structure of the lower Paleozoic Deadwood formation of western Canada; unpublished M.Sc. thesis, *University of Calgary*, 182 pages.

Groom, R.W. and Bailey, R.C., (1989): Decomposition of Magnetotelluric Impedance Tensors in the Presence of Local Three-Dimensional Galvanic Distortion; *Journal of Geophysical Research*, Volume 94, no. B2, pages 1913-1925.

Hayward, T. (2014): Sensitivities of electromagnetic geophysical responses in anisotropic media and applications to a magnetotelluric survey near Churchill, Manitoba; unpublished B.Sc. thesis, *University of Manitoba*, 156 pages.

Hibbs, A. (2013): Test of a new BSEM configuration at Aquistore, and its application to mapping injected CO_2, June 26, 2013. BP project Task 1 report, 7 pp.

Hoffman, P.F. (1988): United Plates of America, the birth of a craton: Early Proterozoic assembly and growth of Laurentia; *Annual Review of Earth and Planetary Sciences*, Volume 16, pages 543-603.

Holloway, S. and Savage, D. (1993): The potential for aquifer disposal of CO2 in the UK; *Energy Conversion and Management*, Volume 34, pages 925-932.

Ingeman-Nielsen, T. and Baumgartner, F. (2006): CR1Dmod: A Matlab program to model 1D complex resistivity in electrical and electromagnetic surveys; *Computers and Geoscience*, Volume 32, pages 1411-1419.

IPCC. (2005): Underground geological storage. In: Metz B, Davidson O, de Coninck HC, Loos M, Meyer LA (eds) IPCC Special Report on Carbon Dioxide Capture and Storage, prepared by Working Group III of the Intergovernmental Panel on Climate Change. Cambridge University Press, Cambridge, UK, and New York, USA, pp 195-276

Irvine, J.A. (1978): Estevan map-area; *in* Coal resources of southern Saskatchewan: A model for evaluation methodology, Whitaker, S.H., Irvine, J.A. and Broughton, P.L. (eds.); *Geological Survey of Canada Economic*, report 30, *Saskatchewan Department of Mineral Resources*, report 209, *Saskatchewan Research Council* report 20, pages 49-67.

Jones, A.G. (1988): Static shift of magnetotelluric data and its removal in a sedimentary basin environment; *Geophysics*, Volume 53, pages 967-978.

Jones, A.G. (1993): The COPROD2 dataset: Tectonic settings, recorded MT data, and comparison of models; *Journal of Geomagnetism and Geoelectricity*, Volume 45, pages 933-955.

Jones, A.G. and Hutton, R. (1979): A multi-station magnetotelluric study in southern Scotland – II. Monte-Carlo inversion of the data and its geophysical tectonic implications; *Geophysical Journal of the Royal Astronomical Society*, Volume 56, pages 351-368.

Jones, A.G., Chave, A.D., Egbert, G., Auld, D., and Bahr, K. (1989): A comparison of techniques for magnetotelluric response function estimation, *Journal of Geophysical Research*, Volume 94, pages 14201-14213.

Jones, A.G. and Craven, J.A. (1990): The North American Central Plains conductivity anomaly and its correlation with gravity, magnetic, seismic, and heat flow data in Saskatchewan, Canada; *Physics of the Earth and Planetary Interiors*, Volume60, pages 169-194.

Jones, A.G., Ledo, J., and Ferguson, I.J. (2005): Electromagnetic images of the Trans-Hudson orogen: the North American Central Plains anomaly revealed; *Canadian Journal of Earth Sciences*, Volume 42, pages 457-478.

Jones, J.W. (1995): Scale-dependent resistivity measurements of the Oracle granite; *Geophysical Research Letters*, Volume 22, pages 1453-1456.

Junge, A. (1996): Characterization of and correction for cultural noise; *Surveys in Geophysics*; Volume 17, pages 361-391.

Kauffman, A.A. and Keller, G.V. (1983): Frequency and Transient Soundings; *Methods in Geochemistry and Geophysics*, 16, Elsevier, New York, 336 pp.

Keller, G.V. (1991): Rock and mineral properties. *Chapter 2 in* Electromagnetic Methods in Applied Geophysics, Volume 1, *edited by* Nabighian, M.N., Society of Exploration Geophysicists, Tulsa, OK, USA, pages 13-55.

Kent, D.M. and Christopher, J.E. (1994): Geological history of the Williston Basin and Sweetgrass Arch; Chapter 27 *in* Geological Atlas of the Western Canada Sedimentary Basin, G.D. Mossop and I. Shetsen (comp.), Canadian Society of Petroleum Geologists and Alberta Research Council, URL <http://www.ags.gov.ab.ca/publications/wcsb_atlas/atlas.html>, accessed on January 7, 2016.

Key, K. (2009): 1D inversion of multicomponent, multifrequency marine CSEM data: Methodology and synthetic studies for resolving thin resistive layers; *Geophysics*, Volume 74, pages F9-F20.

Klappstein, G. and Rostron, B. (2014): Shallow hydrogeological and hydrochemical characterization of the Aquistore CO_2 sequestration site in Estevan, Saskatchewan, Canada; *Energy Procedia*, Volume 63, pages 4971-4976.

Knight, R.J. and Endres, A.L. (2005): An introduction to rock physics principles for near surface geophysics. *Chapter 3 in* Near Surface Geophysics, *edited by* Butler, D.K., Society of Exploration Geophysicists, Tulsa, OK, USA, pages 31-70.

Li, J. and Morozov, I. (2007): Geophysical investigations of the Precambrian basement in south-eastern Saskatchewan and south-western Manitoba; Williston Basin Targeted Geoscience Initiative report, University of Saskatchewan, 19 pages.

Martí, A., Queralt, P., and Roca, E. (2004): Geoelectric dimensionality in complex geological areas: application to the Spanish Betic Chain; *Geophysics Journal International*, Volume 157, pages 961-974.

Martin Nordbotten, J., Celia, M.A., and Bachu, S. (2005): Injection and storage of CO_2 in deep saline aquifers; *Transport in Porous Media*, Volume 58, pages 339-360.

McLean, D.D. (1960): Deadwood and Winnipeg stratigraphy in east-central Saskatchewan; *Saskatchewan Department of Mineral Resources-Sedimentary Geology Division*, Report no. 47, 35 pages.

McLeod, J., Craven, J.A., Ferguson, I.J., and Giroux, B. (2014a): Magnetotelluric and controlled-source EM study of CO_2 sequestration at Aquistore site, near Estevan, Saskatchewan; poster presented at *Electromagnetic Induction Workshop*, 2014, Weimar, Germany.

McLeod, J., Craven, J.A., Ferguson, I.J., Roberts, B.J., Bancroft, B., and Liveda, T. (2014b): Overview of the 2013 baseline magnetotelluric and controlled-source electromagnetic geophysical study of CO_2 sequestration at the Aquistore site near Estevan, Saskatchewan; *Geological Survey of Canada*, Open file 7617, 20 pages.

McLeod, J., Craven, J.A., and Ferguson, I.J. (2015a): Magnetotelluric and controlled-source EM study of CO_2 sequestration at Aquistore site, near Estevan, Saskatchewan; poster presented at *AGU GAC-MAC Joint Assembly*, 2015, Montreal, Canada.

McLeod, J., Craven, J.A., and Ferguson, I.J. (2015b): Magnetotelluric and CSEM study of the Canadian Aquistore CO_2 sequestration site, Estevan, Saskatchewan; presentation at *IUGG General Assembly*, 2015, Prague, Czech Republic.

McLeod, J., Craven, J.A., Ferguson, I.J. and Roberts, B.J. (2015c): Overview of the 2013 and 2014 Baseline Magnetotelluric & Controlled Source Electromagnetic Studies of CO_2 Sequestration at the Aquistore site near Estevan, Saskatchewan, Open File 8101, accepted for publication.

McLeod, J., Ferguson, I.J. Craven, J.A., Roberts, B., Roots, E., and Giroux, B. (2015d): Magnetotelluric and controlled-source EM study of CO_2 sequestration at Aquistore site, near Estevan, Saskatchewan; presentation at *CSPG-CSEG Geoconvention*, 2015, Calgary, Canada.

McLeod, J., Ferguson, I.J., Craven, J.A., and Giroux, B. (2016): Magnetotelluric and controlled-source EM study of CO_2 sequestration at Aquistore site, near Estevan, Saskatchewan, Canada; poster presented at *Electromagnetic Induction Workshop*, 2016, Chiang Mai, Thailand.

Nabighian, M.N. and Macnae, J.C. (1991): Time domain electromagnetic prospecting methods. *Chapter 6 in* Electromagnetic Methods in Applied Geophysics, Volume 2, Part A, *edited by* Nabighian, M.N., Society of Exploration Geophysicists, Tulsa, OK, USA, pages 427-520.

Nakatsuka, Y., Xue, Z., Garcia, H., and Matsuoka, T. (2010): Experimental study on CO_2 monitoring and quantification of stored CO_2 in saline formations using resistivity measurements; *International Journal of Greenhouse Gas Control*, Volume 4, pages 209-216.

Ndiaye, M. (2007): A multipurpose software for stratigraphic signal analysis; unpublished PhD thesis, *University of Geneva*, 113 pages.

Oettinger, G., Haak, V., and Larsen, J.C. (2001): Noise reduction in magnetotelluric time-series with a new signal-noise separation method and its application to a field experiment in the Saxonian Granulite Massif; *Geophysics Journal International*, Volume146, pages 659-669.

Ogaya, X., Ledo, J., Queralt, P., Marcuello, A., and Quinta, A. (2013): First geoelectric image of the subsurface of the Hontomin site (Spain) for CO_2 geological storage: A magnetotelluric 2D characterization; *International Journal of Greenhouse Gas Control*, Volume 13, pages 168-179.

Ogaya, X., Queralt, P., Ledo, J., Marcuello, A., and Jones, A.G. (2014): Geoelectrical baseline model of the subsurface of the Hontomin site (Spain) for CO_2 geological storage in a deep saline aquifer: a 3D magnetotelluric characterisation; *International Journal of Greenhouse Gas Control*, Volume 27, pages 120-138.

Oldenburg, D.W. (1978): The interpretations of direct current resistivity measurements; *Geophysics*, Volume 43, pages 610-625.

Oldenburg, D.W. (1979): One-dimensional inversion of natural source magnetotelluric observations; *Geophysics*, Volume 44, pages 1218-1244.

Osadetz, K.G., Kohn, B.P., Feinstein, S., and O'Sullivan, P.B. (2002): Thermal history of Canadian Willison Basin from apatite fission-track thermochronology – implications for petroleum systems and geodynamic history; *Tectonophysics*, Volume 349, pages 221-249.

Parker, R.L. (1980): The inverse problem of electromagnetic induction: Existence and construction of solutions based on incomplete data; *Journal of Geophysical Research*, Volume 85, pages 4421-4428.

Parker, R.L. (1983): The magnetotelluric inverse problem; *Geophysical Surveys*, Volume 6, pages 5-25.

Parker, R.L. and Whaler, K.A. (1981): Numerical methods for establishing solutions to the inverse problem of electromagnetic induction; *Journal of Geophysical Research: Solid Earth*, Volume 86 (B10), pages 9574-9584.

Parker, R.L. and Booker, J.R. (1996): Optimal one-dimensional inversion and bounding of magnetotelluric apparent resistivity and phase measurements; *Physics of the Earth and Planetary Interiors*, Volume 98, pages 269-282.

Paterson, D.F. (1971): The stratigraphy of the Winnipeg Formation (Ordovician) of Saskatchewan; *Saskatchewan Department of Mineral Resources*, Report 140, 57 pages.

Phoenix Geophysics (2003): V5 System 2000 MTU/MT-A User Guide, Version 1.2, 128 pages.

Phoenix Geophysics (2016): Phoenix web page. http://www.phoenix-geophysics.com/products/sensors/, accessed 22 April, 2016.

Porter, J.W., Price, R.A., and McCrossan, R.G. (1982): The western Canada sedimentary basin; *Philosophical Transactions of the Royal Society of London. Series A, Mathematical and Physical Sciences*, Volume 305, pages 169-192.

Rodi, W.L. and Mackie, R.L. (2012): The inverse problem. *Chapter 8 in* The Magnetotelluric Method: Theory and Practice, *edited by* Chave, A.D. and Jones, A.G., Cambridge University Press, pages 347-420.

SaskPower (2013) SaskPower web page http://www.saskpower.com/, accessed 20 October, 2013.

Schlumberger (2016): Schlumberger web page. http://www.slb.com/services/characterization/petrophysics/wireline.aspx, accessed 11 January, 2016.

Seibel, C. and Bend, S. (2000): An examination of the hydrocarbon-generating potential of the Deadwood Formation and Black Island Member, Winnipeg Formation, Saskatchewan; *in* Summary of Investigations 2000, Volume 1, Saskatchewan Geological Survey, Sask. Energy Mines, miscellaneous report, 20 pages.

SERC - Science and Engineering Research Committee (2013): Aquistore: CO_2 storage at the world's first integrated CCS project, October 29, Calgary, Canada, Presentation to PTAC's 2013 managing CO_2 forum.

Simpson, F. and Bahr, K. (2005): Practical Magnetotellurics. Cambridge University Press, United Kingdom.

Smit, B., Reimer, J.A., Oldenburg, C.M., and Bourg, I.C. (2014): Introduction to Carbon Capture and Sequestration. Imperial College Press, London, United Kingdom.

Smith, M., and Bend, S. (2004): Geochemical analysis and familial association of Red River and Winnipeg reservoired oils of the Williston Basin, Canada; *Organic Geochemistry*, Volume 35, pages 443-452.

Spies, B.R. and Frischknect, F.C. (1991): Electromagnetic Sounding. *Chapter 5 in* Electromagnetic Methods in Applied Geophysics, Volume 2, Part A*, edited by* Nabighian, M.N., Society of Exploration Geophysicists, Tulsa, OK, USA, pages 285-425.

Strack, K.-M., Lüschen, E., and Kötz, A.W. (1990): Long-offset transient electromagnetic (LOTEM) depth soundings applied to crustal studies in Black Forest and Swabian Alb , Federal Republic of Germany; *Geophysics*, Volume 55, pages 834-842.

Stratton, J.A. (1941): Electromagnetic theory: McGraw-Hill.

Streich, R. (2016): Controlled-source electromagnetic approaches for hydrocarbon exploration and monitoring on land; *Surveys in Geophysics*, Volume 37, pages 47-80.

Streich, R., Becken, M., and Ritter, O. (2010): Imaging of CO_2 storage sites, geothermal reservoirs, and gas shales using controlled source magnetotellurics: Modeling studies; *Chemie der Erde*, Volume 70, pages 63-75.

Streich, R., Becken, M, Matzander, U., and Ritter, O. (2011): Strategies for land-based controlled-source electromagnetic surveying in high-noise regions; *The Leading Edge*, Volume 30, pages 1174-1181.

Streich, R., Becken, M., and Ritter, O. (2013): Robust processing of noisy land-based controlled-source electromagnetic data; *Geophysics*, Volume 78, pages E237-E247.

Szarka, L. (1988): Geophysical aspects of man-made electromagnetic noise in the Earth – a review; *Surveys in Geophysics*, Volume 9, pages 287-318.

Varela, F., Tan, M.Y., and Forsyth, M. (2015): An overview of major methods for inspecting and monitoring external corrosion of on-shore transportation pipelines; *Corrosion Engineering Science and Technology*, Volume 50, pages 226-235.

Vigrass, L., Jessop, A., and Brunskill, B. (2007): Regina Geothermal Project; *in* Summary of Investigations 2007, Volume 1, Saskatchewan Geological Survey, Sask. Industry Resources, Misc. Rep. 2007-4.1, CD-ROM, Paper A-2, 21p.

Vilamajo, E. (2016): CSEM monitoring at the Hontomín CO_2 storage site: Modeling, experimental design and baseline results, unpublished Ph.D. thesis, *University of Barcelona*, 181 pages.

Vilamajo, E., Rondeleux, B., Queralt, P., Marcuello, A., and Ledo, J. (2015): A land controlled-source electromagnetic experiment using a deep vertical electric dipole: experimental settings, processing, and first data interpretation; *Geophysical Prospecting*, Volume 63, pages 1527-1540.

Viljanen, A. (2012): Description of the magnetospheric/ionospheric sources. *Chapter 3B in* The Magnetotelluric Method: Theory and Practice, *edited by* Chave, A.D. and Jones, A.G., Cambridge University Press, pages 96-121.

Vozoff, K. (1991): The magnetotelluric method. *Chapter 8 in* Electromagnetic Methods in Applied Geophysics, Volume 2, Part B, *edited by* Nabighian, M.N., Society of Exploration Geophysicists, Tulsa, OK, USA, pages 641-711.

Ward, S.H & Hohmann, G.W., (1988): Electromagnetic Theory for Geophysical Applications. *Chapter 4 in* Electromagnetic Methods in Applied Geophysics, Volume 1, Theory*, edited by* Nabighian, M.N., Society of Exploration Geophysicists, Tulsa, OK, USA, pages 131-311.

Weidelt P. and Chave, A.D. (2012): The magnetotelluric response function. *Chapter 4 in* The Magnetotelluric Method: Theory and Practice, *edited by* Chave, A.D. and Jones, A.G., Cambridge University Press, pages 124-164.

West, G.F. & Macnae, J.C. (1991): Physics of the electromagnetic induction exploration method. *Chapter 1 in* Electromagnetic Methods in Applied Geophysics, Volume 2, Part A, *edited by* Nabighian, M.N., Society of Exploration Geophysicists, Tulsa, OK, USA, pages 5-45.

White, D.J., Roach, L.A.N., Roberts, B., and Daley, T.M. (2014): Initial results from seismic monitoring at the Aquistore CO_2 storage site, Saskatchewan, Canada; *Energy Procedia*, Volume 63, pages 4418-4423.

Whittaker, S. and Worth, K. (2011): Aquistore: a fully integrated demonstration of the capture, transportation and geologic storage of CO_2; *Energy Procedia*, Volume 4, pages 5607-5614.

Wight, D.E., and Bostick, F.X. (1980): Cascade decimation – a technique for real time estimation of power spectra; *Acoustics, Speech, and Signal Processing, IEEE International Conference on ICASSP'80*, Volume 5, pages 626-629.

Zonge and Hughes (1991): Controlled source audio-frequency magnetotellurics. *Chapter 9 in* Electromagnetic Methods in Applied Geophysics, Volume 2, Part B, *edited by* Nabighian, M.N., Society of Exploration Geophysicists, Tulsa, OK, USA, pages 713-809.

Zhdanov, M.S., Endo, M., Black, N., Spangler, L., Fairweather, S., Hibbs, A., Eiskamp, G.A., and Will, R. (2013): Electromagnetic monitoring of CO_2 sequestration in deep reservoirs; *First Break*, Volume 31, pages 71-78.

Zhu, C. and Hajnal, Z. (1993): Tectonic development of the northern Williston basin: a seismic interpretation of an east-west regional profile; *Canadian Journal of Earth Sciences*, Volume 30, pages 621-630.

Description of Appendices

Electronic appendices are available upon request.

Appendix A: Acquisition spreadsheets

Appendix A consists of Excel spreadsheets that contain a log of the acquisition records for the MT and CSEM surveys.

Appendix B: 2013 and 2014 MT data

Appendix B contains .EDI files for the both the preliminary and final MT responses from the 2013 and 2014 MT surveys. The preliminary responses are organized by date of acquisition, while the final responses are organized by receiver station.

Appendix C: Matlab code for statistical analysis

Appendix C contains two original Matlab programs used to produce the results of Chapter 7. The 'compare_MT.m' program is for calculating the RMS misfit between two sets of MT impedance data. The 'read_dmp.m' program is for reading in .dmp files exported from Geotools software and writing out ascii files that are compatible with the 'compare_MT.m' program.

Appendix D: Matlab code for 1D MT inversion

The 'MT_1D_INV.m' program is the code that runs the inversion. The 'sensitivity_1DMT.m', 'fwdMT_B.m', and 'plotresults.m' programs are all subroutines for

calculating the Jacobian, computing forward 1D MT data, and plotting inversion results, respectively. The inputs 'aqi05_data.mat' and 'base_model.mat' are also included.

Appendix E: Matlab code for CSEM forward modeling and sensitivity analysis

Appendix E contains the original CRmod1D package by Ingeman-Nielsen and Baumgartner (2006). The modified version consists of additional code to calculate Fréchet derivatives for the DC resistivity case, provided by Hayward (2014). Additional modifications were made to the EM forward modeling code. Parameters for the numerical perturbation are written into the 'peturb.m' file.